Microstructural Development and Mechanical Properties of Drop Tube Atomized Binary Al-Fe and Ternary Al-Fe-Si Alloys

Mehmet Remzi Abul

Submitted in accordance with the requirements for the degree of

Doctor of Philosophy

The University of Leeds

Institute for Materials Research

School of Chemical and Process Engineering

February, 2022

The candidate confirms that the work submitted is his own, except where work which has formed part of jointly-authored publications has been included. The contribution of the candidate and the other authors to this work has been explicitly indicated below. The candidate confirms that appropriate credit has been given within the thesis where reference has been made to the work of others.

1. Abul, M. R., Cochrane, R. F., & Mullis, A. M. (2022). Microstructural development and mechanical properties of drop tube atomized Al-2.85 wt% Fe. *Journal of Materials Science & Technology*, *104*, 41-51.

2. Abul, M. R., Cochrane, R. F., & Mullis, A. M. (2022). Partitionless solidification and anomalous triradiate crystal formation in drop-tube processed Al-3.9 wt% Fe alloys. *Materials Today Communications*, *31*, 103274.

This copy has been supplied on the understanding that it is copyright material and that no quotation from thus thesis may be published without proper acknowledgement.

The right of Mehmet Remzi Abul to be identified as Author of this work has been asserted by him in accordance with the Copyright, Designs and Patents Act 1988.

Acknowledgements

Abstract

The effect of nonequilibrium solidification on the microstructural development and mechanical properties of Al-2.85 wt% Fe, Al-3.9 wt% Fe, and Al-4.1 wt% Fe-1.9 wt% Fe alloys was studied using a 6.5 m drop tube. Spherical particles with diameters ranging between 850 µm and 38 µm were obtained with the corresponding estimated cooling rates between 155 K s^{-1} and 20,000 K s^{-1}, respectively. The spherical samples were examined using OM and SEM to understand the microstructural evolution, while XRD and TEM were employed for phase identification. Furthermore, microhardness testing was performed to observe the effect of rapid solidification on the mechanical properties of the alloys.

For drop tube atomized Al-2.85 wt% Fe alloys whose diameter were ranging between 850 µm and 53 µm, XRD analysis showed that while α-Al, Al_6Fe, $Al_{13}Fe_4$ were formed in all samples, Al_5Fe_2 was observed in samples with a diameter smaller than 150 µm. SEM and OM results have revealed that samples with a diameter larger than 300 µm had three regions with distinct morphologies: microcellular, dendritic with lamellar interdendritic eutectic, and rod-like eutectic region, which disappeared with decreasing sample size. TEM result has shown that while the interdendritic lamellar eutectic is Al-$Al_{13}Fe_4$, rod-like eutectic is Al-Al_6Fe eutectics. Using EDX, Fe content in α-Al has been found to be rising from 0.37 wt% Fe to 1.105 wt% Fe with decreasing sample size. As a result, the volume fraction of the eutectic measured to be decreasing from 49.7 vol.% to 26.7 vol.% with increasing cooling rate. Microhardness has increased from 55.3 HV$_{0.01}$ to 66.5 HV$_{0.01}$ for ≥ 850 µm and ≤ 75 µm droplets, respectively.

Drop tube atomized Al-3.9 wt% Fe alloy was sieved into 9 different sieve fractions ranging between 850+ µm and 38 µm. In large samples ($d > 212$ µm), large proeutectic $Al_{13}Fe_4$ surrounded by α-Al, dendritic α-Al with interdendritic lamellar eutectic, lamellar eutectic, and rod-like eutectic was observed. The proeutectic $Al_{13}Fe_4$ vanished with decreasing sample size. Featureless Y-shaped structures, which are the first phase to nucleate in the droplet, have emerged in samples with diameters smaller than 212 µm. The solidification in the droplet has proceeded with the formation of divorced eutectic, microcellular α-Al, dendritic α-Al with lamellar interdendritic eutectic and rod-like eutectic. SEM and OM showed that these Y-shaped structures are fragmented. Y-shaped was found to be an internally connected sheet-like morphology by employing serial sectioning. Y-shaped has been revealed to be composed of nano-sized needle-like and spherical precipitates by using TEM. Al_mFe was formed in the Y-

shaped region. The microhardness has increased 50 $HV_{0.01}$ to 83 $HV_{0.01}$ for 850 + µm and $53 \leq d \leq 38$ µm droplets, respectively.

Drop tube atomized Al-4.1 wt% Fe-1.9 wt% Si samples with diameters ranging between 850-53 µm were analysed. XRD results have revealed that there are only two phases: α-Al and Al_8Fe_2Si regardless of sample size. Microstructural analysis has shown dendritic α-Al with interdendritic lamellar eutectic in large samples (d > 300 µm). However, with decreasing sample size, angular nucleation zone has started to emerge in the microstructure. The fraction of samples with such angular nucleation zone has increased with decreasing sample size. EDX analysis from this zone has depicted that while the Fe content is identical to that of the melt, Si content was found to be around 1 wt% Si regardless of sample size. In addition to the angular nucleation zone, propeller-like structures and Y-shaped structures have been observed in fine samples (d < 106 µm). The formation of propeller-like structures indicates that the growth mechanism of angular structure has changed from faceted growth to continuous growth. TEM analysis from the angular region has depicted the formation of clusters of faceted Al_8Fe_2Si formed due to solid-state decomposition. The microhardness of the samples has improved from 72 $HV_{0.01}$ to 90 $HV_{0.01}$ for between 850-150 µm samples, respectively. However, a further decrease in sample size has resulted in the microhardness from 90 $HV_{0.01}$ to 80 $HV_{0.01}$ for 150-53 µm.

Table of Contents

List of Figures

List of Tables

Abbreviations

BSED - Backscatter Electron Dedector

EDX - Energy Dispersive X-Ray

FIB - Focussed Ion Beam

OM - Optical Microscopy

PDF - Powder Diffraction File

SAD - Selected Area Diffraction

SDAS - Secondary Dendrite Arm Spacing

SED - Secondary Electron Dedector

SEM - Scanning Electron Microscopy

TEM - Transmission Electron Microscopy

XRD - X-Ray Diffraction

1. Introduction

Aluminium alloys have been of interest due to their suitable combination of low density, high corrosion resistance, strength and ductility. A considerable amount of Fe and Si is present in most aluminium alloys as alloying elements or impurities [1], [2]. Moreover, the concentration of these elements increases with each recycling process. As the solid solubility of these elements in α-Al is very low, these elements form binary Al-Fe and/or ternary Al-Fe-Si intermetallics [3], [4]. Depending on the processing route, phases formed has detrimental effect on the mechanical properties, corrosion resistance, formability and surface finish of Al alloys [2]. For example, intermetallics such as binary needle-like $Al_{13}Fe_4$ and ternary script-like Al_8Fe_2Si significantly decreases the mechanical properties of the Al alloys [4]. However, rapid solidification can form various thermodynamically metastable binary and ternary phases. The formation of the metastable phases improves the mechanical properties, high temperature strength, elastic moduli of Fe and Si bearing Al alloys[5].

Nonequilibrium (rapid) solidification promotes unique properties of metallic materials such as solid solubility extension, grain size refinement, formation of metastable phases, reduced levels of segregation and formation of amorphous and quasicrystalline phases[6]–[8]. These unique properties improve the mechanical properties of the alloys. There are a number of techniques to achieve rapid solidification such as drop tube processing, electromagnetic levitation, glass fluxing and melt spinning. Among these techniques, drop tube is an important technique because it combines high cooling rates and deep undercooling. Moreover, as the solidification in drop tube takes place during free fall in controlled atmosphere, possible heterogenous nucleation sites such as mould walls are avoided[9], [10]. Furthermore, drop tube is a good analogue for commercial powder production techniques such as high pressure gas atomization (HGPA).

Rapidly solidified aluminium rich Al-Fe alloys promise high temperature use due to the formation of metastable intermetallics. Although, $Al_{13}Fe_4$ is the only stable intermetallic in the Al rich part of the Al-Fe system, nonequilibrium solidification promotes the formation of a number of metastable intermetallic phases. The metastable intermetallics which has been reported include Al_6Fe, Al_5Fe_2, Al_mFe (m=4.0 to 4.4), Al_xFe (x=5.0 to 5.5) and Al_9Fe_2. The formation of these metastable intermetallic phases strongly depends on the cooling rate and the degree of undercooling. For example, Al_xFe forms at relatively low cooling rates while Al_mFe form at higher cooling rate. On the other hand, Al_6Fe, which is the mostly observed metastable

intermetallic, forms at moderate cooling rates. Moreover, rapid solidification has also changed the solidification sequence in Al-Fe alloys. For example, the first phase to solidify in rapidly solidified Al-3.6 wt%Fe [11] and Al-1.9 wt%Fe [5] alloys was found to be α-Al rather than $Al_{13}Fe_4$ although both alloys are hyper eutectic. Similar results have also been reported in rapidly solidified Al-8wt% Fe [12], [13] alloys.

Similar to binary Al-Fe system, many binary Al-Fe, above mentioned phases, and ternary metastable intermetallics, including α-Al_8Fe_2Si, β-Al_5FeSi and δ-Al_4FeSi_2, have been reported in rapidly solidified ternary Al-Fe-Si system. The phase selection of whether binary or ternary phase are dominant strongly depend on cooling rate and Fe:Si ratio[3], [4], [14]. While high cooling rate and low Fe:Si ratio promote ternary intermetallics, vice-versa give rise to binary Al-Fe intermetallics. Al-Fe-Si alloys have widely been studied using melt spinning. In addition to above mentioned ternary phases, nano-sized Si particles were observed in rapidly solidified Al-Fe-Si alloys[15]–[17].

The purpose of this study is to investigate the effect of the rapid solidification on the formation of intermetallics in the binary Al-2.85 wt% Fe and Al-3.9 wt% Fe, and the ternary Al-4.1 wt% Fe-1.9 wt% Si alloys. Microstructural evolution of the drop tube atomized alloys has been analysed as a function of cooling rate. Moreover, in order to understand the effect of rapid solidification on the mechanical properties, microhardness testing was employed.

2. Background Science

There is a strong link between structure and properties of engineering materials (metals, alloys and composites). Most metals and alloys are polycrystalline materials which include many small crystals. In this chapter, some essential background science related to the research are introduced. While the first section focuses on the fundamentals of the crystallography, thermodynamics of solidification is discussed in the second section.

2.1 Fundamentals of Crystallography

A crystal is defined as a solid composed of atoms, ions or molecules arranged in a repeating pattern or periodic array over large atomic distances in three dimensions. Atoms, ions or molecules are sometimes ignored and a crystal structure can be represented as a 'lattice'; an array of points (lattice points) in space coinciding with atom positions where each point has identical surroundings [18]. A point lattice is given in **Figure 1**. In this section, basics of crystallography, such as a unit cell, Miller indices, crystal symmetry, are explained briefly.

2.1.1 Unit Cell

A unit cell is simply the smallest repetitive pattern or building block of a crystal. A unit cell, as shown in **Figure 1**, represents the symmetry of the crystal so that when repeated in all directions, a unit cell develops into the crystal lattice. A unit cell's geometry is described using six lattice parameters; three edge lengths **a**, **b** and **c**, and three interaxial angles; **α** (between **b** and **c**), **β** (between **c** and **a**) and **γ** (between **a** and **b**).
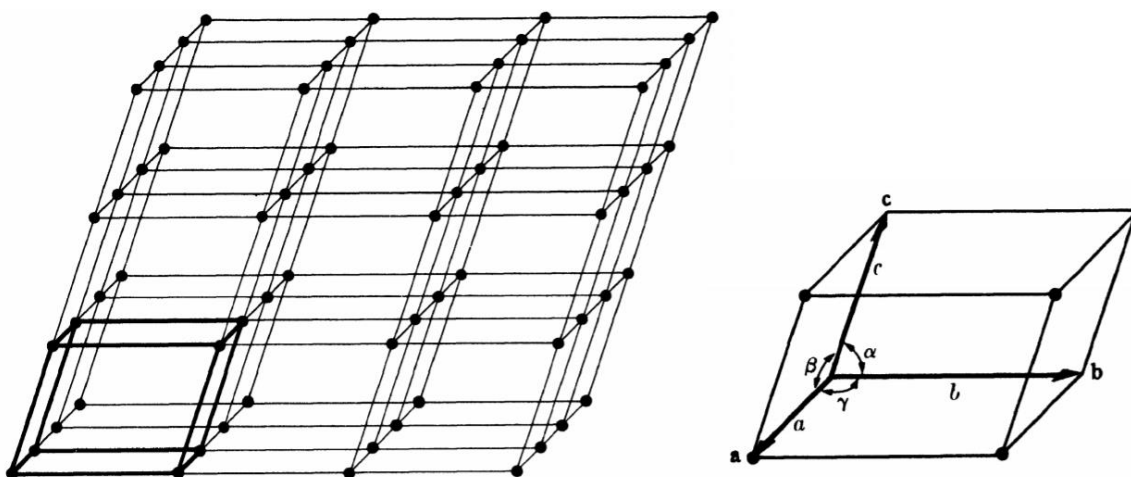
Figure 1: A point lattice and a unit cell showing lattice vectors and lattice angles (a, b, c and α, β, γ) [18].

2.1.2 Crystal systems

Various unit cells can be produced by giving special values to the six lattice parameters. However, there are seven possible combinations of lattice parameters known as the seven crystal systems. These seven crystal systems are cubic, tetragonal, hexagonal, orthorhombic, rhombohedral (also called trigonal), monoclinic and triclinic. Lattice parameters of the seven crystal systems are given in **Table1**. In addition to these seven-point lattices, there are other arrangements of points to fulfil the requirement that each point lattice has identical surrounding. In 1848, Bravais showed that there are fourteen possible point lattices and referred as Bravais lattice or point lattice. The fourteen Bravais lattices are given in **Figure 2**. Moreover, some intermetallics show ordered crystal structures such as B2. B2 structure such as TiAl (**Figure 3**) is a combination of two simple cubic interpenetrating sublattices. The other versions of B2 are DO_3 and $L2_1$.

Table 1: Seven crystal systems and Bravais lattices [18].

System	Axial lengths	Axial angles	Bravais lattice	Lattice symbol
Cubic	a=b=c	$\alpha=\beta=\gamma=90°$	Simple	P
			Body-centred	I
			Face-centred	F
Tetragonal	a=b≠c	$\alpha=\beta=\gamma=90°$	Simple	P
			Body-centred	I
Orthorhombic	a≠b≠c	$\alpha=\beta=\gamma=90°$	Simple	P
			Body-centred	I
			Base-centred	C
			Face-centred	F
Rhombohedral	a=b=c	$\alpha=\beta=\gamma\neq90°$	Simple	P
Hexagonal	a=b≠c	$\alpha=\beta=90°, \gamma=120°$	Simple	P
Monoclinic	a≠b≠c	$\alpha=\gamma=90°\neq \beta$	Simple	P
			Base-centred	C
Triclinic	a≠b≠c	$\alpha\neq\beta\neq\gamma\neq90°$	Simple	P
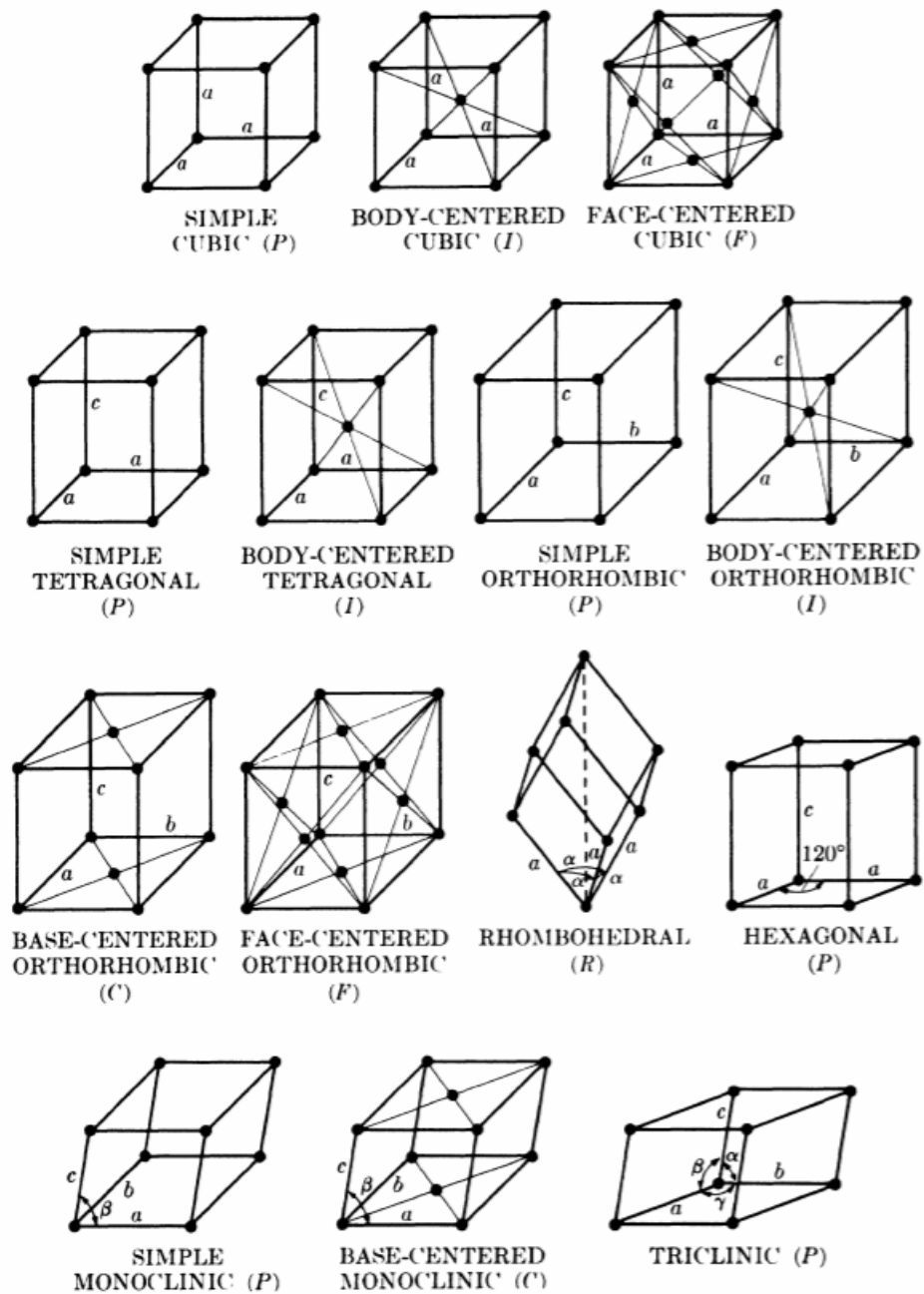
Figure 2: The fourteen Bravais lattices [18].
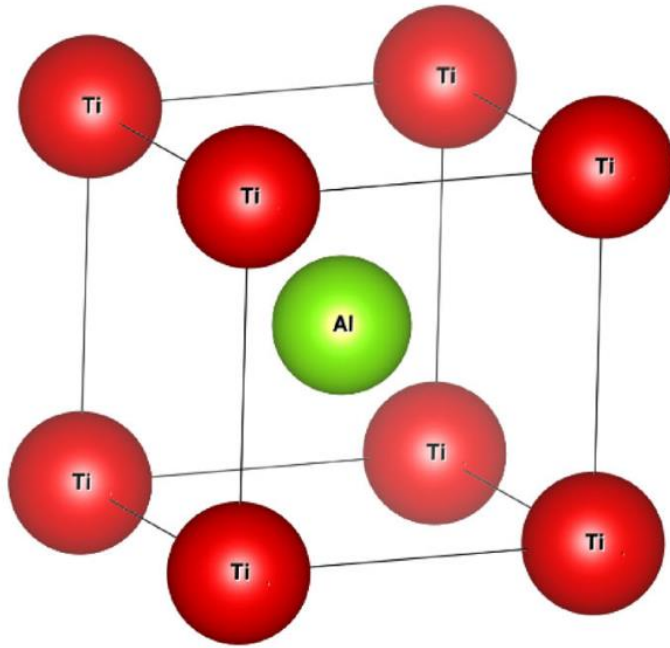
Figure 3: B2 TiAl phase [19]

2.1.3 Crystal symmetry

A crystallographic unit can coincide with itself after performing certain symmetry operations. Reflection symmetry, for example, occurs when a plane passing through the centre of a body shows the mirror image of the body on the other side. There are four types of symmetry operations or elements; reflection, rotation, inversion and rotation-inversion. Some examples of these operations elements are shown in **Figure 4**. A body is said to have n-fold rotational symmetry about an axis if a rotation of 360°/n brings it to self-coincidence. The number of symmetries of the crystal systems varies. For instance, a cubic system has the greater degree of symmetry, while the least degree of symmetry is observed in triclinic as **a ≠ b ≠ c** and **α ≠ β ≠ γ**.
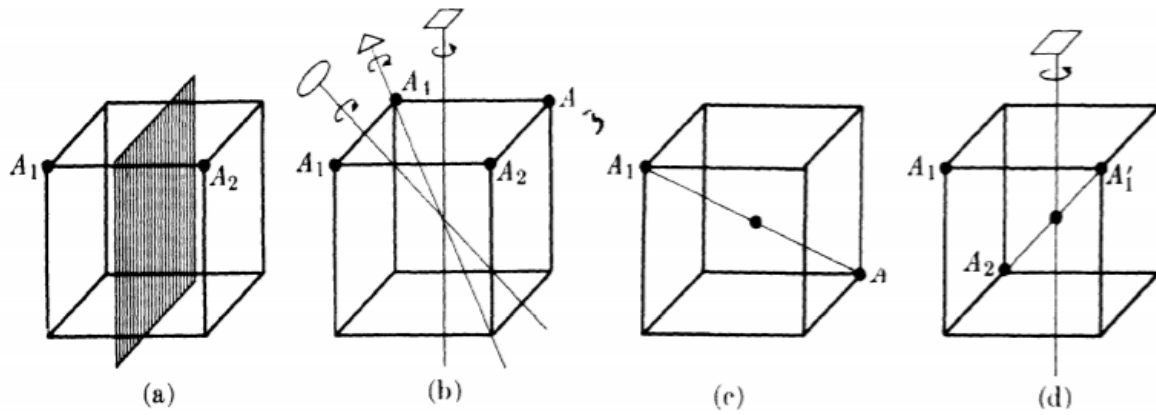
Figure 4: Some symmetry elements of a cube a) Reflection plane b)rotation axis; 4-fold axis, 3-fold axis and 2-fold axis c) inversion centre d) rotation-inversion axis; 4-fold axis [18].

2.1.4   Miller Indices

A plane in a unit cell is represented by three Miller indices as (hkl) (hexagonal crystal system can also use 4 miller indices (hklm)). In this notation, any two parallel planes share identical indices. In order to determine the h, k, l values for a plane:

1) Intersection of each axis is determined in terms of the lattice parameters a, b, c.
2) If a plane is parallel to an axis, it is considered to intercept at infinity and zero index.
3) The reciprocals of the numbers are taken. The numbers are later, if necessary, multiplied by a common factor to the set of smallest integers.

A bar on (hkl) values indicate an intercept on the negative side of the origin. Some planes and their equivalent parallel planes are given in **Figure 5**.
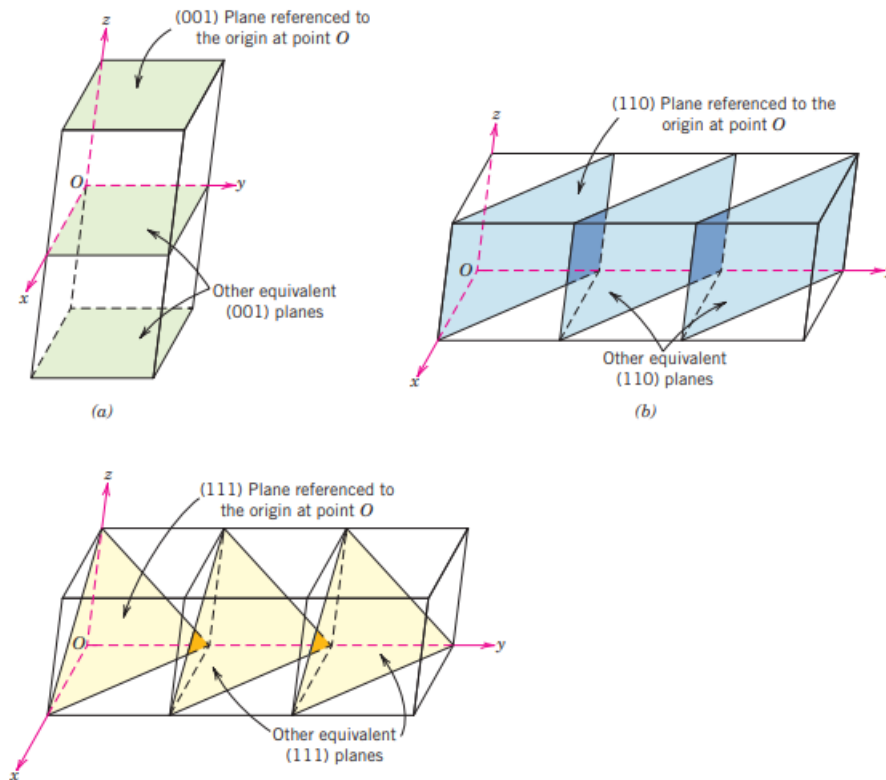
Figure 5: Representation of a series each of the a) (001), b) (110) and c) (111) crystallographic planes[20].

2.2 Thermodynamics of solidification

Solidification, being one of the oldest production processes, is simply the transformation of the liquid matter into solid matter. As most metallic materials are produced from the liquid state, the final phase and microstructures, and thus the properties, of the metallic materials are greatly affected by the solidification process. For example, a non-equilibrium solidification favours refined microstructure, solid solubility extension, formation of metastable phases and glass phase formation [21]. Thus, it is important to understand thermodynamic concept for solidification. In this section, some thermodynamic concepts, e.g. Entropy, Enthalpy, Gibbs free energy, are introduced.

2.2.1   Gibbs free energy

The reason behind a transformation occuring is that the initial state of the alloy is unstable relative to the final state. In other words, the driving force for a transformation is the Gibbs free energy difference between the initial and final states, $G_2 - G_1$ [22]. The Gibbs free energy is defined by

$$G = H - TS \qquad (2\text{-}1)$$

where H is the enthalpy, T is the absolute temperature and S is the entropy of the system. Enthalpy is defined as the heat content of the system and can be expresses as

$$H = E + PV \qquad (2\text{-}2)$$

where E is the internal energy, P is the pressure and V is the volume of the system. The internal energy arises from the atomic vibration and the bonds between the atoms of the system. Enthalpy also depends on pressure and volume change of the system. However, for solids and liquids, PV term, compared to E, is very small and can be neglected. For solid-liquid phase transformation the equation becomes $H \approx E$ [22].

A system is said to be in equilibrium when it is in the most stable state. When a closed system at constant temperature and pressure has the lowest possible value of the Gibbs free energy, it is said to be in equilibrium. In mathematical terms this can be represented as

$$dG = 0 \qquad (2\text{-}3)$$

Figure 6 shows state A and B where both states have $dG = 0$. However, state B does not have the lowest possible value of G. In order to distinguish the stable equilibrium state (A state), B state is called as metastable equilibrium state, which is less stable than the A state. A metastable state will transform into its stable equilibrium state by the time passes. The system is unstable at intermediate states where $dG \neq 0$. Moreover, a system is in unstable equilibrium when $dG = 0$ and the curve exhibits a maximum.
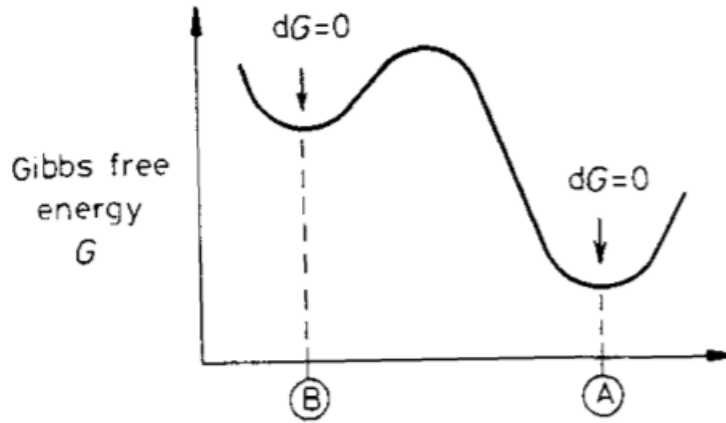
Figure 6: Schematic variation of Gibbs free energy of local equilibrium (B state) and global equilibrium (A state) [22].

A transformation is said to be possible if the transformation results in a decrease in Gibbs free energy. That is

$$\Delta G = G_2 - G_1 < 0 \qquad (2\text{-}4)$$

where G_2 is the free energy of the final state and G_1 is the initial state of the system. However, the rate of the transformation cannot be explained by classical thermodynamics.

2.2.2 Enthalpy

Enthalpy is the heat content of a system and defined by equation (2-5). The change in enthalpy during solidification occurs in 2 ways: decrease in the enthalpy of the system due to cooling and decrease in the enthalpy due to transformation from liquid to solid. The latter is equal to the latent heat of fusion, ΔH_f, and is negative as solidification is exothermic. The enthalpy of solidification can be expressed as:

$$\Delta H = \Delta H_f - \int_{T}^{T_m} C_p \, dT \qquad (2\text{-}5)$$

Where C_p is the heat capacity of the system.

2.2.3 Entropy

Entropy is the degree of the disorder in a system and describes the heat exchanges taking place in a thermal process:

$$dS = dQ_{rev}/T \qquad (2\text{-}6)$$

Where Q_{rev} is the amount of heat exchanged and T is the absolute temperature at which heat exchange occurs. The entropy for a system in equilibrium is given from a microscopic point of view as;

$$S_m = k_B lnW \tag{2-7}$$

where k_B is the Boltzmann constant and W is the occurrence or the frequency.

2.3 Nucleation

A liquid is expected to solidify when it is cooled below its equilibrium melting point, T_m, as there is a driving force for solidification ($G_S - G_L$). However, under suitable conditions a liquid does not undergo a transformation below its melting point, T_m [22]. For example, liquid nickel can be undercooled (supercooled) to 250 K below T_m without any transformation. Solidification does not occur at equilibrium; it requires some undercooling below the equilibrium [23]. This is because the transformation starts by the formation of very small solid particles called as nuclei and extra energy is needed to overcome the energy barrier. In practice, high undercooling is not observed since container walls and impurities in the liquid act as heterogeneous nucleation sites and this phenomenon is called heterogeneous nucleation. In the absence of heterogeneous nucleation sites, large undercoolings are required to form homogeneous nuclei from the liquid. Here, nucleation concept, homogeneous and heterogeneous nucleation, will be explained.

2.3.1 Homogeneous Nucleation

In homogeneous nucleation, the formation of nuclei of the new phase takes place uniformly throughout the parent phase without contacting with the impurities and container walls. Homogeneous nucleation is the most basic nucleation event but it occurs rarely due to the presence of the heterogeneous nucleation sites [22]. When a liquid is undercooled below its melting point, T_m, tiny clusters of solid starts forming. This clusters will create free energy difference between the solid and liquid phases and will create a solid-liquid phase boundary. While the solid formation releases energy, the creation of interface absorbs energy. Total free energy change of the system depends on the size of the solid transformed. Assuming the nucleus formed is spherical with a radius r, the free energy change is given by:

$$\Delta G_r = -\frac{4}{3}\pi r^3 \Delta G_v + 4\pi r^2 \gamma_{SL} \tag{2-8}$$

11

Where ΔG_v is the free energy difference of the solid and liquid per unit volume and γ_{SL} is the solid/liquid interfacial free energy. While the interface term increases as r^2, volume free energy released increases as r^3. The illustration of the equation (2-8) is given in **Figure 7**. When a solid particle starts to form in the liquid, its free energy increases first and after reaching a maximum, ΔG^* where dG = 0, it starts decreasing. The corresponding radius, r*, is called critical nucleus size. If the size of the cluster formed is smaller than critical nucleus size, r < r^*, the system lowers its free energy by melting the solid whereas if r > r^* the system will lower its free energy by growth [20].
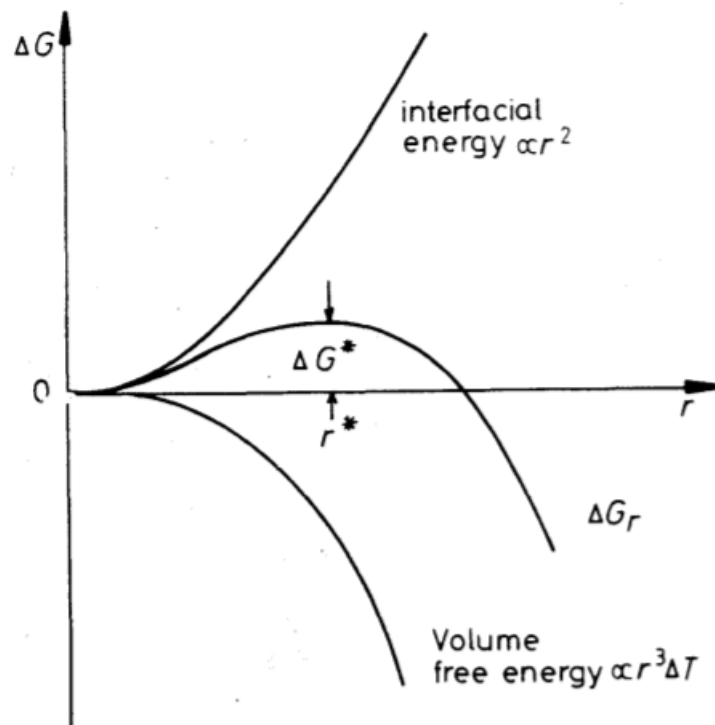
Figure 7: Relationship between radius of nucleus, r, and the free energy change, ΔG [22].

As r^* and ΔG^*, are the maximum of free energy-radius curve, r^* can be found differentiating the equation with respect to r. This is,

$$\frac{d(\Delta G)}{dr} = \frac{4}{3}\pi\Delta G_v(3r^2) + 4\pi\gamma(2r) = 0 \qquad (2\text{-}9)$$

Solving the equation (2-9) leads to

$$r^* = \frac{2\gamma_{SL}}{\Delta G_v} \qquad (2\text{-}10)$$

Substituting r^* into equation (2-8) gives

$$\Delta G^* = \frac{16\pi\gamma_{SL}^3}{3(\Delta G_v)^2} \qquad (2\text{-}11)$$

For an undercooling ΔT, ΔG_v is given as for metals and most alloys

$$\Delta G_v = \frac{H_f \Delta T}{T_m} \qquad (2\text{-}12)$$

where H_f is the latent heat of fusion per unit volume. Substitution of this expression into equation (2-10) and (2-11) gives

$$r^* = \left(\frac{2\gamma T_m}{\Delta H_f}\right)\left(\frac{1}{\Delta T}\right) \qquad (2\text{-}13)$$

and

$$\Delta G^* = \left(\frac{16\pi\gamma^3 T_m^2}{3\Delta H_f^2}\right)\left(\frac{1}{\Delta T^2}\right) \qquad (2\text{-}14)$$

Equation (2-13) and (2-14) states that both critical nucleus size, r^*, and change in free energy ΔG^* decrease with decreasing undercooling ΔT.

2.3.2   Heterogeneous nucleation

Even though the undercooling required for homogeneous nucleation is high, the level of undercooling observed in practice is only around several Kelvin. This is due to the presence of heterogeneous nucleation sites. Heterogeneous nucleation sites reduce the energy barrier (Equation 2-14), ΔG^*, by reducing the surface free energy, γ [24]. **Figure 8** shows a schematic presentation of a spherical solid with a wetting angle of θ forming from a liquid on a flat mould wall.
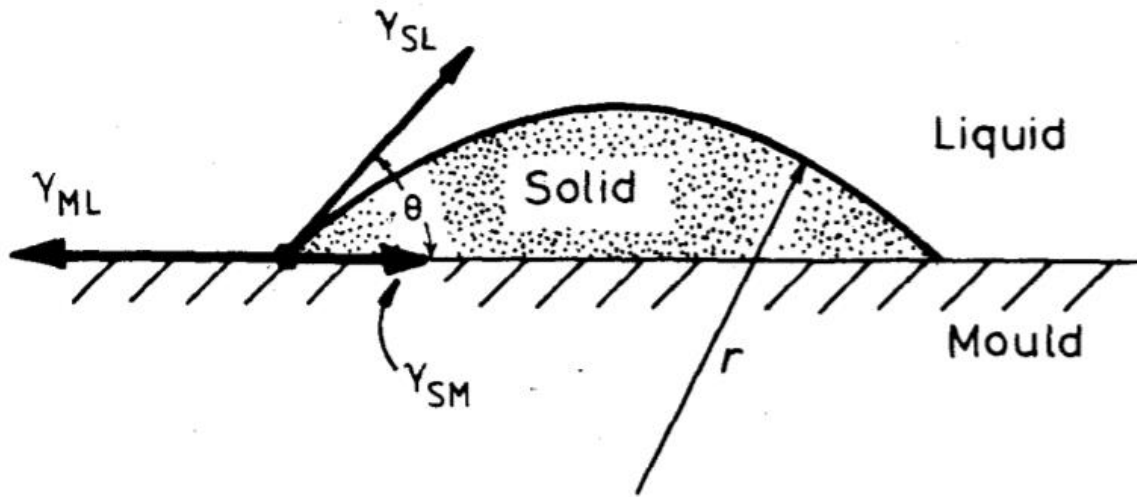
Figure 8: Heterogeneous nucleation of a solid from a liquid on a flat mould wall [22].

Assuming γ_{SL} is isotropic, the total interfacial energy of the system is minimized if the embryo is a spherical cap. Surface tension force balance in the plane of the flat surface can be written as [22];

$$\gamma_{ML} = \gamma_{SM} + \gamma_{SL} \cos\theta \qquad (2\text{-}15)$$

or

$$\cos\theta = (\gamma_{ML} - \gamma_{SM})/\gamma_{SL} \qquad (2\text{-}16)$$

where γ_{SL}, γ_{SM} and γ_{ML} are the free energies of the solid/liquid, solid/mould and mould/liquid interfaces, respectively. The free energy change after associated with the formation of an embryo is given by

$$\Delta G_{het} = \left\{ -\frac{4}{3}\pi r^3 \Delta G_v + 4\pi r^2 \gamma_{SL} \right\} S(\theta) \qquad (2\text{-}17)$$

Where

$$S(\theta) = (2 + \cos\theta)(1 - \cos\theta)^2/4 \qquad (2\text{-}18)$$

It may be noted that Equation (2-8) and Equation (2-17) are identical apart form $S(\theta)$ term. $S(\theta)$ depends only on θ and known as shape factor. Differentiation of Equation (2-17) leads to

$$r^* = \frac{2\gamma_{SL}}{\Delta G_v} \qquad (2\text{-}19)$$

And

$$\Delta G^*_{het} = \frac{16\pi \gamma^3_{SL}}{3\Delta G^2_v} . S(\theta) \qquad\qquad (2\text{-}20)$$

As $S(\theta)$ has a numerical value ≤ 1, the energy barrier against heterogeneous nucleation (ΔG^*_{het}) is smaller than that of homogeneous nucleation (ΔG^*_{hom}) by $S(\theta)$ factor. The energy barrier difference is shown in **Figure 9**. This can be written as

$$\Delta G^*_{het} = S(\theta)\,\Delta G^*_{hom} \qquad\qquad (2\text{-}21)$$
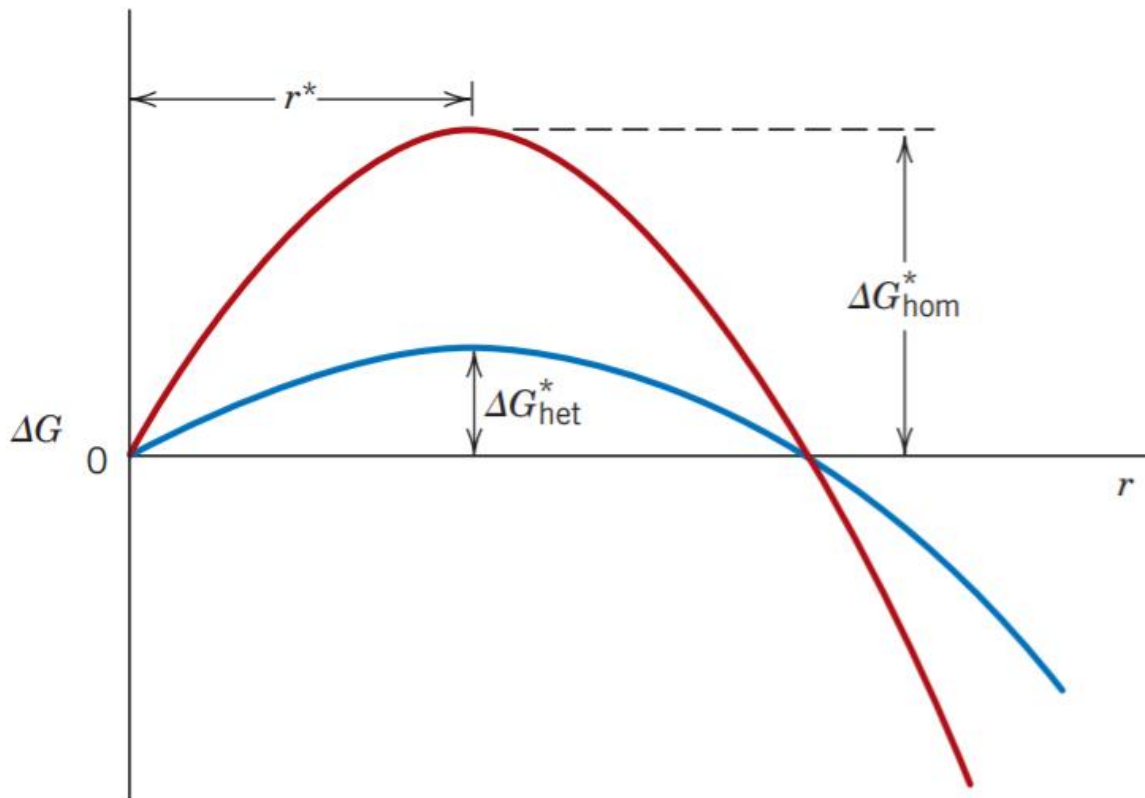
Figure 9: Schematic free energy versus nucleus radius for homogeneous and heterogeneous nucleation [20].

2.3.3   Nucleation rate

Nucleation rate is the number of nuclei formed in a given molten volume and time. The steady state nucleation rate is given by

$$I = I_0 \exp\left(-\frac{\Delta G_n^* + \Delta G_d}{k_B T}\right) \qquad (2\text{-}22)$$

Where I_0 is the preexponential factor, ΔG_n^* is the free energy of the formation of a critical nucleus containing n atoms, ΔG_d is the activation energy for transfer through the solid/liquid interface and k_B is Boltzmann's constant.

Increasing undercooling results in critical nuclei of smaller size and more numerous nuclei formation as given in Equation (2-13) and (2-14). On the other hand, it decreases the atom transfer from the liquid to the nuclei by a decrease in T. At very high cooling rates, nucleation can be avoided due to insufficient time for the formation of nucleus and, as a result, a glassy (amorphous) solid forms [25].

2.4 Undercooling

As explained earlier, solidification will not take place when $\Delta T = 0$, as the system is in equilibrium ($\Delta G_v = 0$). In other words, solidification requires a degree of undercooling below the equilibrium temperature to form nuclei on which growth will take place. Under constant pressure, there are four types of solidification undercooling; kinetic undercooling, ΔT_k, thermal undercooling, ΔT_T, constitutional (solutal) undercooling, ΔT_c, and curvature undercooling, ΔT_r [25].

2.4.1 Kinetic undercooling

When solid /liquid interface moves forward, atoms are transferred from solid to liquid and liquid to solid. In other words, melting process, atoms transfer from solid to liquid, and solidification process, atoms transfer from liquid to solid, take place at the solid/liquid interface. The rate of atoms transferring from liquid to solid and solid to liquid is same in equilibrium. For solidification to proceed, there must be more atom transfer from liquid to solid than that from solid to liquid [22]. This difference indicates that the temperature of the interface is lower than the melting point, T_m, and the temperature difference resulting from the net difference in atoms transported is called as kinetic undercooling,ΔT_k. For metals, the kinetic undercooling is on the order of 0.01 to 0.05 K.

2.4.2 Thermal undercooling

When a nucleation does not take place, a melt can be undercooled below the equilibrium temperature due to heat extraction [25]. This arising thermal gradient in the liquid is called as thermal undercooling and given by;

$$\Delta T_T = T_m - T^* \qquad (2\text{-}23)$$

where T_m is the equilibrium (melting) temperature and T^* is the interface temperature.

2.4.3 Constitutional undercooling

During solidification of an alloy, solute is rejected by the solid and a boundary layer, which is richer in solute, forms at the solid/liquid interface as shown in **Figure 10**. Consequently, liquidus temperature of the solute rich liquid is lower than the actual liquidus temperature. Constitutionally undercooled region forms when the thermal gradient, G_T, is lower than the liquidus gradient, G_L, and the temperature in the boundary layer is lower than the equilibrium liquidus temperature [25]. The constitutional undercooling is given as

$$\Delta T_c = T_L - T^* = -m_L(C_L^* - C_o) \qquad (2\text{-}24)$$

Where T_L is the liquidus temperature, m_L is the slope of the liquidus line, C_L^* is the composition at the interface of the liquid and C_o is the bulk composition of the liquid. As the heat flows out from the solid to the undercooled melt in drop tube process, the thermal gradient is negative in drop tube. In other words, in drop tube the temperature of the liquid is lower than the equilibrium freezing temperature. This is known as the constitutional undercooling.
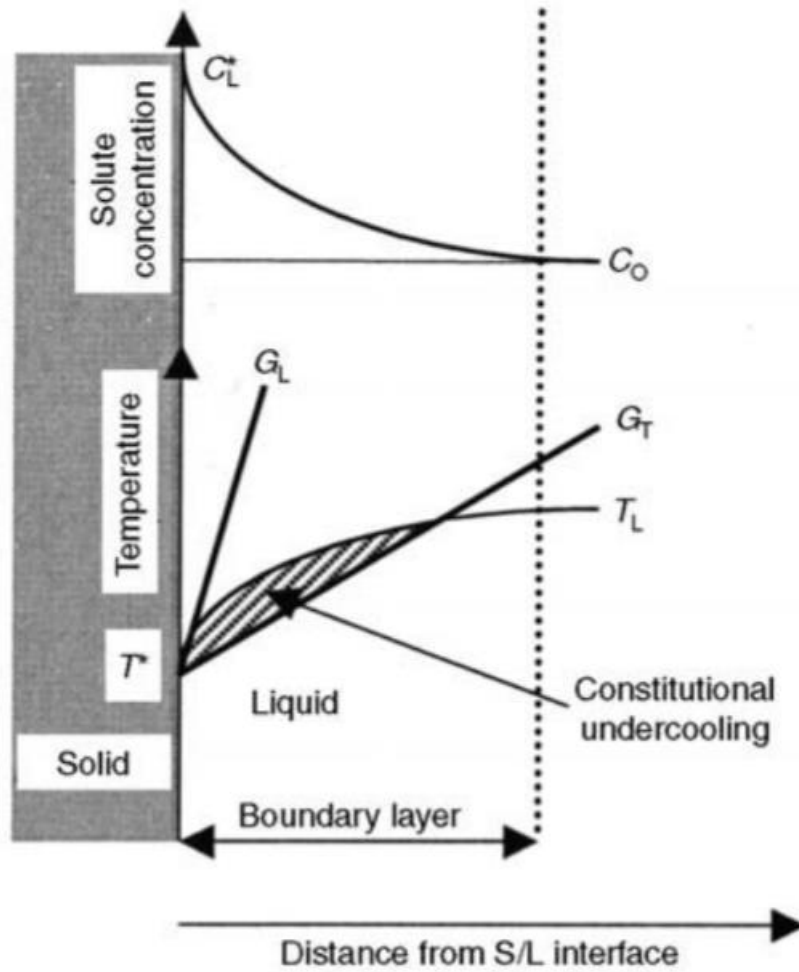
Figure 10: Formation of constitutionally undercooled region due to higher solute content [25].

2.4.4 Curvature undercooling

When liquid transforms into solid, the surface/ volume ratio of a solid particle increases as the solid/liquid interface is not flat in the beginning of the solidification. This will result in the increase of the total free energy of the system by increasing the interface energy. To compensate the free energy change, further undercooling is required. This undercooling resulting from the difference between the normal melting point of the metal and the actual melting temperature of the same metal with finite radius is called as curvature undercooling High curvature undercooling is associated with higher curvature as high curvature (smaller radius) gives a higher surface-to-volume ratio [22]. Curvature undercooling is given by;

$$\Delta T_r = T_e - T_e^r = \frac{\gamma_{SL}}{\Delta S_f} K = \Gamma K \qquad (2\text{-}25)$$

Where T_e^r is the equilibrium temperature for a sphere with a radius r, γ_{SL} is the solid/liquid interface energy, ΔS_f is the entropy of fusion, Γ is the Gibbs-Thomson coefficient and $K = 1/r$, for a cylinder with a spherical end.

2.5 Solidification structures

The simplest solidification observed in alloys is when the liquid transforms into a complete solid solution upon cooling. However, most alloys undergo some other processes such as eutectic, peritectic or monotectic reaction. Most of the solidification microstructures of the metals can be divided into two groups: single-phase primary crystals and polyphase structures. Combination of these make up the grains of any metallic microstructure [24].

2.5.1 Dendritic structure

Dendritic morphology is the most commonly observed growth form in solidification. Dendrites are the tree-like primary crystals that have preferred growth direction. While the growth of dendrites influenced by the heat flow in pure metals, in alloys the growth is influenced by solute diffusion. There are two types of dendrites: columnar dendrites and equiaxed dendrites. While columnar dendrites form at high thermal gradients, equiaxed dendrites form at rather low thermal gradients [25].

When a planar solid/liquid interface becomes unstable due to temperature fluctuations, insoluble particles and grain boundaries, stable protrusions will form provided that there is a region of constitutional undercooling in the liquid. If the temperature gradient is sufficiently low, protrusions, or primary arms of the solid, develop secondary arms perpendicular to the primary arm as shown in **Figure 11**. These cell-like secondary branches will develop tertiary arms if the spacing is enough [22]. Dendrites exhibit crystallographically governed growth direction. The preferred dendrite growth directions are given in Table 2.

300 μm
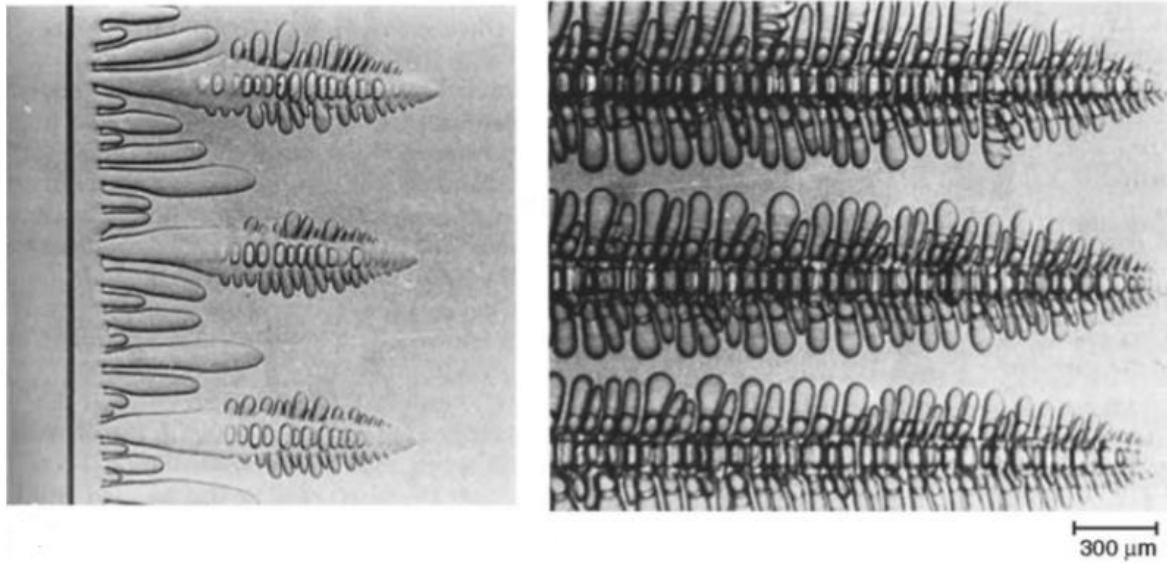
Figure 11: Dendrite formation in a succinonitrile-4% acetone solution [25].

The microstructure is greatly affected by the solidification velocity and the temperature gradient. In addition, the cooling rate and the degree of undercooling have significant influence on the morphology of the dendrites. Dendrite tip radius depends on the solidification velocity: at small velocities dendrites form with very large tip radius while at high velocities tip radius decreases. In rapid solidification, dendrite morphology transforms fully branched to globular/cellular dendrites. The secondary dendrite arm spacing (SDAS), the distance between neighbour dendrite branched growing from the primary dendritic arm, also depends on the cooling rate [25]. The experimentally found relation between SDAS and cooling rate can be given as [26]

$$SDAS = \mu_1 (\dot{T})^{-0.34 \mp 0.02} \tag{2-26}$$

where μ_1 is a material specific constant and $\dot{T}$ is the cooling rate.

Table 2: Preferred dendrite growth directions of various materials [27].

Structure	Dendrite orientation	Example
Face-centred cubic	<100>	Al
Body-centred cubic	<100>	δ-Fe
Body-centred tetragonal	<110>	Sn
Hexagonal close-packed	<10$\bar{1}$0>	H_2O (snow)
Hexagonal close-packed	<0001>	$Co_{17}Sm_2$

2.5.2 Eutectic solidification

Eutectic solidification is one of the most commonly observed solidification structures in alloy solidification. In a binary system of the species of A and B, eutectic morphologies are characterised by the cooperative growth of two phases from the liquid. The eutectic reaction can be written as: L ➜ α + β. Although as many as four phases have been observed in multi component systems growing simultaneously from the melt, most technologically useful eutectic alloys are composed of two phases. Thus, only binary eutectic will be considered here.

The morphology of the eutectic depends on the processing conditions and the nature of the two phases. Typical eutectic microstructures are usually classified as normal (regular) and anomalous (irregular) structures as shown in Figure 10. While normal structures are observed when both phases have low entropies of fusion, anomalous structures occur when one of the phases has a high entropy of melting. In normal structures, both phases grow simultaneously behind the solid/liquid interface. The structure in normal eutectic is either alternate lamella or rods where minor phase is embedded in the other phase. In addition, the volume fractions of the phases effect the resultant structure of the eutectic. If the volume fraction is between 0.25 and 0.5, there is a tendency of the formation of lamellar structure. If the volume fraction of the one phase is between zero and 0.25, the eutectic is expected to be fibrous (rod-like) provided that both phases are non-faceted. This is because fibres have smaller interfacial area, and thus lower interfacial energy, than lamellae. When one phase has a high entropy of fusion, faceting will occur and the eutectic morphology will become irregular. Fe – C (cast iron) and Al-Si are two commercially important alloys in which irregular eutectic is observed [24].

During lamellar eutectic growth, B atoms will be rejected by the A-rich α phase and excess B atoms will diffuse laterally to form B-rich β phase and vice versa as shown in **Figure 12**. The eutectic growth rate depends on this diffusion rate and the interlamellar spacing, λ. Thus, rapid growth leads to small interlamellar spacings. For lamellar eutectic growth, Jackson and Hunt [28] developed a relationship between undercooling (ΔT), growth velocity (V_g) and interlamellar spacing (λ) as:

$$\Delta T = K_1 \lambda V_g + \frac{K_2}{\lambda} \qquad (2\text{-}27)$$

where K_1 and K_2 are material-dependent constants. At the extremum for the growth, $\frac{d(\Delta T)}{d\lambda} = 0$, the equation leads to:

$$\lambda^2 V_g = K_2/K_1 \qquad (2\text{-}28)$$

$$\Delta T^2 = 4V_g K_1 K_2 \qquad (2\text{-}29)$$

$$\Delta T \lambda = 2K_1 \qquad (2\text{-}30)$$
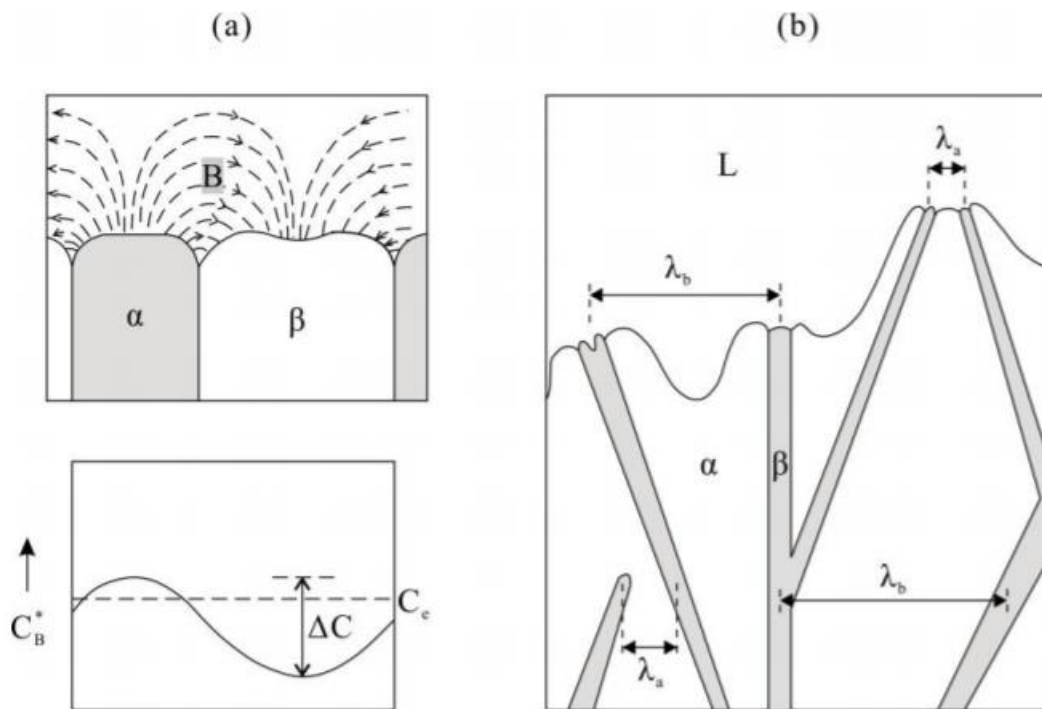
Figure 12: Growth models of (a) regular eutectic and (b) irregular eutectic structures [24].

In irregular eutectics, Jackson-Hunt eutectic model cannot estimate the lamellar spacing as the mean spacing is much larger. These large spacings are due to the branching of the eutectic as shown in Figure 10 (b). Two adjacent lamellae growing with the extremum spacing and diverging will result in the increase of the solute concentration. As the spacing reaches a so large value that low volume fraction phase will exhibit depressions and lamellae will branch into two [24].

2.5.3   Peritectic solidification

Peritectic solidification is common in the solidification of the metallic alloys such as steels and copper alloys. Peritectic solidification is the formation of the secondary solid phase, β, at the peritectic temperature from the mixture of liquid L and the primary solid phase, α, and can be

written as L + α ➜ β. **Figure 13** shows a hypothetical peritectic phase diagram with different reactions occurring along the solidus line.
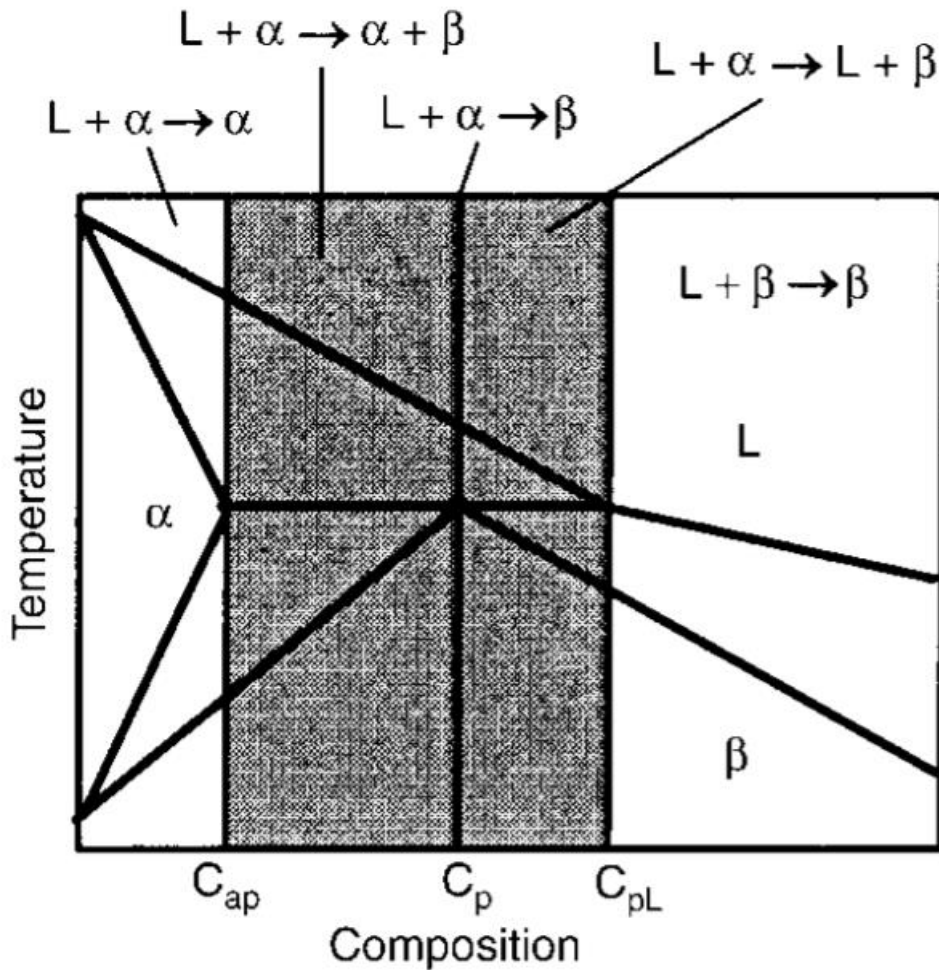
Figure 13: Hypothetical peritectic phase diagram with peritectic reaction [25].

There are two mechanisms involved in the peritectic solidification: peritectic reaction and peritectic transformation. While all three phases are in contact with each other in peritectic reaction, secondary phase separates primary phase and the liquid in peritectic transformation. Thus, long-range solid diffusion is required through the secondary phase and this makes peritectic transformation rarely observed to go to completion [25].

2.5.4 Partitionless Solidification

At high growth velocities, there is no time for the atoms to rearrange themselves for nucleation and growth (solute trapping) as in the equilibrium solidification. As a result, at high solidification rates, liquid can solidify in to a single solid which has the identical composition to liquid. There are two possible mechanisms which can give these microsegregation-free

crystalline structures: planar growth and partitionless solidification [29]. Partitionless solidification takes place at high solidification rates when the interface growth velocity is larger than the diffusion velocity [30]. This results in the entrapment of the solute in the solvent causing the formation of super saturated solid solution with the exact composition of liquid. **Figure 14** shows the possible solid compositions that can form from a liquid with identical composition at ranging temperatures. While it is possible to form partitionless solidification in **Figure 14a** with a liquid composition of C_L^*, **Figure 14b** depicts where partitionless solidification does not occur as T_0 curve (line represents equal free energy for solid and liquid phases) plunges steeply. Partitionless solidification has been reported in various alloys such as rapidly solidified Sn-Bi alloy [31]. However, super saturated solid solution has later decomposed forming binary intermetallic.
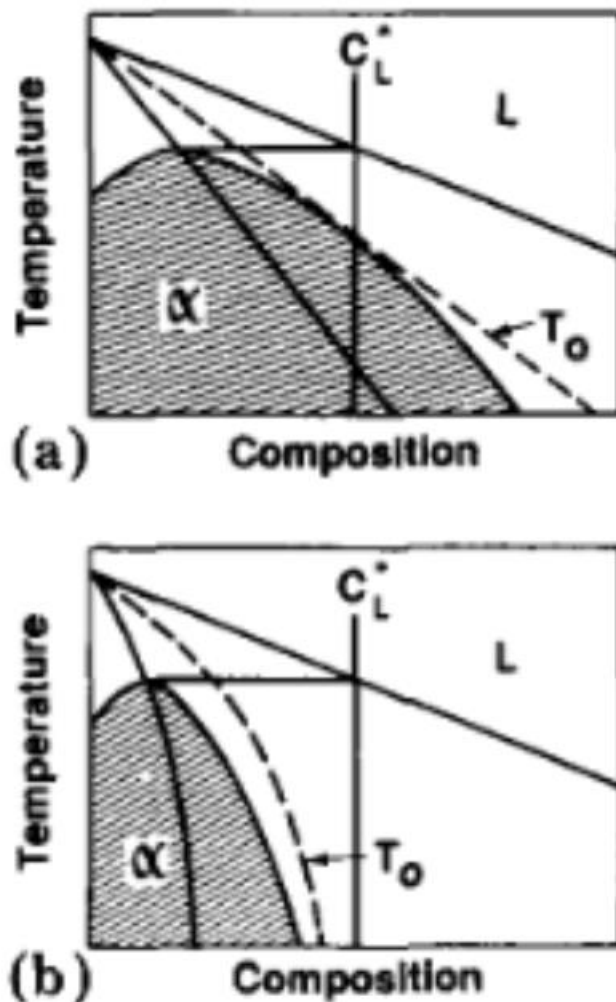
Figure 14: Shaded regions represents thermodynamically allowed solid compositions that may be formed a) the value of T_0 is the highest temperature at which partitionless solidification of a liquid of given composition can occur b) T_0 curve plunges and partitionless solidification is impossible for liquid of composition C_L^*.[29]

3. Literature Review

3.1 Rapid Solidification

Rapid solidification is defined as any solidification process where the cooling rate is higher than 10^3 K/s and/or high undercoolings are achieved prior to solidification. During rapid solidification, high undercooling and high cooling rates are achieved which results in the departure from the equilibrium. Such departures from the equilibrium conditions can give rise to the formation of supersaturated solid solutions, grain refinement, metastable phases, quasicrystalline alloys and/or amorphous metals (metallic glasses). These structures can lead to improved properties in metallic materials. In this section, these expected structures during rapid solidification will be reviewed.

3.1.1 Supersaturated Solid Solution

The formation of supersaturated solid solutions is commonly observed in rapidly solidified alloys. Supersaturated solid solutions increase the mechanical properties of the alloy which is known as solid solution strengthening. Solid solutions hinder the movement of the dislocations due to the interaction between solute atoms.

Figure 15 shows the solidification route of the liquid with the composition of c_0 at different undercoolings. First solid nuclei of α is expected to form between T_L and T_e. Assuming β does not nucleate on α, as the temperature goes below T_e the remaining liquid will solidify into a supersaturated $α_{SS}$ avoiding the formation of β. Partial remelting and segregation may occur as in **Figure 15 (b)** due to recalescence and $α_{SS}$ will transform into α. In order to achieve solute trapping and eventually partitionless solidification, the melt must be undercooled to a temperature, which is called as hypercooling temperature (Figure 14c). If the melt is undercooled to $T < T_{hyp}$ (T_{hyp} is the isenthalpic or hypercooling temperature), the entire melt will solidify into a supersaturated solid solution as the recalescence is not sufficient [32]. The hypercooling is estimated by

$$\Delta T_{hyp} = \Delta H_m / c_p \tag{3-1}$$
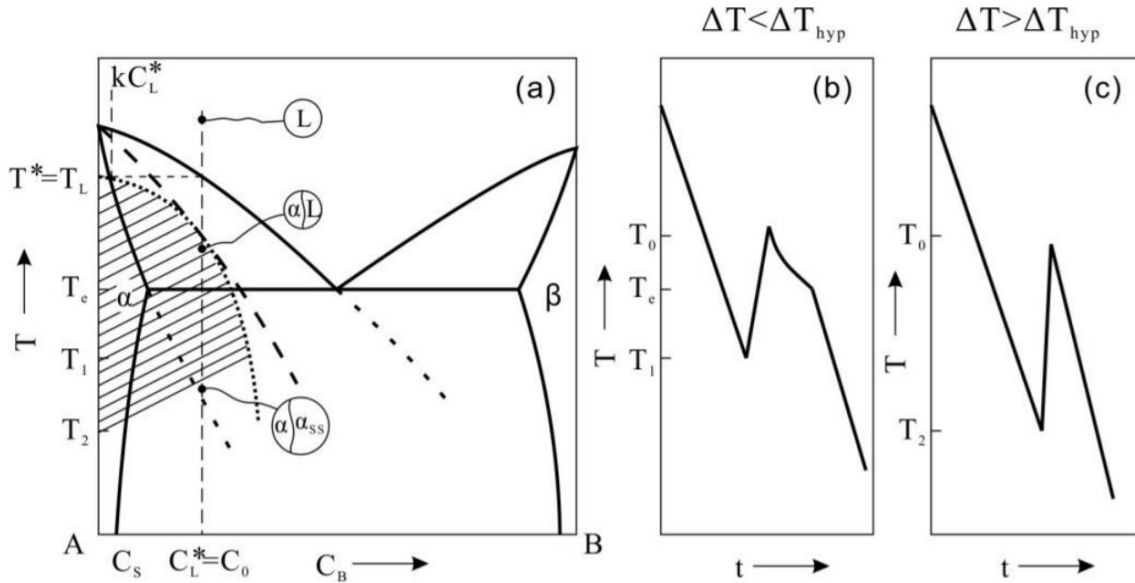
Figure 15: (a)Eutectic phase diagram showing thermodynamic constraints for solute trapping and segregation free crystallization, temperature- time profiles for forming (b) segregation and (c) partitionless solidification [32].

3.1.2 Grain Refinement

Refined grain structures are known for their contribution to structural uniformity and mechanical properties of the metallic materials by inhibiting dislocation glide. The contribution of grain size refinement to the yield stress, for example, is given by Hall-Petch equation;

$$\sigma_y = \sigma_0 + kd^{-1/2} \tag{3-2}$$

Where σ_0 and k are the constants and d is the grain size. For pure Al, σ_0 and k are 14.6 MPa and 2.1 MPa mm$^{0.5}$, respectively. As a result, grain size refinement has a significant effect on yield strength of Al with grain sizes <10 µm[33]. Conventionally, grain size refinement is achieved by mechanical or chemical methods. As the dendrites grow, stirring is applied in order to break the dendrite arms and the broken dendrite arms are swept into the melt and act as nucleation sites. For chemical means, inoculants are added to the melt to increase the number of the heterogeneous nucleation sites.

Rapid solidification promotes the formation of grain-refined structures as the excess free energy of the undercooled melt is stored in the grain boundaries. The grain size of an undercooled melt can be estimated by[34]

27

$$d = \frac{3\sigma_{gb}V_m T_E}{\Delta H_f} \frac{1}{\Delta T} \qquad (3\text{-}3)$$

As the **Equation 3.2** indicates, the degree of undercooling has a strong impact on the grain size. For example, pure Ni has large grain sizes at small undercoolings[35]. As the undercooling increases, grain size gets smaller. There exists a critical undercooling at which an abrupt drop in the grain size by two orders of magnitude is observed. The critical undercooling for Ni is around 175 K. While a dendritic morphology is found below the critical undercooling, an equiaxed microstructure is observed above the critical undercooling. Spontaneous grain size refinement has been observed in many alloy systems including Co-Si [36], Cu-Ni [37] and Ni-Ge [38]. **Figure 16** shows the spontaneous grain size reduction observed in Co-Si alloy. Grain size changes from coarse dendrites to equiaxed grains when undercooling is raised from 23 K to 75 K. This later changes in to coarse dendrites with increasing undercooling.
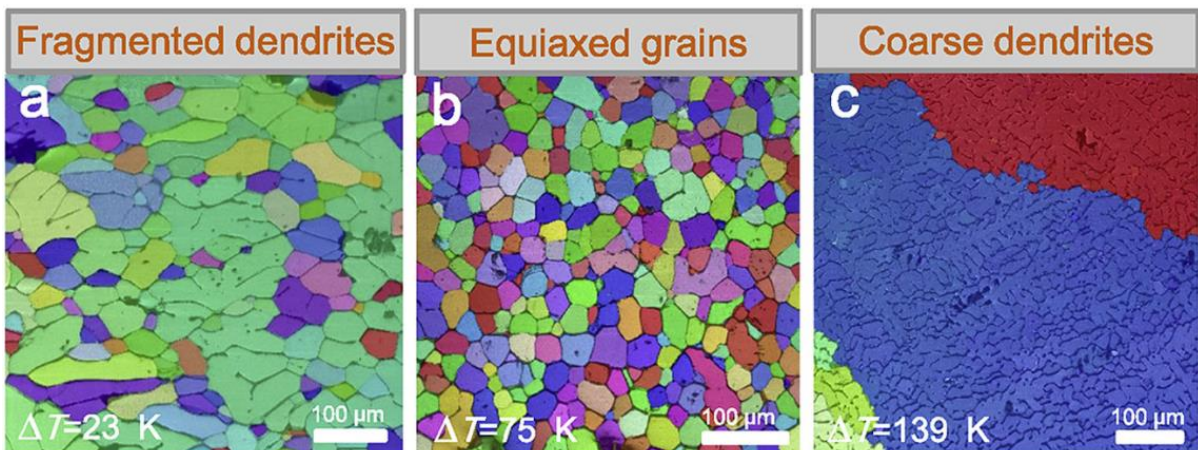
Figure 16: The microstructure of Co-Si alloy at different undercoolings showing the change in the microstructure from coarse dendrites to refined equiaxed grains and then to coarse dendrites[36].

Ag shows a transition from coarse-grained columnar to equiaxed grain-refined structure at undercoolings of around 140 K. In addition, dissolved oxygen was found to reduce the critical undercooling for Ag. The presence of a small amount of oxygen of around 150 ppm leads to a drop in critical undercooling to 100 K. Fe does not show a sudden drop in grain size at high undercoolings up to 340 K[34].

3.1.3   Formation of Metastable Crystalline Phases

In equilibrium solidification, only most stable phases which are shown in phases diagrams are formed. However, rapid solidification with the combination of high undercooling and high cooling rate promotes the formation of metastable phases. For example, droplet-dispersed Ga can form metastable γ, β and δ phases at undercooling of $\Delta T = 0.58 T_E$ which are high pressure phases of Ga[22]. In alloys, the case is more complex as the concentration is another degree of freedom. Metastable phase formation in binary and ternary systems will be discussed in detail in **Section 3.3-3.8** as Al-Fe and Al-Fe-Si alloys form various binary and ternary metastable intermetallics.

3.1.4   Quasicrystals

In addition to crystalline and amorphous solids, there is another type of solid called quasicrystalline solids which correspond to a solid state between crystals and amorphous. Quasicrystals possess rotational symmetry like in crystals but lack long-range translational symmetry. Quasicrystals show five-fold, eight-fold, ten-fold, and 12-fold rotational symmetries which are forbidden for crystals [39]. Quasicrystals are named depending on the rotational symmetries they possess; icosahedral (five-fold), octagonal (eight-fold), decagonal (ten-fold) and dodecagonal (12-fold). Among these, icosahedral and decagonal phases are the most important phases as they are commonly observed in various alloy systems. Some examples of the alloys forming quasicrystalline structures are given in **Table 3**. While icosahedral phase is quasi-periodic in three dimensions, other quasicrystalline phases are quasi-periodic in two dimensions and periodic in the third dimension [40].

Table 3: Some examples of alloys exhibiting quasicrystalline structures[41].

Structure of quasicrystals	Alloys
Icosahedral	Al–Cu–Fe, Al–Mn, Al–Mn–Si, Al–Mn–Cu, Al–Mn–Zn, Al–Cu–Ru, Al–Cu–Os, Al–Cr, Al–V–Si, Al–Pd–Ru, Al–Pd–Mn, Al–Pd–Re
Octagonal	Ni–Cr–Si, Ni–V–Si, Mn–Si
Decagonal	Al–Mn, Al–Fe, Al–Pd, Al–Pd–Fe, Al–Pd–Ru, Al–Pd–Os, Al–Os, Al–Co–Ni, Al–Cu–Co, Al–Cu–Fe–Co, Al–Cu–Co–Si, Al–Co–Fe–Cr–O, Al–Cr–Si, Al–Ni–Fe, Al–Ni–Rh, Al–Cu–Rh, Zn–Mg–Y, Zn–Mg–Sm, Zn–Mg–Ho
Dodecagonal	Ni–Cr, Ni–V, Ni–V–Si, Ta–Te, Co–Cu, Al–Co–Fe–Cr

Quasicrystalline solid was first discovered by Shechtman et al. [42] in 1984 on rapidly solidified $Al_{86}Mn_{14}$ alloy which showed an icosahedral point group symmetry. Since then, quasicrystals have been of interest of many researchers due to their exceptional structure and properties. Quasicrystals have been observed in many alloy systems such as Al, Cu, Ni and Zr based alloys[41]. Quasicrystal are formed at cooling rates slower than that of metallic glass formation and faster than that of crystalline solid formation. Reported cooling rates range for the quasicrystalline phase formation ranges between 500 K/s and 10^6 K/s [32]. Although most of the quasicrystalline phases are metastable phase, there are some thermodynamically stable quasicrystalline phases. Al-Cu-Fe [43], for example, was found to have a stable icosahedral phase after annealing at 1118 K (0.98 T_m) for 48 hours. In addition, Al-Pd-Mn and Al-Pd-Re were also found to form a stable quasicrystalline phase [44].

3.1.5 Metallic Glasses

Metallic glasses, or amorphous metallic alloys, are metallic materials which show neither translational long-range order nor orientational long-range order. Since these materials are noncrystalline and lack of grain and phase boundaries, they exhibit unique mechanical, physical and chemical properties. They possess high fracture toughness, high hardness, high elasticity and are less brittle than their crystalline counterpart. In addition, they show higher tensile strength than the same crystalline alloy[45].

Most metallic glass forming alloys have near eutectic composition. This is because eutectic solidification requires long range diffusion for the segregation of the components of α and β [34], [46]. Thus, eutectic solidification is sluggish especially around the glass transition temperature due to the high viscosity. According to Turnbull [47], a liquid will transfer into glassy phase even at a low cooling rate when T_g/T_m =2/3, that is when a liquid is very sluggish in crystallization. **Figure 17** shows the dependence of the glass-forming eutectic alloys on the concentration. As the T_0 lines (T_0 line represents equal free energy for solid and liquid phases) do not cross near eutectic composition, segregation free solidification is not possible. Therefore, eutectic crystallization or glassy solidification will take place depending on the degree of undercooling[34].
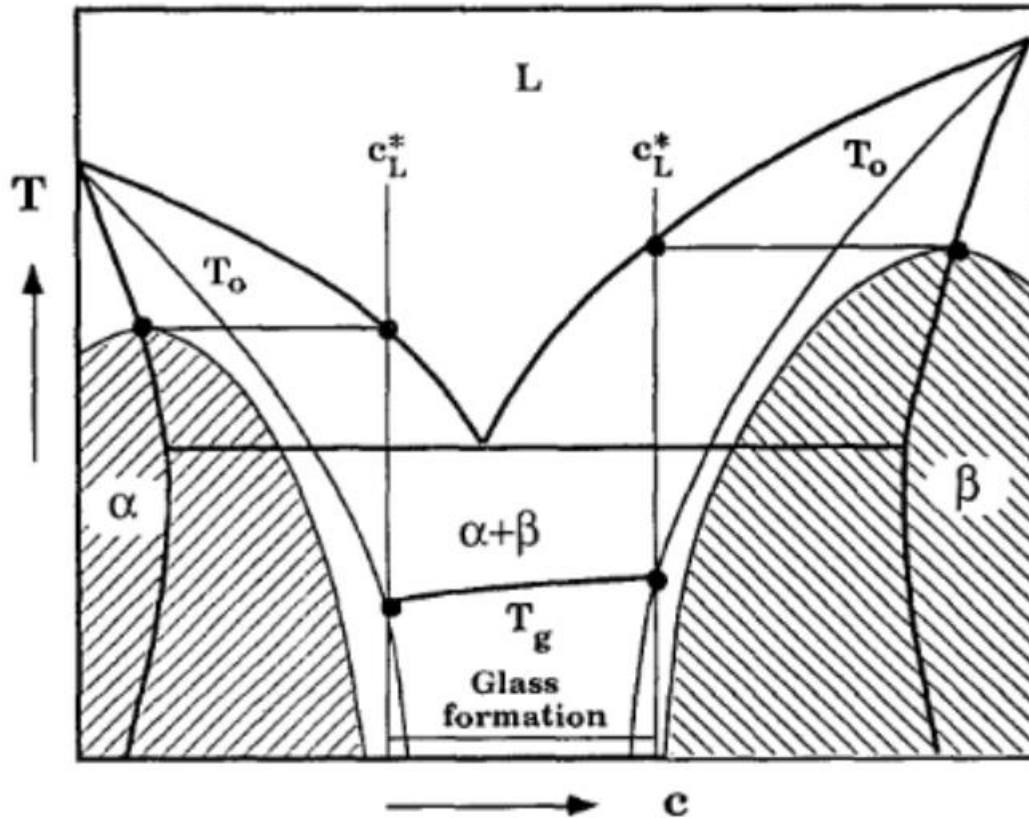
Figure 17: Hypothetical eutectic phase diagram of a glass-forming alloy. Solidification take place either by eutectic crystallization or glass forming in the intermediate concentration range[34].

The first metallic glass was produced by Duwez in 1960 in rapidly quenched near eutectic Au-25 at.% Si alloy with an estimated cooling rate of 10^6 K/s [48]. Since then, many metallic glasses were developed. Any metallic liquid can be transformed into metallic glasses provided that sufficiently high cooling rates are achieved. Recently, Zhong et al. [49] produced monoatomic metallic glasses using ultrafast liquid quenching. High purity liquid tantalum, molybdenum, tungsten and vanadium were vitrified into metallic glasses at the cooling rate of around 10^{14} K/s. However, the high cooling rate requirement for the formation of glassy metals restricted the geometry of these alloys and, thus, the applications. Most glassy metals are manufactured in the shape of ribbons, lines, sheets and powders. Therefore, many researchers tried to produce bulk metallic glasses by decreasing the critical cooling rate for the formation of metallic glasses. One of the principles to reduce the critical cooling rate and produce bulk metallic glasses is to choose elements with large differences in atomic sizes, which creates a complex structure hindering the crystallization. Moreover, alloys with deep eutectic tend to form metallic glass easily as they form liquidus which is stable at relatively low temperatures [50]. Inoue et al. [51] produced bulk metallic glasses in the shape of rods with diameters of

31

ranging between 1 to 7 mm in ternary La-Al-Ni and La-Al-Cu using a high-pressure die casting at cooling rates of around 100 K/s. Using these principles, various bulk metallic glasses have been produced including Pd-Ni-Cu-P, Mg-Cu-Y, Zr-Al-Ni-Cu, Zr-Ti-Cu-Ni-Be, Fe-Co-Ni-Zr-Nb-B, Fe-Ga-P-C-B and Cu-Zr-Ti-Ni systems. Among these alloys, $Pd_{40}Cu_{30}Ni_{10}P_{20}$ [52] and $Zr_{41}Ti_{14}Cu_{12.5}Ni_{10}Be_{22.5}$ (also known as Vitalloy 1) possess the lowest critical cooling rates of 0.1 K/s and 1 K/s, respectively. These alloys are manufactured with a thickness of as large as 10 cm.

3.2 Drop Tube

Rapid solidification methods give an opportunity to make the production of new materials with better properties than materials which are produced conventionally. Rapid solidification can be achieved by different techniques. Glass fluxing, levitation and drop tube methods are different from other techniques since these processes provide containerless solidification which favours homogeneous solidification due to the lack of the heterogeneous nucleation sites like mould walls. Among these containerless methods, drop tube combines high undercooling and high cooling rate [53]. Drop tubes are classified as short (generally 1.5m to 6.5 m tall) and long (taller than 50 m) drop tubes. There are two long drop tubes: NASA Marshall Space Station (105 m) and Grenoble (48 m). Long drop tubes are used to study the effect of the microgravity on the droplet under vacuum. Long drop tubes can achieve undercoolings of as high as 0.21 $\Delta T/T_m$ [54].
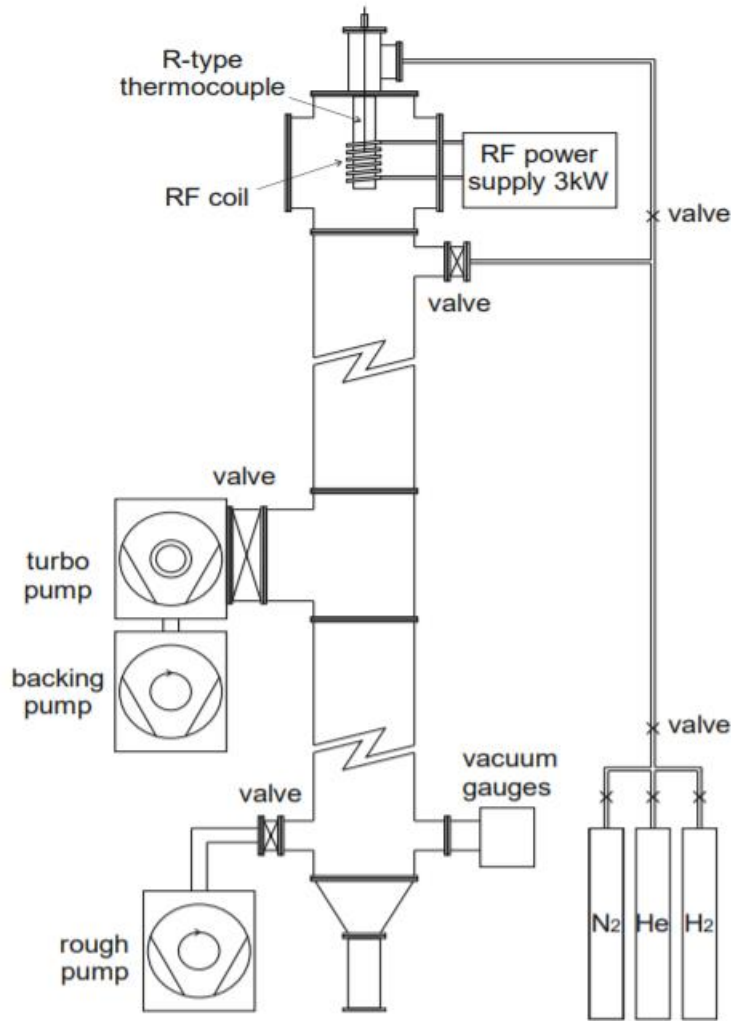
Figure 18: Schematic presentation of the 6.5 m drop tube used in this research [55].

In this study a 6.5 m tall short drop tube was used for the production of samples. The schematic presentation of the drop tube is shown in **Figure 18**. Drop tubes are used to study the effect of nucleation, microstructural and solidification mechanisms on the alloys. In drop tubes droplets solidify during the free fall and, thus, high undercoolings and cooling rates are achieved. As a result, microstructural refinement, extended solid solubility, formation of metastable crystalline phases, formation of quasicrystalline phases and metallic glass formation have been reported [56]–[58]. The geometry and how samples are produced in drop tubes will be explained in detail in Experimental Procedure.

3.3 The binary Al-Fe system

The Al-Fe phase diagram has been investigated several times due to its importance for commercial usage and theoretical studies. The evaluated phase diagram given in **Figure 19** is from the work of Sundman et al. [59]. Fe has extremely low solubility (around 0.052 wt %Fe

33

at the eutectic temperature) in α-Al, and thus Fe is present in the form of aluminides. There are various binary Al-Fe intermetallics in the Al-Fe system. These intermetallics are formed via peritectic, eutectic, peritectoid and eutectoid reactions. These reactions and the temperatures at which the reactions take place are listed in **Table 4**. In addition, space groups and lattice parameters of the stable and metastable phases observed in the Al-Fe system are given in **Table 5**.
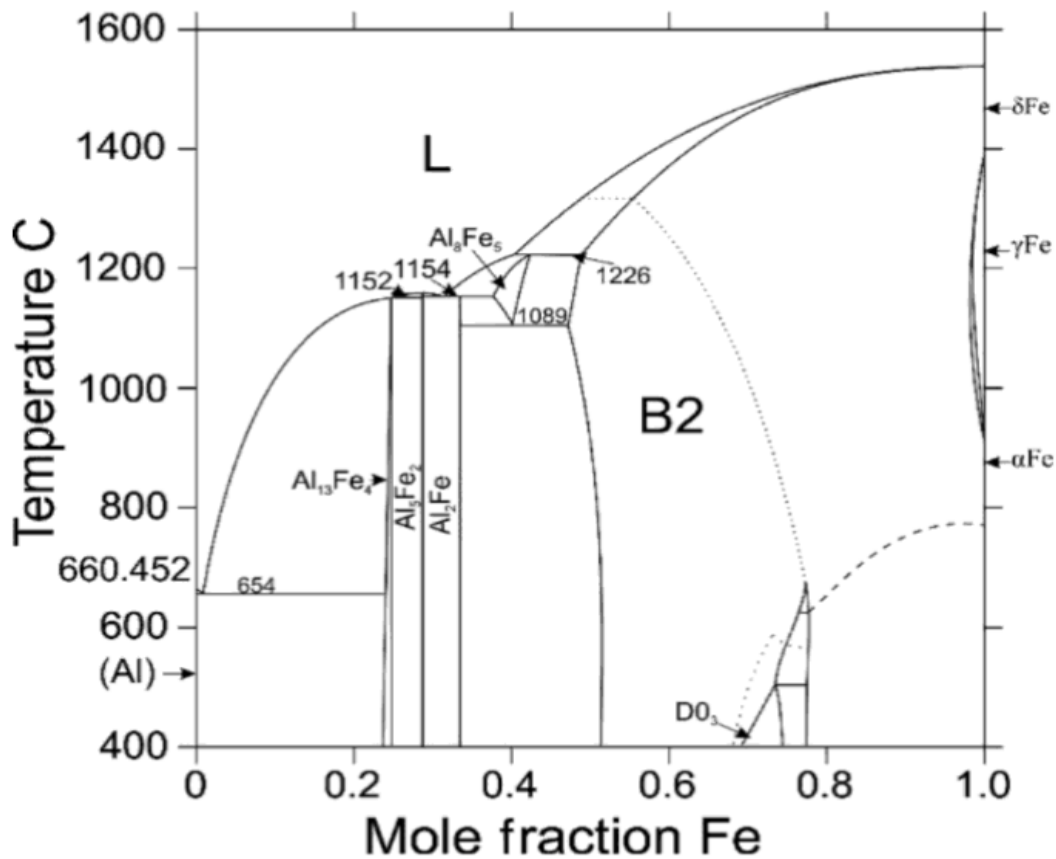
Figure 19: Al-Fe phase diagram [59].

Table 4: Invariant reactions in the Al-Fe system [60].

Reaction	Temperature (°C)	Type of the reaction
L + AlFe ➔ Al_8Fe_5	1226	Peritectic
L ➔ Al_5Fe_2 + Al_8Fe_5	1154	Eutectic
Al_8Fe_5 + Al_5Fe_2 ➔ Al_2Fe	1153	Peritectoid
L + Al_5Fe_2 ➔ $Al_{13}Fe_4$	1151	Peritectic
Al_8Fe_5 ➔ AlFe + Al_2Fe	1089	Eutectoid
L ➔ Al + $Al_{13}Fe_4$	654	Eutectic

Table 5: Intermetallic phases in the binary Al-Fe system and their corresponding Bravais lattice.

Phase	Bravais lattice/Space group	Lattice parameters (Å)	References
$Al_{13}Fe_4$	c-Centred monoclinic C2/m	a = 15.49, b = 8.08 c = 12.48, β = 107.75°	[61]
Al_6Fe	c-Centred orthorhombic Ccmm or Ccm2	a = 6.49, b = 7.44 c = 8.79	[62]
Al_xFe	c-Centred orthorhombic	a = 6, b = 7, c = 4.7	[61], [63]
Al_mFe	Body centred tetragonal I_4mm or I_4mmm	a = 8.84 b = c = 31.6	[64]
Al_9Fe_2	Monoclinic	a = 8.90, b = 6.35 c = 6.32, β = 93.4°	[65]
Al_pFe	Body centred cubic	a = b = c = 10.3	[66]
AlFe	B2-ordered Pm$\bar{3}$m	a = 2.908	[67]
Al_8Fe_5	Body centred cubic I$\bar{4}$3m	a = 8.9757	[68]
Al_2Fe	Triclinic P$\bar{1}$	a = 4.875, b = 6.454, c = 8.736, α = 87.93°, β = 74.396°, γ = 83.062°	[69]
Al_5Fe_2	Orthorhombic Cmcm	a = 7.65, b = 6.41, c = 4.22	[70]

The aluminium rich side of the system has a eutectic reaction, L ➔ Al + Al_3Fe (Al_3Fe is also denoted as $Al_{13}Fe_4$), which takes place at 654 °C close to the melting point of Al ($T_{m,Al}$ = 660.3 °C) with the composition of the liquid 1.8 wt %Fe (0.9 at. %Fe) [60]. According to Mondolfo [71], Al_3Fe has an Fe content a varying homogeneity range between 37.3 to 40.7 wt %Fe. The eutectic point of the Al-Al_3Fe is strongly dependent on the cooling rate as the eutectic point of Al-Al_3Fe shifts to a higher iron concentration with an increasing cooling rate [72]. The eutectic shift at different cooling rates is shown in the metastable extension of the Al-rich side of the phase diagram given in **Figure 20**. For example, the eutectic moves to 2.3 wt %Fe at a cooling rate of 10^3 K/s and a further increase in the cooling rate to 10^6 K/s shifts the iron concentration to 4.3 wt %Fe. Al-Al_3Fe eutectic forms plate-like eutectic morphology as shown in **Figure 221** [73].
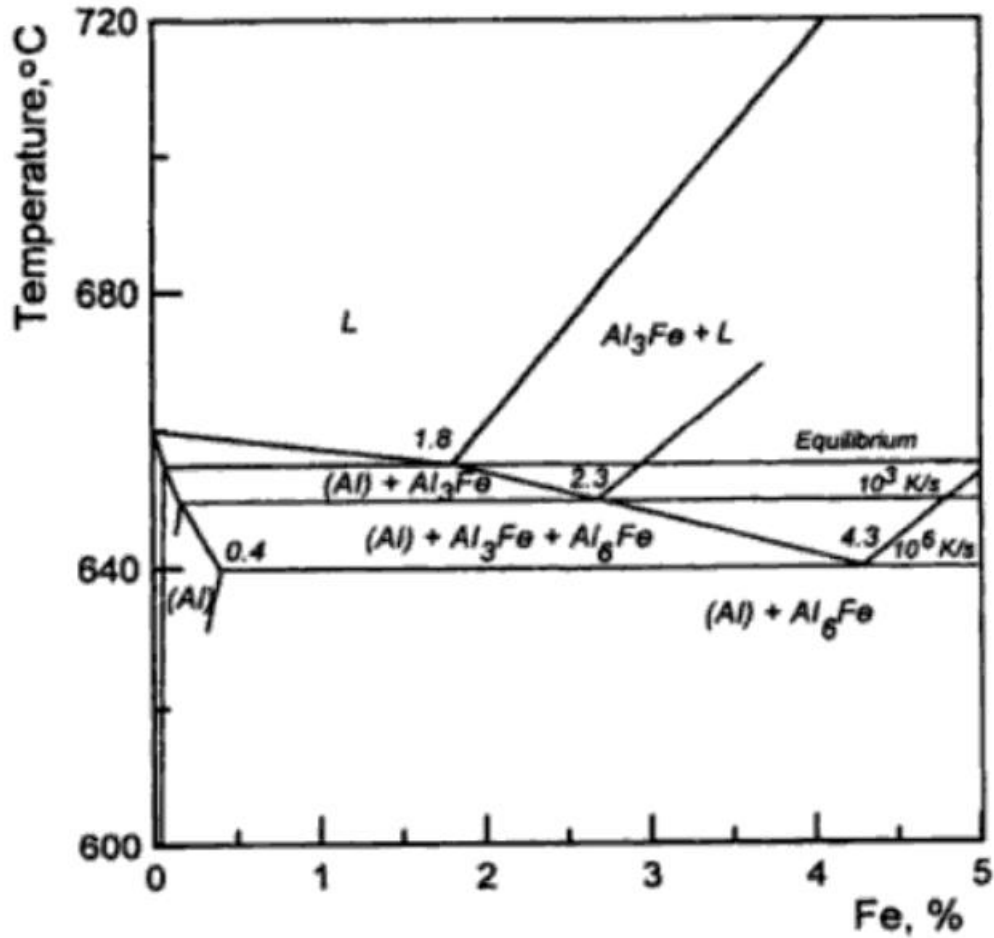
Figure 20: The metastable Al-Fe phase diagram [74].

In addition to the stable Al_3Fe intermetallic, a number of metastable intermetallics are found in the Al rich side of the system under nonequilibrium solidification due to the supercooling and the change in the nucleation and growth conditions. One of the most commonly observed intermetallics in rapidly solidified Al-Fe system is Al_6Fe which is formed via a eutectic reaction [62]. The Al-Al_6Fe eutectic reaction takes place at 652 °C, very close to the Al-Al_3Fe eutectic, at the liquid composition of 2.8wt. %Fe [75]. The Al-Al_6Fe eutectic occurs when the cooling rate exceeds 3 °C/s. However, the Al-Al_6Fe eutectic transition occurs at rather lower solidification velocities of lower than 100 µm/sec. Solidification velocities higher than that favour the formation of Al-Al_3Fe [76]. Solidification velocities also effect the morphology of the Al-Al_6Fe eutectic; the morphology transitions from rod-like to rod-like and cellular with increasing growth velocities[73]. The morphology of Al-Al_6Fe is shown in **Figure 21**. Apart from metastable Al_6Fe, metastable Al_xFe ($x \approx 5.8$), Al_mFe ($m = 4.0$ to 4.4) and Al_pFe ($p \approx 4.5$) phases were also detected in dilute Al-Fe alloys. The Bravais lattice and lattice parameters of

36

these phases are given in **Table 5**. However, the diffraction patterns of these phases cannot be presented due to the lack of XRD patterns in the database.
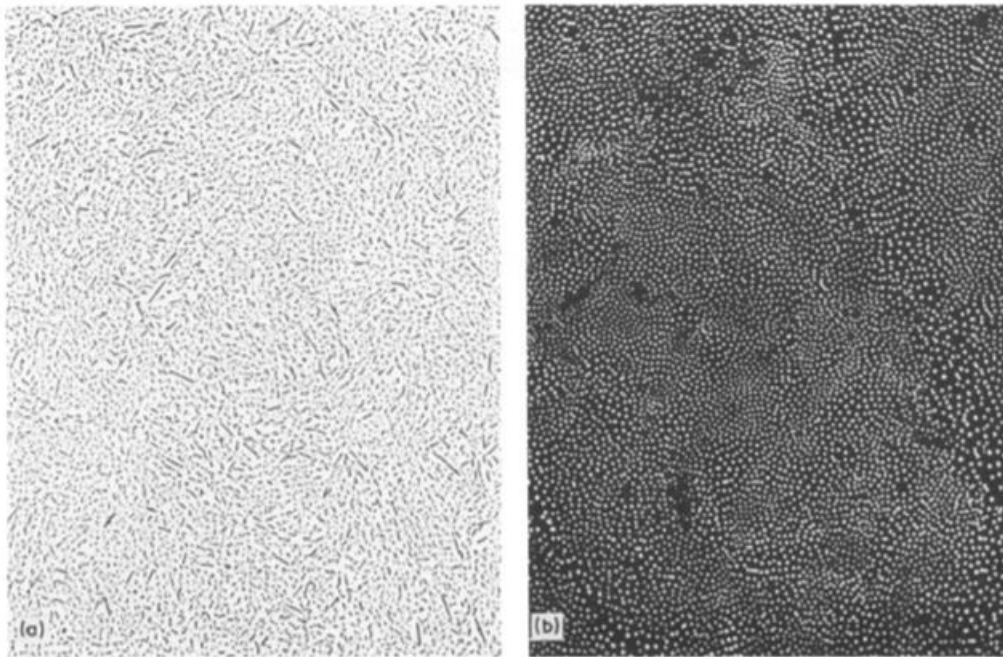
Figure 21: Morphologies of a) Al-Al$_3$Fe, 2.2 wt. %Fe, 9.1 x 10^{-3} mm/s and b) Al-Al$_6$Fe, 2.4 wt. %Fe, 8.1 x 10^{-1} mm/s [77].

3.4 Al-Fe Microstructure Selection Maps

Microstructure selection maps show the solidification pathway of the undercooled liquid to the final state of the metals and alloys. Morphological or phase instabilities caused by the competition between growth and nucleation are illustrated in these maps. Hughes and Jones [77], [78] studied the coupled eutectic growth of Al-Fe alloys at Fe concentration ranging between 2.2 wt.% and 6.1 wt. %Fe using directional solidification with solidification speeds in the range of 5.1 x 10^{-5} to 41 mm/sec. They constructed an Al-Fe microstructure map given in **Figure 22**. Their results show that Al-Al$_3$Fe (EU1) eutectic is the dominant eutectic at low solidification speeds; increasing solidification speed favours the formation of metastable Al-Al$_6$Fe (EU2) eutectic. The transition solidification speed between the eutectics for all compositions is around 0.1 mm/sec. Increasing solidification speed also changes the primary phase; primary phase transitions from Al$_3$Fe to α-Al. The transition velocity for the primary phases increases with increasing Fe concentration. Gilgien et al. [79] also studied the microstructure selection maps of Al-Fe alloys at relatively high solidification rates between 0.01 and 0.1 m/sec using laser remelting technique and completed the upper part of the map shown in **Figure 22**. They observed high velocity solidification bands at higher solidification

velocities than 15 cm/sec. Moreover, eutectic spacing slightly decreases with increasing Fe concentration.
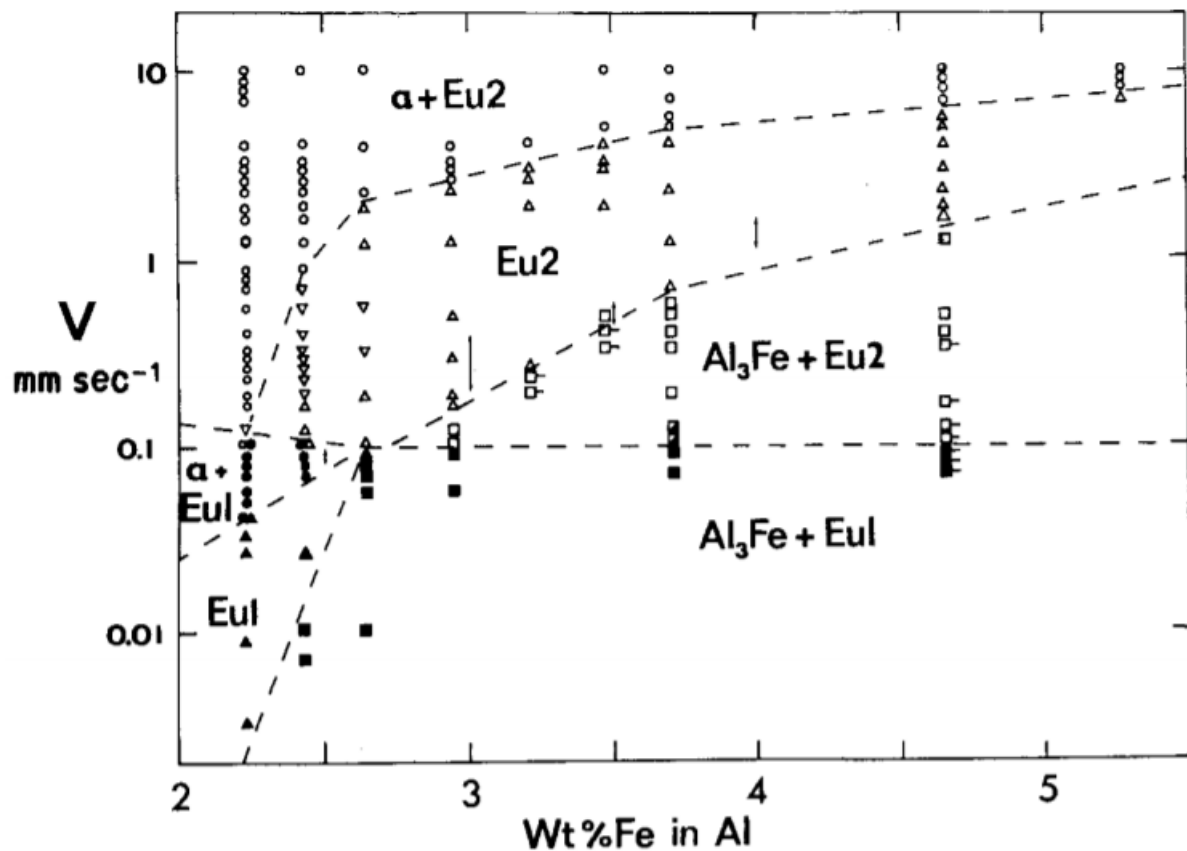
Figure 22: Microstructure selection map of Al-Fe as a function of Fe content and growth rate with a temperature gradient of 20 K/mm. EU1 = Al-Al₃Fe eutectic, EU2 = Al-Al₆Fe eutectic, α = dendritic α-Al solid solution. Inverted open triangles indicate the presence of incipient dendritic α-Al, square with side tag indicate pronounced α-Al halo formation around primary Al₃Fe, half-filled squares indicate mixed EU1/EU2 matrix surrounding primary Al₃Fe [77].

The dependence of the eutectic spacing on the growth velocity was shown by Wang et al. [73] who studied Bridgman growth of Al-3wt. %Fe with growth velocities between 51 and 1030 μm/s. The relation between eutectic spacing and growth rate for the stable and metastable eutectics was given as $\lambda\sqrt{V} = 22.4 \, \mu m^{3/2} sec^{-1/2}$ and $\lambda\sqrt{V} = 13.8 \, \mu m^{3/2} sec^{-1/2}$, respectively. These equations have the same form as the Jackson-Hunt eutectic equation given in **Equation 2.28**. Adam and Hogan [75] also calculated the eutectic spacing and growth rate relation in Al-1.8 wt. %Fe alloy. They found the relation for the stable eutectic as $\lambda^{2.6}V = 3180 \, \mu m^{3.6} sec^{-1}$ and $\lambda^2 V = 10.2 \, \mu m^3 sec^{-1}$ for the metastable eutectic. Recently, Goulart et al. [80] found the relation as $\lambda\sqrt{V} = 1.6$ (where V is in mm/sec and λ is in μm) in Al-1.5 wt% Fe alloy using Bridgman and water cooled solidification with solidification velocities ranging between 0.03 and 2 mm/sec for both stable and metastable eutectics as given in **Figure 23**.

Tiller [81] proposed that for $\lambda^n V = constant$ the growth rate of the eutectic phase is determined by the solute species at the interface if n=2. If n>2, the rate is determined by the atomic attachment kinetic.
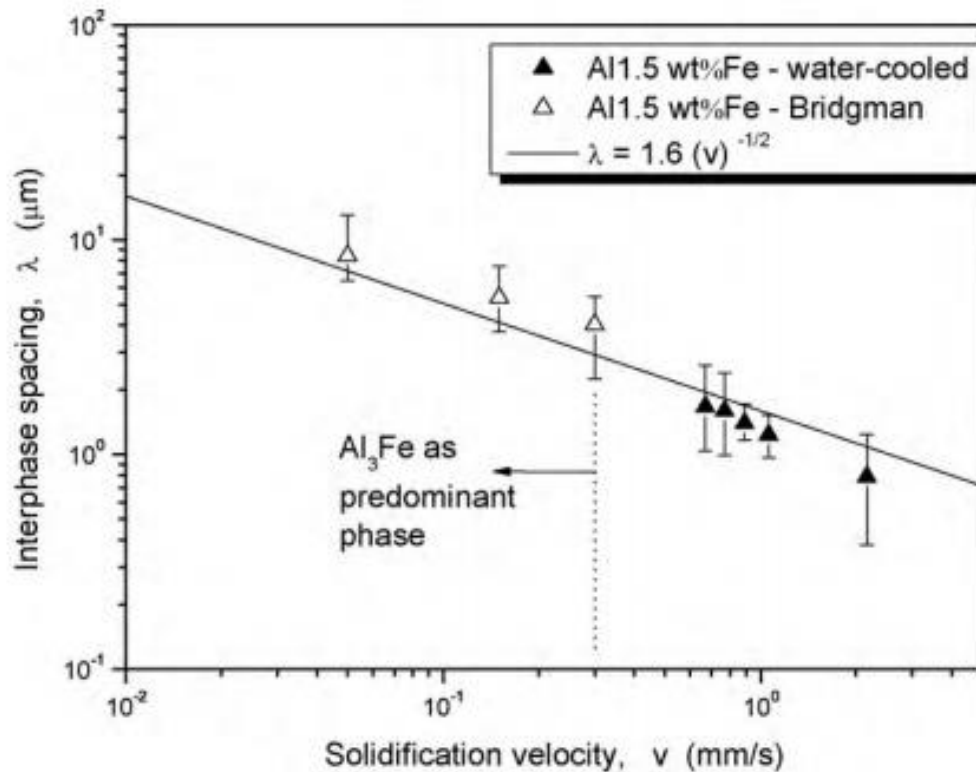
Figure 23: Eutectic interphase spacing for an Al-1.5 wt. %Fe alloy as a function of solidification velocity [80].

3.5 Al-Fe eutectic coupled zone

During the solidification of a liquid with non-eutectic composition, fully eutectic microstructures can be observed. The final microstructure (fully eutectic or eutectic with primary phase formation) is decided by the growth velocity of the phases. Coupled zone depicts the transition between the formation of a fully eutectic structure and the formation of primary dendrites with interdendritic eutectic. Two types of eutectic coupled zones are symmetric and asymmetric. While the growth temperature of the eutectic is higher than that of the dendrite in symmetric coupled zone eutectic, the eutectic growth temperature is lower in asymmetric one. Moreover, symmetric coupled zones are mostly observed in regular eutectics and irregular eutectics show asymmetric coupled zones [82]. Coupled zone maps are useful in rapid solidification as they allow the determination of required solidification velocity to achieve desired microstructure.

Al-Fe eutectic coupled zone was studied by Gilgien et al. [79] using laser remelting with solidification velocities ranging between 0.01 and 0.1 m/s. They constructed Al-Fe eutectic coupled zone given in **Figure 24**. As discussed earlier, these diagrams are important in rapid solidification. For example, during the rapid solidification of a hypereutectic Al-2.0 at. %Fe alloy, primary α-Al dendrites can be formed provided that high solidification rates and, thus high undercoolings are achieved. If the same alloy solidified slowly, primary Al_3Fe is expected to form. Cooling rates between these favour the formation of complete eutectic of either Al-Al_3Fe or Al-Al_6Fe. While stable eutectic forms at rather low solidification rates, metastable eutectic becomes dominant at higher solidification rates. From **Figure 24**, in addition to which eutectics are dominant, interlamellar spacings of these phases can also be found. Interlamellar spacing decreases with increasing undercooling as shown in the figure.
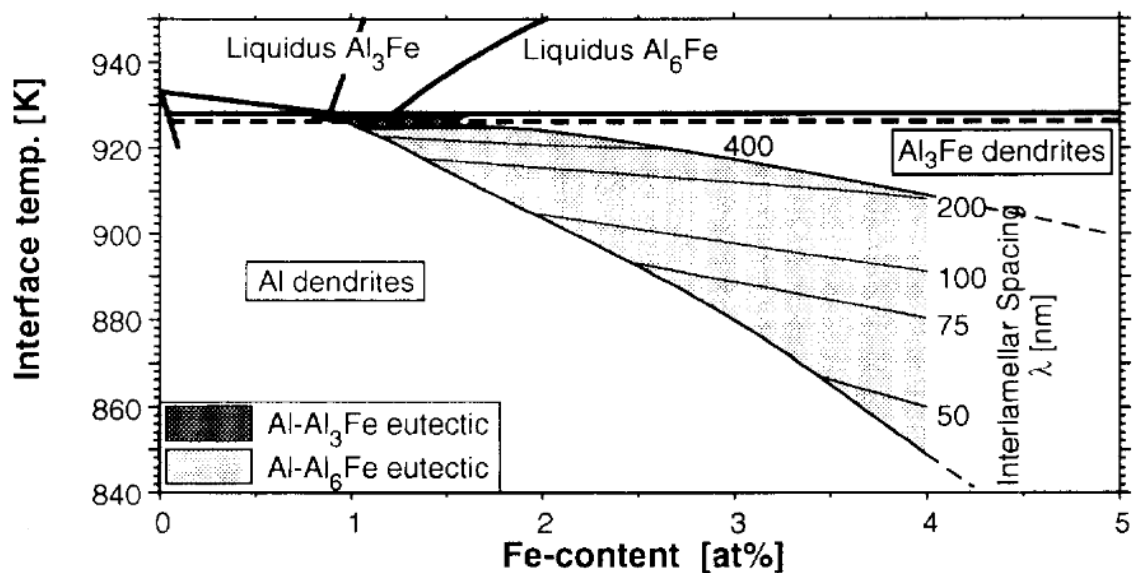
Figure 24: Calculated solidification microstructure selection map drawn in the interface temperature-composition plane showing the coupled zone of Al-Fe system with its phase diagram [79].

3.6 The Binary Al-Si phase diagram

Aluminium-silicon alloys are technologically important casting alloys. The Al-Si phase diagram is one of the simplest eutectic phase diagrams as illustrated in **Figure 25**. There is a eutectic at 577 °C and the liquid composition of Al- 12.2 wt% Si. Al and Si do not form any compound for all composition ranges and the solubility of the elements in each other is limited: at room temperature the solubility of Si in α-Al is around 0.02 wt.% Si. However, nonequilibrium solidification has been reported to increase the solubility of Si in Al [83], [84]. Roehling et al. [84] investigated pulsed-laser melt Al- 1-9 at% Si alloys. They observed a super

saturated solid solution of α-Al up to Si content of 3 at % without any eutectic formation. Similarly, Uzun et al. [83] reported solid solubility extension of 8.8 wt% Si in melt-spun Al-16 wt% Si alloy. They also reported that an average of 55% Si is dissolved in Al up to Si composition of 16 wt% Si. Ge et al. [85] studied rapid solidification behaviour of Al-50 at.% Si alloy using a 3 m drop tube. They found refinement in the primary silicon phase with increasing cooling rate. Increasing cooling rate also changed the morphology of the Al-Si eutectic from needle-like to worm-like forms.
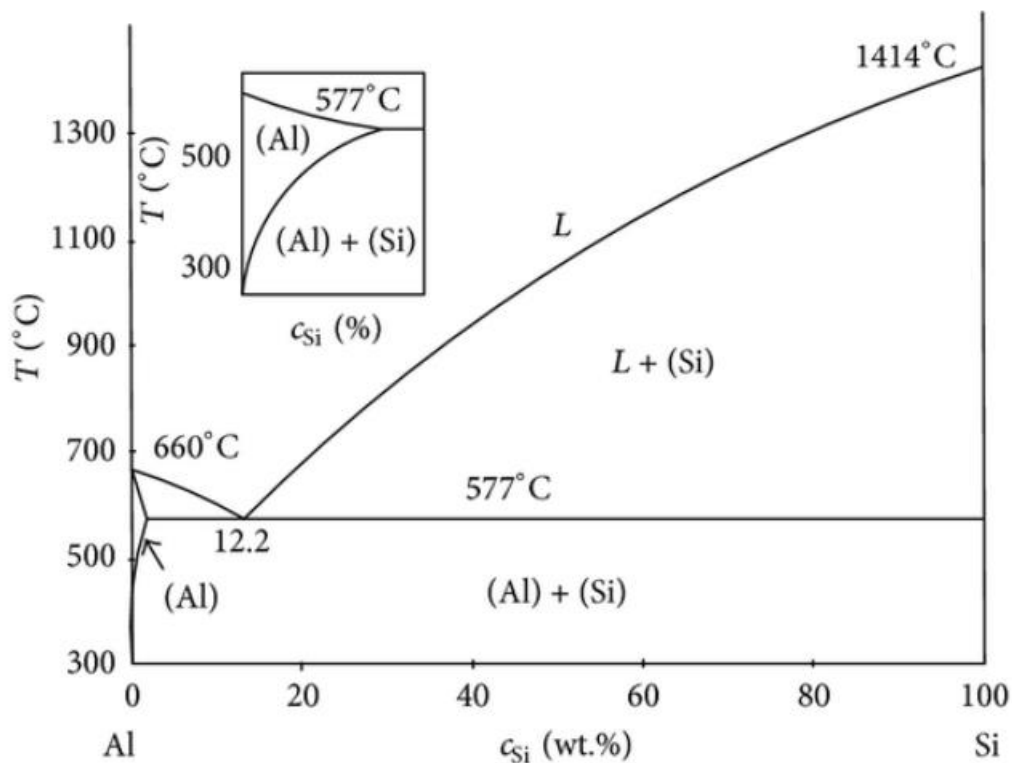
Figure 25: The Al-Si phase diagram [60].

3.7 The Ternary Al-Fe-Si Phase Diagram

The ternary Al-Fe-Si system is commercially important as most Al alloys contain Fe and Si either as an alloying element or impurities. Moreover, upon solidification, these elements precipitate as ternary Al-Fe-Si phases which are hard and brittle leading to a decrease in mechanical properties. Thus, the ternary Al-Fe-Si phase diagram has been studied by many researchers. There are 11 stable ternary phases in the ternary Al-Fe-Si system, many of which exist over considerable ranges of homogeneity, making it an extremely complex system. Therefore, for the simplicity, the liquidus surface of the Al-rich part of the Al-Fe-Si phase

diagram and the polythermal section of the ternary Al-Fe-Si phase diagram with an Fe concentration of 4 wt%Fe is given in **Figure 26** and **27**, respectively.
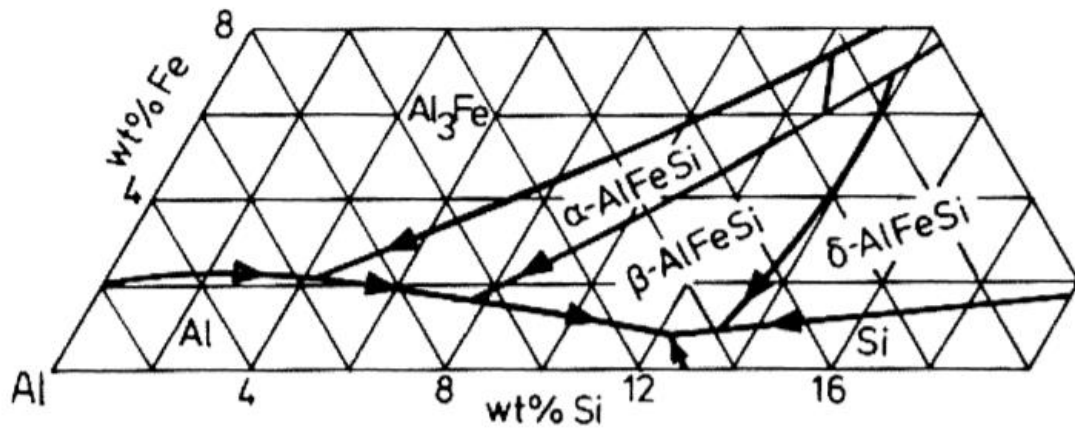
Figure 26: Liquidus surface of the Al-rich part of the Al-Fe-Si system[86].
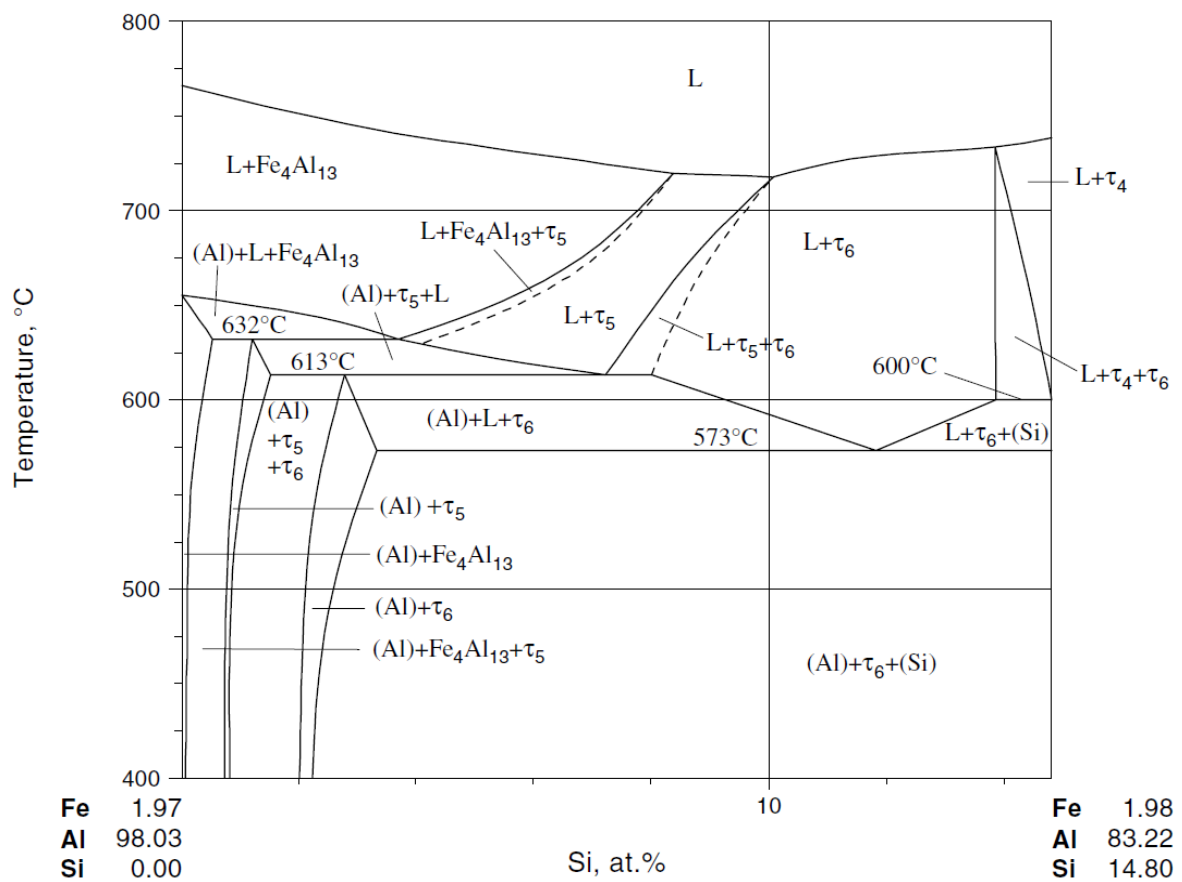
Figure 27: Polythermal section of the Al-Fe-Si phase diagram at a constant Fe content of 4 wt% Fe.

If Si content is high enough to form ternary phase, under equilibrium solidification two ternary phases are formed at the Al-rich part of the Al-Fe-Si phase diagram: Fe_2SiAl_8 (also known as α phase) and $FeSiAl_5$ (also known as β phase). These phases are formed via the following peritectic and eutectic reactions at the given invariant temperatures [71]:

1. Liquid+ $FeAl_4$ ➔ Al + α-Al_8Fe_2Si (620-638 °C)
2. Liquid + Fe_2SiAl_8 ➔ Al + β-Al_5FeSi (611-615 °C)
3. Liquid ➔ Al + Si + β-Al_5FeSi (576-577 °C)

Both α and β phases exist over a range of compositions. **Figure 28** gives the homogeneity range of these phases as well as the homogeneity ranges of the binary Al-Fe intermetallics and the Si solubility of these phase.
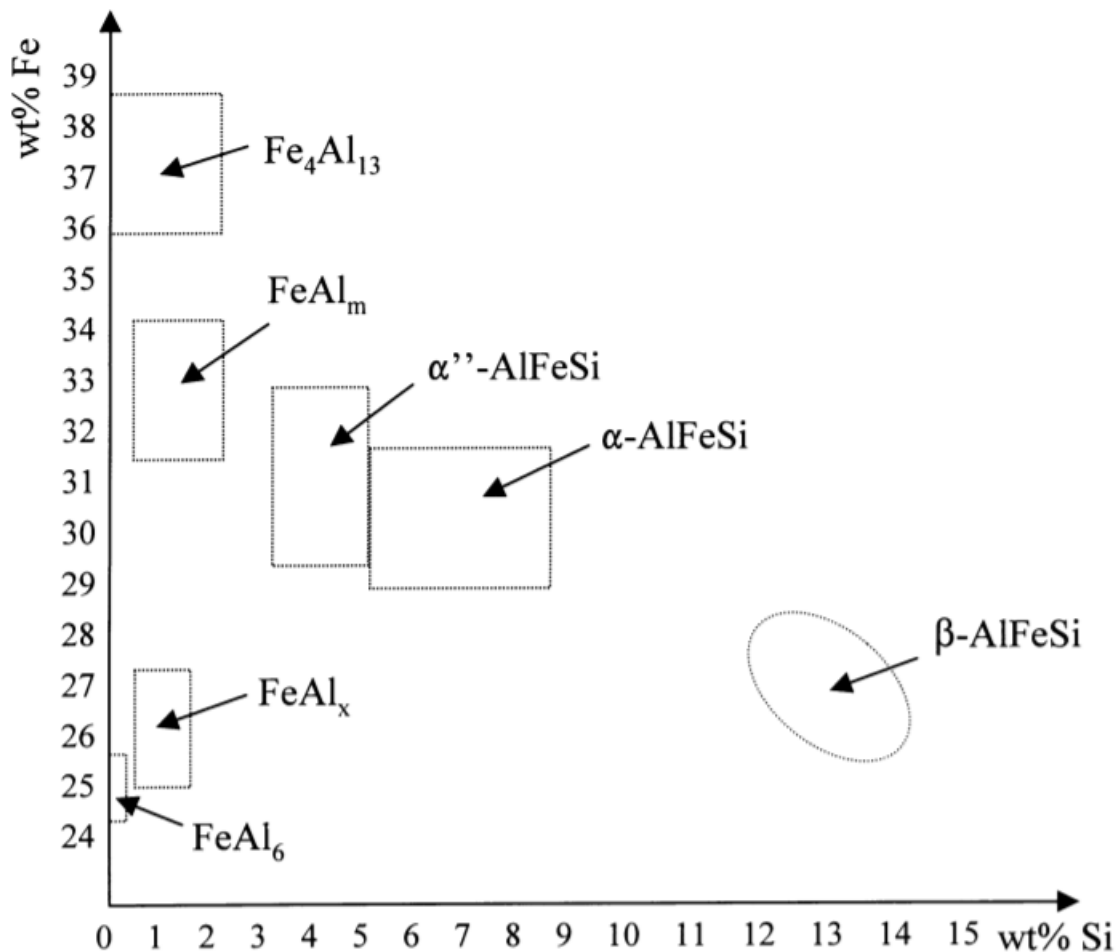
Figure 28: compositions of the binary and ternary phases in dilute Al-Fe-Si system [71].

3.8 Recent Progress

Considerable attention has been paid to the Al-rich part of the Al-Fe system. Effect of cooling rate on the formation of stable and metastable intermetallics has been investigated by many researchers. Melt-spinning, splat-quenching and gas atomization, which cover a range of cooling rates from 10^3 to 10^6 K/s have been employed to reveal the microstructures and properties. Solid solubility extension, formation of metastable phases, formation of quasicrystalline and amorphous phases have been reported in Al rich Al-Fe alloys. Nayak et al. [87] studied the effect of the cooling rate on Al- 2.5, 5, 10, 15, and 20 at. %Fe alloys using melt spinning at wheel speeds of 20, 30 and 40 m/sec. They observed primary α-Al and metastable Al_5Fe_2 (up to 10 at. %Fe) in Al-2.5 at. %Fe alloy. With increasing iron concentration primary α-Al transitioned to primary Al_3Fe and at the highest Fe concentration, only Al_3Fe was formed. They also calculated the solubility of Fe in α-Al using Al (311) peaks. Highest Fe solubility was reported as 1.67 at. %Fe in 2.5 at. %Fe alloy and it was reported that Fe solubility decreased with increasing Fe content as well as increasing wheel speed and, consequently, increasing cooling rate. Moreover, quasicrystalline and amorphous phases formed in alloys with Fe content up to 10 at. %Fe. Amorphous phase formation in Al-Fe system also reported by Mukhopadhyay et al. [6] who studied Al-Fe alloys with Fe content up to 25 at. % using mechanical alloying at room temperature. Complete amorphization occurred at the highest Fe containing alloy while lower Fe content resulted in the combination of amorphous phase and solid solution. The only intermetallic formed was Al_5Fe_2 in the samples. The effect on the mechanical properties was also investigated using microhardness. Microhardness was observed to improve with increasing iron concentrations and reached a peak at 10 at. %Fe and with increasing cooling rate. However, further increase in Fe content resulted in a decrease in microhardness values for all cooling rates [87].

Chen et al. [5] studied the impulse atomized (IA) Al-0.61 and 1.90 wt. %Fe alloys using IA with estimated cooling rate of 170 K/s. Rapid solidification favoured the formation of metastable Al_mFe. In both alloys, similar microstructures were observed so that dendritic α-Al is the primary phase and interdendritic eutectic although the latter alloy is hypereutectic. This is because the undercooling reached was below the metastable extension of the α-Al solidus. Similar results related to the extension of the α-Al liquidus was also reported by Boettinger et al. [12] and Cochrane et al [88]. They were able to form α-Al first in hypereutectic Al-Fe system where Fe concentration was as high as 8 wt. %. However, they had to reach high cooling rates of around 1000 K/s to observe primary α-Al. Rapid solidification also changed the dendritic

growth direction of α-Al to (111) from (100), which is the most common dendritic growth direction for cubic alloys [5].

Henein et al. [89] studied the IA Al-0.61 and 1.90 wt. %Fe with powder ranges between 120 and 900 µm with corresponding cooling rates of 20 to 10000 K/s under He and N_2 atmosphere. They observed the formation of Al-Al_3Fe, -Al_6Fe and -Al_5Fe_2 eutectics which formed at the primary α-Al interdendritic region with lamella structure. The average fractions of these eutectics are reported to be 33.1 vol.% and 18.2 vol. % for Al-0.61 and 1.90 wt. %Fe alloys, respectively. Cell spacing was reported to decrease with decreasing particle size and increasing Fe content. In addition, solidification under He yielded finer dendritic and cellular structure. They found the relation between cell spacing and cooling rate as $\lambda=40.7 \times \dot{T}^{-0.25}$ and $\lambda= 23.9 \times \dot{T}^{-0.21}$ ($\mu m(K/s)^{-n}$) for Al-0.61 and 1.90 wt. %Fe alloys, respectively. Henein et al. also conducted 3D projection of 550 µm droplet of Al-0.61Fe using X-ray tomography. Microtomography given in **Figure 29** showed the formation of large needle-like primary phase with branches along the whole sample, which they reported as α-Al, scattering from its single nucleation point
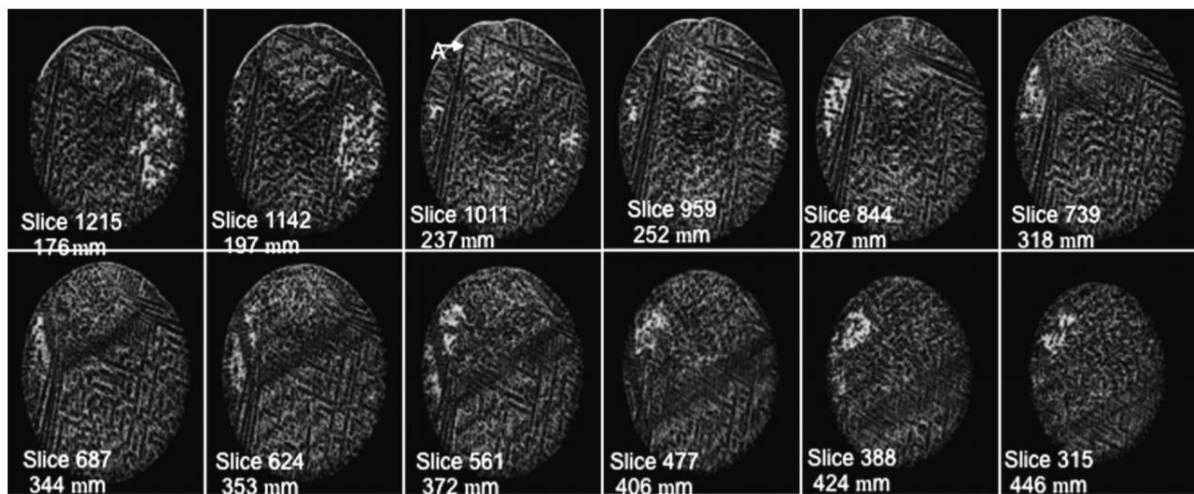
Figure 29: Sequence of slices from the tomographic image of a 550 µm powder atomized in nitrogen. The lighter colour in the particle represents the eutectic. Point A identifies the region where nucleation and initial growth was initiated.[89]

Goulart et al. [80] investigated the effect of directional solidification on Al-0.5, -1.0 and -1.5 wt. %Fe alloys using Bridgman furnace with growth rates ranging between 0.05 to 2.5 mm/s. While the dominant eutectic is plate-like Al-Al_3Fe at slow growth rates, the rod-like Al-Al_6Fe eutectic, which formed at the cell boundaries of the α-Al, became dominant phase with increasing growth rate. Cell size of the α-Al was found to be decreasing with increasing growth rates. The effect of the cell size on the mechanical properties was later investigated by Silva et al. [90] who studied the directionally solidified Al-1.0 and -1.5 wt. %Fe with cooling rates

ranging between 1.9 K/s and 22.8 K/s. They found that the microhardness of the alloys is increasing with increasing cooling rate, Fe content and decreasing cell size.

Boettinger et al. [12] studied the atomized Al-8 wt. %Fe powders with diameters between 5 to 45 µm. Primary Al_3Fe intermetallic, fully $Al-Al_6Fe$ eutectic structure, cellular α-Al and microcellular α-Al was observed with respect to the decreasing powder size. Cochrane et al. [13]also studied the same alloy but with wider powder diameters ranging between 50 to 2000 µm and the corresponding cooling rates between 160000 and 520 K/s using a drop tube. While large powders (600-2000 µm) consisted of primary Al_3Fe and $Al-Al_6Fe$ eutectic, coarse cellular α-Al (zone A) and fine cellular α-Al (zone B) structures (zone A and zone B structures are depicted in **Figure 30**) started to form with decreasing powder size and replaced primary Al_3Fe. These zone A and zone B structures were also observed by Sharma et al. [91]who studied drop tube atomized Al-3.6 wt.%Fe powders with diameter of 500 µm. Solidification initiated by the formation of zone B and transitioned into zone A, which later transitioned into dendritic α-Al due to recalescence. They concluded that undercooling plays a critical role in the phase selection of drop tube processed alloys. Cooling rate also plays a critical role in the phase selection of Al-Fe system. Chen et al. [92] studied the same alloy as Cochrane et al. [13] under microgravity conditions using electromagnetic levitation. Although they reached high undercoolings of around 155 K, the microstructure consisted of primary star-like Al_3Fe and coexisting eutectics of $Al-Al_3Fe$ and $Al-Al_xFe$. This is due to the cooling rate they achieved (95 K/s) was lower than that of achieved by Cochrane et al.
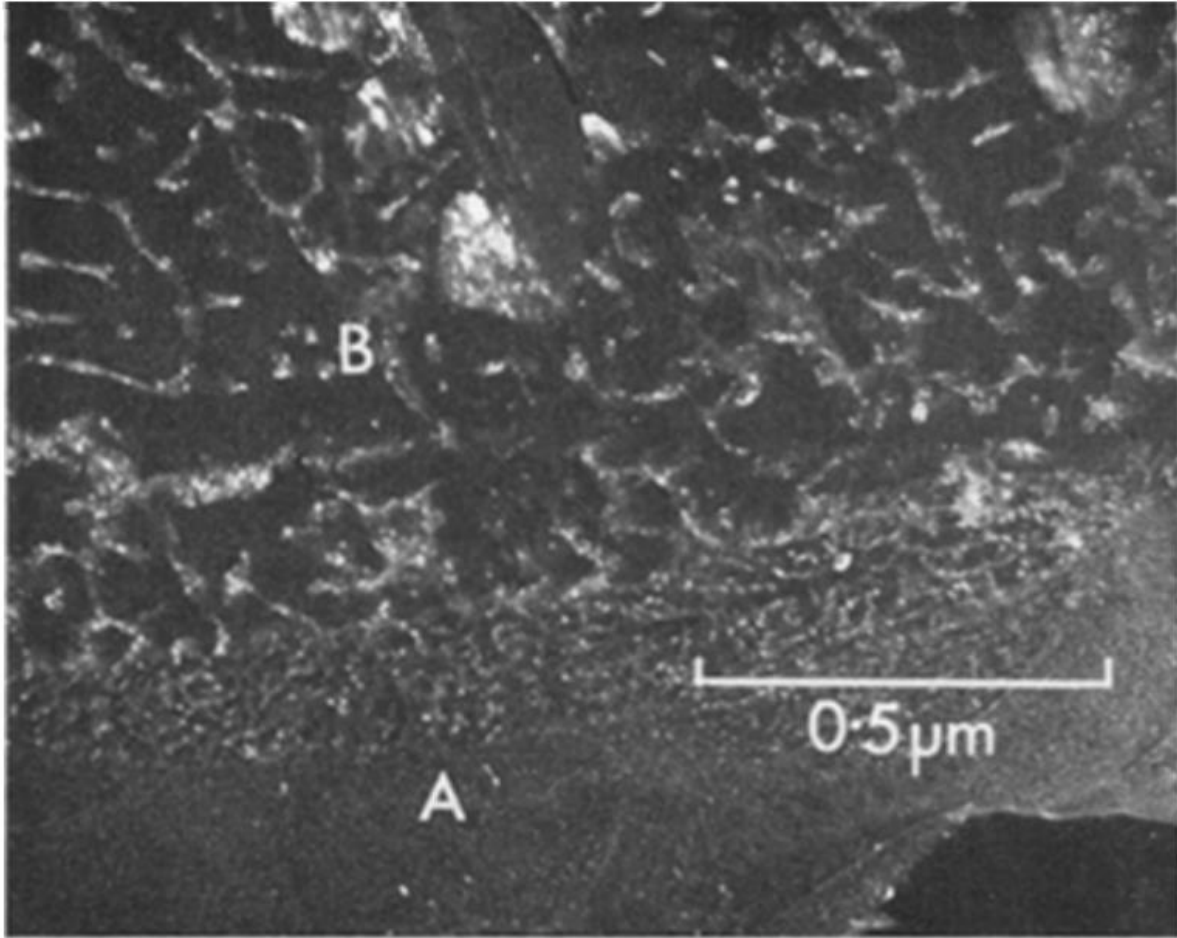
Figure 30: Microstructure of Al-8wt.%Fe as quenched splat showing both zone A and zone B as labelled.[93]

Jacobs et al. [93] investigated the microstructural development of the splat-quenched Al-8 wt. %Fe. They found zone A and zone B structures in the alloy with primary particles (either Al_6Fe or Al_3Fe) randomly distributed in both zones. The difference in the cell size of zone A and zone B can be as high as 15 times [94]. They also investigated the effect of the heat treatment on the microhardness of the alloy and the decomposition of the zone A and zone B. Annealing temperature up to 600 K did not make any change in the microhardness of the alloy but higher annealing temperatures sharply decreased the microhardness. For example, microhardness dropped to half when the temperature increased from 600 to 650 K. During annealing of zone A up to 570 K, Al_6Fe is formed at the α-Al grain boundaries but higher annealing temperatures favoured the formation of Al_3Fe needles. Similarly, Kim and Cantor [95] and Griger and Stefaniay [14] reported the formation of Al_3Fe at higher annealing temperatures and at lower annealing temperatures they reported the formation of Al_6Fe and Al_mFe from the decomposition of quasicrystalline phase and supersaturated α-Al solid solution.

Mukhopadhyay et al.[6] studied the structural evolution of Al-Fe alloys with Fe content up to 25 at. % using mechanical alloying at room temperature. Al_5Fe_2 was the only intermetallic observed in the samples due to low temperature. They also found the formation of fully amorphous phase in Al-25 at. %Fe alloy while the other alloys formed a mixture of amorphous phase and solid solution.

Ternary Al-Fe-Si system has been studied at ranging Fe and Si contents. During the solidification of the ternary alloy the formation of binary Al-Fe and ternary Al-Fe-Si phases have been reported but the formation of any Fe-Si intermetallics have not been observed. The formation of these phases depends on the alloy composition, cooling rate and Fe:Si ratio. Khalifa et al. [4] investigated solidification behaviour of the various ternary Al-Fe-Si alloys with Fe concentration up to 1.03 wt.% and Si content of 6 wt. % at low cooling rates ranging between 0.1 to 15 K/s. They found that the binary Al-Fe eutectics occur up to cooling rates of 0.3 K/s and cooling rates above this favoured the formation of the ternary intermetallics. Dominant ternary intermetallic also ranges depending on the cooling rate. While β-Al_5FeSi was stable in slow cooled samples, higher cooling rates promoted the formation of δ-Al_4FeSi_2 and α-Al_8Fe_2Si. Similar results have also been reported by Griger and Stefaniay [14] and Zhang et al [3]. Griger and Stefaniay [14] also stated that at relatively low cooling rates the phase selection in the ternary alloy is strongly dependant on the Fe:Si ratio so that high Fe:Si ratio promotes the formation of binary Al-Fe while low ratio results in the formation of ternary phases.

High cooling rates drastically influence the phase selection, morphology of the phases and mechanical properties of the ternary Al-Fe-Si system. Unlu et al. [15] studied the melt-spun hypoeutectic Al-10wt%Si-3.3wt%Fe and hypereutectic Al-20wt%Si-3.3wt%Fe alloys with an estimated cooling rate of around 10^5 K/s . They could not observe the formation of any intermetallic compounds in both alloys. While the microstructure of the former alloy only consisted of α-Al, nanosized (5-150 nm) spherical Si particles formed between α-Al dendrites in the latter alloy. The size of the Si particles was found to be decreasing close to wheel side, where the highest cooling rates observed. Similar spherical nano-size Si particles were also observed by Kilicaslan et al.[16] who studied melt-spun Al-25Si-5Fe (in wt. %) with an estimated cooling rate of 10^5 K/s. However, due to higher solute concentration, they also found δ-Al_4FeSi_2, which was not present in the work of Unlu et al.[15]. Ahmed and Ebrahim [17] studied higher Fe bearing ternary alloy with composition of Al-11Si-11Fe (in wt. %) with an estimated cooling rate of 10^5 K/s. They observed the formation of primary α-Al and α-AlFeSi

and β-AlFeSi phases. The morphology of these ternary phases was reported to be script-like at cooling rates up to 100 K/s [3]. However, increasing cooling rate transformed these phases in to fine needle-like morphology [17]. Rapid solidification also improved the mechanical properties of the Al-Fe-Si system. Unlu et al. [15] reported that microhardness of the melt-spun Al-Fe-Si alloy tripled as compared to the conventionally cast counterpart. The improvement in hardness is due to the formation of supersaturated solution as they were not able to form any intermetallics in the alloy. Similar improvement was also reported by Ahmed and Ebrahim in the melt-spun Al-11Si-11Fe (in wt. %). Moreover, Ahmed an Ebrahim [17] showed that microhardness of the rapidly solidified can further be improved by heat treatment. They were able to increase the microhardness of the alloy from 277 HV to 450 HV after annealing at 150 °C for 15 hours. The improvement is due to the formation of the precipitation of very fine ternary intermetallics from the supersaturated solid solution.

3.9 Aims and Objectives of This Research

The aim of this research is to investigate the effect of cooling rate on the phase formation and the microstructural evolution in drop tube atomized powders. Two alloy systems will be investigated in this research: binary Al-Fe and ternary Al-Fe-Si because Fe is the mostly observed impurity element in Al and Si is the mostly used alloying element especially in cast Al alloys. The objectives in this research are:

1. To assess the formation of the metastable phases, like intermetallics and quasicrystalline phases at high cooling rates.
2. To study the microstructural evolution which is expected to change by changing particle size, consequently cooling rate.
3. To study the microstructural difference between rapidly solidified and the predicted structure by the phase diagram.
4. To study the effect of the cooling rate on the mechanical properties, microhardness, of the binary Al-Fe and ternary Al-Fe-Si alloys.

These evaluations are expected to help to understand the effect of the rapid solidification on the microstructure of Al-Fe and Al-Fe-Si alloys. The expected outcome of this research consists of proper knowledge on the phase formation in these systems via rapid solidification, which can increase the solubility of Fe and can be used to form finely dispersed precipitates. Therefore, it is expected to positively affect the mechanical properties of Fe and Si bearing aluminium alloys.

4. Experimental Procedure

This project investigates the effect of non-equilibrium solidification on the binary Al-Fe and ternary Al-Fe-Si alloys and the resulting microstructural development of the alloys. This includes the production of the samples and the characterization of the samples produced. To achieve non-equilibrium solidification, a 6.5 m tall drop tube was employed. Moreover, drop tube was also employed for the production of the master alloys; raw materials were mixed and melted in drop tube in order to prevent the oxidation of the samples. The samples, later, was subjected to characterization techniques. The characterization techniques used in this research are Optical Microscopy (OM), Scanning Electron Microscopy (SEM), X-Ray Diffraction (XRD) and Transmission Electron Microscopy (TEM). In this section, equipment used for the sample production and the characterization techniques employed will be explained in details.

4.1 Sample Production and Preparation

A high purity Al rod (>99.9 wt.%) supplied by Norsk-Hydro, high purity (99.9 wt.%) fine iron wires supplied by Goodfellow and high purity Si lump supplied by GoodFellow used for the sample production. As Al is very susceptible to oxidation, alloying of the Al-2.85 wt% Fe and Al-3.9 wt% Fe samples were performed in a 6.5 drop tube, which provides oxygen free environment, and furnace cooled to room temperature. Al-4.1 wt% Fe-1.9 wt% Si master alloy was prepared using an arc melting furnace.

4.1.1 Drop Tube

In this project, a 6.5-meter-long drop tube was used. The schematic diagram of the drop tube used in this research is given in **Figure 18.** The 6.5 m drop tube used in this project consists of 1) a stainless steel tube through which atomized droplets solidify during free fall; 2) a top flange where the sample is placed and melted by the RF generator as shown in **Figure 31**; 3) gas cylinders which supply desired gas (nitrogen, helium or argon) to the drop tube; 4) a pumping system (2 rough pumps and a turbo pump) which is used to remove air in the drop tube; 5) cooling system which keeps the temperature of the RF generator and the turbo pump low.

Appropriate amounts of samples were placed in an alumina crucible which has three laser drilled holes at the bottom with a diameter of 300 μm. The alumina crucible is then put in a graphite susceptor which has a 1 cm diameter hole at the bottom allowing the passage of the ejected melt. The graphite susceptor is connected to the top flange and sealed. Two alumina heat shields are placed around the graphite susceptor and two graphite foils are placed at the

top of the graphite susceptor in order to decrease the heat loss from the sample. The top flange is put to the top of the drop tube and drop tube is sealed by using a copper ring between top flange and the stainless steel tube. Top flange also includes an R-type thermocouple which goes to the top of the alumina crucible and connected to the digital monitor.
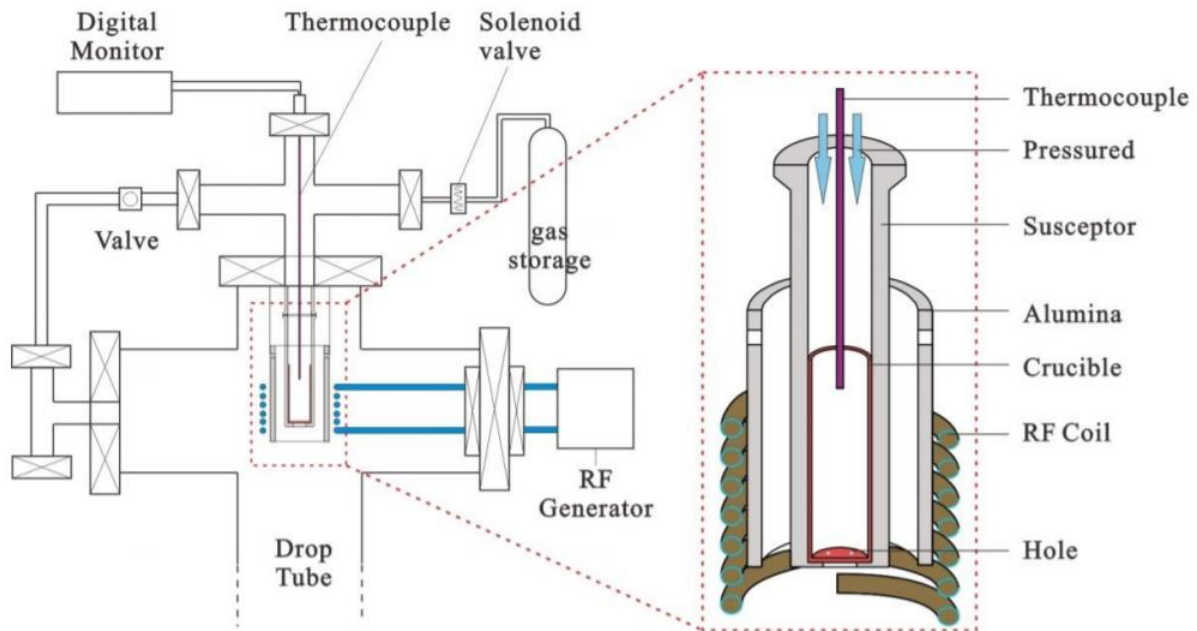
Figure 31: Schematic diagram of the top section of the 6.5 m drop tube [96].

The air inside the drop tube was evacuated to a pressure around $1.5*10^{-2}$ mbar by a rough pump (oil-sealed rotary-vane pump) after sealing the top flange to the drop tube. The drop tube was then backfilled with the desired gas (nitrogen, helium or argon) to the pressure of 500 mbar and pumped back using the rough pump. Pumping and backfilling processes were repeated 3 times in order to make sure there is no oxygen left in the system. Since aluminium is very prone to oxidation, further pumping was required by using the turbo pump. The turbo pump was used to reach high level of vacuum which is around $1.5*10^{-5}$ mbar after 3-4 hours of pumping. After turbo pumping, drop tube was backfilled with a desired gas to a pressure of around 400 mbar for the melting and the ejection of the melt.

A 3 kW RF-generator with a frequency of 210 kHz produced by Stanelco RF Technologies was used to melt the sample. When the sample reached to the set temperature (800 °C), the ejection stage began. The solenoid valve between the gas tank and the top flange was closed and the tank assembled between the gas tank and the solenoid valve was filled with the desired gas to a pressure of 4 bar. Finally, the melt was ejected by opening the solenoid valve to spray the melt through the holes at the bottom of the alumina crucible. Once the ejection was

completed, selenoid valve was turned off and RF-generator was gradually switched off. Drop tube was left to cool down. After the temperature of the drop tube reached to room temperature, the pressure inside was normalized to atmospheric pressure and the powders were collected from the catch pot. The collected powders were then sieved in to 9 different sizes: 850+, 850-500, 500-300, 300-212, 212-150, 150-106, 106-75, 75-53, 53-38 and 38- µm. The sieved powders were then prepared for characterization.

4.1.2   Arc-Melting Furnace

The Al-4.1 wt% Fe-1.9 wt% Si master alloy was prepared using an arc-melting furnace, which operates under protective atmosphere, Ar. Appropriate amount of Al, Fe and Si were placed in the furnace on water cooled copper plate. The lid of the furnace was closed and the air inside was evacuated to 5×10^{-4} Pa and the chamber was backfilled with Ar to a pressure of 3.4×10^{3} Pa. This process was repeated 5 times to make sure there is no oxygen left in the chamber. After that, the sample was melted using electric arcs. The sample was turned over after each melting cycle in order to make sure the homogeneity of the sample.

4.1.3   Sample Preparation

Before mounting, the powders were investigated in XRD since mounting media can give diffraction pattern which can contaminate the XRD results. After XRD, powders were hot mounted in Bakelite. The mounted powders were then ground using SiC grinding papers progressively using 800 and later 1200, 2000 and 2500 Grit SiC papers. After each grinding stage samples were washed using running water and dilute detergent, cleansed in ethanol and dried using a hot air blower. After the final grinding, the samples were subjected to the polishing with a diamond paste with particle sizes of 6 µm, 3 µm and 1 µm, starting from the coarsest paste to the finest paste, on a rotating wheel with polishing cloths. Between polishing stages, the samples were cleaned as explained earlier and checked under optical microscopy in order to ensure scratches from the previous stages were removed. Final polishing is done using MasterMet colloidal silica on a semi-automatic polisher. The samples are washed after each step so that there is no contamination on the samples. Furthermore, the samples were cleaned in ultrasound bath in order to make sure there is no debris left on the surface which can reduce the effect of the etchant. After polishing the samples were etched using Keller's reagent (a mixture of 95 mL water, 2.5 mL HNO_3, 1.5 mL HCl and 1 mL HF) in order to reveal the microstructure for the optical microscope investigation. The samples were submerged in the

etchant solution and held there for 8 to 15 seconds depending on their diameter as finer powders tend to require less time for etching.

4.2 Characterization of the Samples

For the microstructural characterization of the samples Optical Microscopy (OM), Scanning Electron Microscopy (SEM) with a built in Energy Dispersive X-ray Spectrometry (EDX), X-ray Diffraction (XRD), Focused Ion Beam Scanning Electron Microscope (FIB SEM) and Transmission Electron Microscope (TEM) were employed. In this section, these techniques will be explained.

4.2.1   X-Ray Diffraction

X-Ray Diffraction is an effective characterization technique which is used to acquire information about the structure of the crystalline materials. X-rays are electromagnetic radiation, like visible light, but with a shorter wavelength in the range of 0.5-2.5 Å, which is comparable to lattice spacing and a higher energy than visible light, which make X-rays more penetrating than visible light. Thus, X-rays can be used to evaluate lattice constant, orientation, phases present in the sample as well as the quantity of the phases present in the specimen for crystalline materials.

When an X-ray photon interacts with an atom the X-ray can be scattered, diffracted, reflected or absorbed. Diffraction occurs from a crystalline material only when scattered beams from the material reinforce each other. In other words, diffraction occurs only when path difference between incident and scattered beams is integer multiple of the wavelength of the X-ray used as shown in **Figure 32**. This relation was discovered and formulated by W. L. Bragg and this relation is known as Bragg's law. Bragg's law as given in equation (4-10; where n is the order of the reflection and must be an integer, λ is the wavelength of the X-ray beam, d is the distance between adjacent planes, and θ is the diffraction angle of the X-ray beam.

$$n\lambda = 2d\sin\theta \qquad\qquad (4\text{-}1)$$
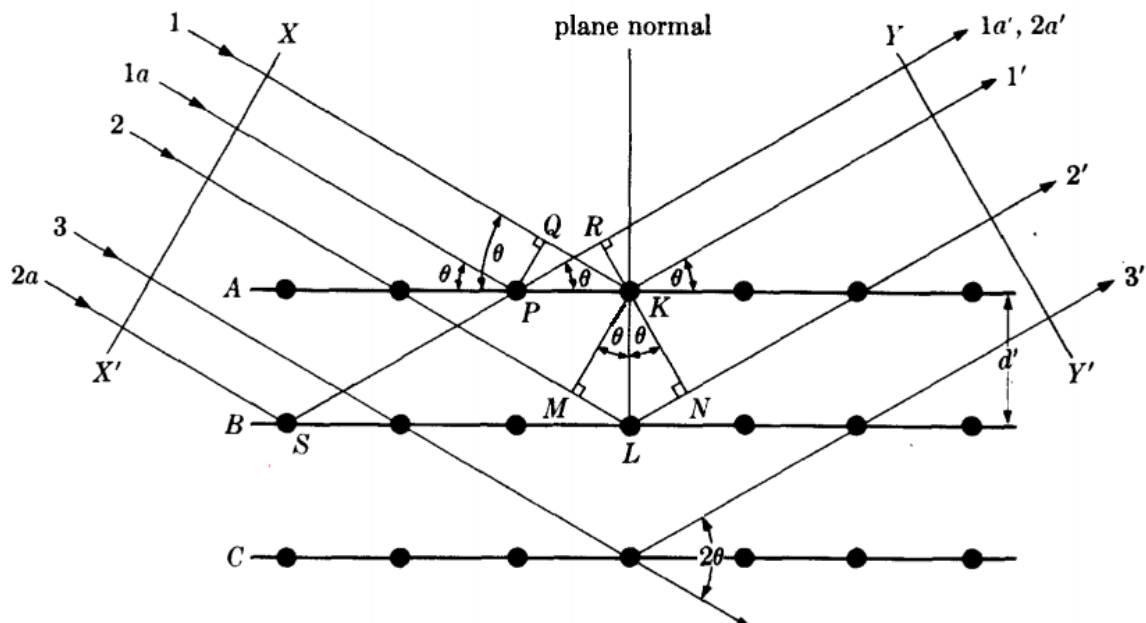
Figure 32: Diffraction of X-rays by a crystal [97].

Monochromatic X-rays were employed for X-ray diffraction in this project using a Philips X'Pert MPD X-Ray diffractometer. Monochromatic X-rays are directed at the sample incident angle and the diffraction occurs from different interplanar spacing (d-spacing) which satisfies Bragg's law. For the X-ray diffraction monochromatic Cu Kα_1, which has a wavelength of $\lambda=$ 1.5406 Å were used with step size 0.033 between 2θ ranges of 20° to 80°. A detector is used to detect and count the diffracted X-ray beams. Characteristic X-ray diffraction patterns of a sample can be obtained by plotting 2θ vs intensity curve. The results, then, can be compared with the Powder Diffraction File (PDF) cards. For the analysis of the phases in the samples, X'Pert HighScore Plus produced by Malvern Panalytical was employed.

4.2.2 Optical Microscopy (OM)

For the optical microscopy investigation Olympus BX 51 light microscope with a built in Carl Zeiss Axiocam MRc5 digital camera, which is connected to a computer for storing the images, was used. The microscope has different objective lenses for various magnifications (including 5, 10, 20, 50 and 100 times). In order to make sure, the surface investigated under microscope was flat, Plasticene was put under the samples and a levelling press was used.

4.2.3 Scanning Electron Microscope (SEM)

The Scanning Electron Microscope (SEM) uses an accelerated beam of electrons (generally produced from tungsten filament) which are directed to the specimen with the help a condenser

lenses as shown in **Figure 33** to get information from the surface or near surface of the specimen. Topography, morphology and elemental composition of the specimen can be studied using an SEM. Electrons targeted to the specimen hit the sample and this interaction provide signals which can be used to characterize the sample. There are three types of detectors in SEM; Secondary Electron Detector (SED), Backscattered Electrons Detector (BSED) and X-ray Detector.

Secondary electron imaging is the most common imaging mode in SEM. Secondary electrons have low energy. Thus, these electrons are emitted from a few nanometres of the sample surface. This imaging technique is used to get topographic information of the specimen. Backscattered electrons have higher energies than the secondary electrons and, consequently, interaction volume is higher than that of secondary electrons. These electrons are emitted from a few micrometres of the sample. This imaging technique uses the backscattered electrons emitted from the sample. Since the backscattered electron energy differs with atomic number of the elements, so that energy of electron backscattered form high atomic number element is higher than that of low atomic number element, heavier elements appear brighter in this technique while lighter elements appear darker. X-ray detector can be used qualitative and quantitative analysis. When an electron hits an atom, the atom emits its characteristic X-ray. Measurement of this characteristic x-ray energies enables to determine the elements present in the sample. In addition, counting the X-rays can give information about the quantity of these elements.
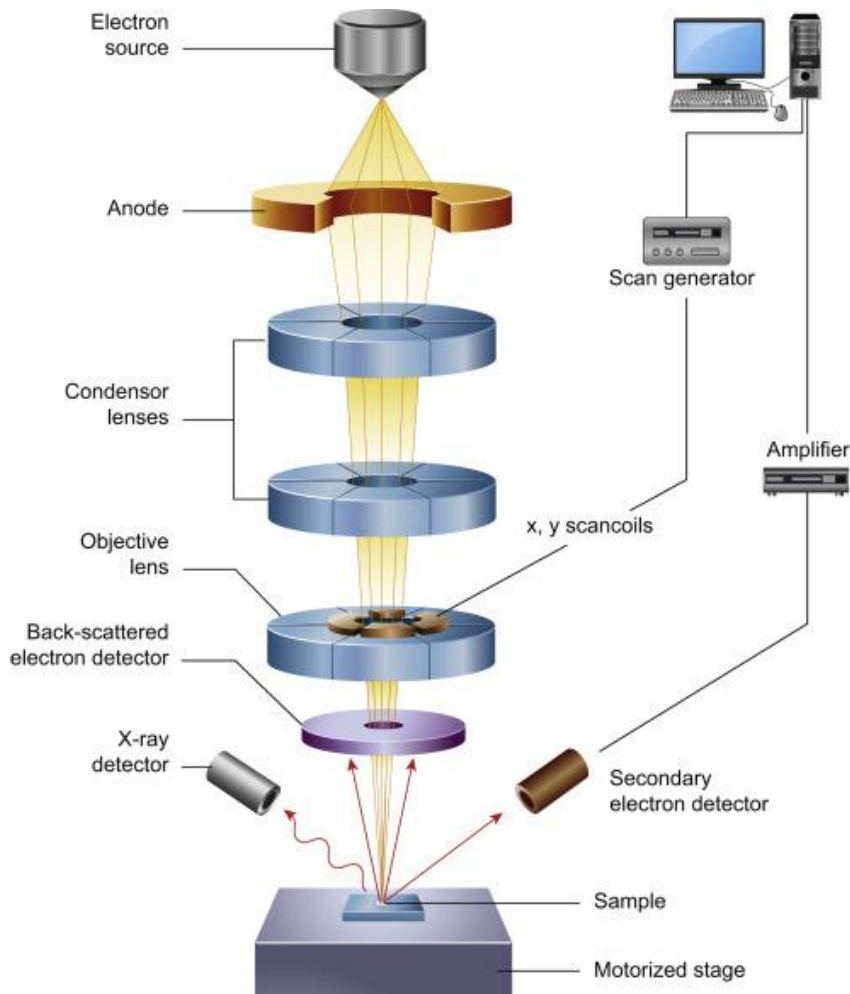
Figure 33: Schematic presentation of an SEM [98].

SEM can reach higher resolutions compared to OM. The reason is given by Rayleigh criteria, which gives the resolution as [99];

$$r_1 = \frac{d_1}{2} = \frac{0.61\lambda}{\mu sin\alpha} \tag{4-2}$$

where λ is the wavelength of the light (or beam), μ is the refractive index and α is the semi-angle ($\mu sin\alpha$ is referred as numerical aperture). To achieve better resolution, that is obtaining smaller r_1, λ should be reduced. As electrons have much lower wavelength than light, electron microscopes can reach higher resolution than optical microscopes. To illustrate, while the minimum achievable resolution in optical microscope is 150 nm when green light is used, this can be reduced to 0.02 nm when electrons with an acceleration voltage of 100 kV are used [99]. Electron microscopes operates at high vacuum as they interact with the air more than light and are scattered. In addition, the specimen must be electrically well conductive to be examined

under SEM to reduce the electron pile up on the specimen. Thus, a thin layer of carbon or iridium coating is applied prior to the SEM.

In this project for the characterization of the samples, a Hitachi SU8230 with accelerating voltage of around 15 kV and with built-in above mentioned three SEM modes were used. After polishing, the samples were carbon coated in order to make them electrically conductive. Backscattering mode was used to investigate where intermetallics precipitate and the compositions of the precipitates were evaluated using Energy-dispersive X-ray. Moreover, some measurements were taken using SEM images, this will be explained in the next chapter.

4.2.4   Transmission Electron Microscope (TEM)

Similar to Scanning Electron Microscope (SEM), Transmission Electron Microscope (TEM) uses electron to create images of the specimen. However, they differ in working principal; in SEM electrons are used to scan the surface of the sample, in TEM electrons pass through the sample. Thus, TEM samples must be less than 100 nm in thickness to allow electron passage. A TEM consists of an electron gun, condenser lenses, an objective lens, a projector lens and apertures[99].

TEM uses focussed high energy electrons. Therefore, TEM provides high magnification images as well as high resolution from a small spot of less than a μm. There are two modes in TEM; diffraction mode and imaging mode. As in XRD, TEM allows to obtain diffraction pattern from the sample but TEM allows the diffraction from a very small spot, which is called as Selected Area Diffraction (SAD). A single crystalline material gives a spot pattern, a polycrystalline material gives powder or ring pattern. An amorphous material gives a series of diffuse halos. Diffraction angle (θ) in TEM is very small which is 9 mrad for a Au (200) reflection[100]. Lattice parameters of a crystalline material can be determined by using this diffraction pattern and Bragg's Law (Equation 4-1).

Imaging mode includes bright-field microscopy, dark-field microscopy, high-resolution electron microscopy and EDX for chemical analysis. In bright-field microscopy, nondiffracted electrons are used for imaging. Contrast of the image depends on compositional variations or structural anomalies in the sample. High-resolution TEM requires the transmitted beam and at least one diffracted beam. A FEI Titan3 Themis 300 operating at 300 kV was employed in this research which is capable of performing above mentioned imaging modes.

4.2.4.1 TEM Sample Preparation

As TEM requires very thin sample of around 100 nm or less to allow electrons pass through the sample, TEM sample preparation was performed using a Focussed Ion Beam (FIB) SEM. A coated sample was placed in FEI Helios G4 CX DualBeam FIB SEM. This FIB uses accelerated Ga ions to cut samples for TEM. The stages of TEM sample preparations using FIB SEM are shown in **Figure 34**. Before starting the cutting operation, the area of interest was platinum coated. The area on each side of the coating was removed using accelerated ions. A needle-like sample carrier was welded on the sample and the sample was removed to the sample holder and welded on to the holder. Further sectioning on the sample was applied until the thickness of the sample is compatible for TEM investigation. The thickness of the sample was around 50-60 nm.
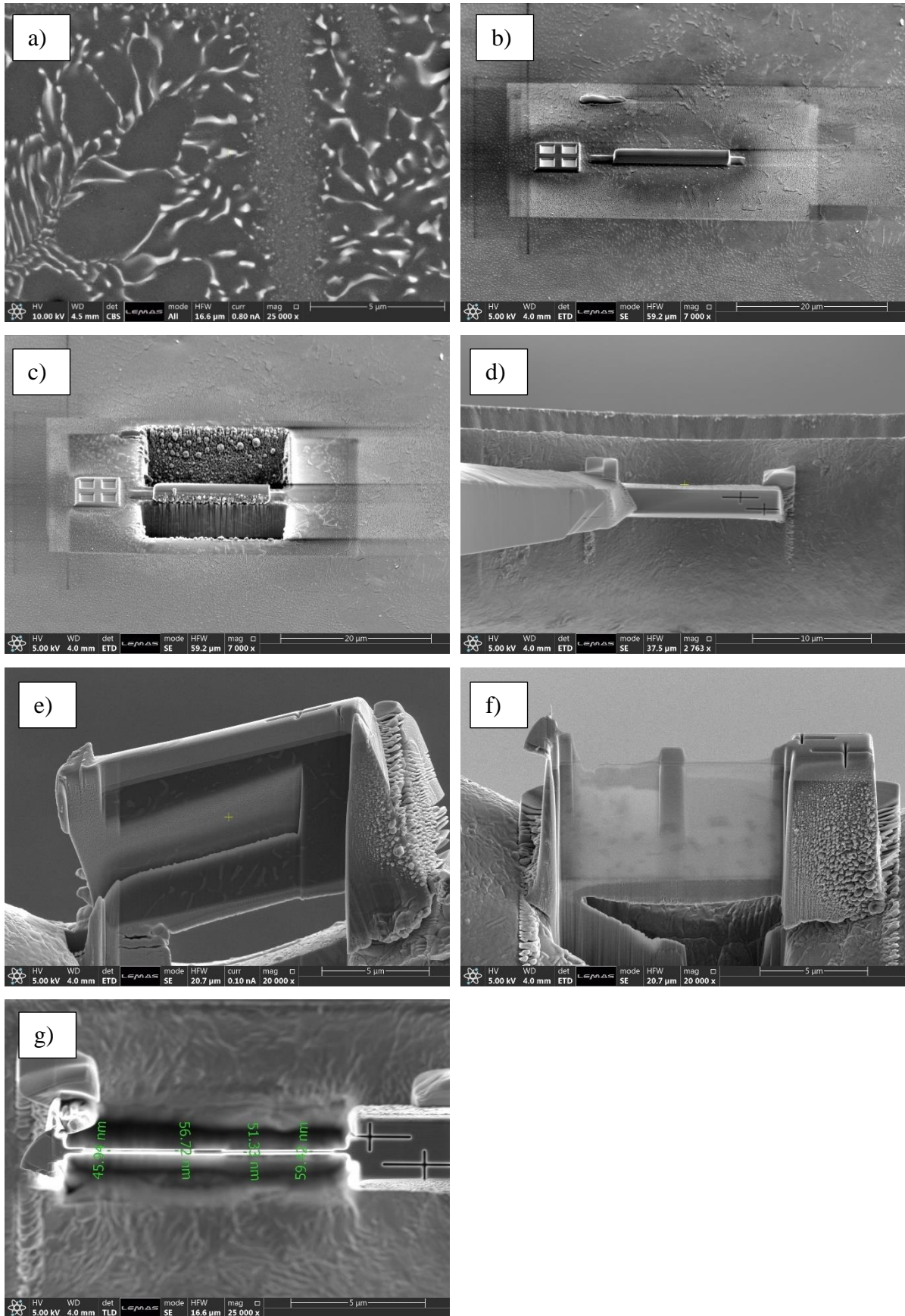
Figure 34: FIB cutting of a sample a) area of interest is found, b) the area is platinum coated, c) using the accelerated ions area near the sample is removed d) the cut sample is welded on

sample carrier and then removed to a sample holder and welded on the holder, e) the sample is further thinned using the ion beam, f) side view of the final sample and g) top view of the final sample showing the thickness of the sample.

4.2.4.2 TEM Indexing

TEM lets diffraction from tiny spot, that is from a single phase, which is called Selected Area Diffraction (SAD). Depending on the sample type, SAD pattern can be either ring pattern for polycrystalline phases and spot patterns for single crystalline phases. One of the SAD patterns taken from Al-2.85wt%Fe is given in **Figure 35**. For the analysis of SAD patterns both d-spacings of planes and the angles between them are measured. The following equations were used to calculate the angle, Φ, between the plane $(h_1k_1l_1)$ with spacing d_1 and the plane $(h_2k_2l_2)$ with spacing d_2. The angles in the following equations are given for cubic (α-Al), monoclinic ($Al_{13}Fe_4$), orthorhombic (Al_6Fe) and tetragonal systems (Al_mFe), respectively. These systems are possessed by some Al-Fe intermetallics. PDF cards for these systems are given in Appendix.

$$cos\Phi = \frac{h_1h_2 + k_1k_2 + l_1l_2}{\sqrt{(h_1^2 + k_1^2 + l_1^2)(h_2^2 + k_2^2 + l_2^2)}}$$

(4-3)

$$cos\Phi = \frac{d_1d_2}{sin^2\beta}[\frac{h_1h_2}{a^2} + \frac{k_1k_2sin^2\beta}{b^2} + \frac{l_1l_2}{c^2} - \frac{(l_1h_2 + l_2h_1)\,cos\beta}{ac}$$

(4-4)

$$cos\Phi = \frac{\frac{h_1h_2}{a^2} + \frac{k_1k_2}{b^2} + \frac{l_1l_2}{c^2}}{\sqrt{(\frac{h_1^2}{a^2} + \frac{k_1^2}{b^2} + \frac{l_1^2}{c^2})(\frac{h_2^2}{a^2} + \frac{k_2^2}{b^2} + \frac{l_2^2}{c^2})}}$$

(4-5)

$$cos\Phi = \frac{\frac{h_1h_2 + k_1k_2}{a^2} + \frac{l_1l_2}{c^2}}{\sqrt{(\frac{h_1^2 + k_1^2}{a^2} + \frac{l_1^2}{c^2})(\frac{h_2^2 + k_2^2}{a^2} + \frac{l_2^2}{c^2})}}$$

(4-6)
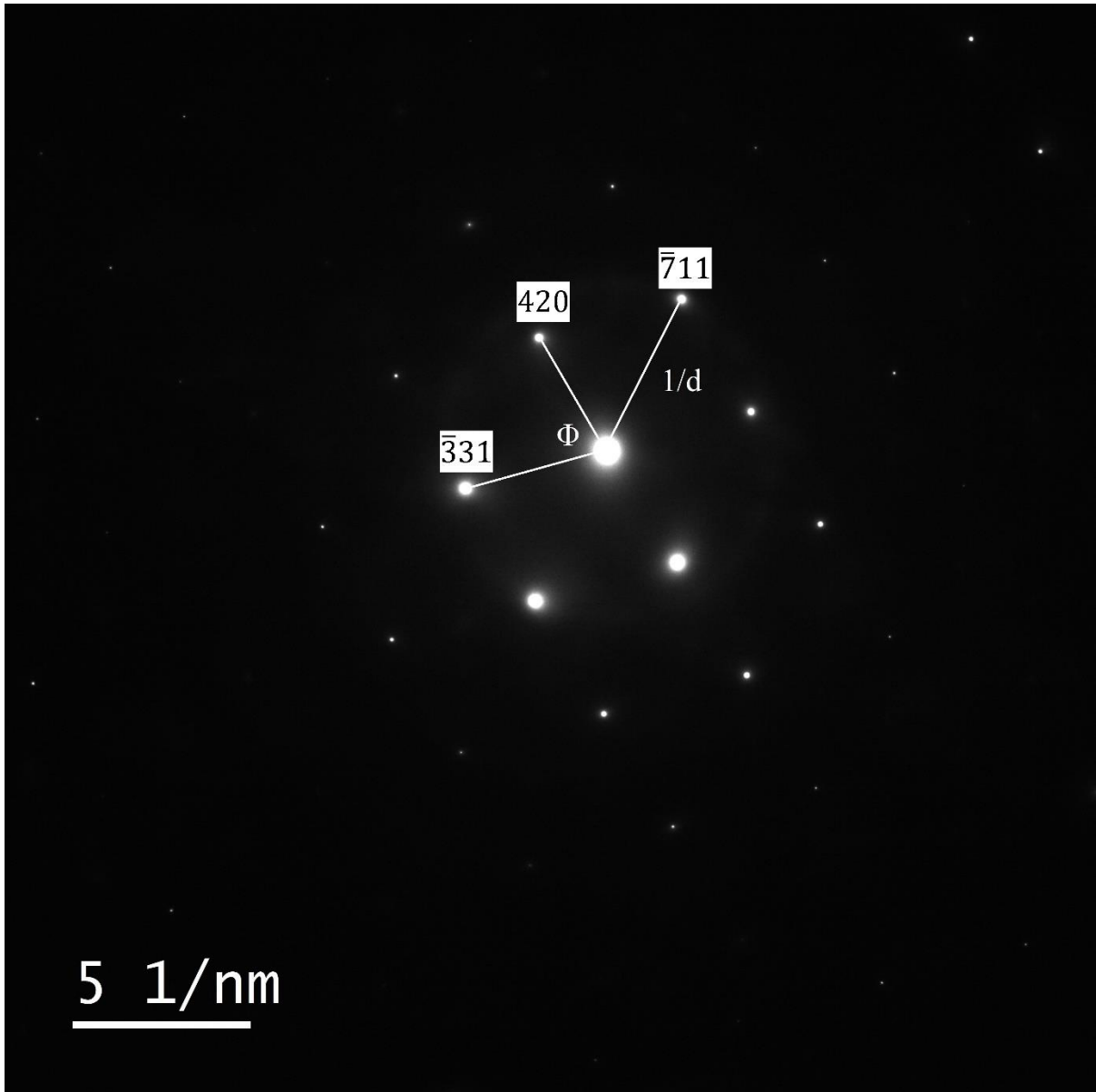
Figure 35: An example of SAD patterns showing spot patterns. SAD pattern was taken from $Al_{13}Fe_4$ which has a monoclinic crystal structure and indexing performed using Equation (4-4).

4.2.5 Image Analysis

The image processing software 'Image J' was used for the measurement of the volume fraction of the phases and the inter-lamellar spacing from the SEM and optical microscope images. Eutectic spacing and secondary dendrite arm spacing were measured by using the software. Lines with a length, l, were drawn perpendicular to the lamellar eutectic and the number of lamellar eutectics, c, were count. The lamellar eutectic spacing, λ, were, then, determined by the following equation:

$$\lambda = \frac{l}{c} \tag{4-7}$$

With the same procedure being used to measure the Secondary Dendrite Arm Spacing (SDAS).

'Image J' was also used to measure the volume fraction of the phases. The fraction of eutectic was measured by converting the area of interest in the RGB images to grey scale and using the 'threshold' function in the software. An example of this is provided in **Figure 36**. A SEM image is converted to grey scale image in which the black region is α-Al while the white region represents the interdednritic eutectic region. For this specific example the volume fraction of α-Al was calculated as 78 ± 3%.
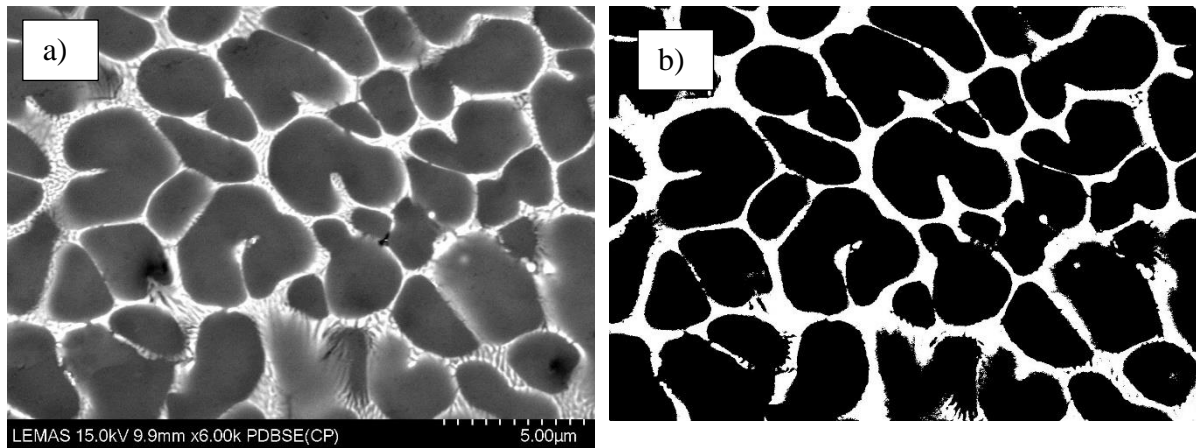
Figure 36: a) SEM image of 106-75 µm sample b) converted grey scale image of a).

4.2.6 Microhardness

In order to understand the effect of rapid solidification on the mechanical properties of the alloys, microhardness measurements were conducted. Microhardness measurements were performed using a Tukon^{TM} 1202 Wilson Hardness (Vickers) using 10g load at room temperature, with such measurements being made on the mounted and colloidal silica polished samples. For each sample, at least 10 measurements were made. Average of the results are given.

4.2.6.1 Calculating the Depth of Polishing

Consecutive polishing and etching were conducted on 150-106 µm sample in order to reveal the 3D structure of the Y-shaped phase. The depth difference was measured by using the microhardness machine. When calculating the depth difference before and after polishing, the geometry relation of the Vickers indent as shown in **Figure 37** was used. Before polishing, a

sample close to the sample of interest was indented using the microhardness machine. The average diagonal length, l (as indicated d in **Figure 37**), of the indent before and after polishing stages, Δl, was measured. The change in the depth of the sample, Δt, was calculated using the geometrical properties of Vickers microhardness indent as

$$\Delta t = \Delta l/7$$

After the change in the depth of the sample was measured, sample was etched and investigated under OM.
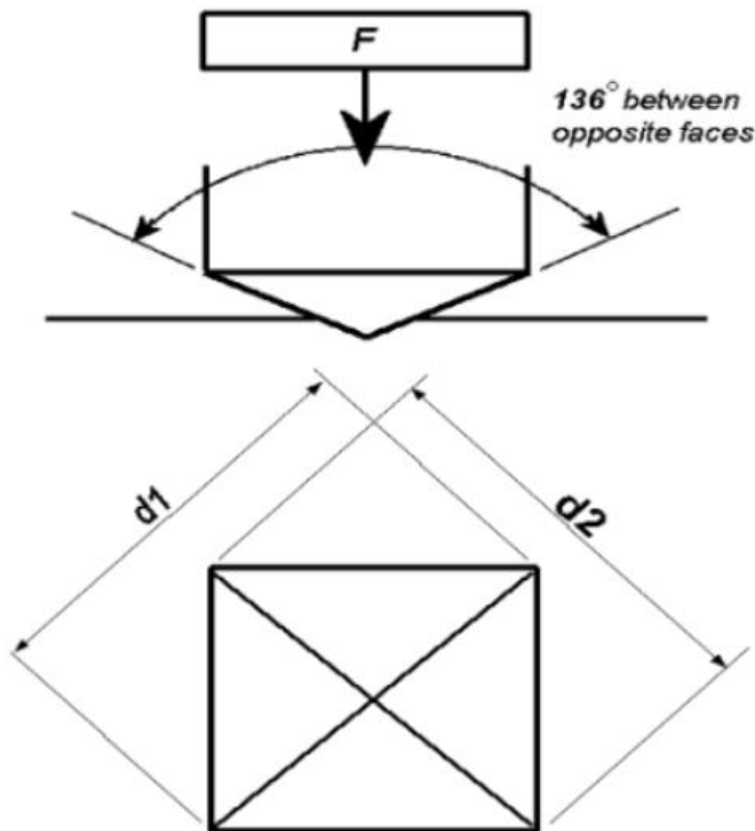
Figure 37: Geometry of Vicker's indent[101].

5. Results

In this chapter, the results of this research will be presented. Firstly, results for the estimation of the cooling rate are given. Later, experimental results for Al-2.85 wt% Fe, Al-3.9 wt% Fe and Al-4.1 wt% Fe-1.9 wt%Si alloys are presented in different sub-sections, respectively. When presenting the experimental results, following order is employed. Firstly, XRD results are introduced to understand the phases formed in the samples. Secondly, optical microscopy (OM) results and Scanning Electron Microscopy (SEM) results are given to show the effect of rapid solidification on the samples. When providing OM and SEM results, the microstructure of furnace cooled alloys and the microstructure of the drop tube atomized alloys with decreasing sample size will be shown to reflect the effect of non-equilibrium solidification on the microstructure. Thirdly, results for the measurements performed using OM and SEM images, and EDX are provided. Later, Transmission Electron Microscopy (TEM) results are introduced. Finally, Microhardness results are provided in order to show the effect of the rapid solidification on the mechanical properties of the alloys.

5.1 Estimation of the Cooling Rate

In drop tubes, it is impossible to monitor the thermal history of the solidifying droplets as solidification takes place during free fall. In other words, it is impossible to measure the cooling rates of the solidifying droplets. There are two methods to estimate the cooling rates of the droplets: 1) using the secondary dendrite arm spacing (SDAS) 2) using mathematical models. Former method will be discussed in later sections. Latter method involves the estimation of the cooling rates using the heat balance of the solidifying droplets. The heat balance can be determined as: the heat released from the molten droplet equals to heat absorbed by the environment. The heat balance can be expressed as [55], [102]

$$\frac{dT}{dt}\left[C_p^l\left(1-f\right)+C_p^s f\right]+L\frac{df}{dt}=\frac{6}{d\,\rho_l}\left[\varepsilon\,\sigma_{SB}\left(T^4-T_R^4\right)+\left(h_m(T-T_R)\right)\right] \qquad (5\text{-}1)$$

where d is the droplet diameter, C_p^l is the specific heat of the melt, C_p^s is the specific heat of the solid, f is the solid fraction, L latent heat, ρ_l is the density of the melt, ε is the surface emissivity, σ_{SB} is the Stephan-Boltzman constant, T is the instantaneous temperature of the droplet, T_R the temperature of the gas (room temperature) and h_m the heat transfer coefficient of the droplet falling through a gas. The heat transfer coefficient, h_m, is given as:

$$h_m = \frac{\kappa^g}{d} \left(2.0 + 0.6 \sqrt{Re} \sqrt[3]{Pr}\right) \tag{5-2}$$

where κ^g is the thermal conductivity of the gas, Re the Reynolds number and Pr the Prandtl number, with the Reynolds and Prandtl numbers being given by:

$$Re = \frac{v^r \, \rho^g \, D}{\eta^g} \tag{5-3}$$

$$Pr = \frac{C_p^g \, \eta^g}{\kappa^g} \tag{5-4}$$

where ρ^g is the density, η^g the dynamic viscosity, v^r flow velocity and C_p^g the specific heat of the back-fill gas. In this research, N_2 gas was used as ball-filling gas.

The thermophysical constants used in the calculation of the cooling rate are listed in Table 6.

Table 6: Thermophysical properties of N_2 [103] gas and Al [94] used in the estimation of the cooling rate.

Material	Parameter	Value
Nitrogen gas	C_p^g	1039 (J kg^{-1} K)
	η^g	1.78 x 10^{-5} (N s m^{-2})
	κ^g	2.6 x 10^{-2} (W m^{-1} K^{-1})
	ρ^g	1.16 (kg m^{-3})
Aluminium	C_p^l	1180 (J kg^{-1} K^{-1})
	C_p^s	910 (J kg^{-1} K^{-1})
	ρ_l	2385 (kg m^{-3})
	L	396 (kJ kg^{-1})

Using the above equations and thermophysical constants provided in **Table 6**, the cooling rates were calculated on MatLab. The results were later transferred to OriginPro and drawn. The results are given in **Figure 38**. Each black point on the graph represents the sieves utilized in this research. That is, from right to left, 850, 500, 300, 212, 150, 106, 75, 53 and 38 µm sieve sizes are provided on the graph. Using the power law fit function of the OriginPro, the equation of the fitting curve, cooling rate, was found as:

$$\mathrm{d}T/\mathrm{d}t = 9.7 \times 10^6 \times (d/\mu m)^{-1.707} \tag{5-5}$$
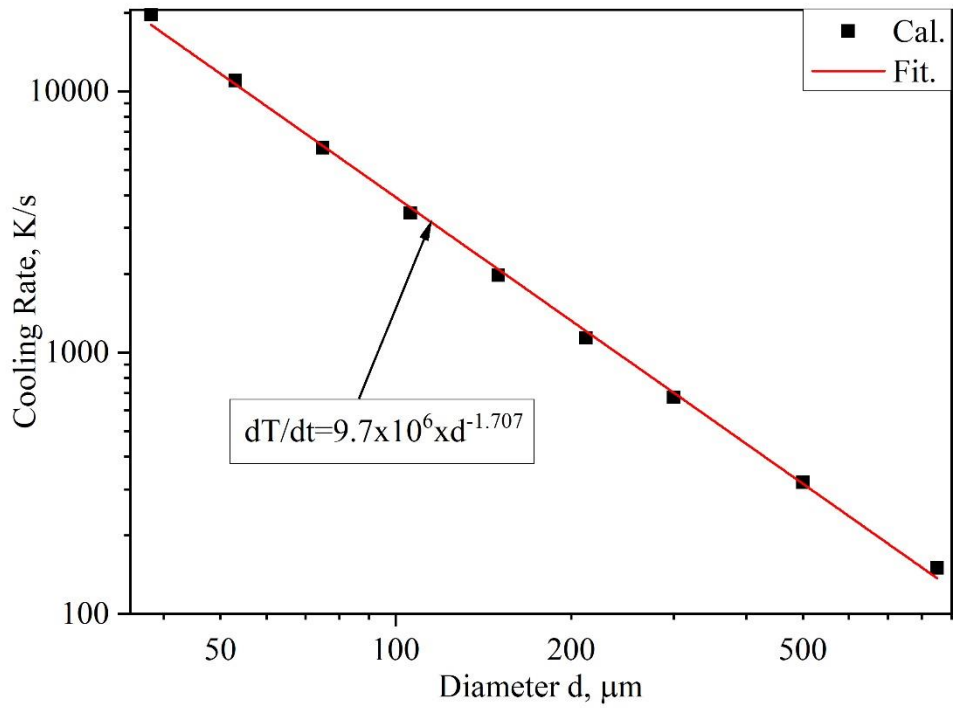
Figure 38: Estimated cooling rates of the droplets as a function of droplet size, *d*.

The estimated cooling rates of the solidifying droplets are shown in **Figure 38**. It is clear that the cooling rate increasing with decreasing droplet size. The cooling rate ranges between 20,000 K s^{-1} and 150 K s^{-1} for 38 µm and 850 µm samples, respectively. As the smallest diameter of the samples produced in the drop tube is 38 µm, the estimation below that is not provided in the graph.

The estimated average cooling rate is summarized in **Table 7**. **Table 7** also summarizes the diameters of the powders produced in drop tube. While the widest powder size was observed in Al-3.9 wt%Fe alloy and the powder size ranged between 850+ and 38 µm, Al-2.85wt%Fe alloy showed size range between 850 and 53 µm. That is, increasing Fe concentration provided droplets with wider diameter. Similar results has been reported by Henein et al. [89]. Increasing Fe concentration from 0.61 wt% Fe to 1.9 wt% Fe resulted in powders with wider diameter range. Al-4.1wt%Fe-1.9wt%Si alloy, on the on the other hand has yielded intermediate size fractions being similar to Al-2.85wt%Fe alloy.

Table 7: Estimated average cooling rates for sieve fraction of produced samples. (NP: not produced in drop tube), (*: As it is hard to get the accurate diameter from 2D images, the diameters of 850+ µm samples was assumed as 900 µm and corresponding cooling rate is provided)

Material	850+	850-500	500-300	300-212	212-150	150-106	106-75	75-53	53-38
Al-2.85wt%Fe	NP	225	496	907	1,548	2,689	4,745	8,500	NP
Al-3.9wt%Fe	100*	225	496	907	1,548	2,689	4,745	8,500	15,000
Al-4.1wt%Fe-1.9wt%Si	NP	225	496	907	1,548	2,689	4,745	8,500	NP

5.2 Results for Al-2.85 wt% Fe

5.2.1 Phase Analysis and Microstructure of the Furnace Cooled Sample

Al-2.85 wt% Fe master alloy (furnace cooled sample) was prepared in drop tube and slowly cooled to room temperature. Phase analysis and the microstructure of the furnace cooled sample is performed as explained in **Chapter 4**. **Figure 39** shows the XRD pattern of the furnace cooled Al-2.85 wt% Fe sample. There are two phases present: α-Al and Al$_{13}$Fe$_4$. As the cooling rate of the alloy is low (around 20 K min^{-1}), there was not any metastable intermetallic observed in the sample. Thus, the only intermetallic present in the microstructure is the only stable intermetallic, Al$_{13}$Fe$_4$, in the Al rich part of the Al-Fe phase diagram. **Figure 40** shows the SEM micrograph of the same sample. It is clear from the figure that there are two different microstructures on α-Al matrix. These are large blocky phases and needle-like phases. As XRD result suggests that the only intermetallic is Al$_{13}$Fe$_4$, both microstructures are Al$_{13}$Fe$_4$. As the alloy is hypereutectic and the cooling rate is low, the solidification takes place according to what Al-Fe phase diagram suggests. That is, the first phase to form is large blocky proeutectic Al$_{13}$Fe$_4$. The needle-like eutectic phase which is radiating from the primary phase forms later when the temperature drops below eutectic temperature. This needle-like morphology causes significant drop in the mechanical properties of the alloy as the tips cause notch-effect by increasing stress concentration.
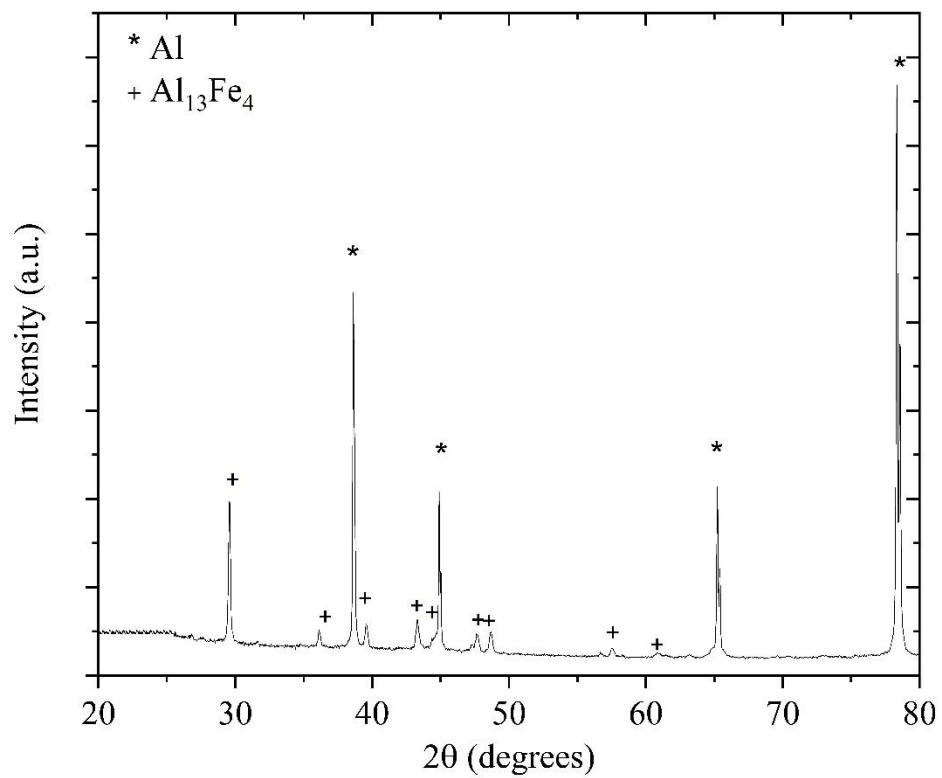
Figure 39: XRD pattern and phase identification of the furnace cooled Al-2.85 wt% Fe sample.
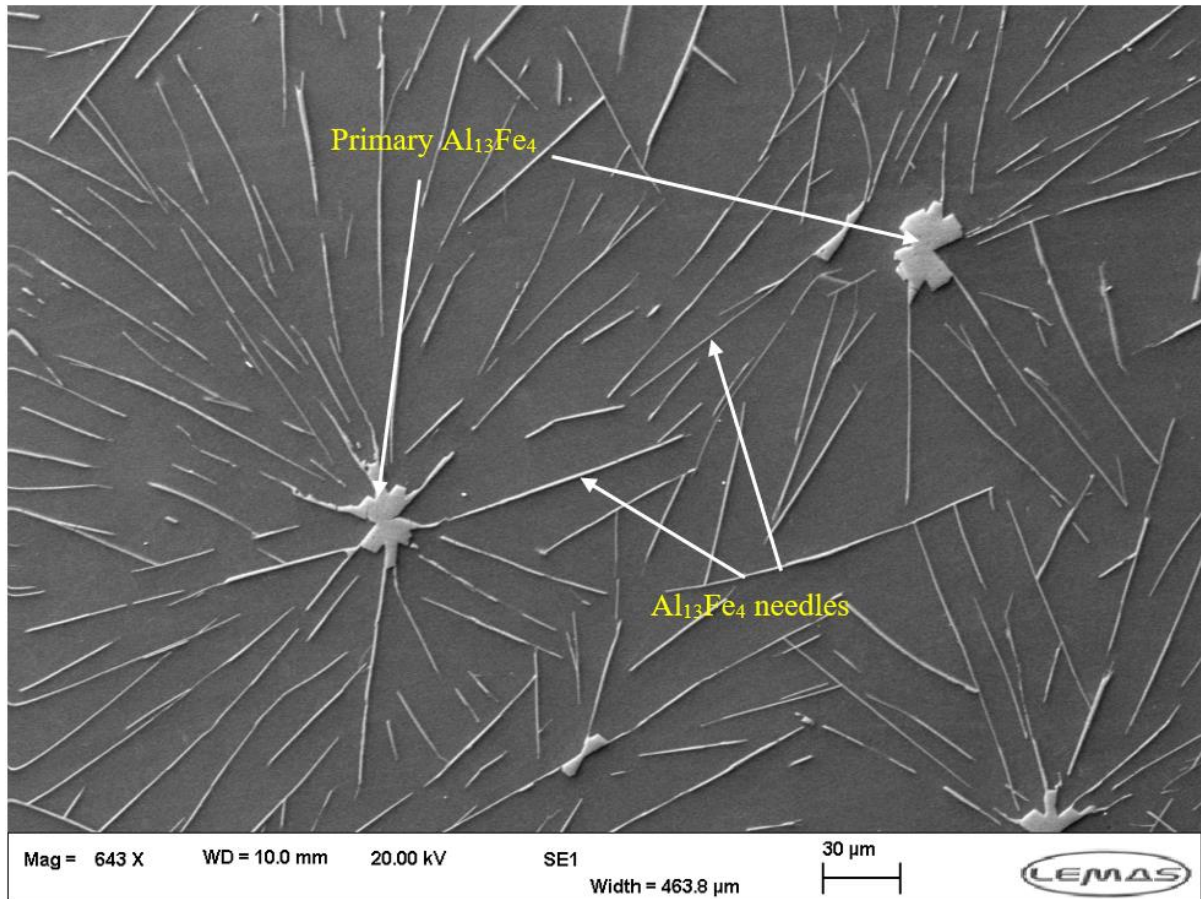
Figure 40: SEM micrograph of furnace cooled Al-2.85 wt% Fe alloy showing proeutectic $Al_{13}Fe_4$ and $Al_{13}Fe_4$ needles.

5.2.2 XRD Results of Drop Tube Atomized Al-2.85 wt% Fe

XRD results for some drop tube atomized Al-2.85 wt% Fe samples are given in **Figure 41** as a function of sample size. The remaining XRD results are provided in **Appendix B**. The XRD results show that there are three intermetallics together with α-Al. These intermetallics are equilibrium, monoclinic $Al_{13}Fe_4$, metastable, orthorhombic Al_6Fe and metastable, orthorhombic Al_5Fe_2. While $Al_{13}Fe_4$ and Al_6Fe intermetallics are observed in all sample sizes, Al_5Fe_2 was only found in samples with diameters smaller than 106 µm. That is, Al_5Fe_2 was formed in samples with cooling rates higher than 3300 K s^{-1}.

69
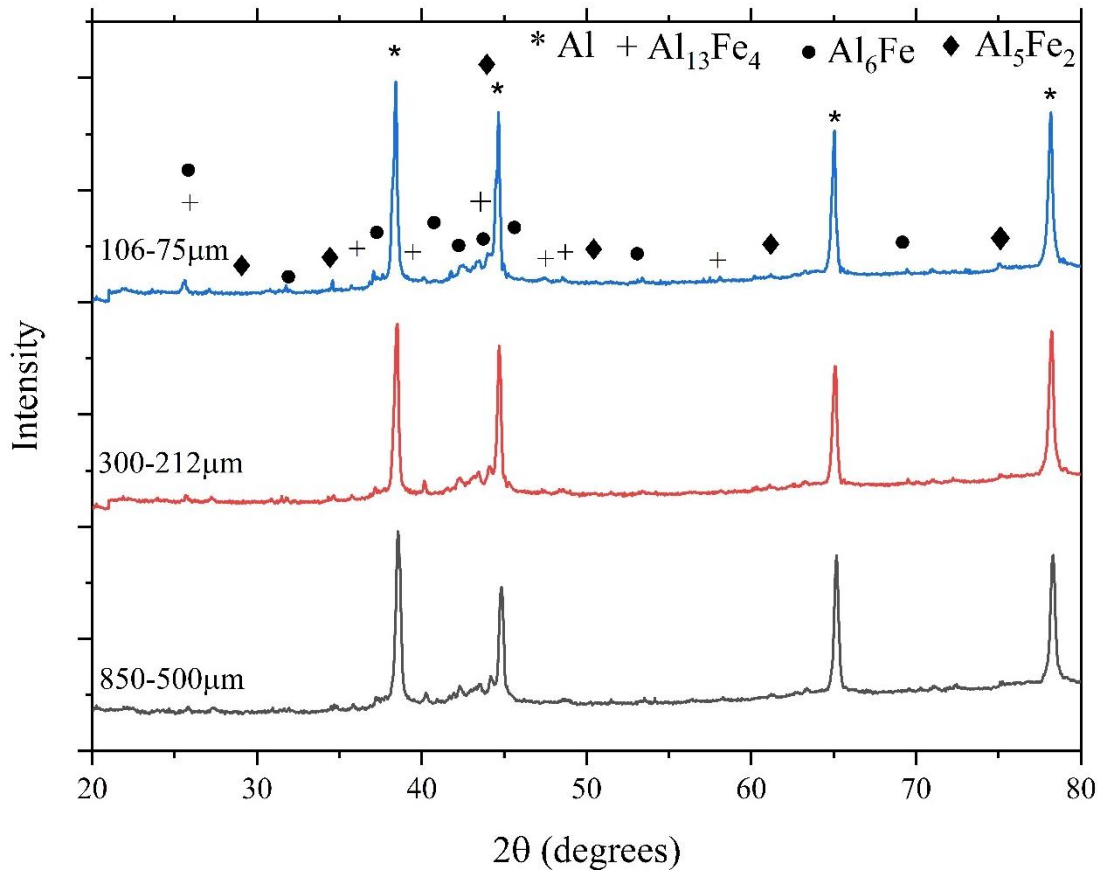
Figure 41: XRD patterns of some selected drop tube atomized samples as a function of size range.

5.2.3 Microstructural Characterization and Phase Identification

The microstructures of drop tube atomized Al-2.85 wt% Fe alloy have been analysed using both OM and SEM. The OM analysis was done first and as the microstructure was very fine further analysis was performed using SEM. SEM was also applied for EDX analysis, the results of EDX will be given in later sections (**Section 5.2.4**). OM and SEM results are given in **Figure 42-48**. **Figure 42-45** show the microstructure of large sieve fractions with a diameter between 850-300 µm. In these large samples, there are three distinctive regions. These regions are microcellular region, dendritic region and eutectic region as seen in **Figure 42-44**. Microcellular region has finer structure compared to other regions and α-Al dendrites grow out of this region. This means that nucleation initiated in this zone and later transitioned in to dendritic α-Al. Later, dendritic growth was stopped due to recalescence. The recalescence results in an overall warming of the droplet and, thus, a reduction in the undercooling towards the end of the solidification. Therefore, the remaining liquid solidified in to complete eutectic. The presence of dendritic α-Al indicates that first phase to form in the sample was α-Al instead

of $Al_{13}Fe_4$ although the alloy is hypereutectic and $Al_{13}Fe_4$ is expected to form first. For α-Al to nucleate first in a hypereutectic alloy means that the undercooling experienced in the droplet prior to solidification was so high that the liquid was on the α-Al side of the eutectic coupled zone. It might be noted here that in a faceted-non-faceted eutectic, the coupled zone is heavily skewed towards the intermetallic. This means that at high undercooling it can be by-passed allowing access to the non-faceted phase.

As the microstructures of these three regions are very fine, SEM was used to identify the microstructures. **Figure 45** provides high magnification SEM micrographs of 850-500 µm samples taken from three distinctive regions. The microcellular region shown in **Figure 45 a** consists of fine cellular α-Al which is surrounded by lamellar intermetallics as also shown in **Figure 44b**. **Figure 45 c** shows the microstructure of interdendritic eutectic which adopted lamellar structure, while eutectic region is rod-like eutectic (**Figure 45 d**) with coarser boundary phase. According to Wang et al. [73] the microstructure of $Al-Al_{13}Fe_4$ is lamellar while $Al-Al_6Fe$ eutectic adopts rod-like structure. Moreover, the XRD results shown in **Figure 41** indicates the presence of both stable $Al_{13}Fe_4$ and metastable Al_6Fe. This was later confirmed after a sample taken from the boundary region, which includes both lamellar and rod-like eutectic, was investigated under TEM and the results are given in **Section 5.2.8**.

Further increase in cooling rate, and hence, decrease in powder size has slightly changed the microstructure of the samples. Typical OM and SEM microstructures of small samples (300-53 µm) are given in **Figure 46** and **Figure 47**, respectively. As seen from the figures, the main difference between these size fractions and larger size fractions (850-300 µm) is that fully eutectic region was not observed in these smaller size fractions. That is, only microcellular region and dendritic region were present in the small samples. Moreover, some samples as shown in **Figure 46 a** and **b** and **Figure 47a** and **e** have shown multiple nucleation sites as shown with circles. The boundaries of the radiating dendrites from nucleation zones caused by multiple nucleation zones are designated by arrows. **Figure 46 f** shows that the interdendritic eutectic remains as lamellar eutectic. Furthermore, with decreasing cooling rate, volume fraction of α-Al in dendritic region is higher compared to larger samples (850-300 µm). This indicates that dissolved Fe content in α-Al has increased with decreasing sample size and, thus, increasing cooling rate. This will later be discussed in next sections with EDX results (**Section 5.2.4**) and volume fraction of phases (**Section 5.2.5**).

Furthermore, 75-53 µm samples given in **Figure 44d** show two regions as well as Y-shaped structures (indicated with an arrow in **Figure 44d**). Y-shaped structures are structures with triradiating arms which appear to be featureless under OM and SEM. Y-shaped structure was rarely observed in drop tube atomized Al-2.85 wt% Fe and was only found in the smallest sieve fractions (75-53 µm) and, thus, in the fastest cooled samples. Y-shaped will be discussed in detail in **Section 5.3** where this type of Y-shaped structure has widely been observed in drop tube atomized Al-3.9 wt% Fe alloy.

Increasing cooling rate has also resulted in a change in the microstructure of solidification start zone, microcellular region. **Figure 48** shows the micrographs of the nucleation start zones of 106-75 µm and 75-53 µm samples. 106-75 µm sample (**Figure 48 a and b**) depicted both microcellular structure which is surrounded by lamellar eutectic and divorced eutectic with various sizes and morphologies in nucleation start zones. Thus, this size fraction marks where the transition from microcellular to divorced eutectic takes place. **Figure 48 d** shows that the divorced eutectic formed at the centre of the nucleation zone and later transformed in to cellular structure which later transitioned in to dendritic structure. The transition from microcellular to divorced eutectic has occurred when the estimated average cooling rate is around 4745 K s^{-1}.
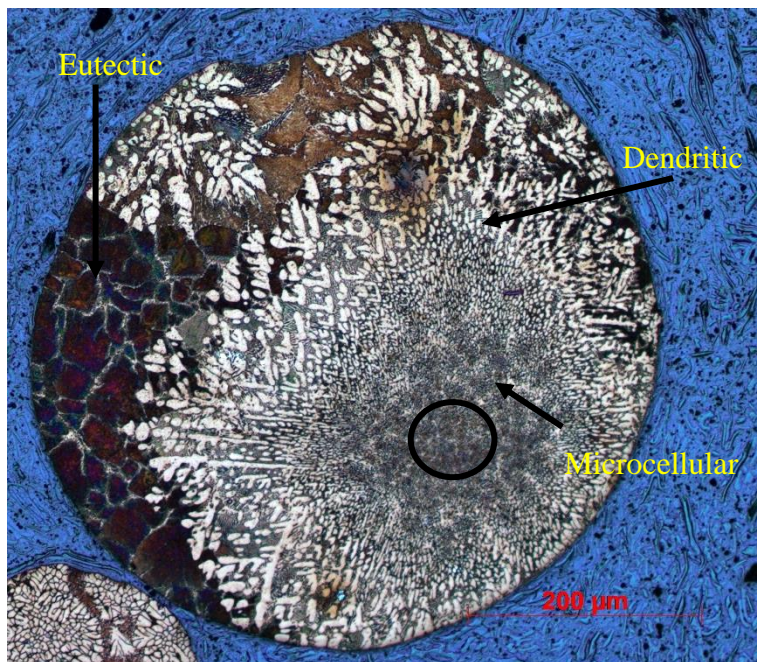
Figure 42: Microstructure of drop tube atomized 850-500 µm sample (circle showing where the nucleation initiated).
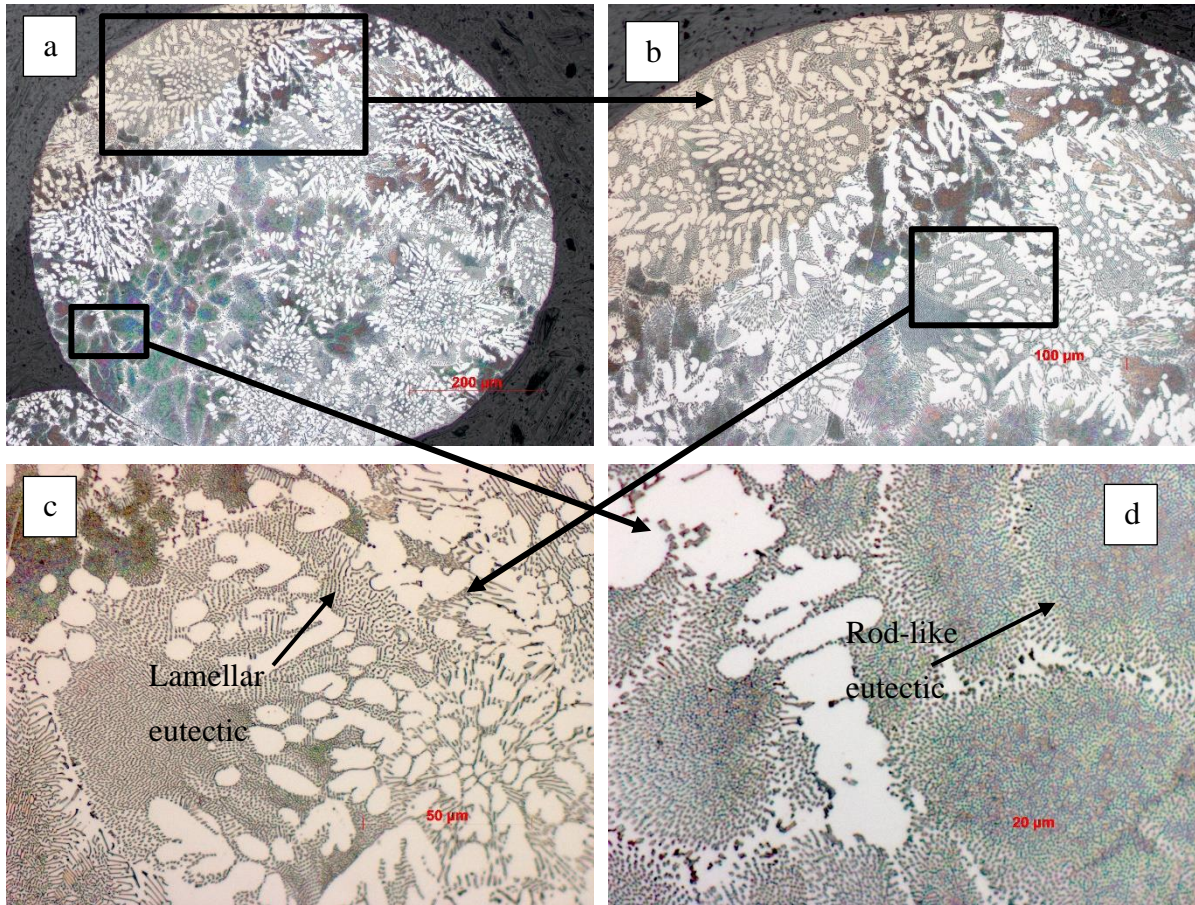
Figure 43: OM micrographs of drop tube solidified 850-500 µm sample. Sample consists of dendritic α-Al, lamellar interdendritic eutectic, and rod-like eutectic.
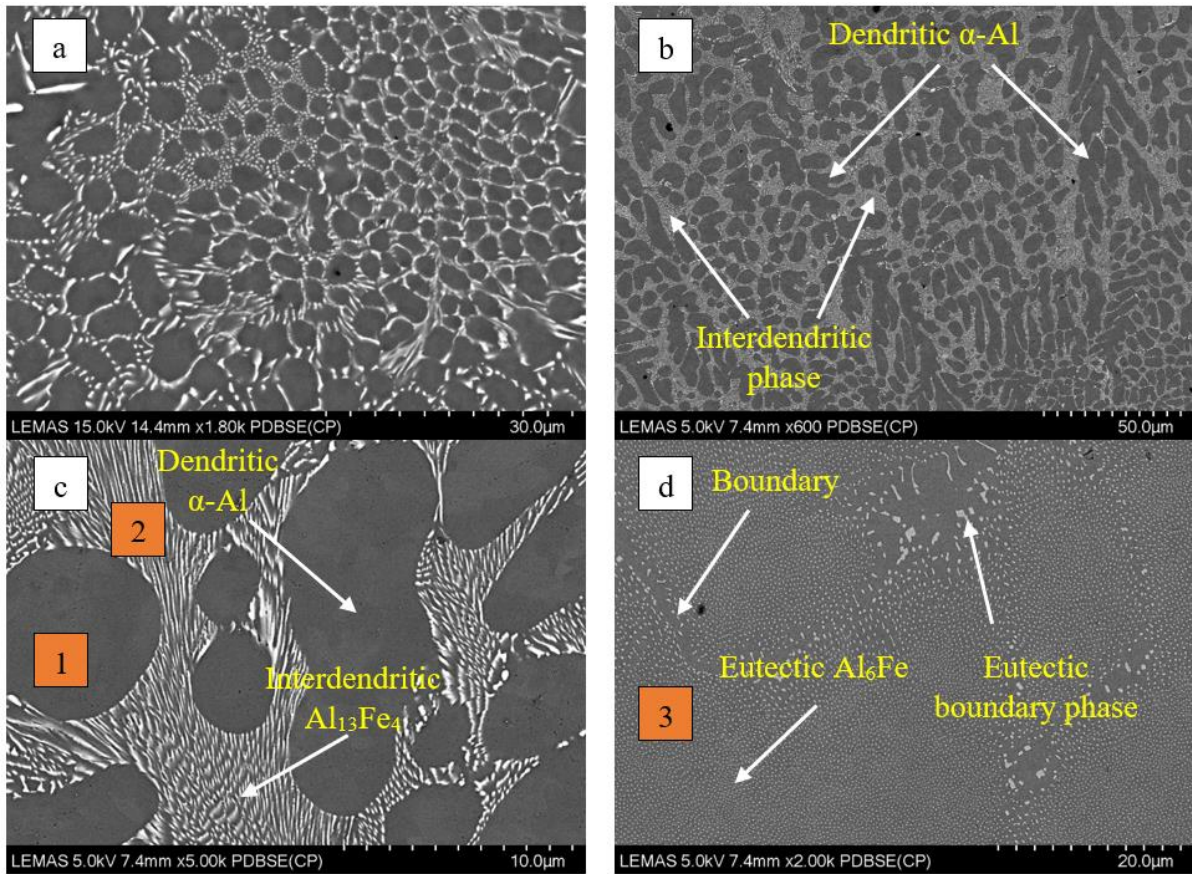
Figure 44: Typical microstructures of large droplets 850 µm< d < 500 showing a) magnified image of the nucleation region, microcellular region b) dendritic region, c) magnified image of the dendritic region with interdendritic $Al_{13}Fe_4$ and d) eutectic region consists of rod-like Al_6Fe eutectic.
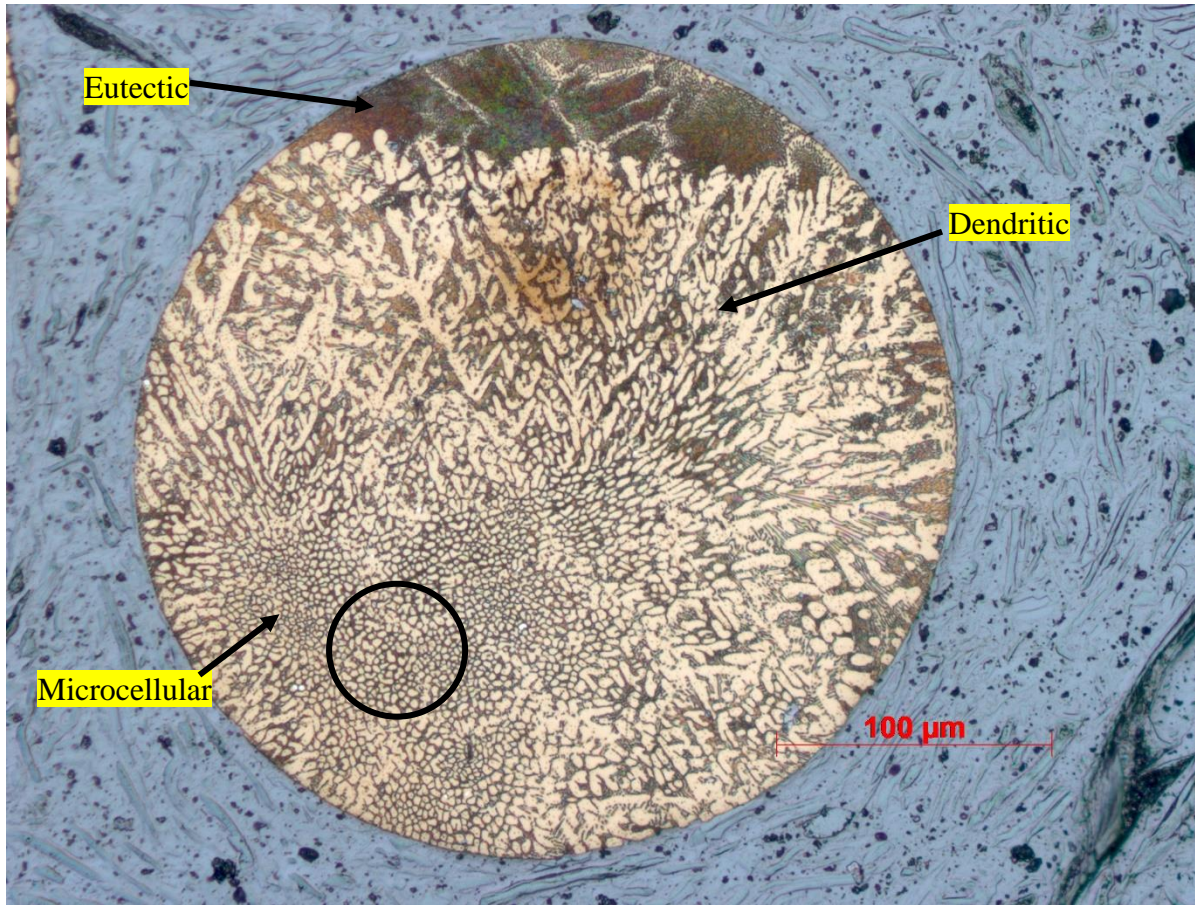
Figure 45: OM micrograph of 500-300 µm sample showing microcellular, dendritic and eutectic regions (circle indicated nucleation initiation zone).
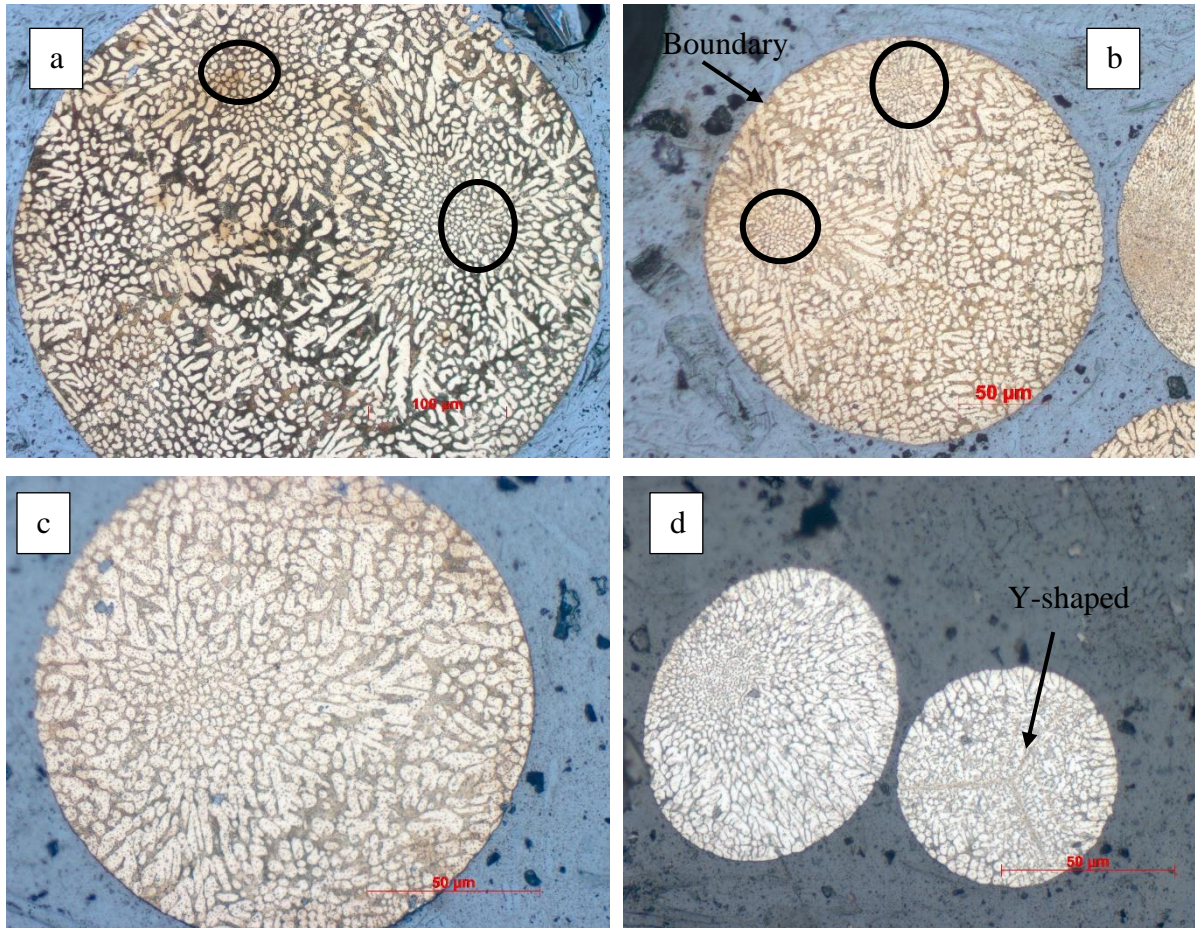
Figure 46: OM micrographs of drop tube atomized Al-2.85 wt% Fe alloy with size fractions of a) 500-300 µm showing multiple nucleation zones, b) 300-212 µm depicting multiple nucleation zones, c) 212-150 µm consists of α-Al and interdendritic eutectic and d) 75-53 µm showing Y-Shaped structure.
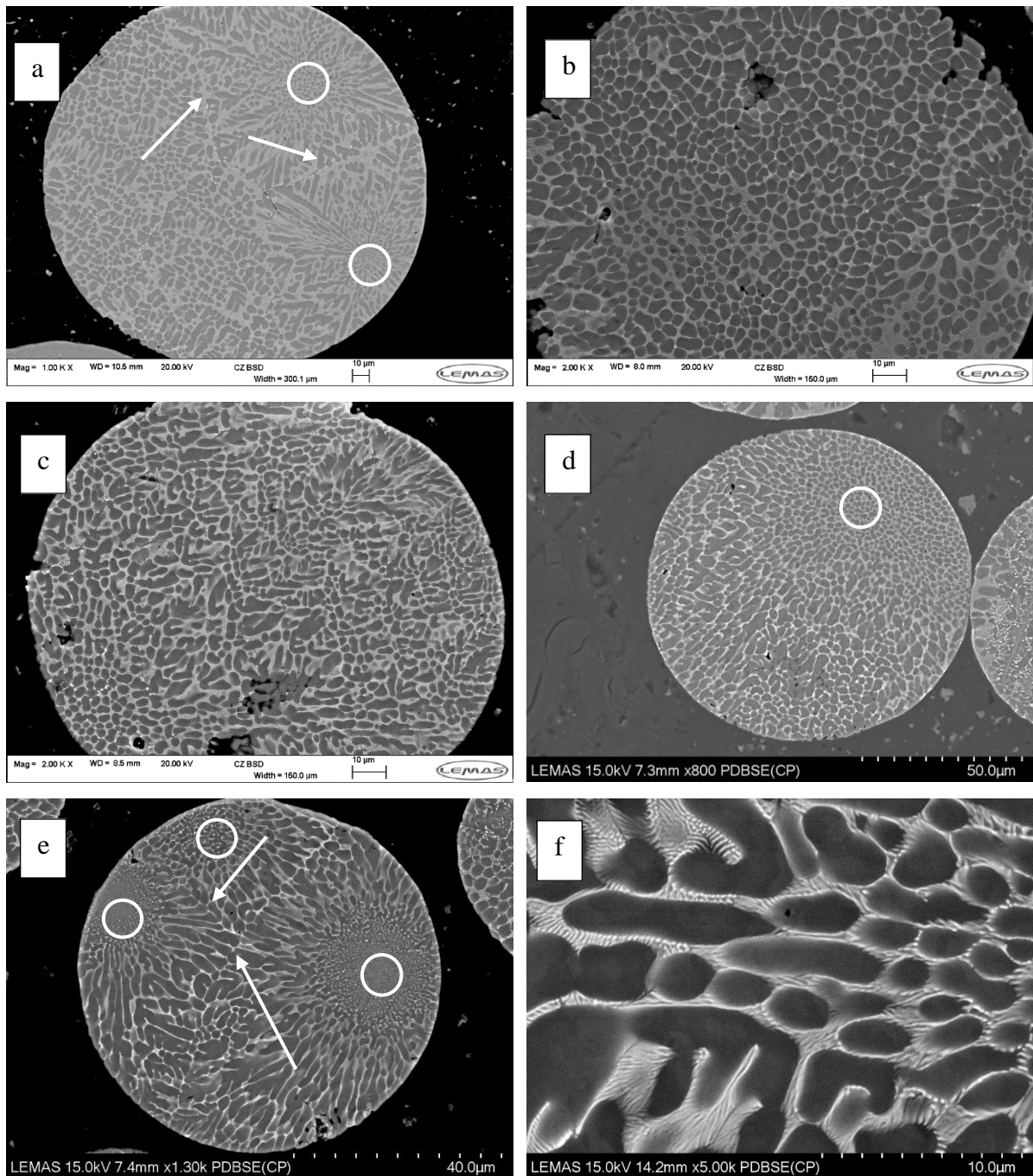
Figure 47: Microstructures of a) 300<d<212, b) 212<d<150, c) 150<d<106, d) 106<d<75 and e) 75<d<53 size fractions, with arrows showing boundaries of growing dendrites and circles showing the nucleation start zones. f) Enlarged view of the $106 < d < 75$ μm sieve fraction showing that the interdendritic eutectic remains of the lamella morphology irrespective of sieve fraction/cooling rate.
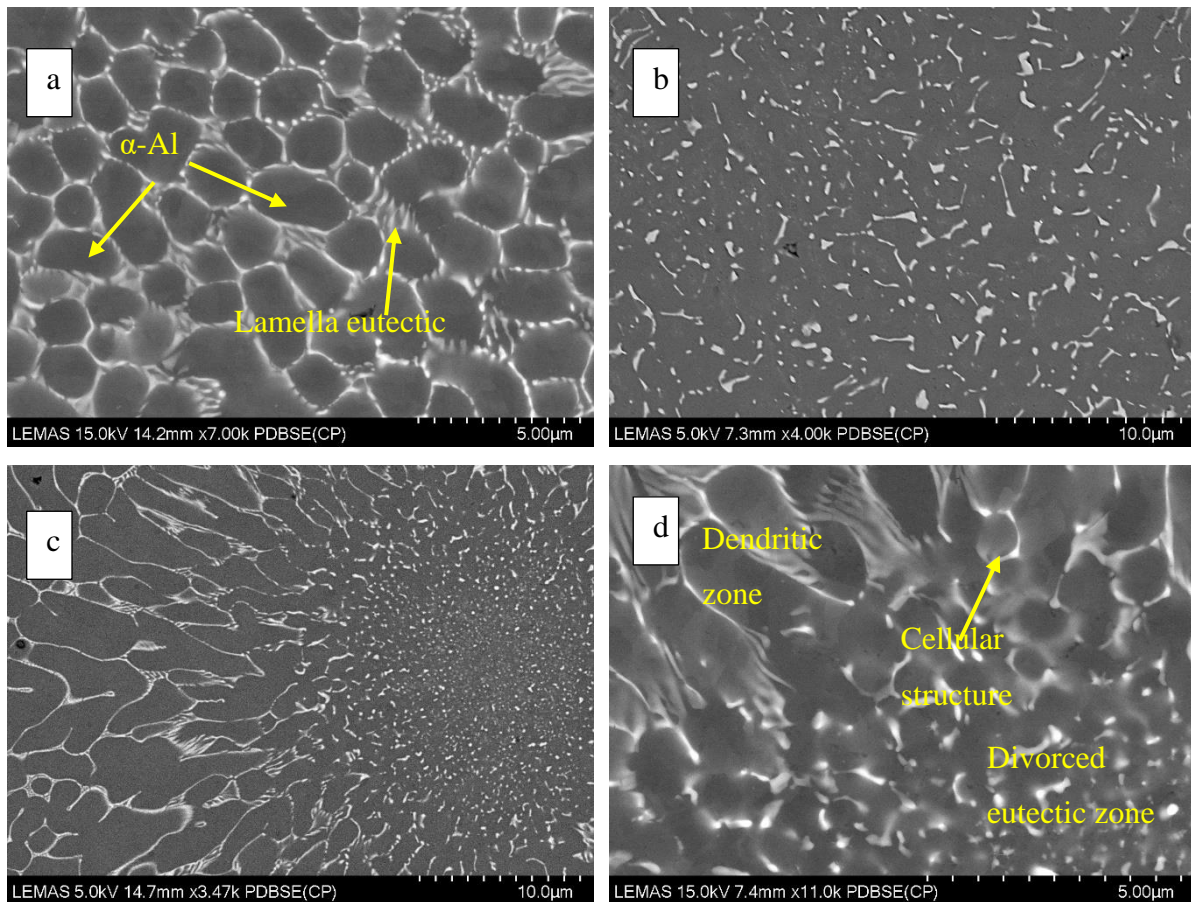
Figure 48: SEM BSE micrographs taken from the solidification start zone of a) 106-75 µm sample showing cellular α-Al surrounded by lamella-like eutectic, b) 106-75 µm sample showing divorced eutectic with intermetallics with various size and morphology, c) 75-53 µm sample depicting divorced eutectic on which dendritic α-Al grows with lamellar-like intermetallic and d) magnified image of solidification zone of c).

5.2.4 EDX Analysis

Five to ten EDX measurements for each of dendritic α-Al, interdendritic eutectic and eutectic regions were taken as explained in **Section 4.2.3**. Regions where the EDX measurement were taken are labelled in **Figure 44** as 1, 2, and 3 for dendritic α-Al, interdendritic eutectic and eutectic regions, respectively. Results for Fe content in dendritic α-Al and interdenritic lamellar eutectic are given in **Figure 49** and **50**, respectively. It must be noted here that as complete eutectic region was only observed in 850-500 µm and 500-300 µm samples, composition of this region is not put in a graph. Moreover, EDX results from this region has shown close Fe content to the composition of the master alloy (composition of the melt) which was measured as 2.9 ± 0.2 wt.% Fe. This composition is expected as this is the only microstructure in this region and it is very unlikely that there would be any macro-segregation in a drop tube sample.

78

Fe solubility in α-Al is very low at the equilibrium being around 0.05 wt.% Fe at eutectic temperature. However, rapid solidification has resulted in an extension of the Fe solubility in α-Al. **Figure 49** shows that slowest cooled sample (850-500 µm) with corresponding average cooling rate of 235 K s^{-1} has Fe concentration of 0.37 wt.% Fe. Moreover, with increasing cooling rate Fe solubility increased with increasing cooling rate and reached a maximum of 1.105 wt.% in the fastest cooled sample. That is, Fe solubility in α-Al has been extended by around 20 times. These results are used to calculate the undercooling in the droplet assuming that this increase in Fe content is related to the metastable extension of α-Al. Moreover, the metastable extension of α-Al was assumed as linear. The results are given in **Table 8**. The minimum undercooling experienced in drop tube was found as 96 K in 850-500 µm samples. The figure increases with decreasing sample size and reaches a maximum of 189 K in 75-53 µm sample.

The composition of the interdendritic eutectic measured using EDX and the results are given in **Figure 50**. It was found that Fe content increases with increasing undercooling as well as increasing cooling rate. The minimum Fe content was found in 850-500 µm sample as 3.9 wt% Fe and the maximum Fe content was measured as 4.8 wt% Fe in 75-53 µm sample. It must be noted here that Fe concentration in both dendritic α-Al (**Figure 49**) and interdendritic eutectic (**Figure 50**) has been found to be increasing with increasing cooling rate. This is possible in a sample with fixed composition provided that eutectic volume fraction decreases. Thus, eutectic volume fraction has been measured and given in **Section 5.2.5**.
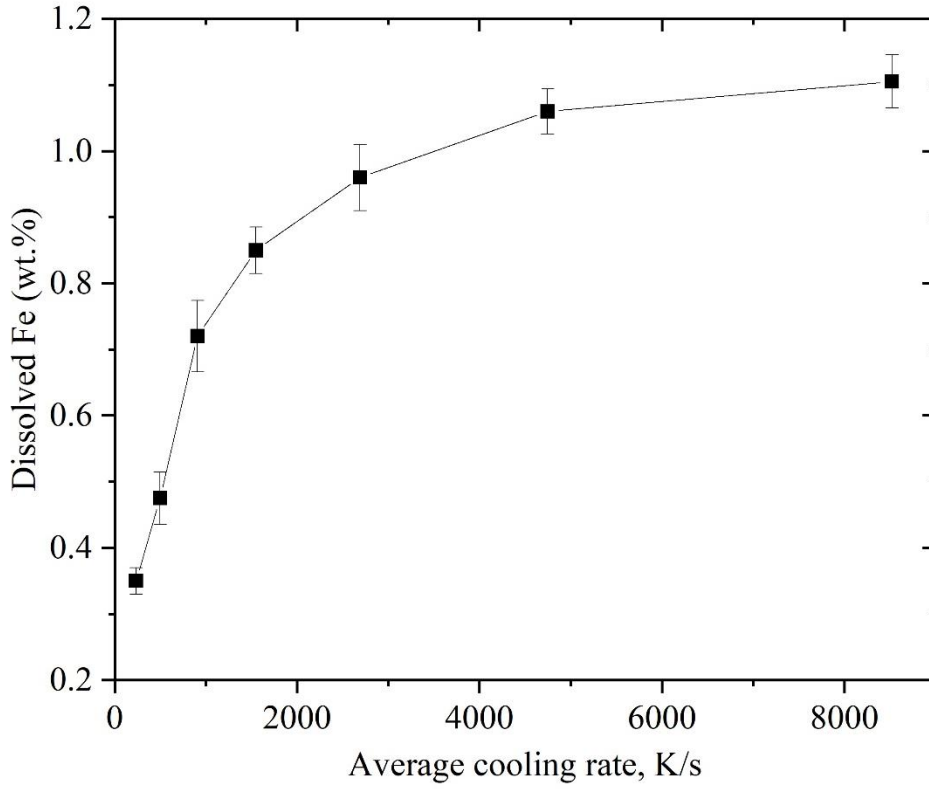
Figure 49: Dissolved Fe in α-Al as a function of average cooling rate.

Table 8: Corresponding undercooling of size fractions calculated using EDX data in **Figure 49**.

Powder size(µm)	850-500	500-300	300-212	212-150	150-106	106-75	75-53
Undercooling (K)	96	109	140	156	170	183	188
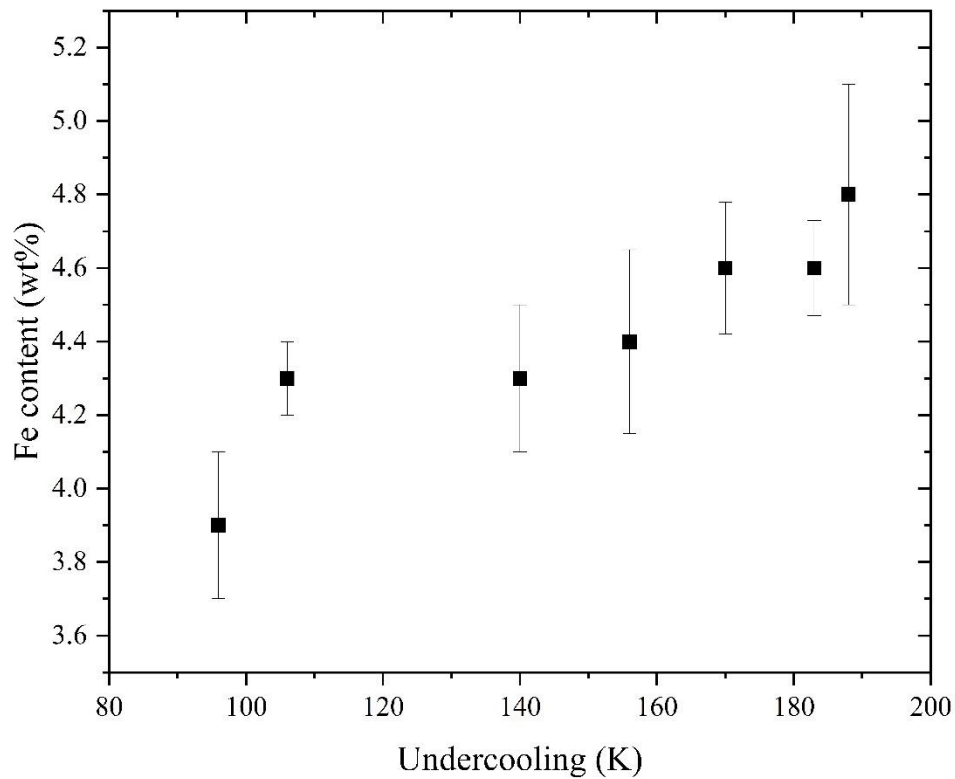
Figure 50: Composition of the interdendritic eutectic as a function of estimated undercoling.

5.2.5 Eutectic Volume Fraction

The volume fraction of the interdendritic eutectic was calculated as explained in **Section 4.2.5** by converting SEM images in to grey scale images. The results are given in **Figure 51**. It is clear from the figure that volume fraction of the eutectic decreases with rising undercoling and, as a result, the volume fraction of α-Al increases with increasing cooling rate. While around 50% of the microstructure is interdendritic eutectic in 850-500 μm sample, the figure dropped to 26.7 vol. % in 75-53 μm sample. This is in good agreement with EDX results given in **Figure 49** which shows an increase in dissolved in Fe content in α-Al with increasing cooling rate. As more Fe is dissolved in α-Al, there remains less Fe to form intermetallic. This results in decrease in the volume fraction of the eutectic as shown in **Figure 51**.
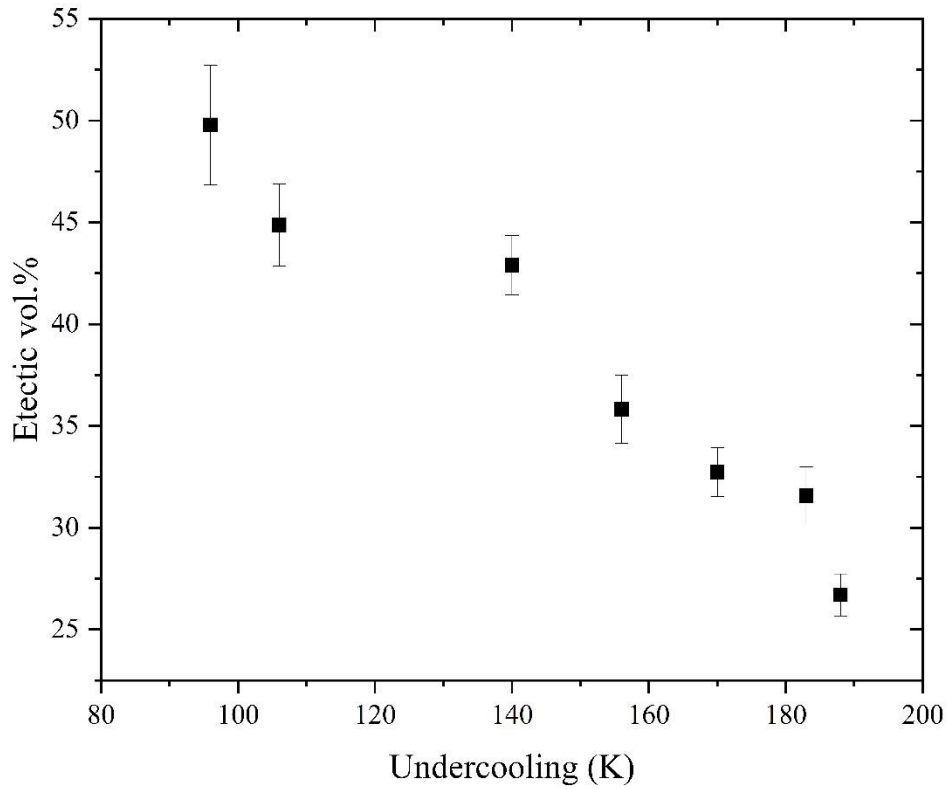
Figure 51: Eutectic volume per cent as a function of the estimated undercooling.

5.2.6 Secondary Dendrite Arm Spacing

As mentioned earlier, it is impossible to monitor the thermal history of the solidifying droplet in drop tube and there are two methods to estimate the cooling rate. First method has already been covered in **Section 5.1**. Second method is to measure the secondary dendrite arm spacing (SDAS) and use published relation between cooling rate and SDAS. Therefore, SDAS for each size fractions of the drop tube atomized samples were measured. The results are given in **Figure 52** as a function of average estimated cooling rate. It shows that the SDAS is decreasing with increasing cooling rate ranging between 4.2 µm and 1.4 µm. Using a fitting function on OriginPro, the relation was found as

$$SDAS = 31.06 * \dot{T}^{-0.367} \tag{5-6}$$

This result is very close to the published result of Miki et al.[104] who measured the SDAS at different cooling rates of Al-0.55 wt% Fe alloy and found the relation as

$$SDAS = 33.4 * \dot{T}^{-0.333} \tag{5-7}$$

82
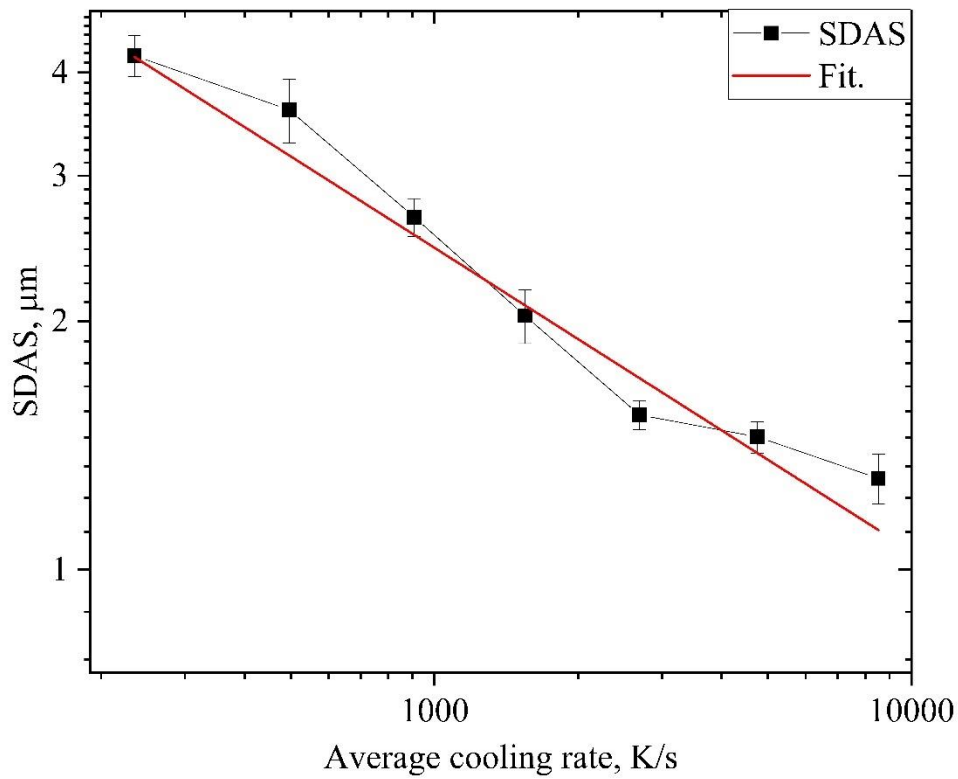
Figure 52: Secondary dendrite arm spacing (SDAS) as a function of average sample size.

5.2.7 Eutectic Spacing

Eutectic spacing of the interdendritic eutectic was measured for all sieve fraction in order to show the effect of the cooling rate on the eutectic spacing. The results are given in **Figure 53**. It is clear that eutectic spacing drops with increasing cooling rate. The highest eutectic spacing was measured as 0.75 µm in slowest cooled sample. This figure drops to a minimum in the fastest cooled to sample and measured as 0.15 µm.
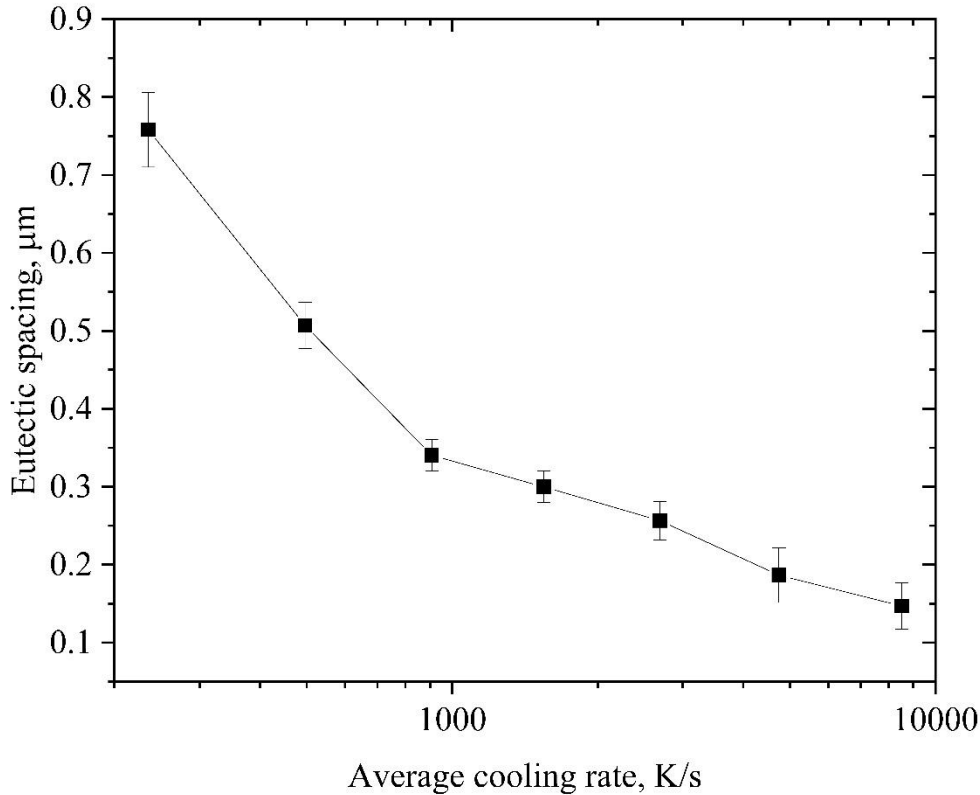
Figure 53: Interdendritic eutectic spacing as a function of average cooling rate.

5.2.8 TEM Results

A FIB SEM sectioned sample from the boundary of interdendritic region and eutectic region of 850-500 µm sample is further analysed under TEM to confirm the intermetallic phases. **Figure 54** shows the FIB SEM view of the sectioned sample which includes rod-like eutectic region, interdendritic region and transition region. TEM figure of this region is shown is **Figure 55**. SAD patterns were taken from the phases in this region. Where SAD patterns were taken and the corresponding SAD patterns are given in **Figure 56**. **Figure 56** shows precipitates with different morphologies: rod-like (**Figure 56 a**), lamellar (**Figure 56c**), compact and acicular phases (**Figure 56e**) formed between interdendritic lamellar eutectic and rod-like eutectic. Analysis have been made using both d-spacings and the angle between the planes as explained in **Section 4.2.4**. SAD pattern in **Figure 56** revealed that while the rod-like intermetallic is Al_6Fe, lamellar intermetallic is $Al_{13}Fe_4$. Moreover, compact intermetallic in the transition zone was found to be $Al_{13}Fe_4$.

84
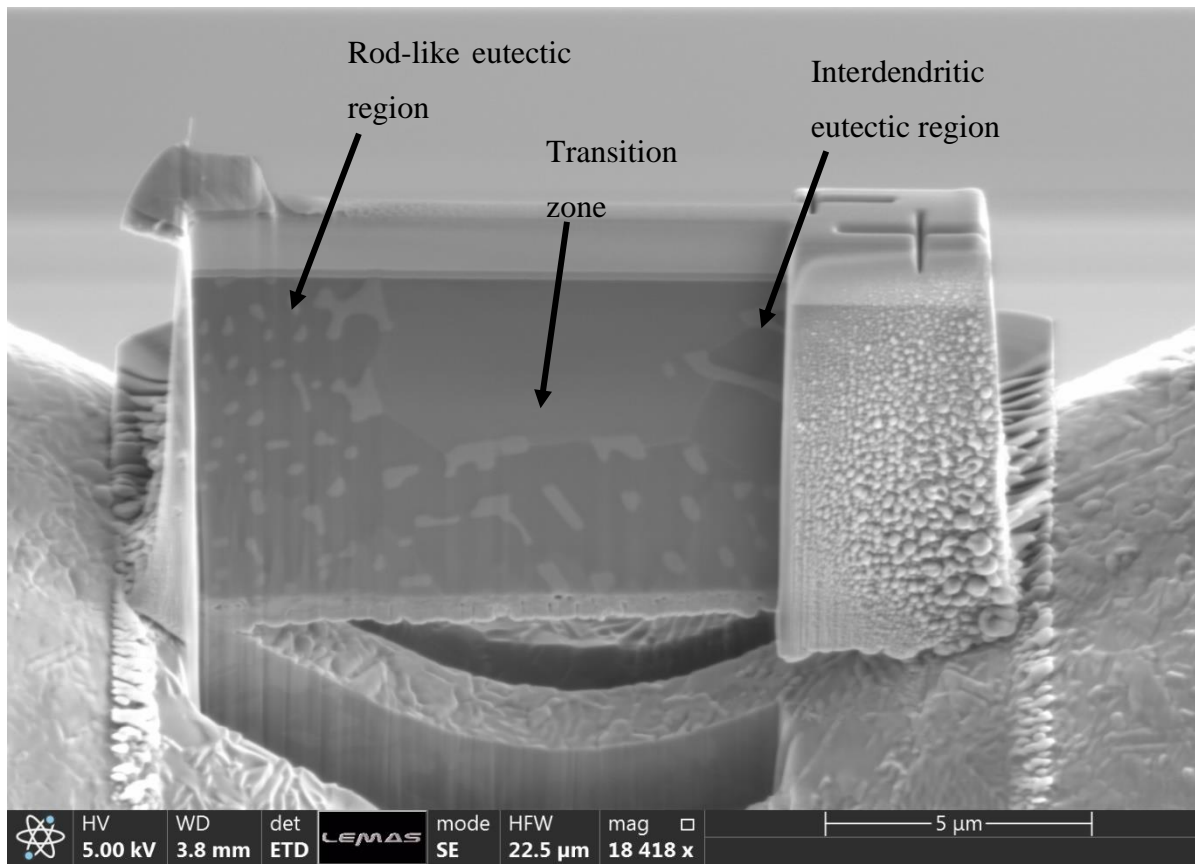
Figure 54: SEM micrograph of the FIB sectioned sample from the boundary between interdendritic region and eutectic region.
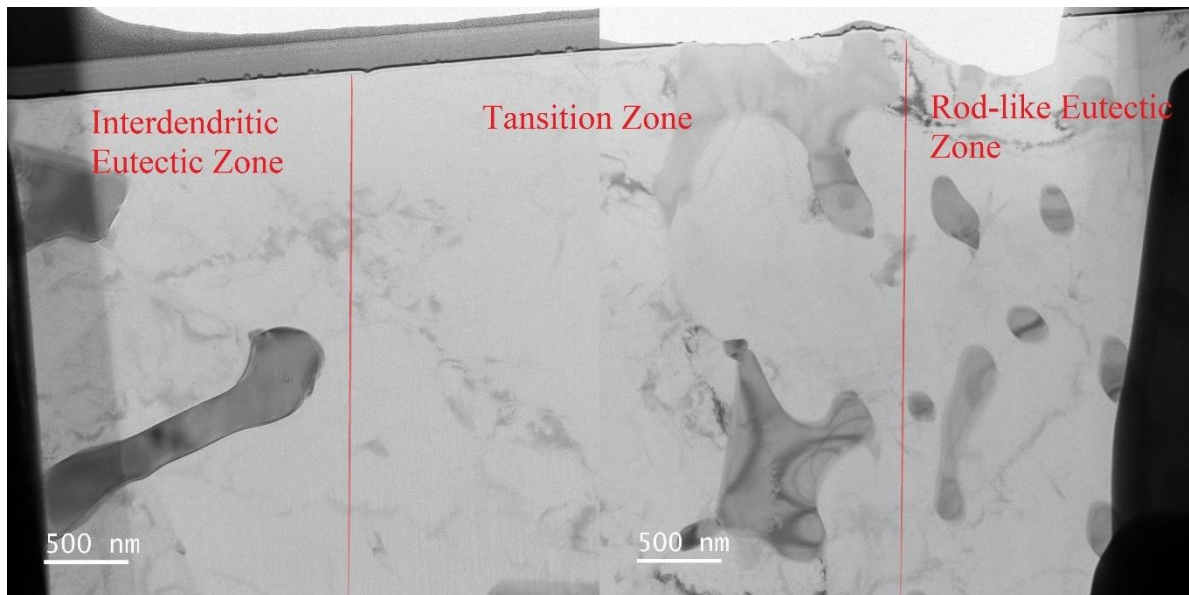
Figure 55: TEM image of the FIB cut sample shown in **Figure 54**.
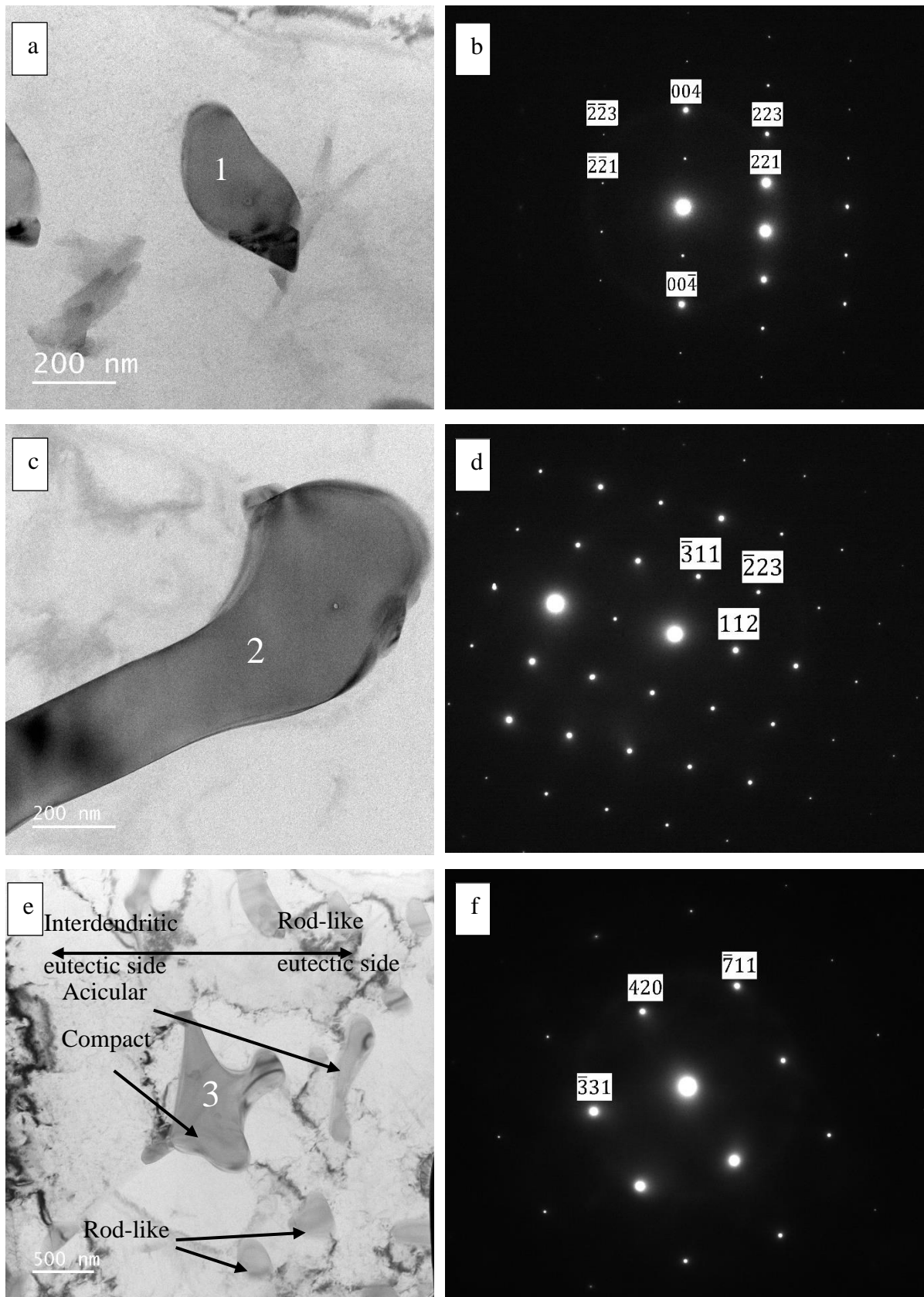
Figure 56: a) TEM bright field image of the rod-like eutectic, b) TEM diffraction pattern of point 1 showing the diffraction pattern of Al_6Fe along the $[1\bar{1}0]$ zone axis, c) TEM bright field image of the lamella-like interdenritic eutectic, d) TEM diffraction pattern of point 2 depicting the diffraction pattern of $Al_{13}Fe_4$ along the $[\bar{1}\bar{7}4]$ zone axis, e)TEM bright field image of point

the intermetallic formed between rod-like eutectic and interdendritic eutectic, f) TEM diffraction pattern of point 3 depicting $Al_{13}Fe_4$ along the $[1\bar{2}3]$ zone axis.

5.2.9 Microhardness

In order to understand the effect of the cooling rate on the mechanical properties of the samples, the microhardness of the samples was measured. At least ten measurements were taken from each sieve fraction. Vickers microhardness with a standard indenter using 10 g load and 10 s dwell time was employed on each sieve fractions and the results are given in **Figure 57**. One can see that microhardness values are increasing with increasing cooling rate. Microhardness of the slowest cooled sample (850-500 µm) is around 53.5 ± 2 $HV_{0.01}$. This figure rises with increasing cooling rate and reaches a maximum of 66.14 ± 1.14 $HV_{0.01}$ in the sample with a diameter of 106-75 µm. The change in the microhardness is limited being around 20%. This is probably due to the competition between solid solution hardening and scale refinement, and decreasing volume fraction of the intermetallics. Intermetallics are known for their contribution to the hardness of the alloys. As seen from **Figure 50** volume fraction of the eutectic decreases with increasing cooling rate. This means that less intermetallics forms in the samples with smaller diameters, which has a negative effect on the microhardness. Furthermore, refinement in the microstructure (**Figure 53**) is observed with increasing cooling rate, having a positive effect on the microhardness. In addition, Fe content in α-Al (**Figure 49**) was found to be rising with increasing cooling rate. This has a positive effect in the microhardness as solid solution increases the microhardness in alloys.
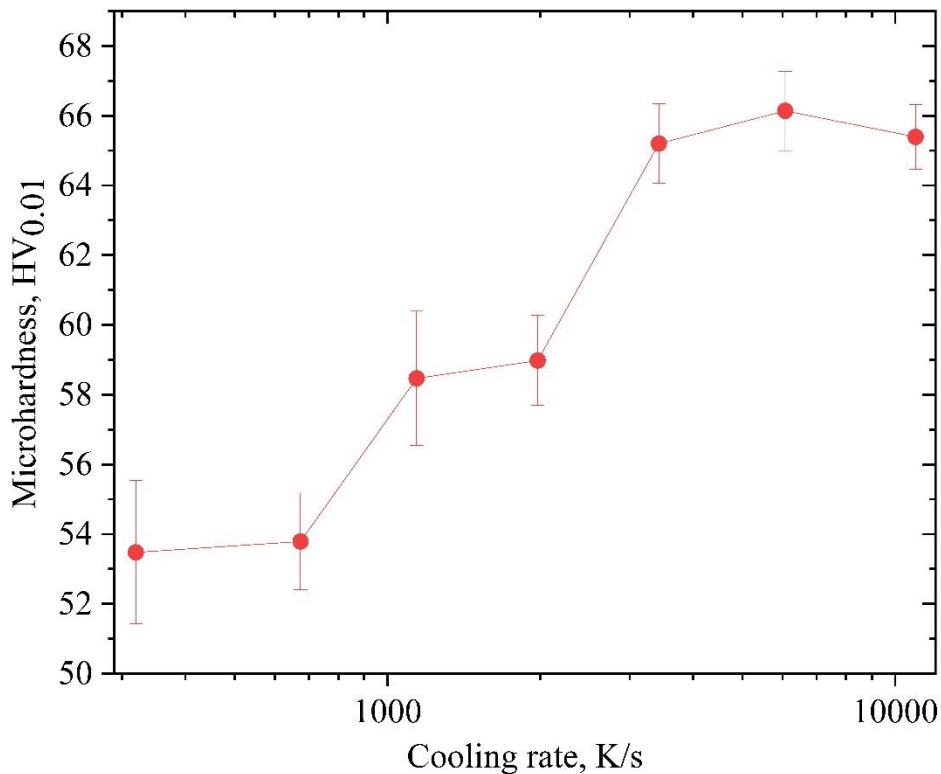
Figure 57: Microhardness values (in $HV_{0.01}$) as a function of cooling rate.

5.3 Results for Al-3.9 wt% Fe

5.3.1 Phase Analysis and Microstructure of the Furnace Cooled Sample

Microstructure of the furnace cooled Al-3.9 wt% Fe was investigated using SEM. The microstructure of the furnace cooled sample is given in **Figure 58**. The microstructure is similar to the microstructure of the furnace cooled Al-2.85 wt% Fe given in **Figure 40**. It consists of primary blocky $Al_{13}Fe_4$ and needle-like $Al_{13}Fe_4$ radiating from primary $Al_{13}Fe_4$ on α-Al matrix. As the cooling rate is low (around 20 K s^{-1}), solidification takes place according to the stable Al-Fe phase diagram. Therefore, phases observed are $Al_{13}Fe_4$ and α-Al. The refined nature of Al-$Al_{13}Fe_4$ eutectic is a result of the liquid being depleted in Fe close to proeutectic phase due to the growth of the proeutectic $Al_{13}Fe_4$.
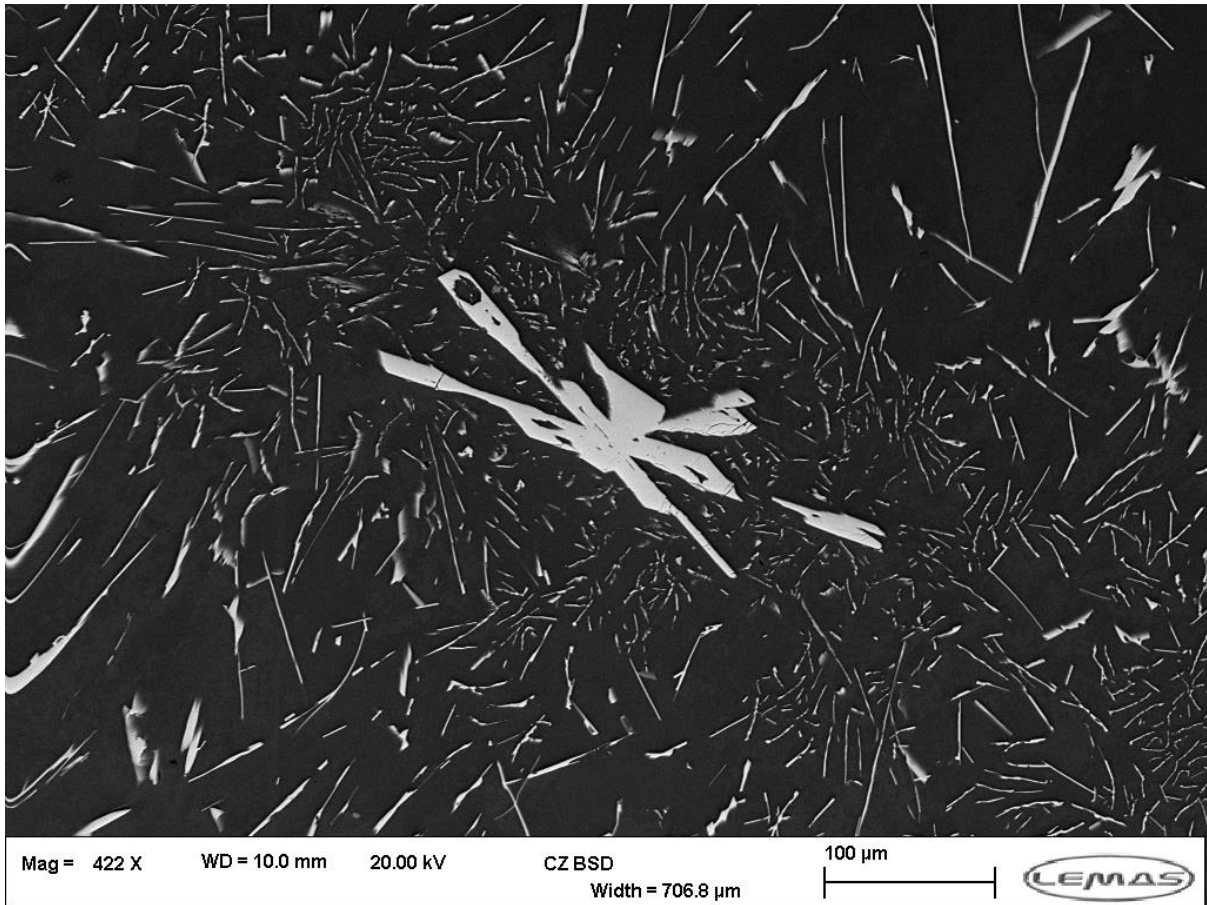
Figure 58: SEM micrograph of the furnace cooled sample depicting blocky $Al_{13}Fe_4$, $Al_{13}Fe_4$ needles on α-Al matrix.

5.3.2 XRD Results of Drop Tube Atomized Al-3.9 wt% Fe

XRD patterns of some selected samples, namely: 850-500, 212-150 and 75-53 µm, are given in **Figure 59**. These sample sizes are chosen to reflect the wide range of cooling rates so that XRD for slow cooled, medium cooled and fast cooled samples are given. Remaining XRD patterns are provided in **Appendix B**. As can be seen from the figure, there are three phases which are $Al_{13}Fe_4$, Al_6Fe and α-Al regardless of the diameter of the sample and, consequently, their cooling rate. It must be noted here that, as there is no PDF card for Al_mFe in the database and the strongest peaks of Al_mFe is very close to either $Al_{13}Fe_4$ or Al_6Fe [105], it is hard to determine the presence of Al_mFe using XRD data.
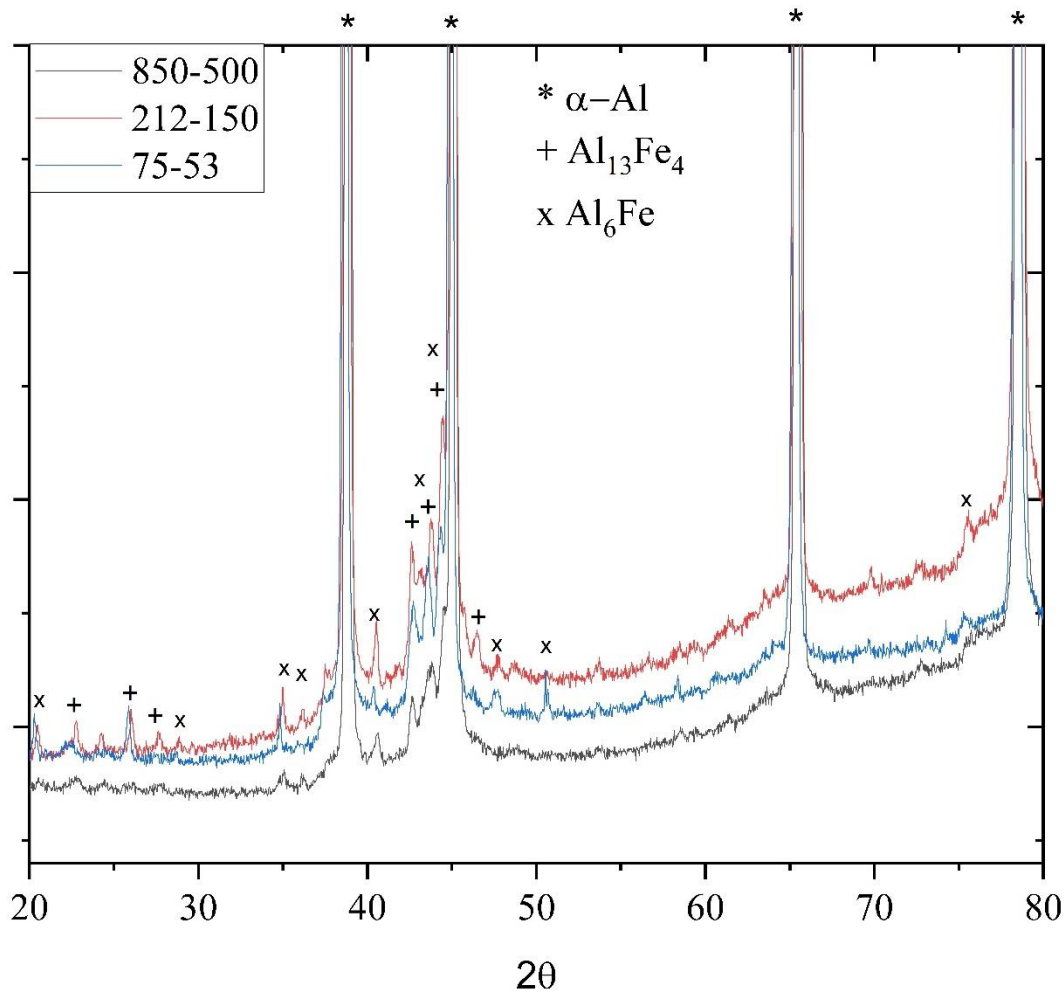
Figure 59: XRD results for 850-500 µm, 212-150 µm and 75-53 µm samples.

5.3.3 Microstructural Characterization and Phase Analysis

The microstructures of the drop tube atomized Al-3.9 wt% Fe have been analysed using both OM and SEM. A wide range of microstructures has been observed with increasing cooling rate. **Figure 60** shows the optical micrographs of the largest ($d > 850+$ μm) drop tube atomized sample. It is clear from the **Figure 60** that the microstructure of the sample is mostly eutectic. The sample consists of primary $Al_{13}Fe_4$, rod-like eutectic, lamellar eutectic, dendritic α-Al and α-Al surrounding the primary $Al_{13}Fe_4$ as each being labelled on the figure. As the sample size is large with a corresponding relatively low cooling rate of around 100 K s^{-1} and the difference between eutectic and liquidus temperature of the sample is relatively high (100 K), there is time to form primary $Al_{13}Fe_4$ in the melt without any constraint. Thus, it formed a bulky morphology. A number of primary $Al_{13}Fe_4$ is formed randomly in the sample with different sizes and morphologies as shown in **Figure 60a**, and all are surrounded with α-Al. Fe in the melt diffuses to form $Al_{13}Fe_4$, liquid surrounding $Al_{13}Fe_4$, as a result, becomes poor in Fe. Thus,

90

surrounding melt solidifies as α-Al without sufficient Fe to form eutectic. While the primary Al$_{13}$Fe$_4$ shown in **Figure 60c** is thick needle-like radiating from the its nucleation point with a length of 20-40 μm and thickness of around 5-10 μm, the primary Al$_{13}$Fe$_4$ shown in **Figure 60d** is more compact clover-like morphology, with a length of 40 μm and a thickness of 20 μm. As the temperature of the liquid drops below the eutectic temperature most of the remaining liquid transformed into eutectic. **Figure 60d** shows that both rod-like and lamellar eutectic with different sizes and densities are present in the sample and these eutectics are divided with a boundary. As TEM results for drop tube atomized Al-2.85 wt% Fe given in **Figure 56** showed that rod-like eutectic is Al$_6$Fe while Al$_{13}$Fe$_4$ forms lamellar eutectic. That is, both stable Al$_{13}$Fe$_4$ and metastable Al$_6$Fe phases have been formed in the sample. This is in good agreement with the XRD results given in **Figure 59** which says both phases are observed in the sample. A small amount of dendritic α-Al was also formed in the sample as shown in **Figure 60b**. For dendritic α-Al to be formed in a hypereutectic Al-Fe alloy, the temperature of the remaining melt should go below α-Al side of the coupled zone. Overall, if the sequence of the solidification is given for the sample, it would be simultaneous growth of dendrites of α-Al and the primary Al$_{13}$Fe$_4$ and eutectics (it is not clear from the **Figure 60** that which eutectic formed first) and interdendritic eutectic.

Figure 61 shows the SEM images of the 850-500 µm, 500-300 µm and 300-212 µm samples. The microstructures shown in **Figure 61** is similar to **Figure 60**. That is, the microstructure consists of primary Al$_{13}$Fe$_4$, dendritic α-Al, rod-like and lamellar eutectics and α-Al surrounding primary Al$_{13}$Fe$_4$.Overall, it can be seen from the figures that volume fraction of the dendritic α-Al is increasing with decreasing sample size and, consequently, that of the eutectics is decreasing. The microstructure of 800-500 µm sample as shown in **Figure 61 a** and **b** consists of primary Al$_{13}$Fe$_4$ surrounded with α-Al and eutectics. In addition to the primary Al$_{13}$Fe$_4$ morphologies observed in 850+ µm sample as shown in **Figure 60**, the primary Al$_{13}$Fe$_4$ adopted rosette-like morphology. **Figure 61 c** and **d** shows the microstructure of 500-300 µm sample with the presence of dendritic α-Al in addition to phases observed in 850-500 µm sample. This can be seen clearly in **Figure 61 e** and **f**, which shows the micrographs of 300-212 µm sample.

Decreasing sample size fraction from 300-212 µm to 212-150 µm changed the microstructure of the droplet drastically. **Figure 62** shows the microstructure of 212-150 µm sample. First of all, primary Al$_{13}$Fe$_4$, which was observed in samples with d > 212 µm as shown in **Figure 60** and **Figure 61** was not formed in the droplet. As 212-150 µm sample experiences higher

cooling rate, and, thus, higher undercooling than d > 212 µm, other phases may become either thermodynamically or kinetically favoured. The microstructure of 212-150 µm sample is composed of featureless Y-shaped structure (these featureless structures will be referred as "Y-shaped structure" regardless of their geometry, shown with dashed black lines passing thorough it's centre in **Figure 62a** and **c**), cellular α-Al, dendritic α-Al, lamellar eutectic and rod-like eutectic. Y-shaped structure was observed in all samples with sizes smaller than 212 µm. As the dendritic α-Al grows out of Y-shaped structure and dendrite arms get coarser away from Y-shaped structure, it can be said that this Y-shaped structure is the first phase to form in the droplet (further evidence for this presented in **Figure 67**). That is, Y-shaped is where the nucleation initiated in the droplet and the solidification continued with the formation of cellular α-Al, dendritic α-Al with lamellar interdenritic eutectic and both lamellar and rod-like eutectics, respectively. Although Y-shaped looks like a continuous phase, **Figure 62c** and **d** show the fragmented nature of the Y-shaped (indicated with white arrows) each of which acted as a nucleation site for α-Al. **Figure 62c** shows that cellular α-Al nucleated on Y-shaped structure and is followed with the formation of dendritic α-Al. Moreover, lamellar eutectic formed in the interdendritic area as shown in **Figure 62c** and **d**. Dendritic growth is later halted due to a decrease in undercooling occurring as a result of recalescence, wherein fully eutectic growth takes over. Remaining liquid in the droplet solidified and formed complete eutectic structure as shown in **Figure 62b**. It is clear from **Figure 62b** that there are both lamellar eutectic and rod-like eutectic. While the lamellar eutectic formed close to dendritic region, the formation of rod-like eutectic took place away from the dendritic area and, consequently, away from Y-shaped structure where the nucleation started. The angles between the arms of Y-shaped in **Figure 62a** are measured as 104°, 121° and 135°.

EDX measurements have been performed for all sieve fractions which have Y-shaped to identify the composition of the Y-shaped regions. One example of the EDX results taken from Y-shaped region is provided in **Figure 62e**. EDX results from Y-shaped showed that the composition of Y-shaped is similar to the composition of the melt (Al-3.9 wt.% Fe) for all sizes. This is consistent with the Y-shaped morphology appearing somewhat lighted than the dendritic α-Al in the backscatter images.

Featureless Y-shaped structure was observed in all powders with d < 212 µm and was formed in different morphologies. **Figure 63** shows OM micrographs of the different morphologies of Y-shaped structure formed in 150-106 µm droplets. While Y-shaped in **Figure 63a** and **e** is similar to the one in **Figure 62a**, **Figure 63b** and **c** show more complex Y-shaped structure.

Y-shaped adopts a pentagon in **Figure 63b**. Moreover, **Figure 63c** shows the second branching of Y-shaped as indicated by dashed lines in the figure. While the angles between the first branches of Y-shaped shown in **Figure 63c** is close to 120°, the angle between second branches was measured as around 60°. The angles between the arms of Y-shaped can adopt a number of values as given in the figure. The angles in the upper part of Y-shaped given in **Figure 63a**, for example, is close to 120° ranging between 114° and 124°. However, the angles between the lower arms are ranging between 146° and 81°. Moreover, three right angles and two 135° angles were measured in the pentagon given in **Figure 63b**.

SEM BSE micrographs of Y-shaped structures of 150-106 µm samples are given in **Figure 64** and **65**. These samples show Y-shaped throughout the samples. The solidification has proceeded with the formation of divorced eutectic, cellular α-Al, dendritic α-Al with lamellar interdendritic eutectic and eutectic in order as moving away from the Y-shaped. Such order of formations of morphologies in all samples with Y-shaped structures. That is the sequence of the phase formations in samples is Y-shaped, divorced eutectic, cellular α-Al, dendritic α-Al with lamellar interdendritic eutectic and eutectic.

Figure 66 shows the microstructures of 106-75 µm samples. As seen from the figure Y-shaped obtained more complex structure with increasing cooling rate. Divorced eutectic is formed in the regions close to Y-shaped. This later transitioned in to cellular α-Al and dendritic α-Al. Moreover, **Figure 66c** shows the formation of spherical and needle-like phases in the middle of Y-shaped perfectly aligned parallel to Y-shaped. The diameter of the spherical precipitates was measured as around 200 nm, while the length of the needle-like precipitates is around 500 nm and the thickness is around 100 nm.

 Figure 67 shows 106-75 µm sample with its satellite with a diameter of around 38 µm in both of which Y-shaped structure has formed. Moreover, it can be seen from the figure that fine structures at the contact between the sample and the satellite were formed. The satellite acted as a heterogenous nucleation site for the larger sample and formed very fine structures at the contact. That is, when samples collided the contact part of large droplet was still liquid. This can be clearly seen from the concave contact surface between the large and small samples. On the other hand, when the collision took place, the smaller droplet had already been solidified completely. That is because smaller particles experience higher cooling rate than larger droplets in drop tube and, therefore, require less time for complete solidification. Moreover, it can be seen from the figure that there is no connection between the heterogeneous nucleation site and

Y-shaped structure in larger droplet. This indicates that, Y-shaped in the large sample had already been formed in the sample while remaining liquid was forming dendritic α-Al and eutectic, the collision took place. That is, Y-shaped is the first phase to solidify in the sample as discussed earlier. Furthermore, the angles between Y-shaped in **Figure 67** were measured and range between 108° and 137°. As can be seen from the figures dendritic α-Al gets coarser away from Y-shaped. The equivalent circular diameter based upon area of dendritic α-Al were measured 5, 10, 15, 20 µm away from Y-shaped and found as 1.05, 1.6, 2.6 and 3.3 µm, respectively for 106-75 µm sample. Moreover, the volume fraction of dendritic α-Al was measured to be decreasing away from Y-shaped so that volume fraction α-Al decreases from 80 vol% to 72 vol% 10 µm and 20 µm away from Y-shaped.

Increasing cooling rate increased the volume fraction of the Y-shaped structure in the samples and, as a result, that of the eutectic and α-Al decreased. This can be seen from the **Figure 68** which shows the microstructure of 75-53 µm and 53-38 µm samples. Y-shaped formed in 75-53 µm as shown in **Figure 68a** adopted dendrite like morphology whose secondary arms grow perfectly parallel to each other. Similar morphology can also be seen in 53-38 µm sample as depicted in **Figure 68c**.
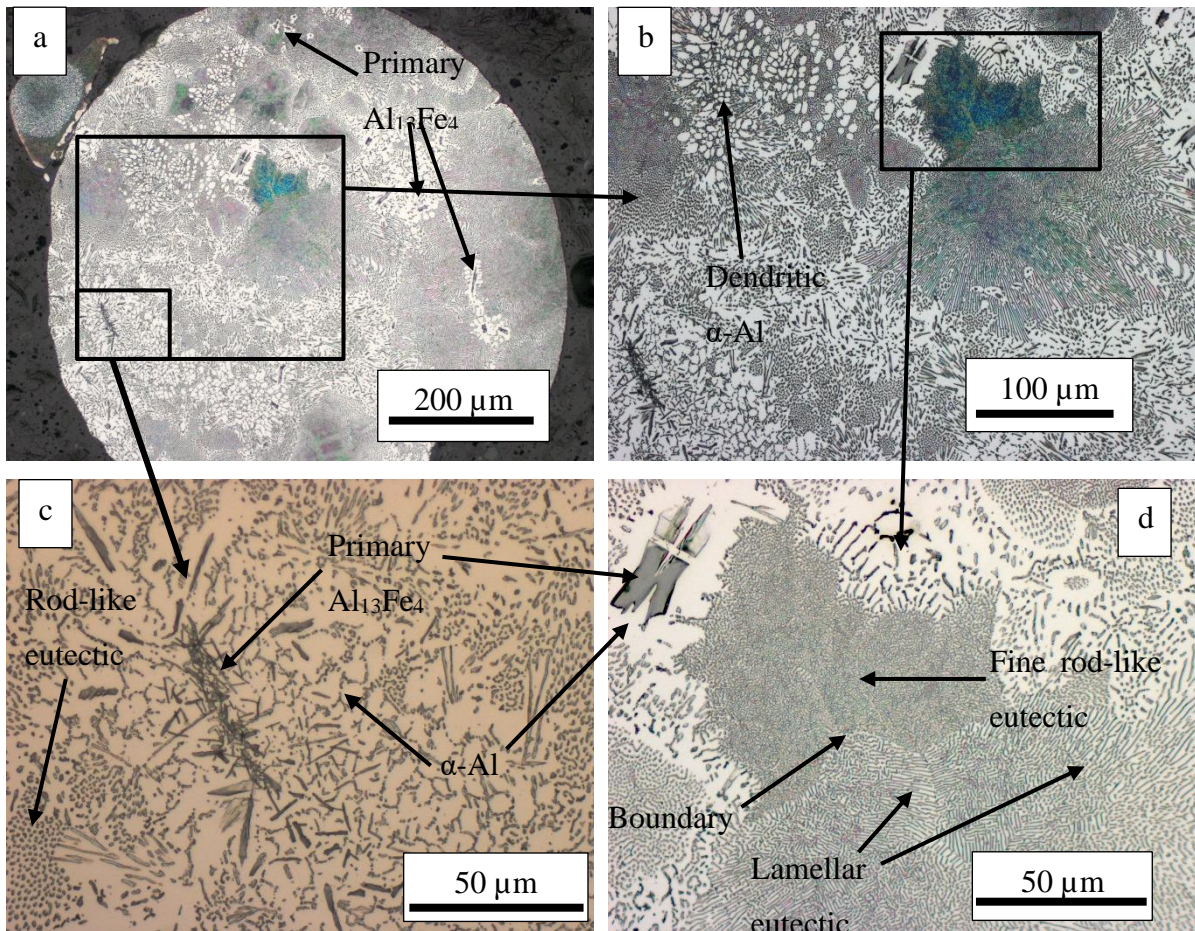
Figure 60: Microstructures of the rapidly solidified Al-3.9 wt% alloy with sample diameter of 850+ µm showing primary $Al_{13}Fe_4$, rod-like eutectic, lamellar eutectic, α-Al and dendritic α-Al.
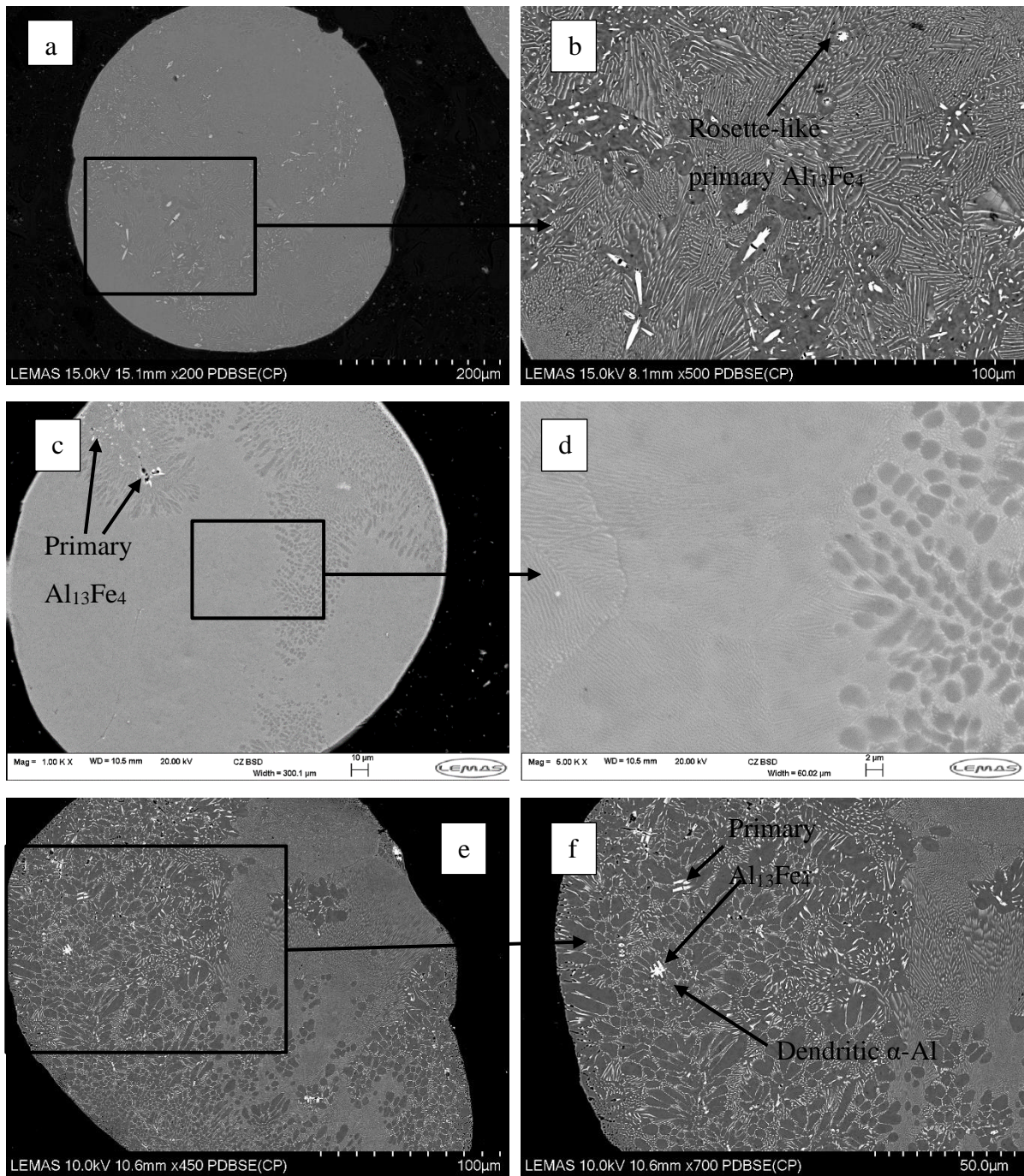
Figure 61: SEM micrographs of a) 850-500 µm sample, b) magnified image of a), c) 500-300 µm sample, d) magnified image of c), d) 300-212 µm sample and e) magnified image of d).
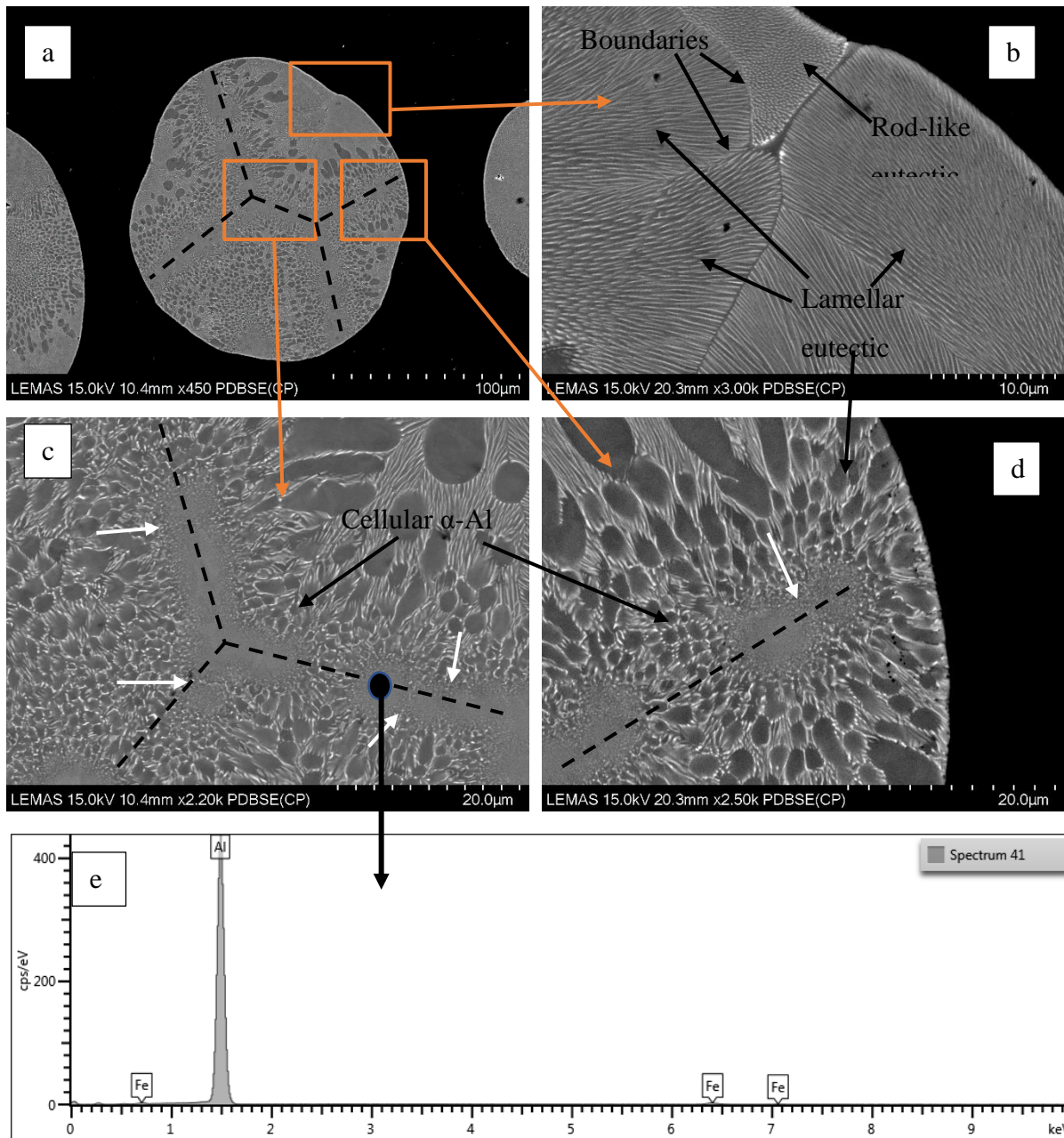
Figure 62: SEM micrographs of 212-150 µm sample showing Y-shaped phase, cellular α-Al, dendritic α-Al, interdendritic lamellar eutectic, lamellar eutectic and rod-like eutectic. (White arrows show the boundaries of the nuclei which form Y-shaped phase and dashed black lines show the structure of Y-shaped) e) EDX measurement taken from the Y-shaped region showing identical composition to the melt.
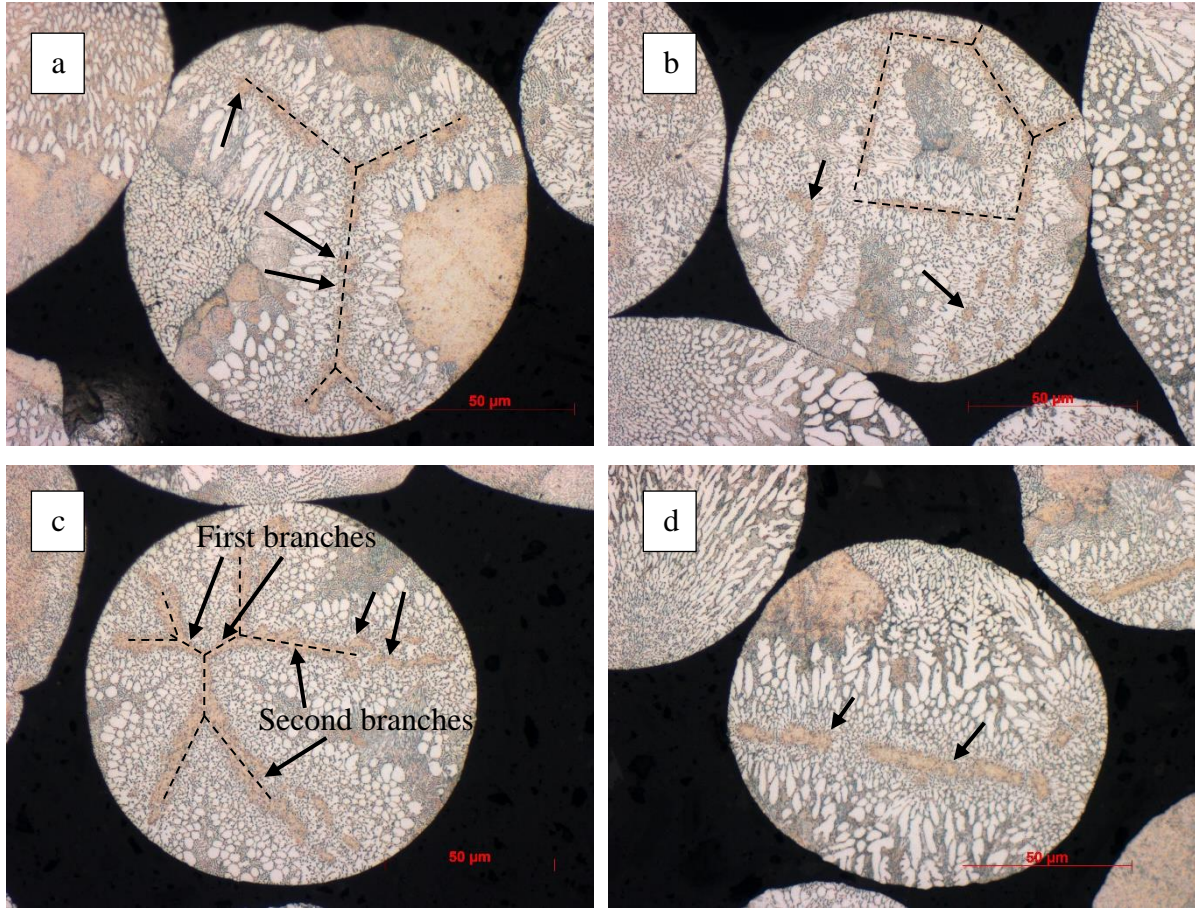
Figure 63: OM micrographs of 150-106 µm sample depicting different morphologies of featureless Y-shaped structure. Arrows show the broken nature of the Y-shaped which acted as nucleation sites for dendritic α-Al.
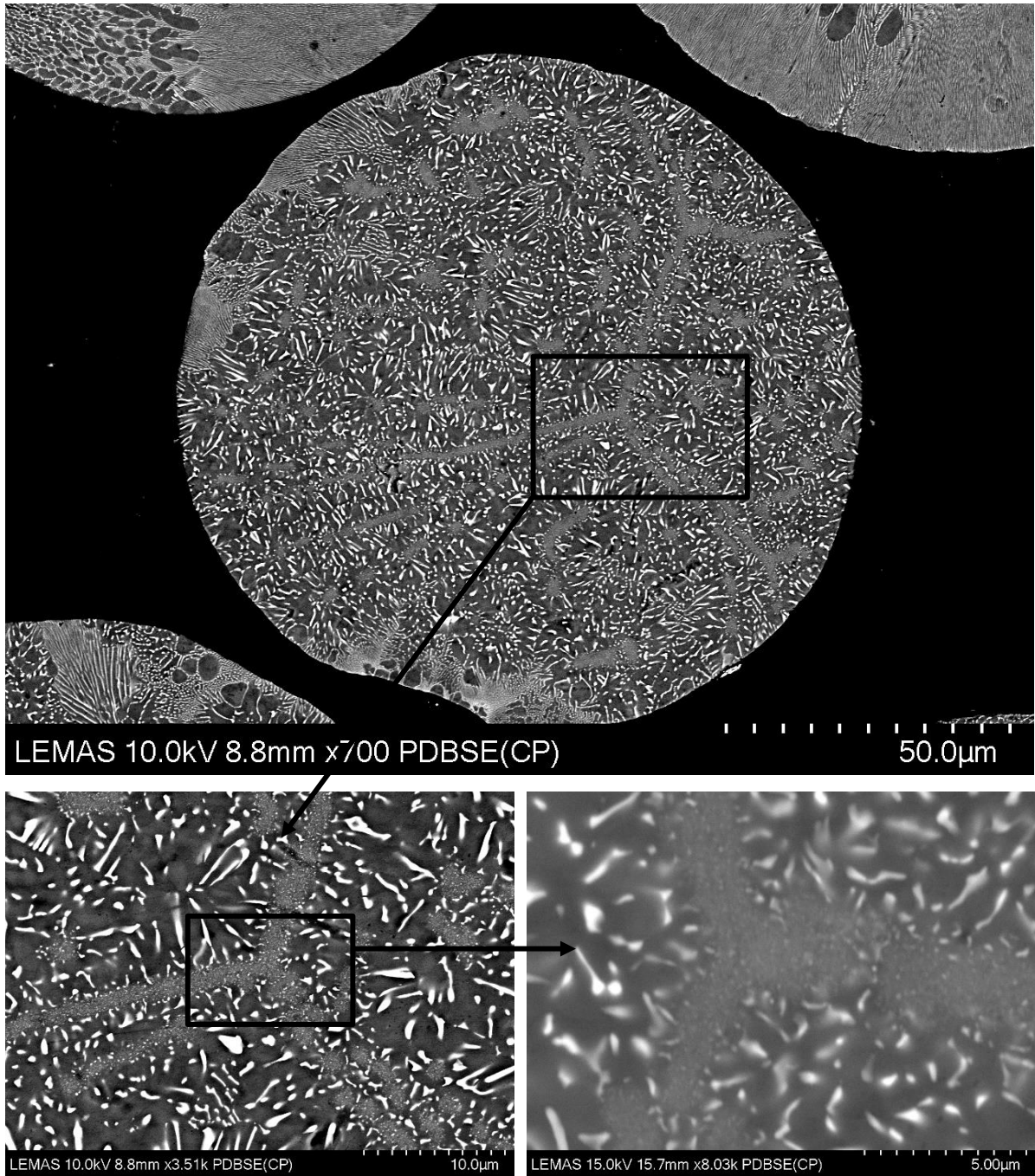
Figure 64: SEM BSE micrographs of 150-106 µm samples showing Y-shaped structure.
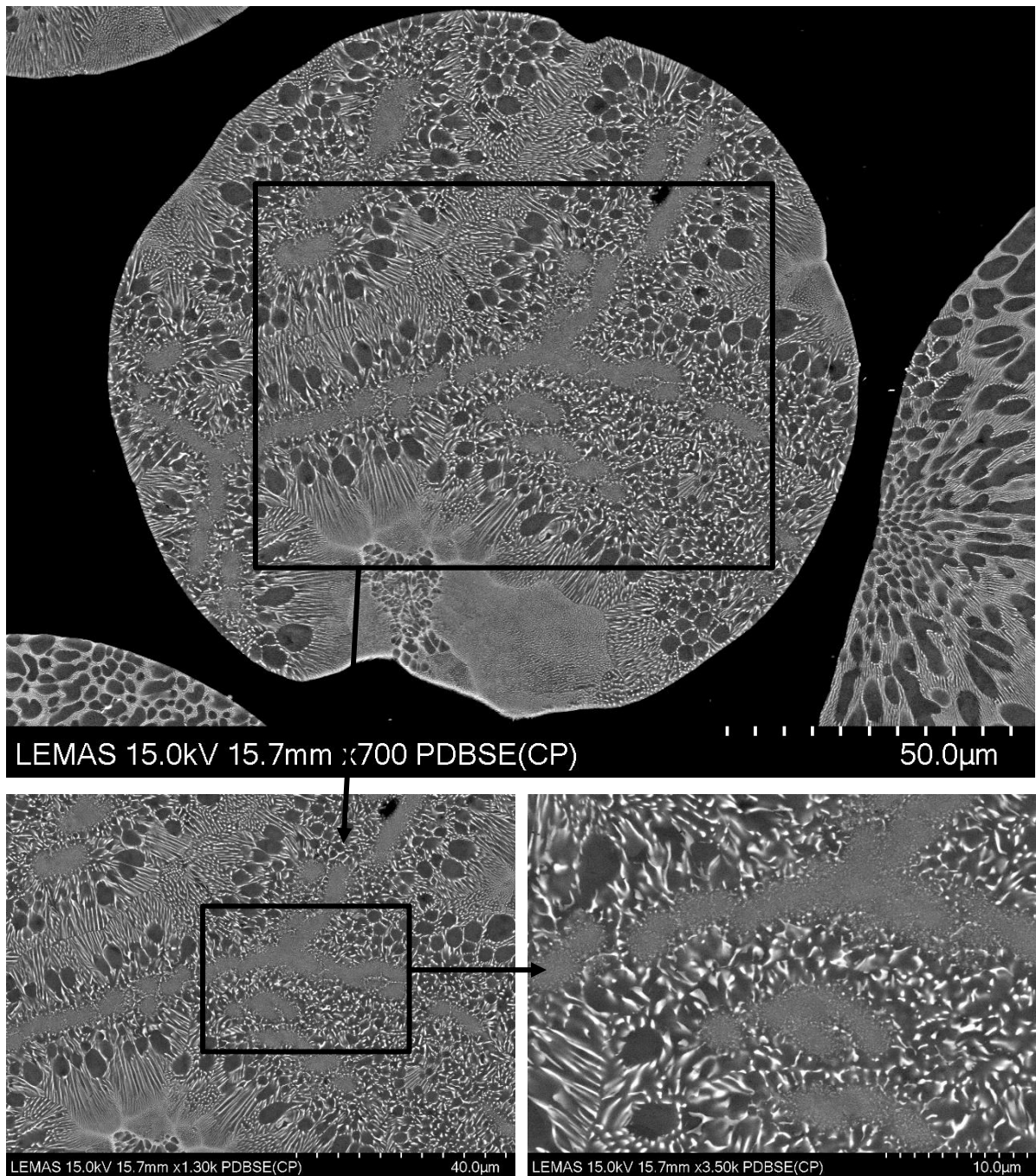
Figure 65: SEM BSE micrographs of 150-106 µm samples showing Y-shaped structure.
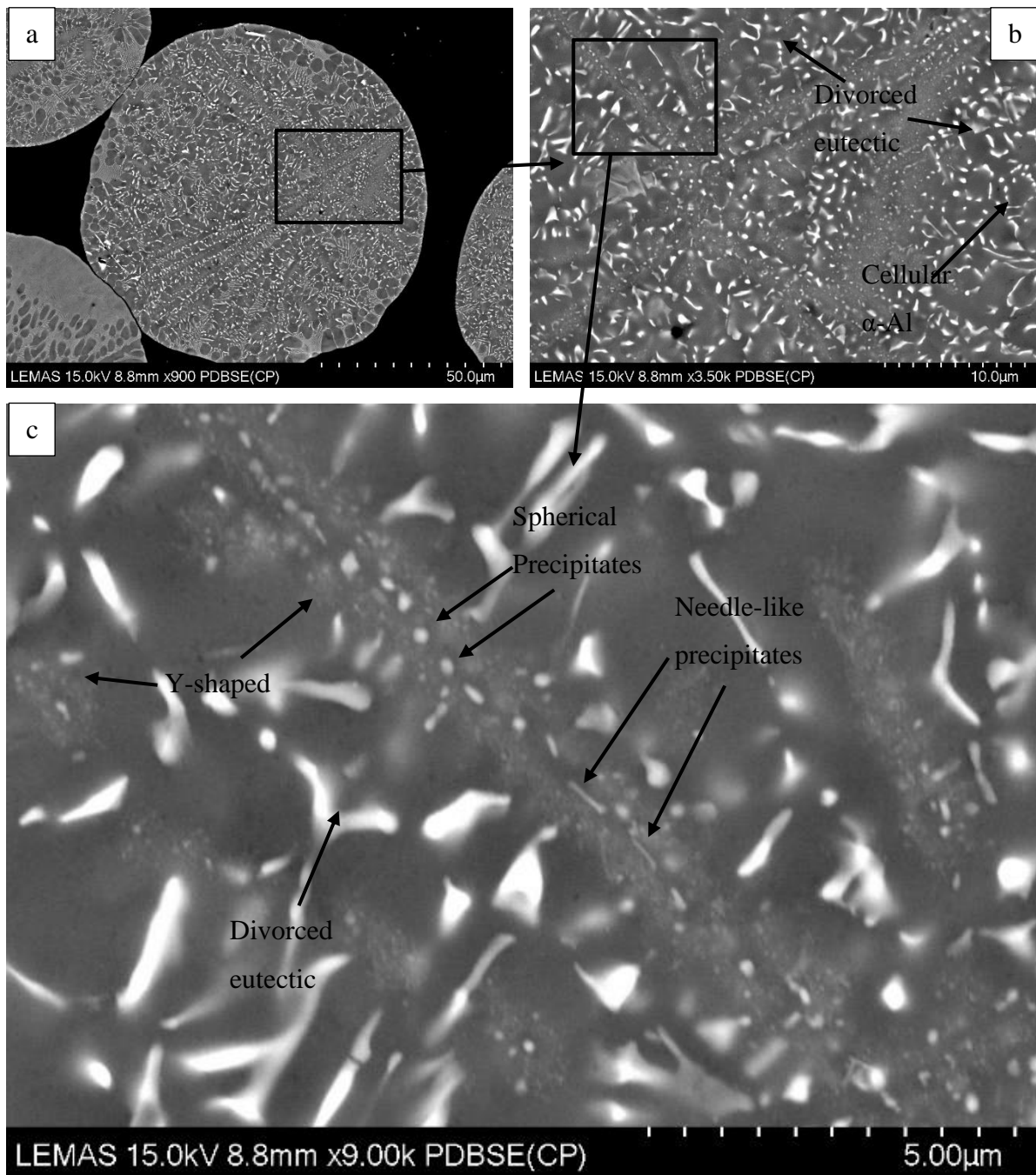
Figure 66: SEM micrographs of the 106-75 µm sample depicting featureless Y-shaped structure with spherical and needle-like precipitates formed in the centre of Y-shaped.
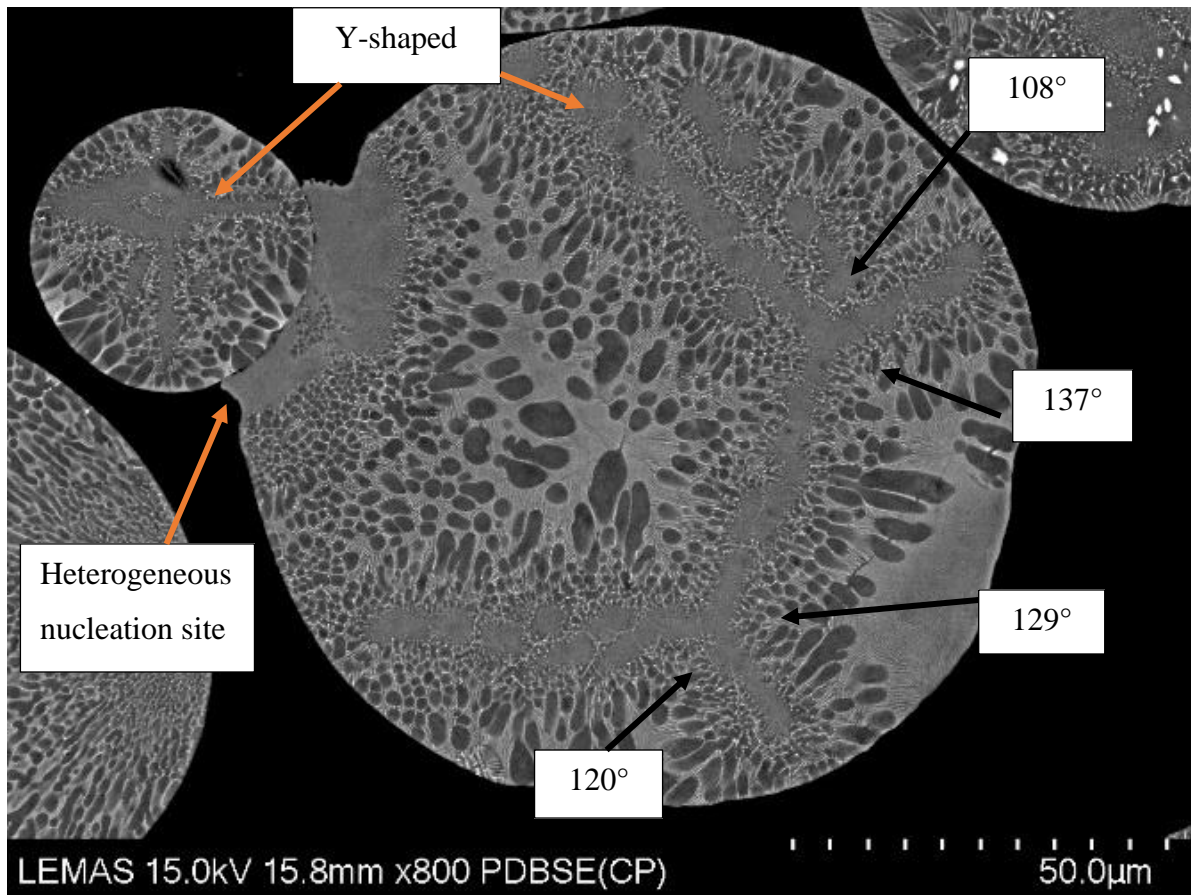
Figure 67: SEM micrograph of 106-75 sample with Y-shaped structure and a satellite with an average diameter of around 38 µm which acted as a heterogeneous nucleation site and formed fine structure in the large droplet.
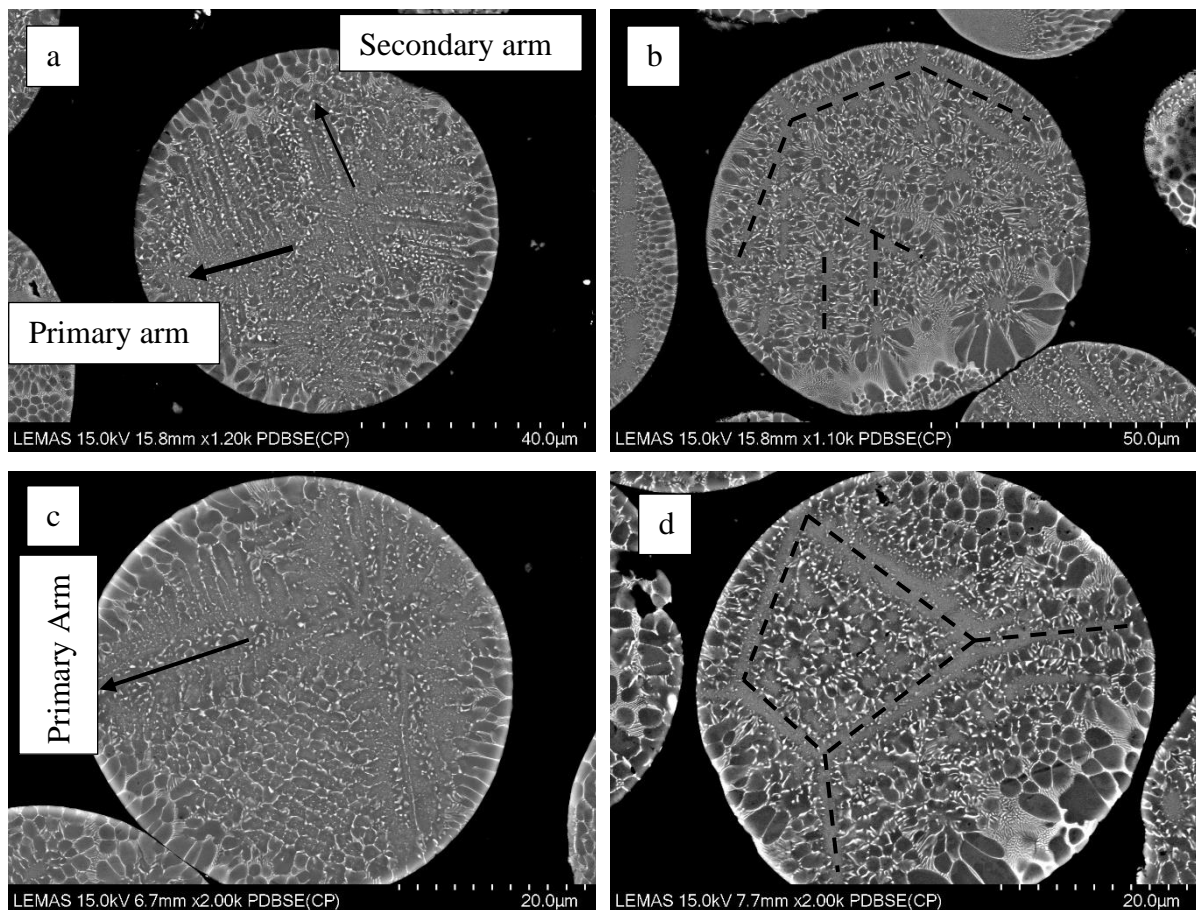
Figure 68: SEM micrographs of a) and b) 75-53 µm samples c) and d) 53-38 µm samples. While a) and c) depict dendrite-like Y-shaped morphology b) and d) show classical Y-shaped morphology.

5.3.4 3D Structure of Y-Shape: Serial Sectioning

As seen from the above figures (**Figure 62-68**) Y-shaped can adopt different types of microstructures from dendrite-like structures to closed shape structures. However, it is not clear whether these structures are internally connected or not in 3D. Thus, consecutive polishing and etching were performed on 150-106 µm sample to reveal the 3D structure of the Y-shaped phase with a total cumulative depth of 20.2 µm. The polishing depth was measured using a microhardness indent as explained in **Section 4.2.6.1**. The results are given in **Figure 69**. Firstly, it is clear from the figures that dendritic α-Al gets coarser away from Y-shaped for all cross sections. **Figure 69 a-g** shows simple Y-shaped structure. This later (**Figure 69h-k**) transitions in to a closed shape (kite shaped quadrilateral). This shows that a closed form can originate from a Y-shaped, which is related to the argument about the pentagon shown in **Figure 63b**. The angles between the arms of Y-shaped are given in the figure. The angles are 144 °, 96° and 120°. While the angle 144° does not change with the change in depth, other angles differ. Moreover, as show in the figure, it is impossible to get accurate volume fractions

103

of each morphology. For example, **Figure 69j** shows higher volume faction of dendritic α-Al compared to others.
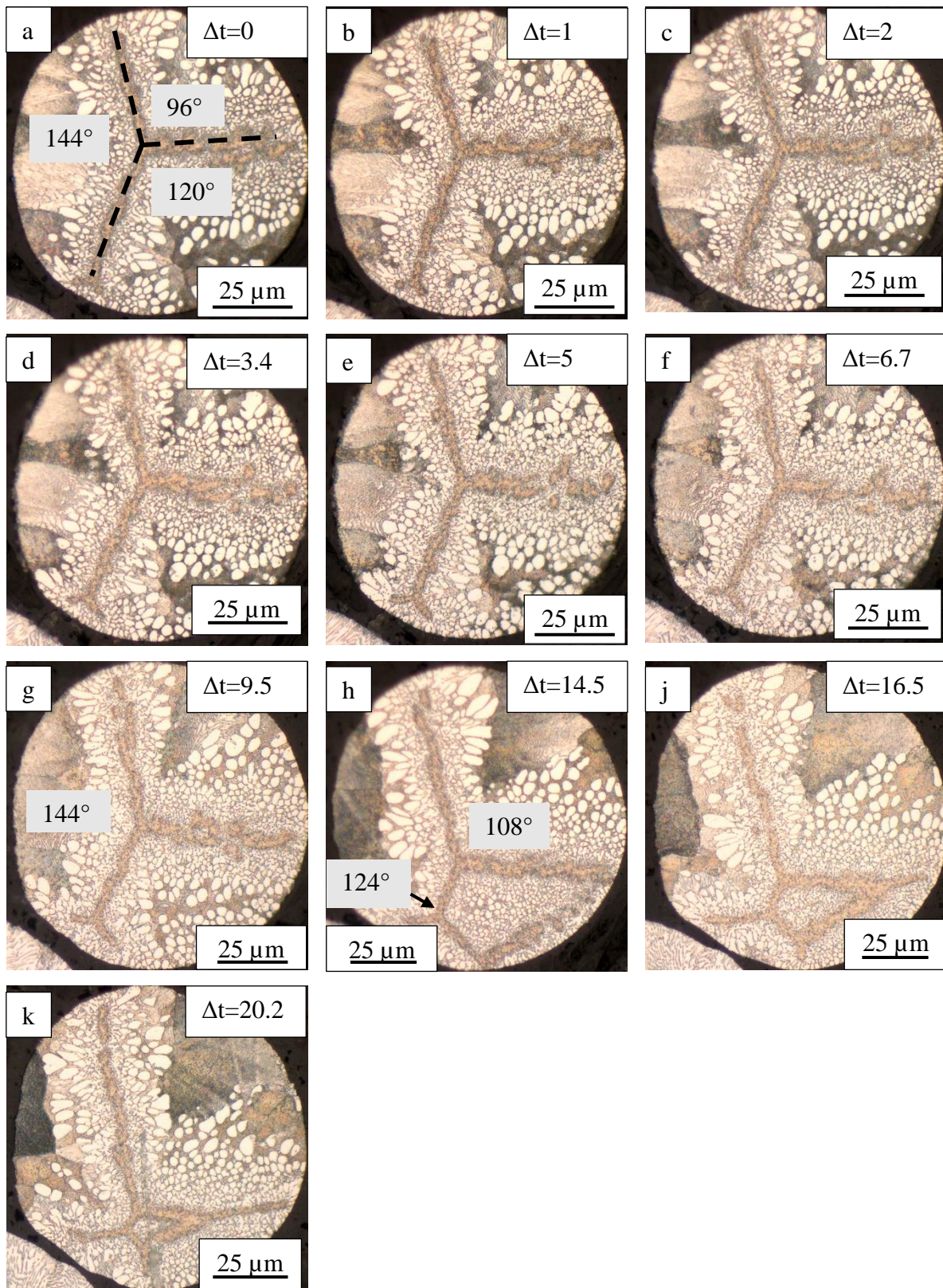
Figure 69: 3D structure of Y-shaped phase formed in 150-106 µm sample. Δt is the cumulative depth of the samples after polishing in µm.

5.3.5 Eutectic Spacing

Eutectic spacing of the lamellar eutectic was measured and the results are given in **Figure 70**. Eutectic spacing of 850+ µm sample was measured as 1.3 µm and this figure decreased with increasing cooling rate and measured 0.35 µm for 300-212 µm sample. However, further increase in the cooling rate resulted in a slight increase to 0.44 µm in 212-150 µm sample. It must be noted here that this size fraction (212-150 µm) is the one in which featureless Y-shaped structure started to emerge. Even the eutectic spacing for 150-106 µm sample was found to be higher than that of 300-212 µm. After slight increase eutectic spacing kept decreasing with decreasing powder size and increasing cooling rate. The smallest eutectic spacing was measured as 0.23 µm for 53-38 µm sample.
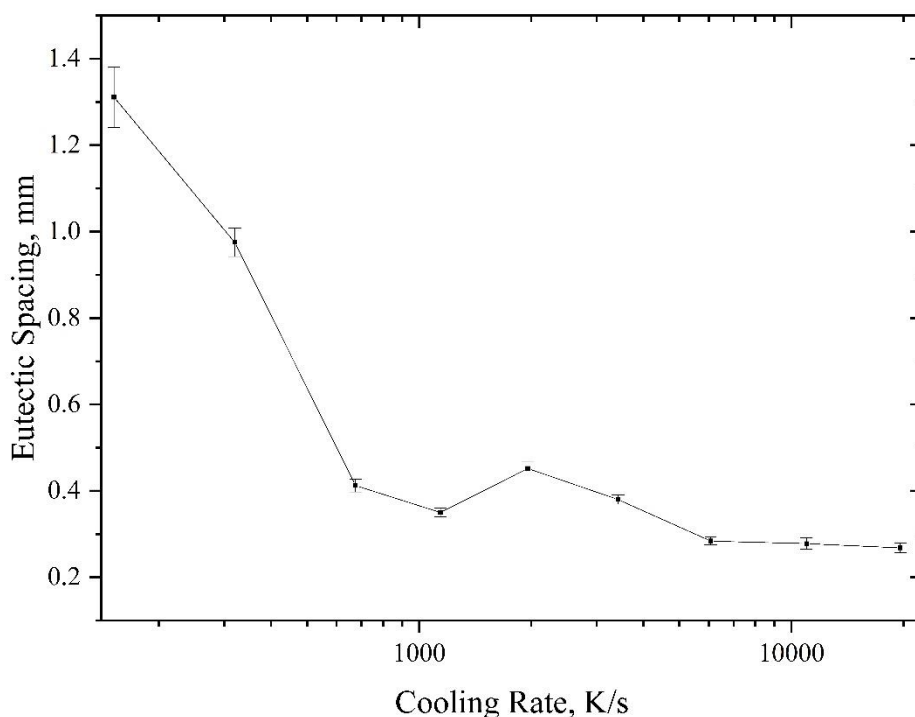
Figure 70: Eutectic spacing as a function of estimated cooling rate.

5.3.6 TEM Results

Two FIB cut samples from the Y-shaped regions of 106-75 µm and 53-38 µm as given in **Figure 71** and **Figure 72**, respectively, were further analysed under TEM in order to reveal the microstructure of this region and the results are given in **Figure 73** and **Figure 74**.

It was found that this region consists of very fine spherical and needle-like precipitates. The diameters of spherical precipitates range between 5 to 50 nm. The dimensions of the needle-

like precipitates are 5x50 nm. EDX mapping given in **Figure 73 b** and **c** show that these are iron rich precipitates. EDX measurements results are not given as the thickness of the precipitates is smaller than that of the TEM sample, thus, EDX results will not be accurate. **Figure 73d** shows the SAD pattern taken from **Figure 73a**. When analysing SAD pattern both d-spacings and the angles between the spot patterns are used as explained in **Section 4.2.4**. Ring pattern indicates the polycrystalline nature of the Y-shaped region. While the large bright spot pattern belongs to α-Al the weaker spot pattern shows the Al$_m$Fe from [0$\bar{1}$0] zone axis. SAD pattern in **Figure 73e** is also taken from Y-shaped region. Spot patterns on or close to the ring pattern belong to four strongest peaks of Al$_m$Fe [105] with very close d-spacings; namely [307], [330], [413] and [321]. As the Y-region is polycrystalline, the strongest peaks appear close to or on the ring pattern in SAD pattern.

As seen from **Figure 68**, Y-shaped adopted dendrite like morphology. However, morphology of this region is not clear from SEM figures. Thus, a FIB sectioned sample from the dendrite-like region of 53-38 µm sample was analysed under TEM. **Figure 74** shows that this region consists of very fine spherical and needle-like phases between which larger intermetallics are formed. Moreover, coarse precipitates surrounded by a band of Al free from any intermetallic as well as fine particles forming wavy bands can be seen. Therefore, it is clear that Y-shaped and dendrite-like morphology given in **Figure 68** are composed of the same material.
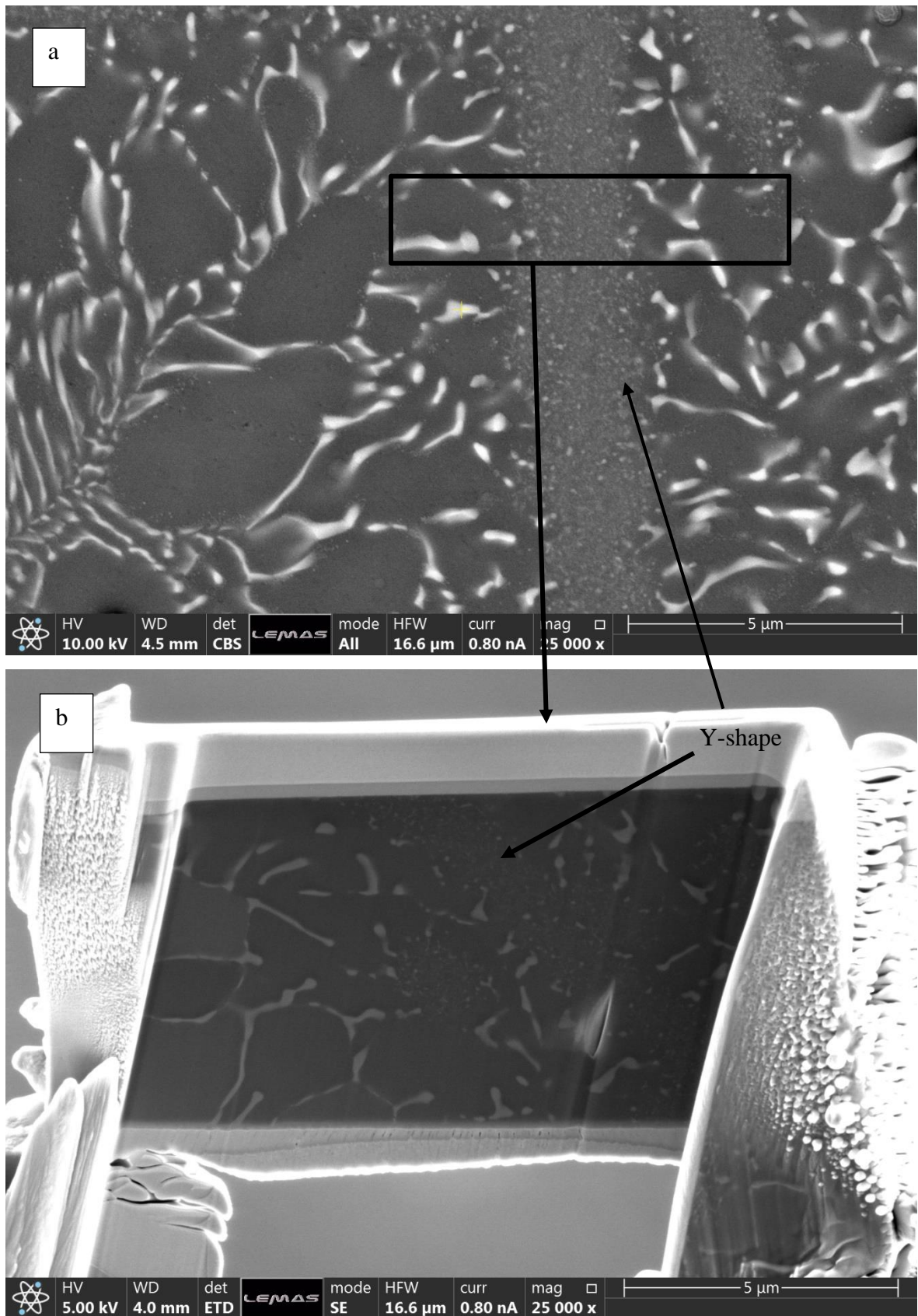
Figure 71: SEM micrograph of 106-75 µm sample showing a) where the TEM sample was taken and b) TEM sample after FIB sectioning
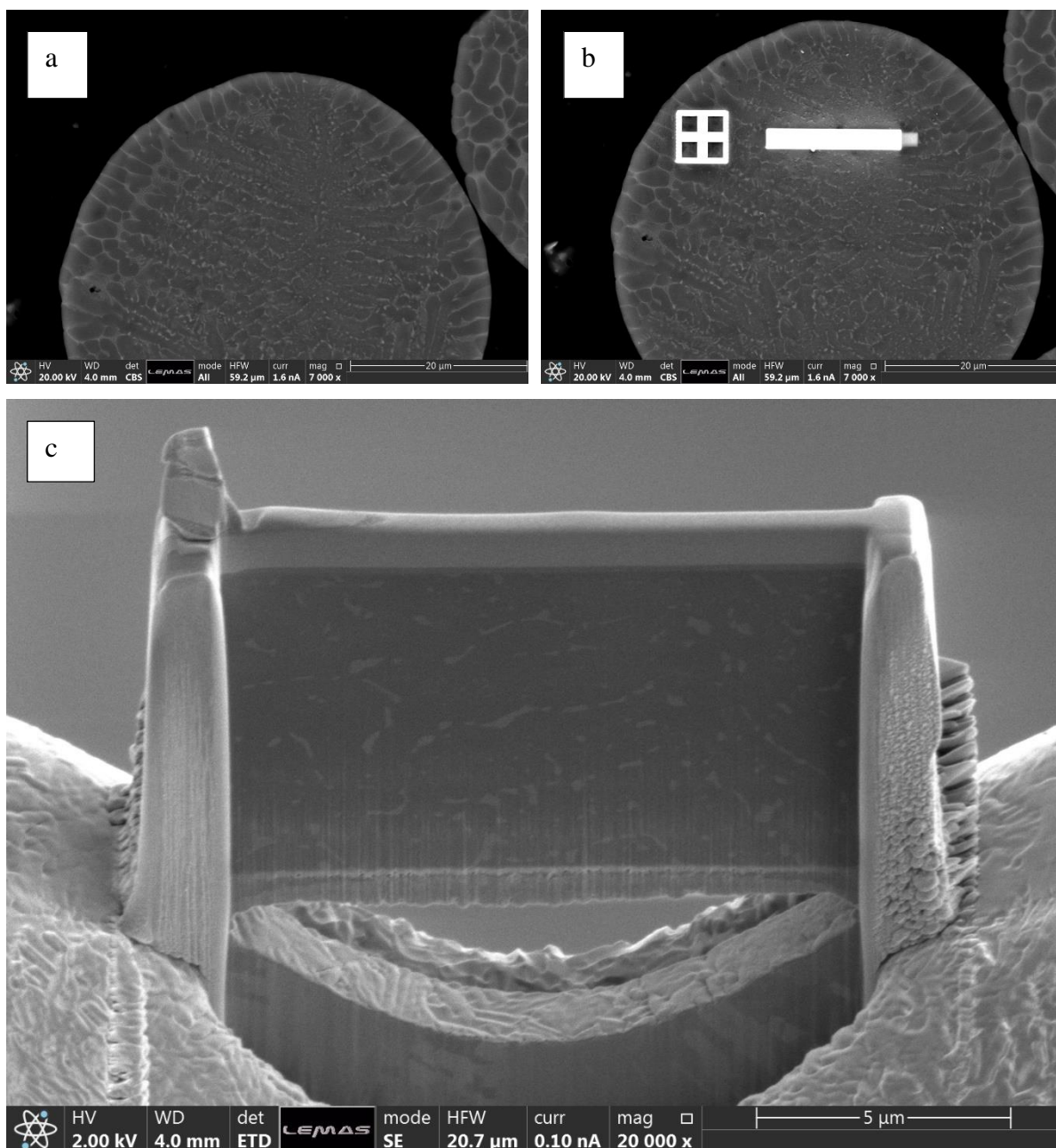
Figure 72: SEM micrograph of 53-38 µm sample showing a) the sample with dendrite-like Y-shape b) where the TEM sample was taken and c) FIB SEM sectioned TEM sample.
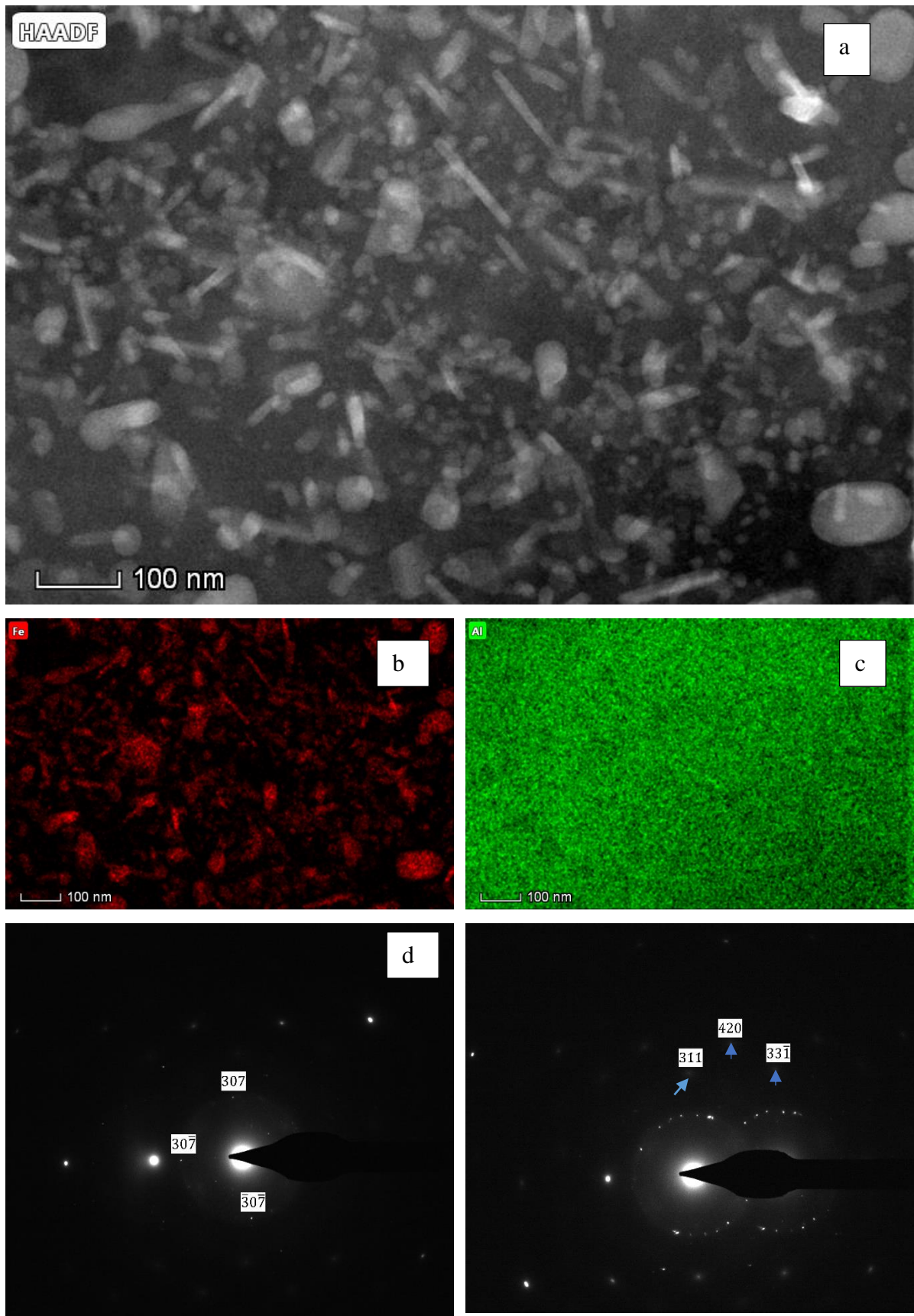
Figure 73: a) TEM micrograph of Y-shaped region showing nanosized spherical and needle-like precipitates, b) and c) EDX mapping of the region showing Fe and Al, respectively, d) SAD pattern taken from Y-shaped region showing Al_mFe taken from $[0\bar{1}0]$ zone axis e) SAD

pattern taken from Y-shaped region spot patterns on the ring pattern corresponds to four strongest peaks of Al_mFe while the labelled patterns (shown with arrows) belong to α-Al.
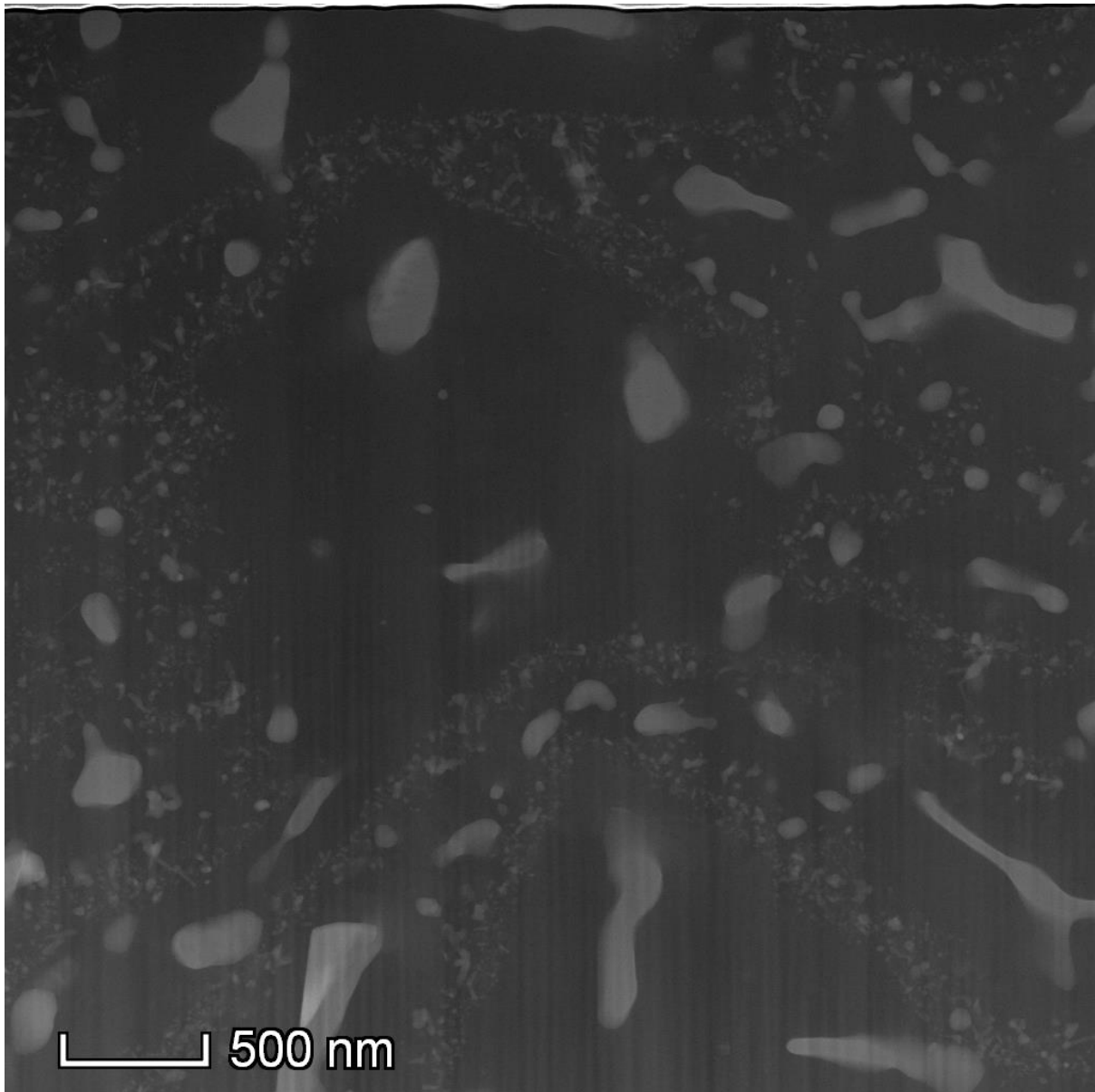
Figure 74: TEM micrograph taken from dendrite-like Y-shaped region of 53-38 µm sample.

5.3.7 Microhardness

In order to understand the effect of the non-equilibrium solidification on the mechanical properties of the alloy, Vickers microhardness measurement were employed on all sample fractions with a standard indenter using 10 g load and 10 s dwell time. 10 measurements were performed for each sample fraction and the results are given in **Figure 75**. Overall, the microhardness of the alloy is gradually increasing with increasing cooling rate. The minimum microhardness was observed in the slowest cooled sample (850+ µm) as 50 $HV_{0.01}$ and this value rise and reached a maximum of 83 $HV_{0.01}$ in 53-38 µm sample. The total increase in the

microhardness of the alloy is around 60%. This increase in likely due to the competition between increasing supersaturation and scale refinement, both of which will tend to increase the microhardness. It must be noted here that the microhardness value for 300-212 µm samples is slightly lower than 500-300 µm samples. This slight decrease happens one sieve size before the onset of Y-shaped crystal growth, where eutectic spacing starts to increase.

Similar increase in microhardness with increasing cooling rate was given in **Figure 57**, microhardness for Al-2.85 wt% Fe alloy. It must be noted here that the sieve fraction for Al-3.9 wt% alloy ranges between 850+ µm and 38 µm, while the sieve fraction for Al-2.85 wt% Fe ranges between 850-53 µm. Comparing the same sieve fractions (850-53 µm) for both alloys, Al-3.9 wt% Fe alloy has shown slightly higher microhardness ranging between 55 $HV_{0.01}$ and 73 $HV_{0.01}$ than the microhardness Al-2.85 wt% Fe which range between 53 $HV_{0.01}$ and 66 $HV_{0.01}$. As the estimated cooling rate for these sieve fractions has estimated to be same, the difference in the microhardness is due to the increase in Fe content. Higher Fe content has provided the formation of more intermetallics which in turn has improved the microhardness.
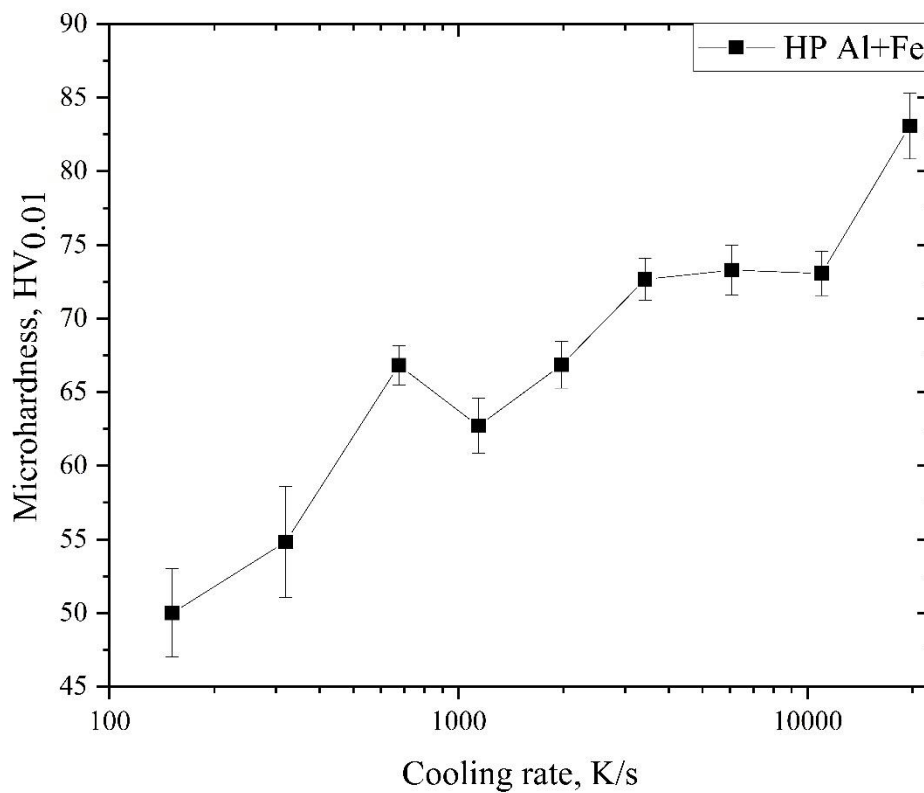
Figure 75: Microhardness value (in $HV_{0.01}$) as a function of cooling rate.

5.4 Results for Al-4.1 wt% Fe-1.9 wt% Si

5.4.1   Phase Analysis and Microstructure of Al-4.1 wt% Fe-1.9 wt% Si Master Alloy

The Al-4.1 wt% Fe-1.9 wt% Si master alloy was prepared using an arc-melting furnace as explained in **Section 4.1.3**. The master alloy was investigated using XRD, OM and SEM before drop tube atomization in order to confirm the homogeneity of the alloy. XRD results of the master alloy is given in **Figure 76**. XRD results suggest that the phases present in the master alloy are α-Al and Al_8Fe_2Si. That is the only intermetallic formed in the sample is the ternary Al_8Fe_2Si. OM and SEM images of the master alloy are provided in **Figure 77** and **78**, respectively. **Figure 77** shows that the microstructure of the master alloys is sea-weed eutectic formed on α-Al matrix. This sea-weed eutectic is surrounded by coarse script-like intermetallic which adopted various sizes and shapes (**Figure 77c**). The sample was further investigated under SEM. **Figure 78** shows that the microstructure consists of eutectic colonies. Each eutectic colony has rod-like eutectic at the centre and this rod-like eutectic is surrounded by coarse script-like intermetallic (**Figure 78b**). SEM also used to get EDX measurements from both coarse script-like intermetallic (**Figure 78c**) and α-Al matrix. However, EDX measurement was not performed on rod-like eutectic as this eutectic is so fine that it is impossible to get an accurate result. The composition of the α-Al matric was found as 0.7 to 0.8 wt% Si and 0.2- 0.3 wt% Fe. It must be noted here that although both Fe and Si have very low solubility in Al, furnace cooling has resulted in the extension of solid solubility of both Fe and Si. EDX results from script-like intermetallic (**Figure 78b**) have shown that the average composition of script intermetallic is 72 at% Al, 9.2 at% Si and 18.59 at% Fe, which corresponds to the ternary Al_8Fe_2Si phase. This is in good agreement with XRD result shown in **Figure 76**. Moreover, according to XRD result given in **Figure 76** the only intermetallic present in the sample is the ternary Al_8Fe_2Si phase. That is, the rod-like eutectic is also Al-Al_8Fe_2Si (further TEM analysis of rod-like eutectic is provided in **Section 5.4.5**).
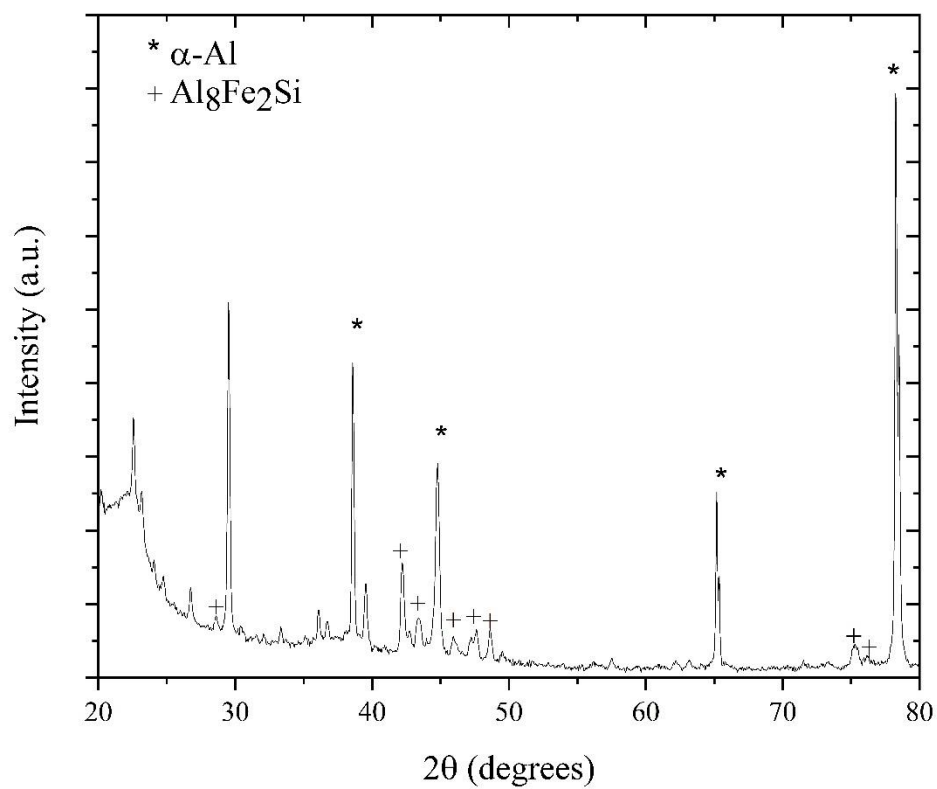
Figure 76: XRD results of the master alloy (unlabelled peaks belong to the mounting media, Bakelite).
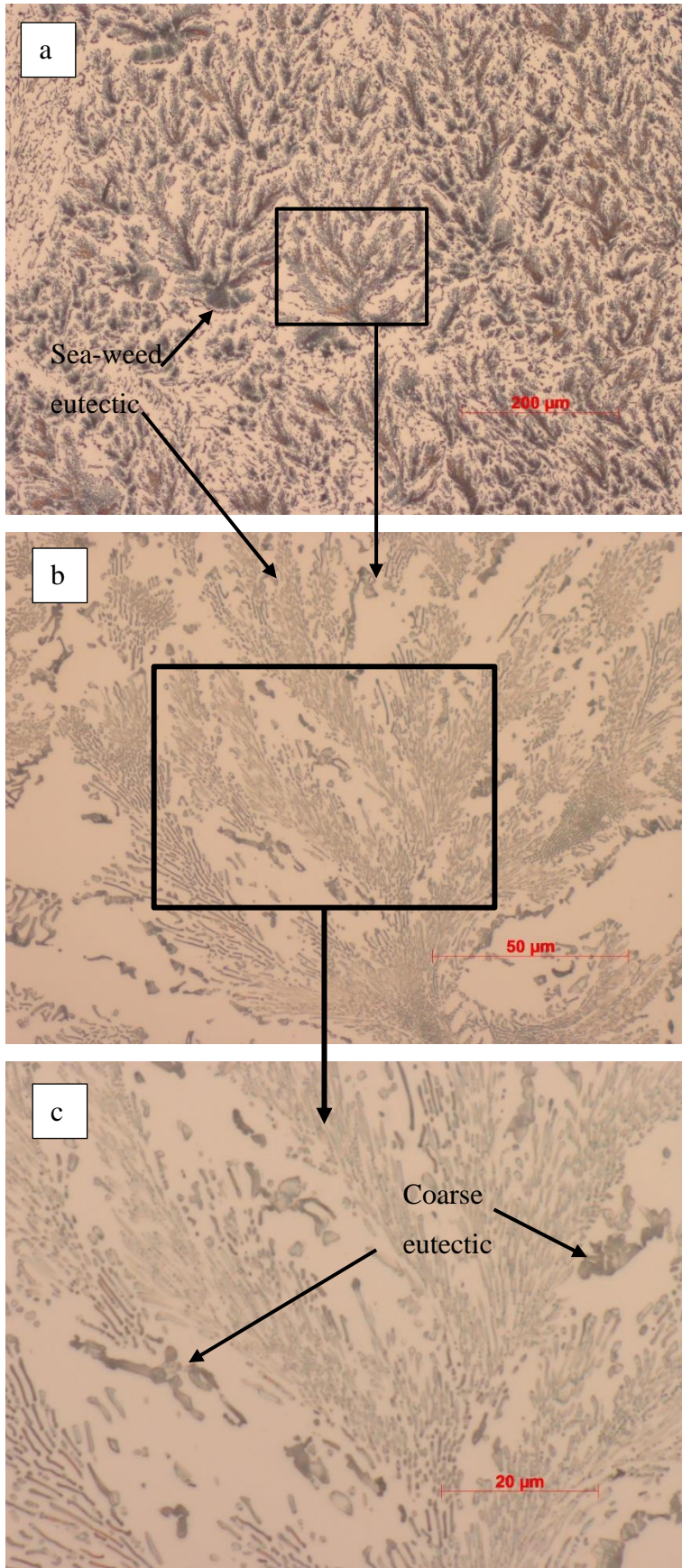
Figure 77: OM micrographs of Al-4.1 wt% Fe- 1.9 wt% Si master alloy at different magnifications showing sea-weed eutectic surrounded by coarse script-like eutectic.
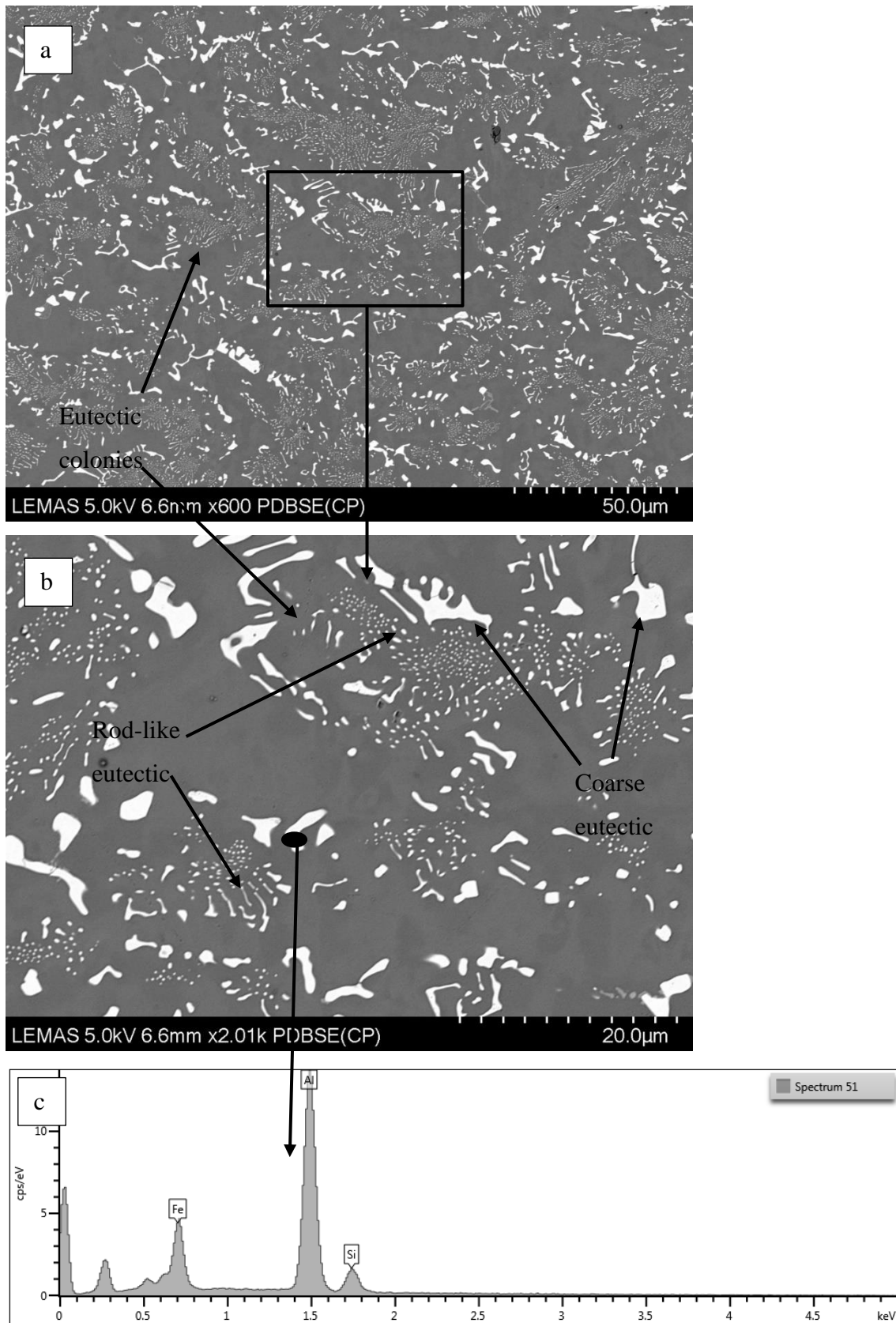
Figure 78: a) and b) SEM micrographs of the master alloy showing eutectic colonies with rod-like eutectic at the centre and surrounded by coarse eutectic, c) an example of EDX analysis taken from coarse intermetallic.

5.4.2　XRD Results of Drop Tube Atomized Al-4.1 wt%Fe-1.9 wt%Si

XRD results for some selected drop tube atomized samples: 500-300 µm, 212-150 µm and 106-75 µm (XRD graphs of the remaining sieve fractions are provided in **Appendix B**), are given in **Figure 79**. The only intermetallic found to be present in all samples is the ternary Al_8Fe_2Si phase. In other words, regardless of the cooling rates the samples experience the only intermetallic phase is Al_8Fe_2Si. However, as shown with two black arrows in **Figure 79**, there are 2 peaks close to 2θ values of 30° which were not identified using HighScore. Although, some of the peaks of the binary Al-Fe phases Al_6Fe and Al_mFe match with these two peaks, the highest intensity peaks of these binary Al-Fe phases do not match with the other peaks in the **Figure 79**.
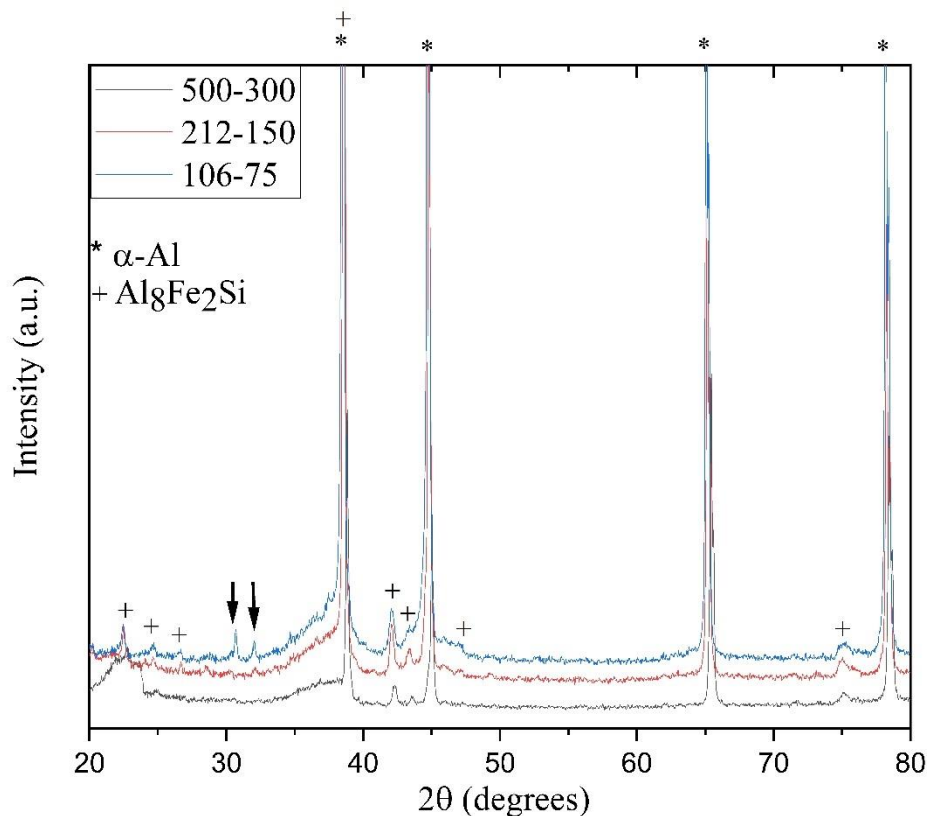
Figure 79: XRD results of some selected sieve fractions: 500-300 µm, 212-150 µm and 106-75 µm.

5.4.3　Microstructural Characterization and Phase Analysis

The Al-4.1 wt% Fe-1.9 wt% Si master alloy has been subjected to drop tube atomization and samples with diameters ranging between 850-53 µm were produced. The microstructures of

the samples were examined using OM and SEM. Various microstructures have been observed with decreasing powder size.

The microstructures of the large sieve fractions (850-500 µm and 500-300 µm) are given in **Figure 80**. As seen from the figure, these large samples have two distinct regions: microcellular region and dendritic region. Microcellular region is where the nucleation was initiated and later transformed into dendritic α-Al. As compared to the master alloy, the slowest cooling rate in drop tube has resulted in a change in the microstructure from pure eutectic to dendritic with interdednritic eutectic. Lamellar eutectic has formed between both regions. This can be clearly seen in **Figure 82**, which shows the same morphology of interdendritic eutectic at higher magnification taken from 300-212 µm sample. As seen from the **Figure 80**, the microstructure is mostly dendritic α-Al. This means that the first phase to form in the drop tube sample is α-Al. Moreover, dendrite tip splitting has widely been observed in all drop tube atomized samples. This can be seen as labelled in **Figure 80**.

These microcellular and dendritic microstructures have also been observed in 300-212 µm samples as shown in **Figure 81a**. Although most powders in 300-212 µm sieve fractions have similar structures to large sieve fractions, some samples have shown different microstructures (**Figure 81b** and **c**). This change in the microstructure has started in 300-212 µm samples and the number of samples with such structures has increased with decreasing sample size and, therefore, increasing cooling rate. This is shown in low magnification OM image of 150-106 µm sieve fraction given in **Figure 83a**, which depicts that around half of the samples with such region. **Figure 78b** and **c** show the microstructure of 300-212 µm samples with the presence of very fine region. This fine region appears to be brownish yellow (similar to Y-shaped structures) under OM in samples with such region. As this region is very fine and dendritic α-Al grows out of this region, this region is most likely where the nucleation initiated in the droplet. The solidification has proceeded with the formation of microcellular region and, later, dendritic region as shown in **Figure 82**. As seen from **Figure 81c**, the nucleation initiation is angular (probably cube-like in 3D) rather than circular (spherical in 3D). In most samples with such zones, the morphology of such regions has been found to be similar. Therefore, this region will be referred as angular structure or angular nucleation zone for simplicity. In some samples (**Figure 83b-d** and **Figure 84c**) have shown multiple angular nucleation zone with boundaries separated by growing dendrites.

SEM micrographs given in **Figure 82** and **Figure 84** shows a sample with an angular nucleation zone. The microstructure of this region is so fine (this was later confirmed using TEM) that it is impossible to resolve the microstructure using SEM (**Figure 84b**). Moreover, the interdendritic eutectic is lamellar. EDX analysis has also been employed to analyse the composition of the angular zone for all sieve fractions. Regardless of the sample size and, therefore, cooling rate, the composition of this region has been found to be containing 4 ± 0.1 wt% Fe and 1 ± 0.15 wt% Si. It must be noted here that Fe content of this angular zone was measured to be identical to the composition of the master alloy (also the melt), while Si content is lower than the melt. Moreover, as also shown in large samples, dendrite tip splitting has widely been observed in this sample size.

In addition to above discussed microstructures, a number of different microstructures has been observed in samples with d < 106 µm. These structures are given in **Figure 85** and **86**. **Figure 85** shows propeller-like structures with three or four arms each arm of which has different length. **Figure 85a** and **b** show 4-armed propeller-like structures radiating from its nucleation point with a right angle between adjacent arms. **Figure 85a** shows presumably an earlier stage of the growth of propeller-like structure where the arms of the propellers are shorter compared to that of in **Figure 85b,** whose longest arm has reached the length of almost half of the diameter of the sample. The longest arm is the one which grows towards the centre of the droplet as there is no hindrance in that direction: the growth of the other arms being stopped as they reached the surface of the droplet. Furthermore, **Figure 85c** and **d** show propeller structures with three arms. Other difference between 3-armed and 4-armed propeller-like structures is that while 3-armed propeller-like structures have a circular central hub (**Figure 86b**) unlike 4-armed ones. Moreover, the angle between each adjacent arms in 3-armed propels is around 120°. Cellular α-Al has formed around these propeller-like structures and later transformed in to dendritic α-Al.

Y-shaped structures have also been observed in the small sieve fractions (106-75 µm and 75-53 µm). **Figure 87** shows three different Y-shaped structures found in 75-53 µm samples forming close shape (**Figure 87a**) and dendrite-like (**Figure 87c**) structures. These Y-shaped structures looks similar to the ones observed in drop tube atomized Al-3.9 wt% Fe alloy (see **Section 5.3.3**). However, the arms of the Y-shaped given in Figure 85 is thicker than the ones observed in Al-3.9 wt% Fe alloy. OM images of Y-shaped observed in 106-75 µm and 75-53 µm samples are given in **Figure 88**. It is clear from the figure that these Y-shaped structures have identical colour, gold/brown, to Y-shaped observed in Al-3.9 wt% Fe alloy (**Section**

5.3.3). Furthermore, angular structure as well as Y-shaped share the same colour as shown in **Figure 88b**.
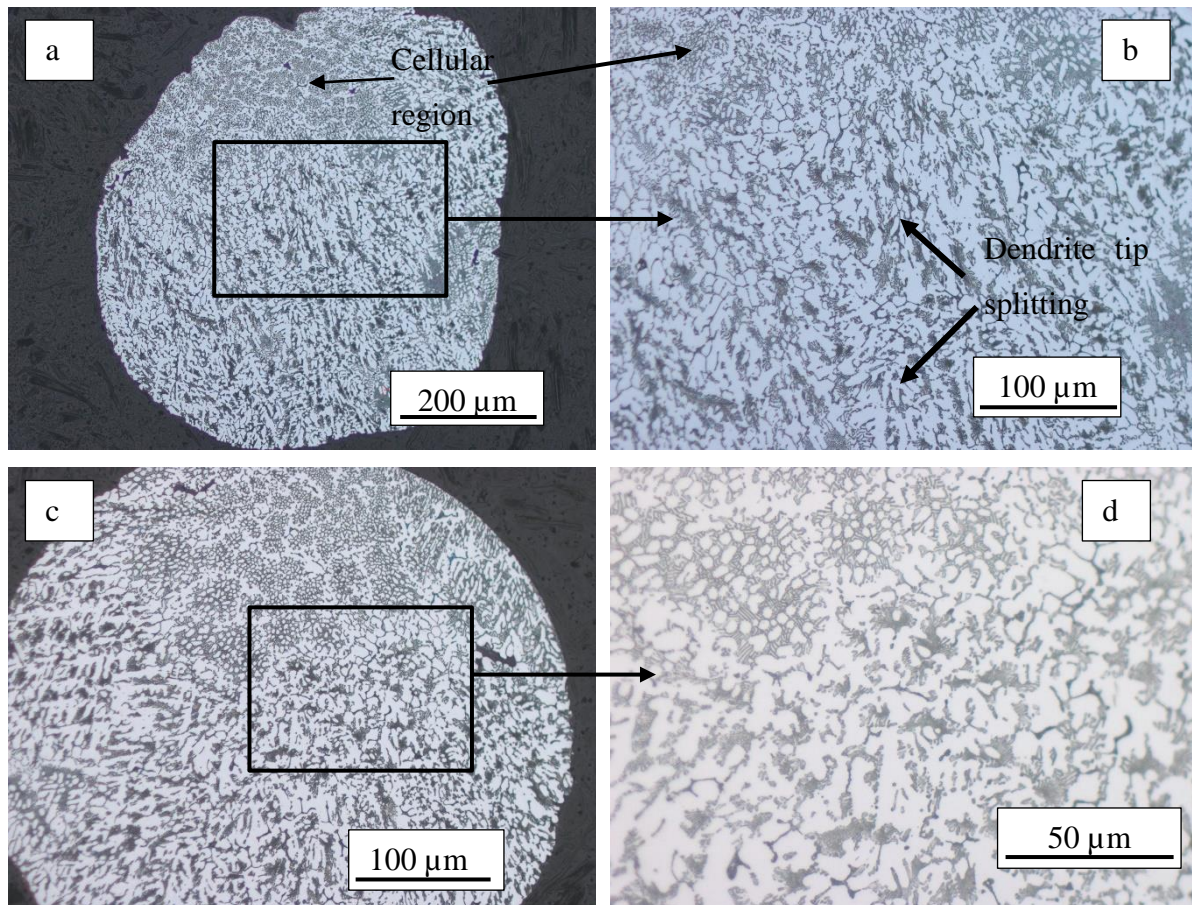
Figure 80: OM images showing two distinct regions: microcellular and dendritic regions formed in a) and b) 850-500 µm and c) and d) 500-300 µm samples.
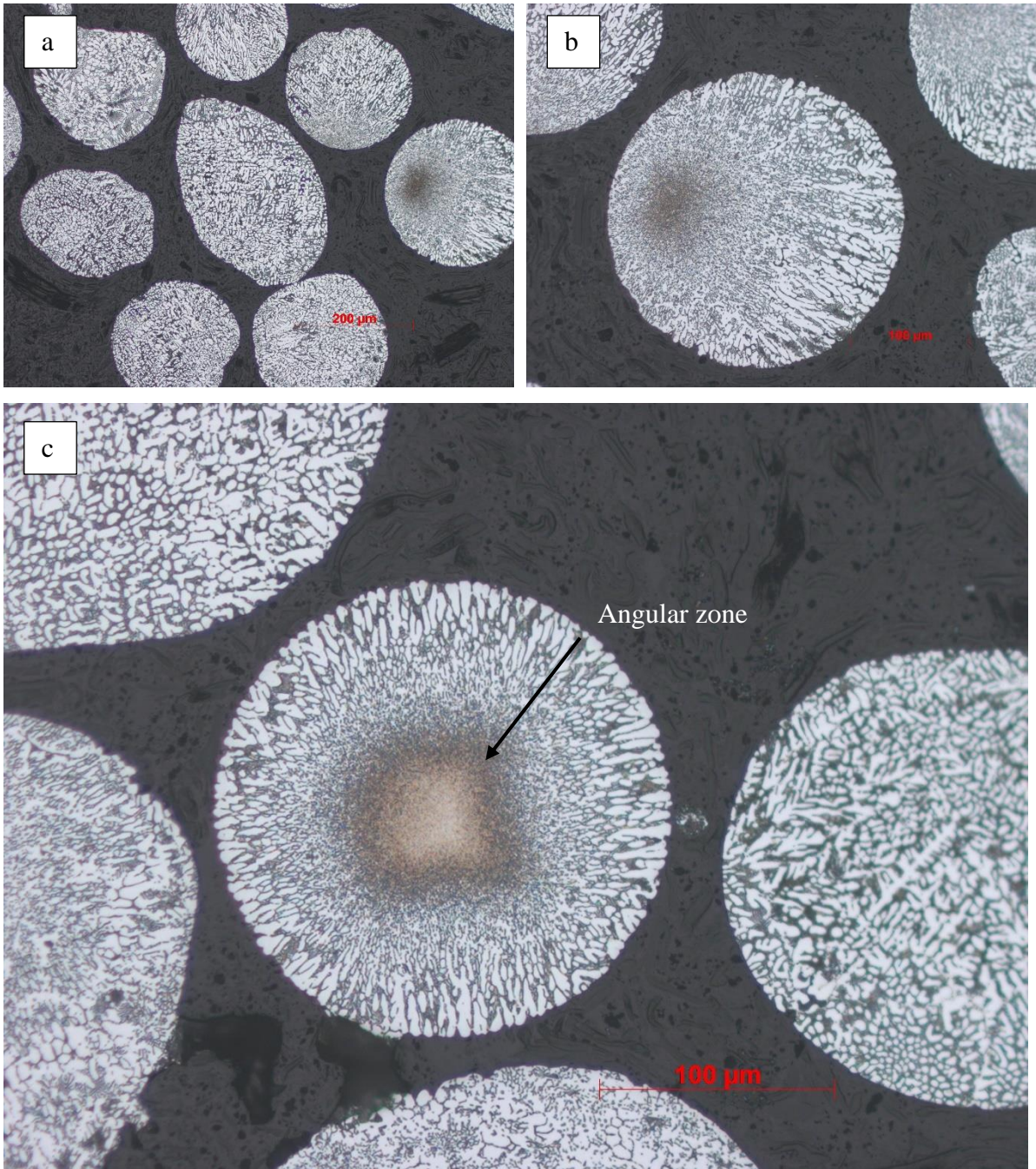
Figure 81: OM images of 300-212 µm samples showing a) two region microstructures and b) and c) angular nucleation zone structure.
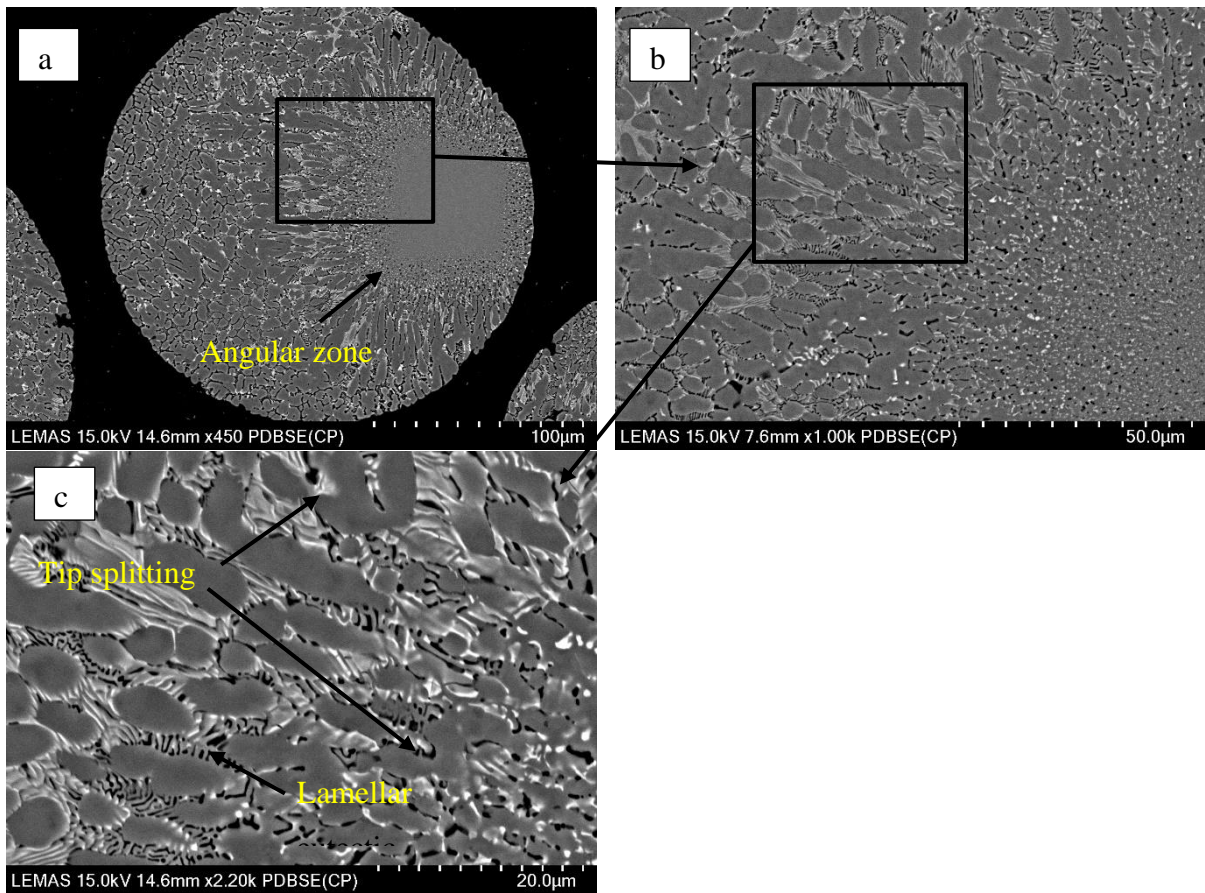
Figure 82: SEM micrographs of 300-212 µm sample depicting a) and b) the formation of very fine angular nucleation zone and c) lamellar interdendritic eutectic.
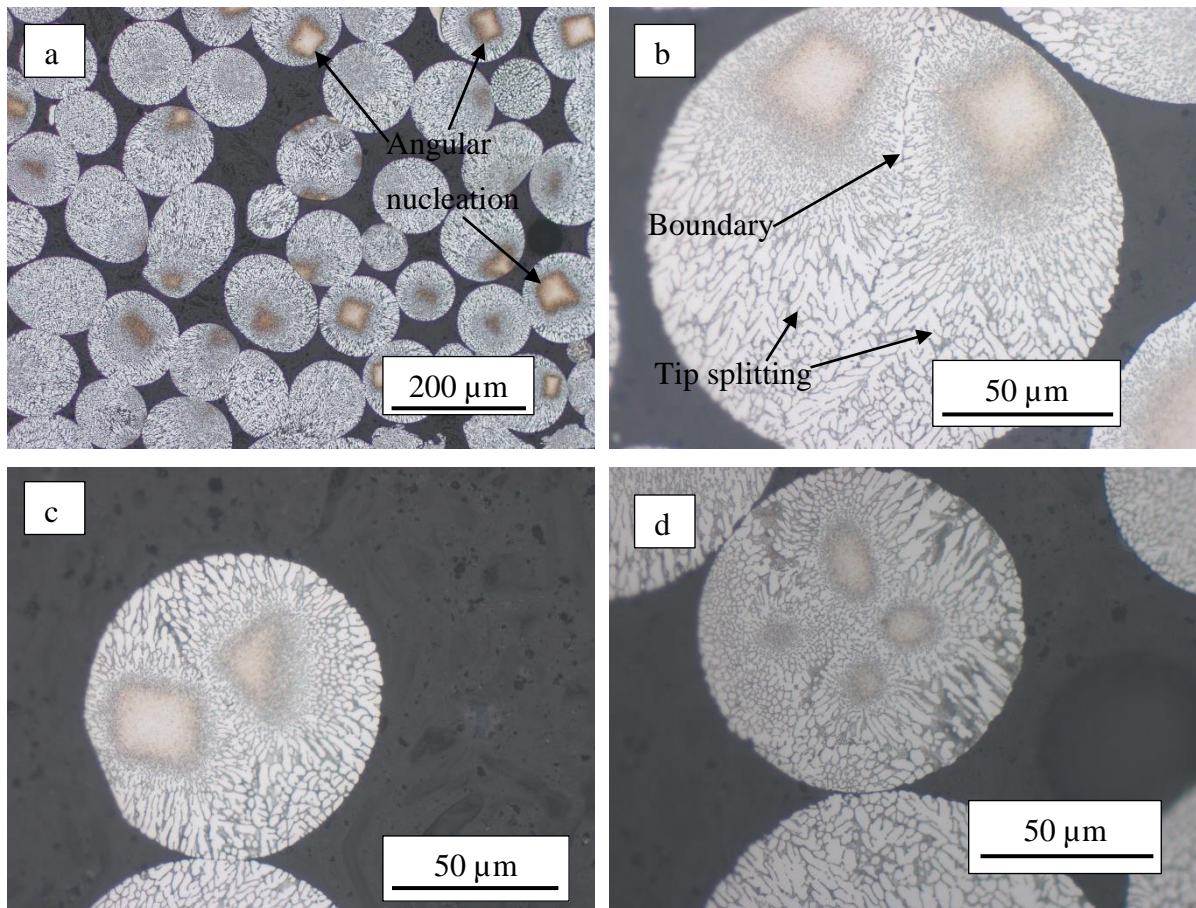
Figure 83: OM images of 150-106 samples showing a) general view of 150-106 µm samples with around half having angular nucleation zone (brown regions), b) and c) multiple angular nucleation zones and d) angular nucleation zone from different cross section.
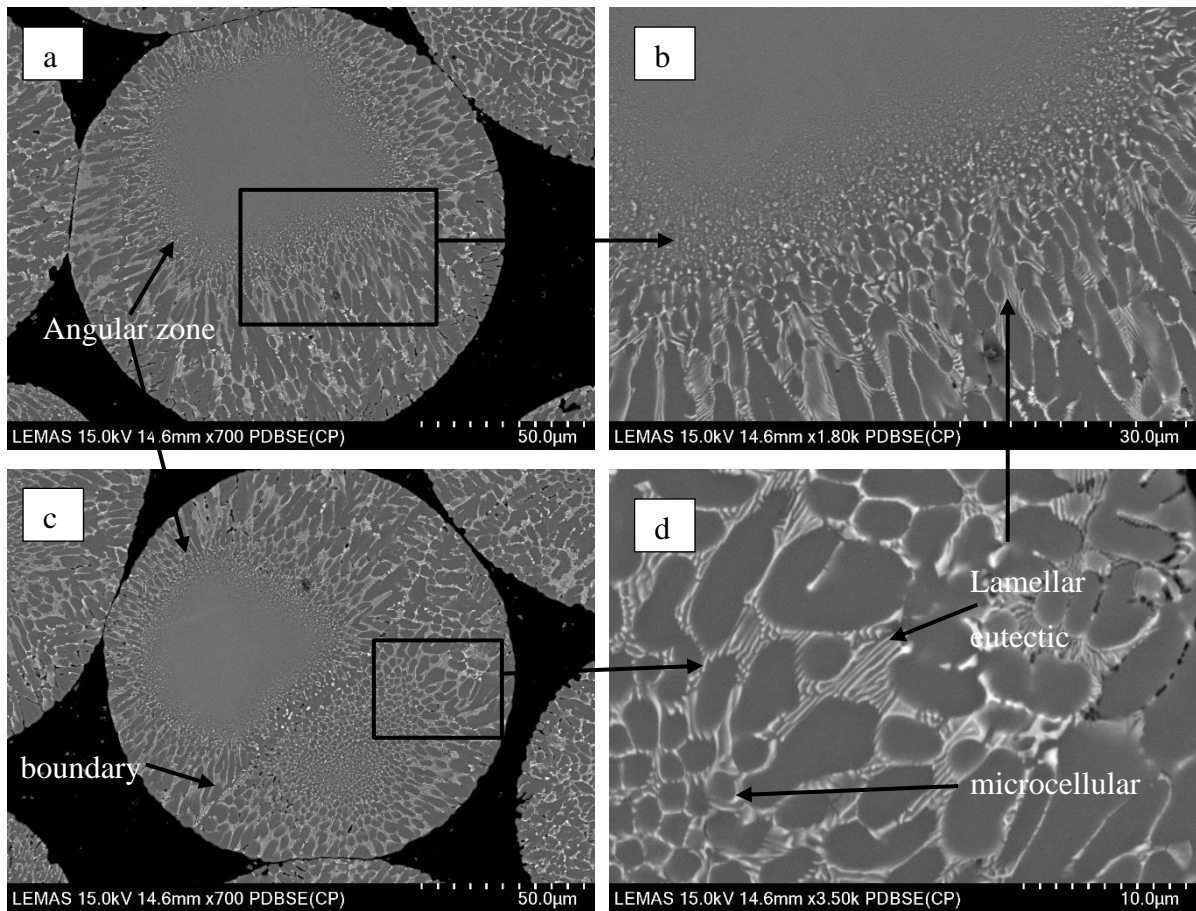
Figure 84: SEM micrographs of 150-106 µm samples showing a) and b) single nucleation zone c) multiple nucleation zone and d) magnified image of c) depicting transition from cellular to dendritic with lamellar eutectic.
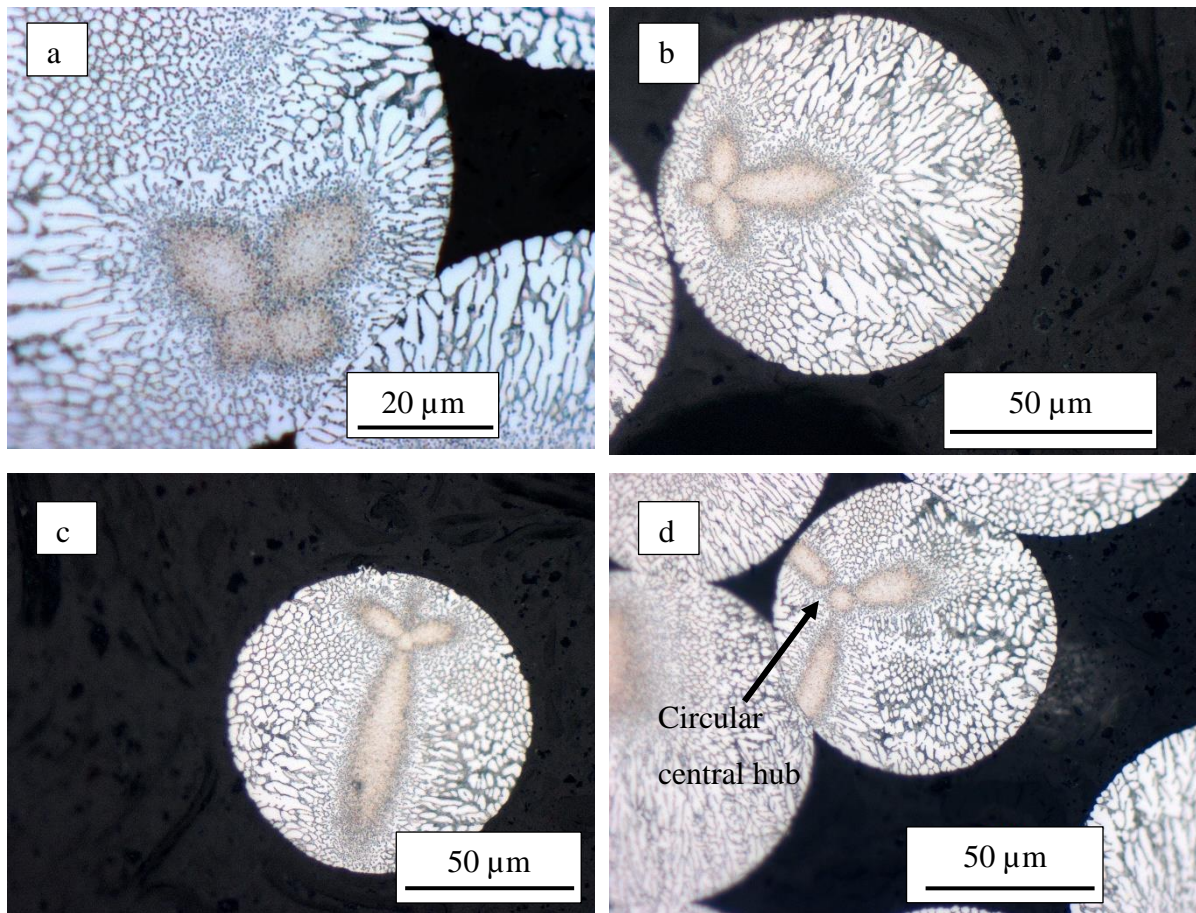
Figure 85: Propeller-like structures observed in 106-75 µm sieve fractions a) early sage of propeller growth, b) one arm has grown larger than others c) one arm has reached the circumference and d) 3-armed propeller growth with circular centre.
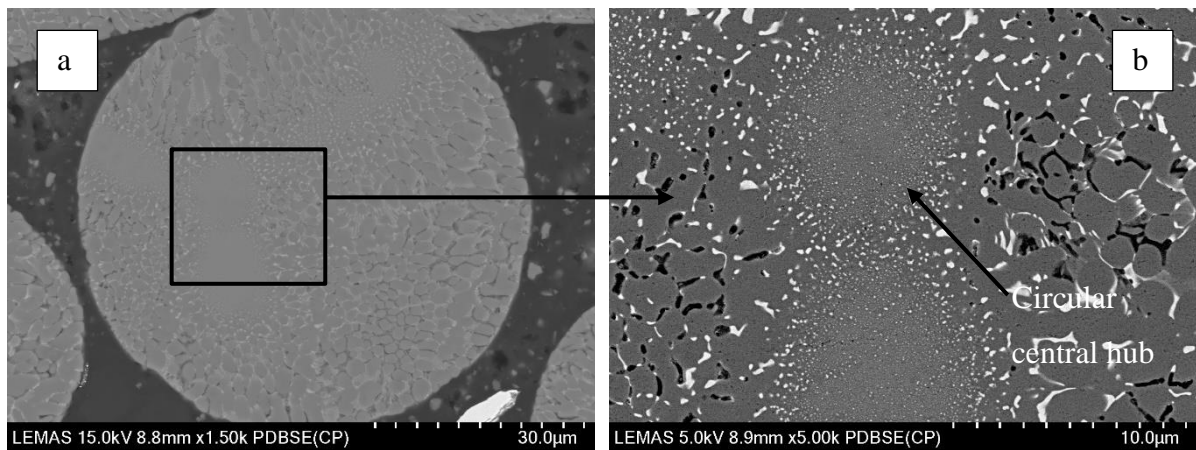
Figure 86: SEM micrographs of propeller-like structures observed in 75-53 µm sample with circular central hub.
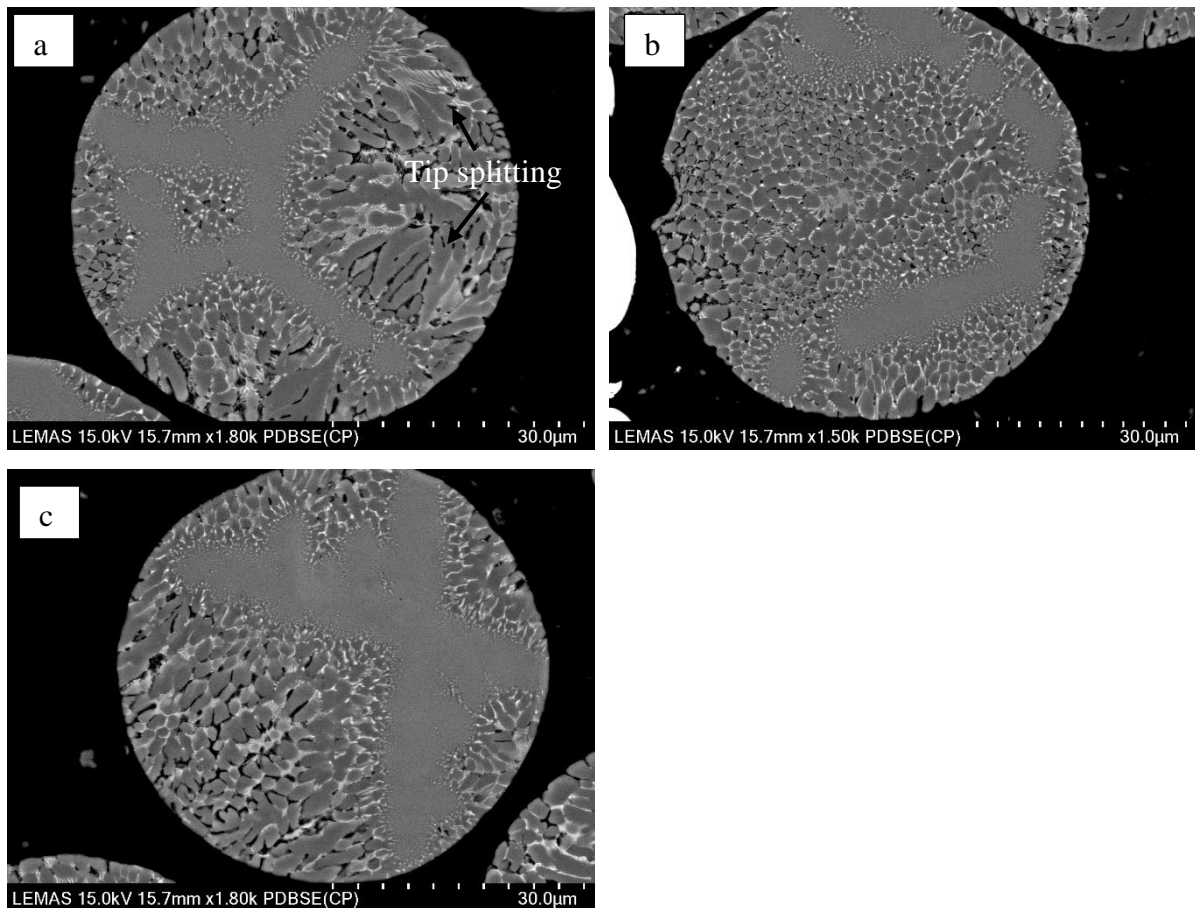
Figure 87: Microstructures of 75-53 µm samples showing different Y-shaped structures.
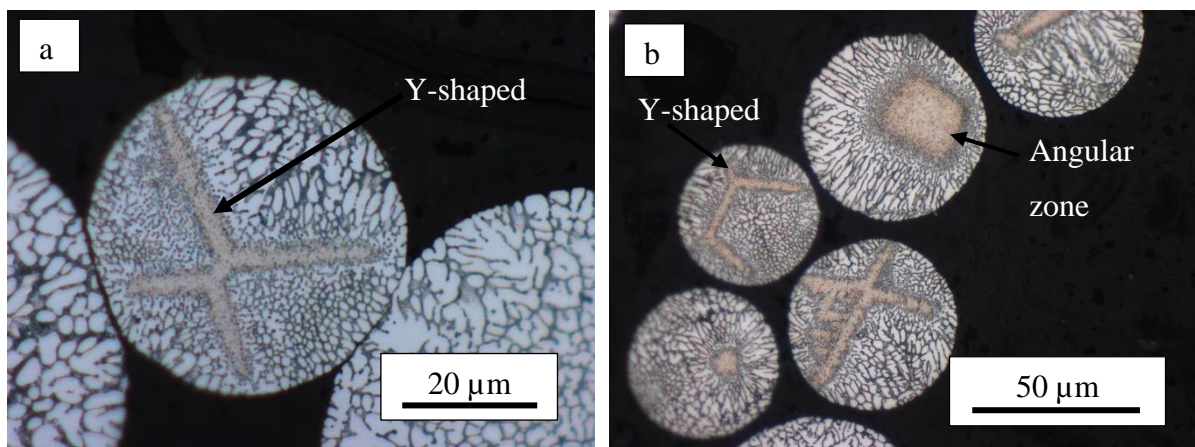
Figure 88: OM micrographs of a) 106-75 µm and b) 75-53 µm samples showing Y-shaped structures as well as angular nucleation zone.

5.4.4 Eutectic Spacing

Eutectic spacing of the drop tube atomized samples has been measured and the results are given in **Figure 89** as a function of average cooling rate. Eutectic spacing has been found to be decreasing with rising cooling rate. The maximum spacing was measured as 0.76 µm in 850-500 µm sample. This figure dropped continuously to 0.15 µm in the fastest cooled sample (75-

53 µm). Moreover, 300-212 µm and 212-150 µm samples have identical eutectic spacings of around 0.36 µm. it must be noted here that angular nucleation zone was firstly observed in 300-212 µm samples and the fraction of angular zone has been found to be increasing with increasing cooling rate.
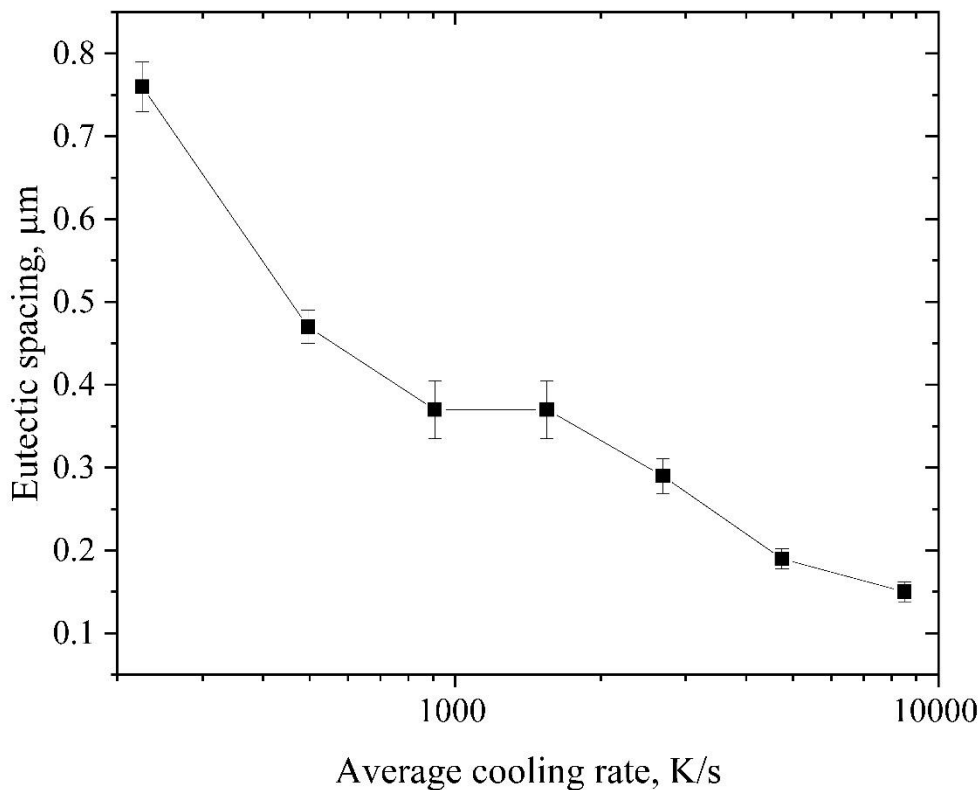
Figure 89: Eutectic spacing as a function of average estimated cooling rate.

5.4.5 TEM Results

In order to further analyse the angular region and interdendritic eutectic two TEM samples from 150-106 µm sample were sectioned using FIB. **Figure 90** shows where these samples were taken and the TEM results are provided in **Figure 92-94**. **Figure 92a** and **93a** show TEM micrographs taken from the angular nucleation zone. It is clear from these figures that the angular region consists of nano-sized faceted precipitates with a diameter of around 100 nm on α-Al matrix. Moreover, these precipitates have formed clusters which are the combination of several precipitates and each cluster has a different number of precipitates. **Figure 92b-d** and **Figure 93b-d** show the EDS elemental mapping of Al, Fe and Si, respectively. It reveals that

126

these precipitates are ternary intermetallics of Al-Fe-Si as Fe and Si have higher concentration in these precipitates than the α-Al matrix. In addition to the qualitative EDX given in **Figure 92b-d** and **Figure 93b-d**, quantitative analysis has also been made on the precipitates and the α-Al matrix. The composition of α-Al matrix includes 0.71 at. %Si and 0.15 at. %Fe. That is, more Si is dissolved in α-Al than Fe. This can be seen from the Figure 88c and d, which show the elemental maps of Fe and Si. Where the quantitative EDX analysis of the precipitates are taken are labelled as 1 and 2 in **Figure 92a**. These places were chosen because they include the largest clusters and, thus, it is expected to reflect more accurate EDX results compared to smaller precipitates. The composition of these two regions is found to be very close to each other as 72 at. %Al, 19.5 at. %Fe and 8.5 at %Si. This composition is within the homogeneity range of Al_8Fe_2Si [71] as provided in **Figure 28**.

TEM micrograph taken from interdendritic region of 150-106 µm sample is shown in **Figure 94a**. TEM micrograph depicts the interdednritic eutectic is lamella eutectic. Moreover, **Figure 94b-d**, which depict EDX mapping, show that the intermetallic is ternary intermetallic of Al, Fe and Si. The compositions of the intermetallic were taken from the regions which were labelled as 1 and 2 in **Figure 94a** and the results were found very close to composition of intermetallics in the angular region as 72 at. %Al, 19 at. %Fe and 9 at %Si. That is, both intermetalics in the eutectic region and in the angular region share the same composition and are the same intermetallic, Al_8Fe_2Si [71] as provided in **Figure 28**.

In addition to analysing drop tube atomized sample using TEM, a FIB SEM sectioned sample was further analysed under TEM. This was performed to confirm that the only intermetallic in the master alloy is Al_8Fe_2Si as XRD result for the master alloy given in **Figure 76** is contaminated by the mounting media, Bakelite. **Figure 91** shows where the sample was taken and the TEM results are shown in **Figure 95**. TEM has revealed that the intermetallic is rod-like. EDX mapping is also provided in **Figure 95b-d**. The composition of the rod-like intermetallic taken from the label 1 in **Figure 95a** has shown that the composition is in the homogeneity range of ternary intermetallic Al_8Fe_2Si being 73 at% Al, 18 at% Fe and 9 at% Si. Moreover, SAD pattern was taken from the same region as given in **Figure 95e** and has indexed as belonging to Al_8Fe_2Si from $(0\bar{1}0)$ zone axis.

127
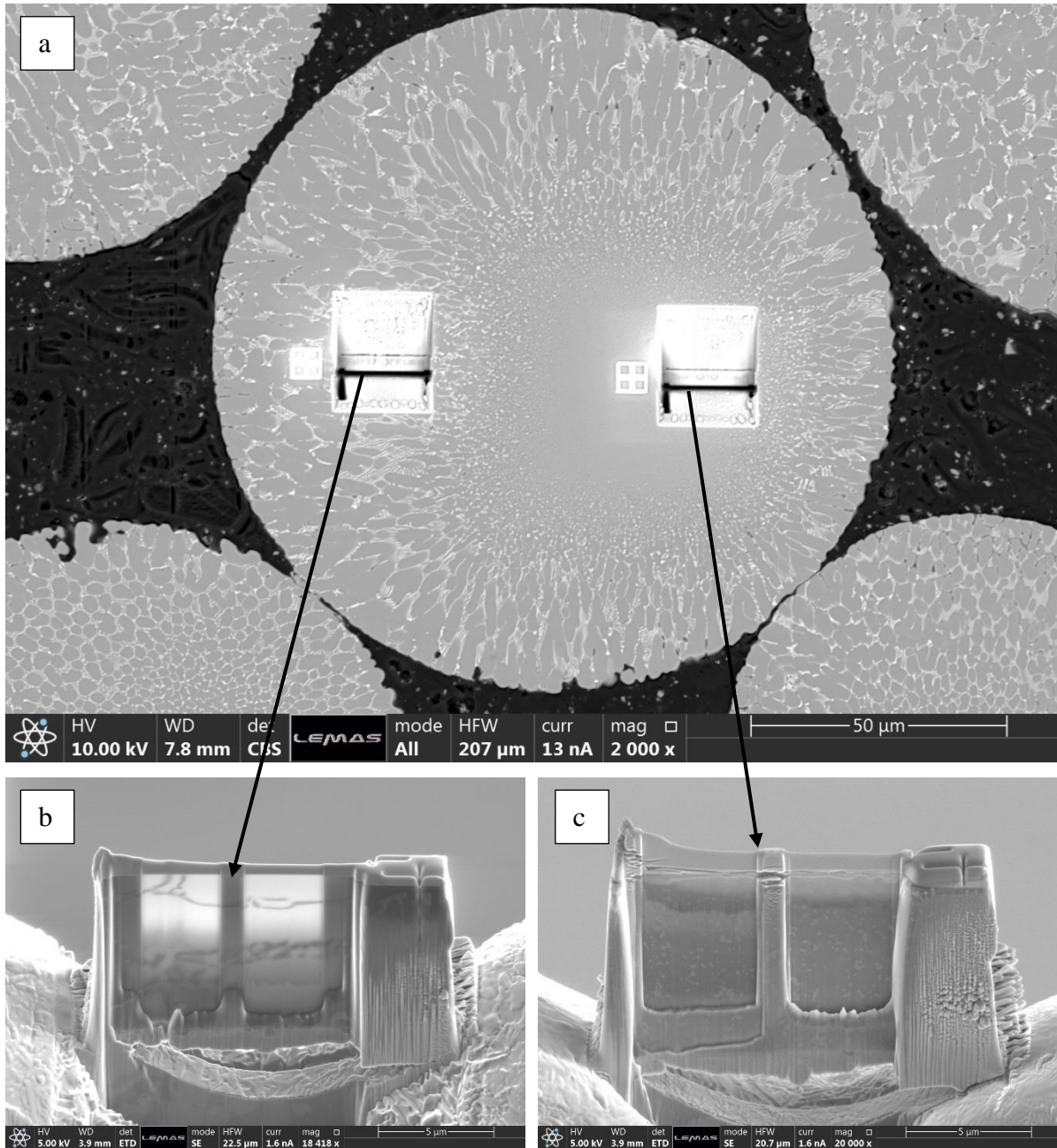
Figure 90: FIB sectioned 106-75 µm sample depicting a) where the TEM samples were taken b) TEM sample taken from interdendritic eutectic and c) TEM sample taken from angular zone.
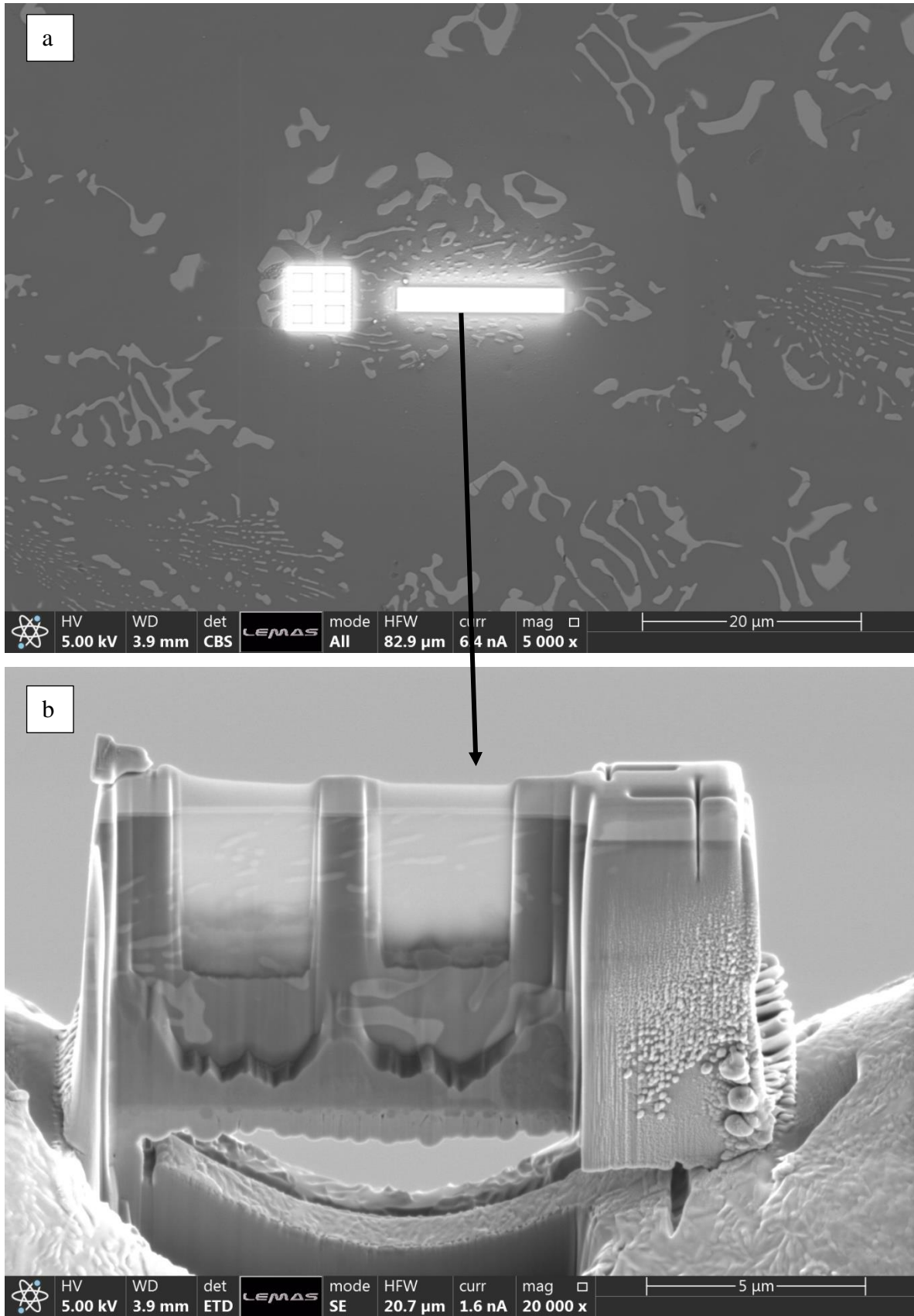
Figure 91: FIB SEM sectioning of Al-4.1 wt% Fe-1.9 wt% Si master alloy (arc-melted sample) a) where the sample was taken and b) TEM sample after thinning.
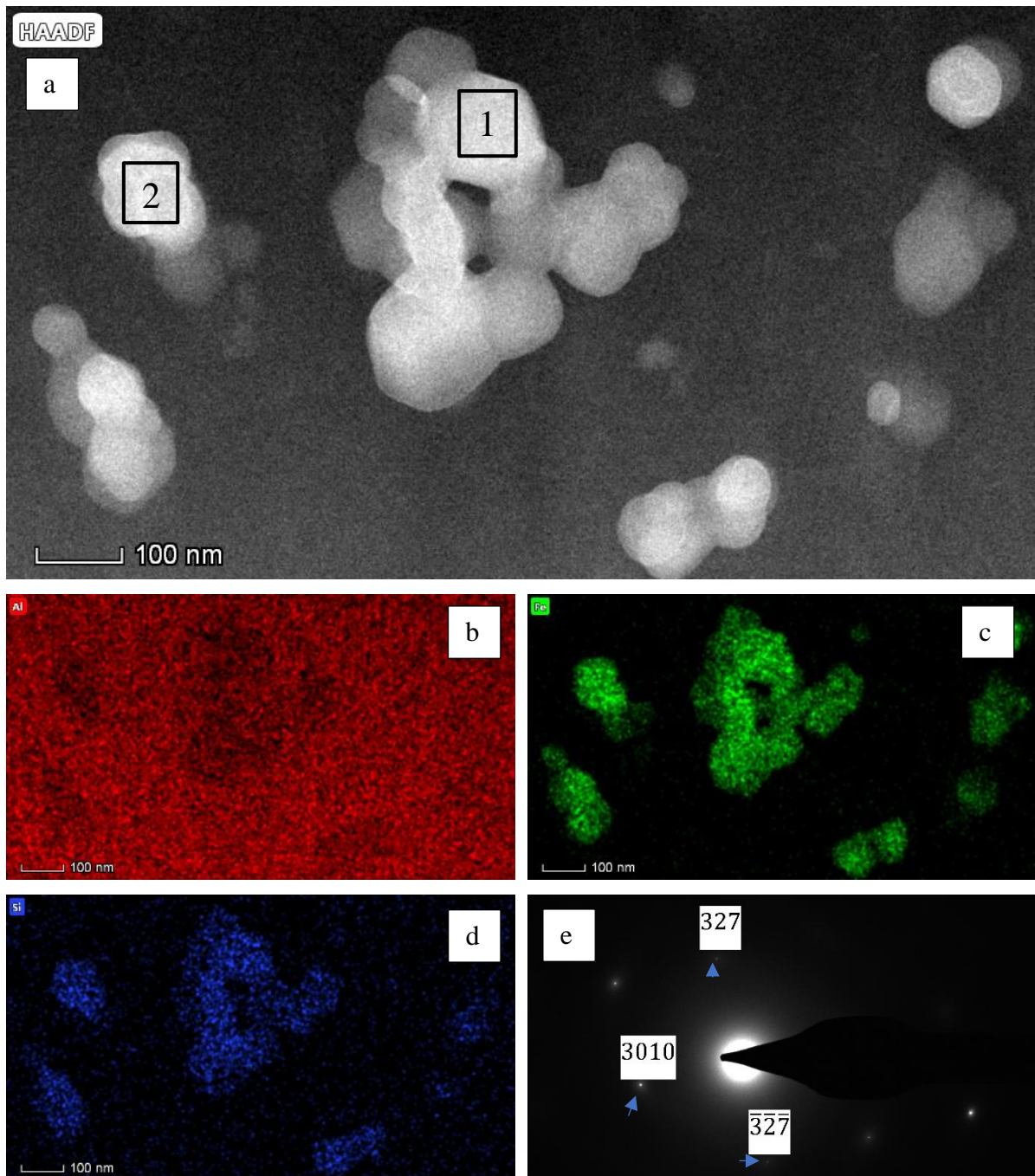
Figure 92: a) TEM micrograph taken from the angular region of 150-106 µm sample showing intermetallics forming clusters b), c) and d) EDS mapping of Al, Fe and Si, respectively and e) SAD pattern from the region labelled as 1 in a) taken from ($2\bar{3}0$) zone axis of Al_8Fe_2Si.
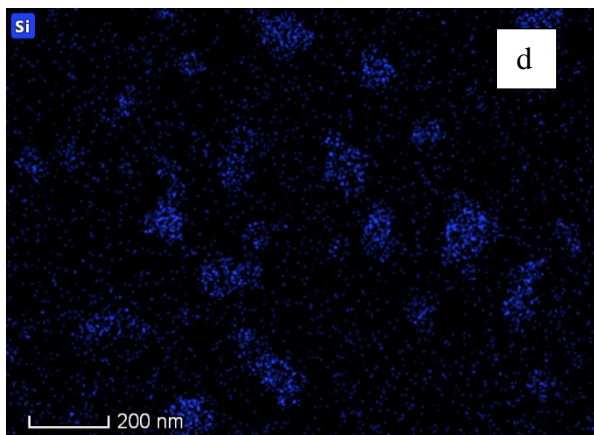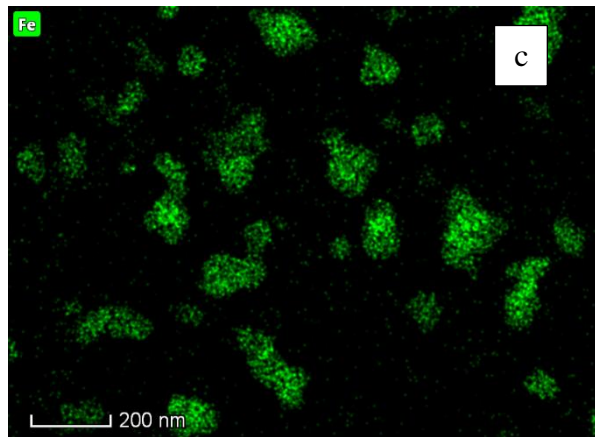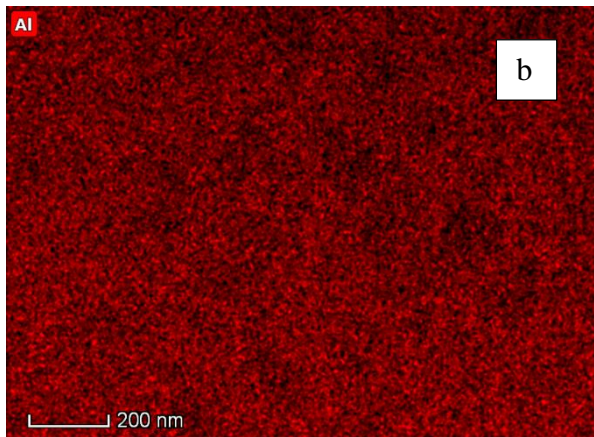
Figure 93: a) TEM micrograph taken from the angular region of 150-106 µm sample showing intermetallics forming clusters b), c) and d) EDS mapping of Al, Fe and Si, respectively.
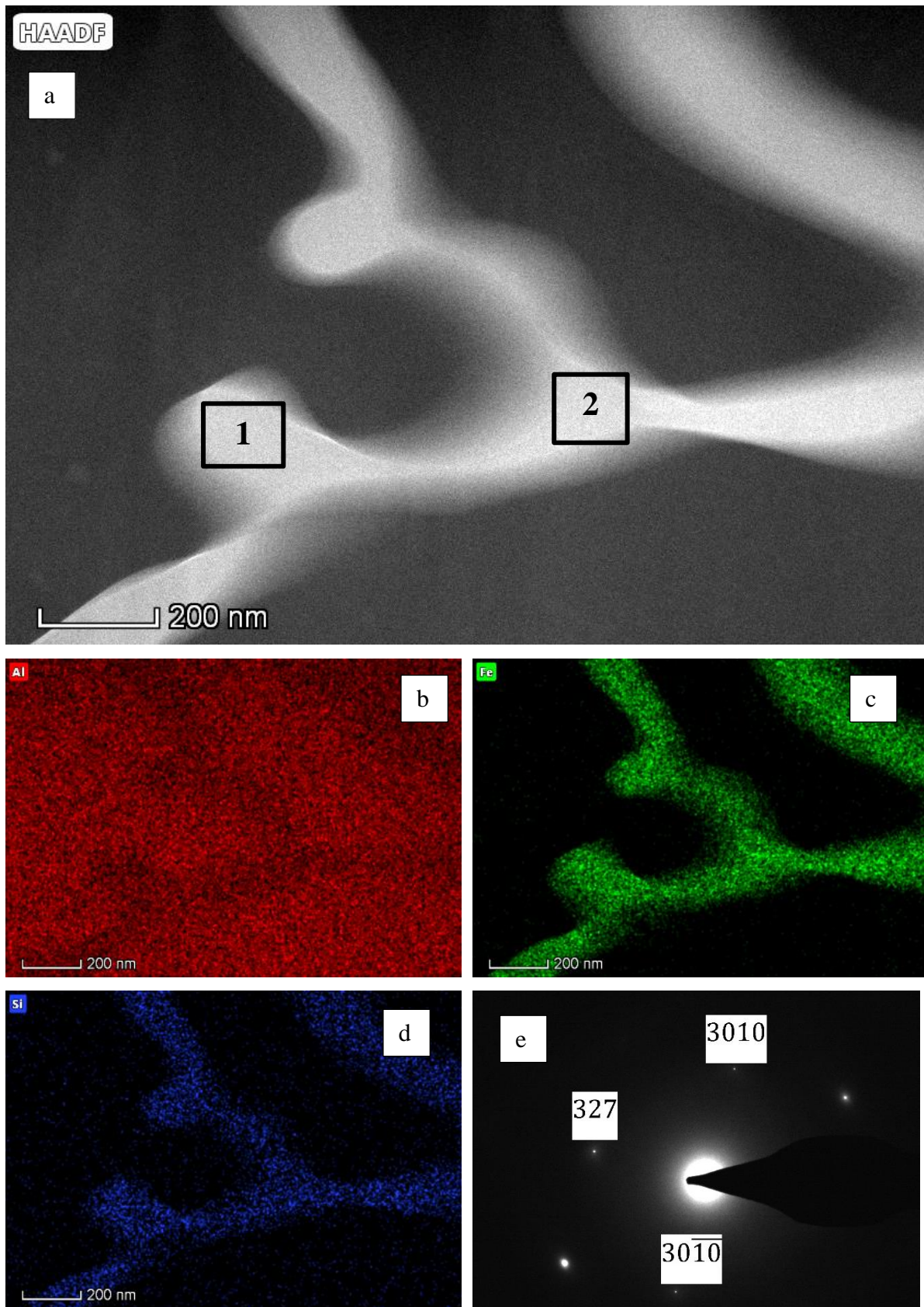
Figure 94: a) TEM micrograph taken from interdendritic region showing lamellar eutectic, b), c) and d) EDS mapping of Al, Fe and Si, respectively and e) SAD pattern taken from region labelled as 1 in a) showing taken from $(2\bar{3}0)$ zone axis of Al_8Fe_2Si.
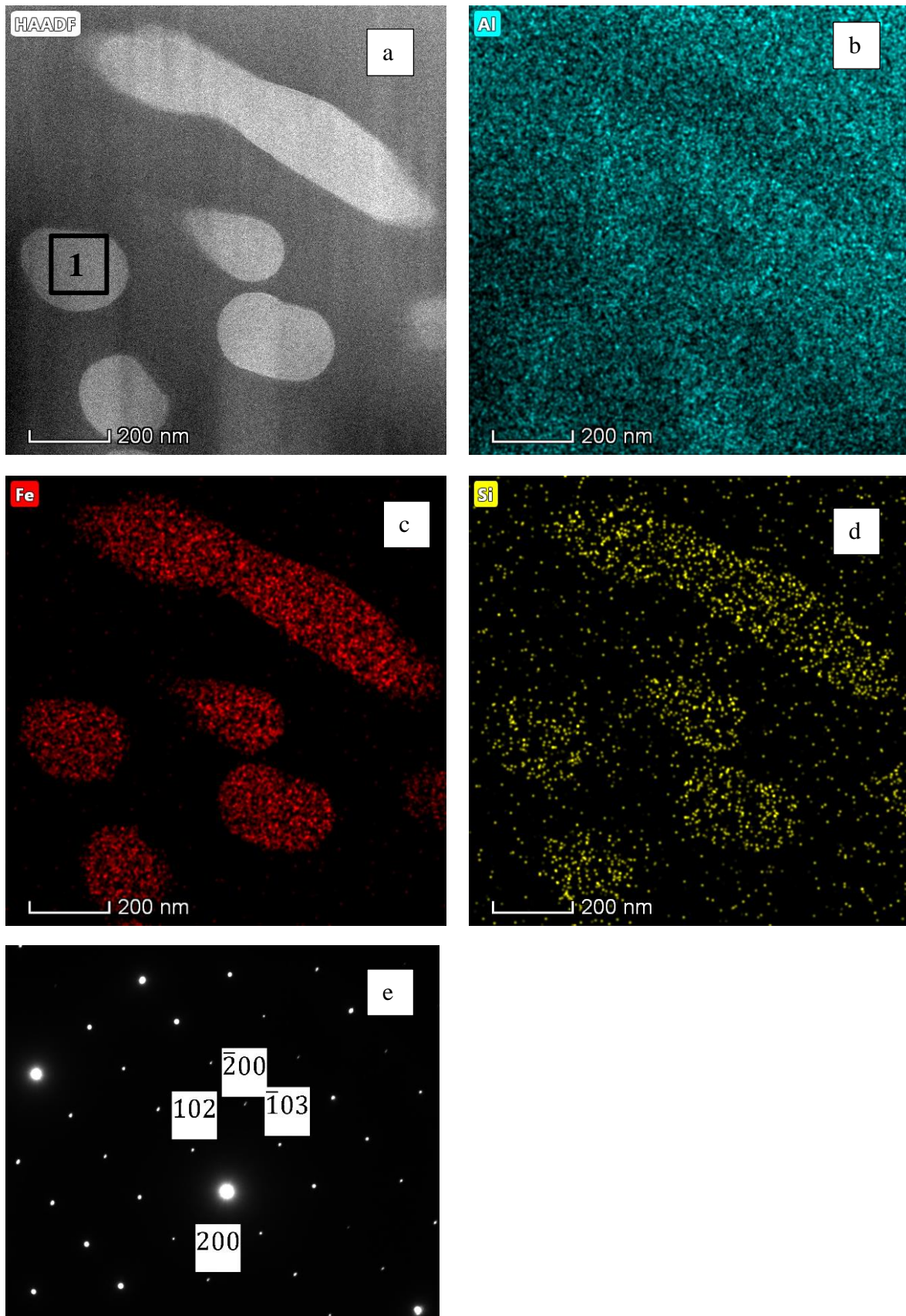
Figure 95: a) TEM micrograph taken from the rod-like intermetallic of Al-4.1 wt% Fe-1.9 wt% Si master alloy b), c) and d) EDS mapping of Al, Fe and Si, respectively and d) SAD pattern taken from the region labelled as 1 in a) depicting Al_8Fe_2Si from (010) zone axis.

5.4.6 Microhardness

In order to understand the effect of the cooling rate on the mechanical properties of the alloy, the microhardness of the samples was measured. At least ten measurements were taken for each size fraction and the results are provided in **Figure 94**. The minimum microhardness value was measured in slowest cooled sample (850-500 µm) being around 72 ± 2 $HV_{0.01}$. This figure has risen with increasing cooling rate and reached a peak of 90 ± 3 $HV_{0.01}$ in 212-150 µm sample. This corresponds to around 30% increase compared to slowest cooled sample. However, further increase in cooling rate has resulted in a slight decrease in the microhardness in the fast cooled samples. The microhardness of the fastest cooled sample (75-53 µm) has been measured as 80.2 ± 2.4 $HV_{0.01}$, which is around 10% lower than the maximum microhardness value. It must be noted here that angular structure has appeared in 300-212 µm samples and has occupied 50% in 212-150 µm samples. Moreover, most of the samples with d < 150 has shown angular structures, which are made up of very fine precipitates.
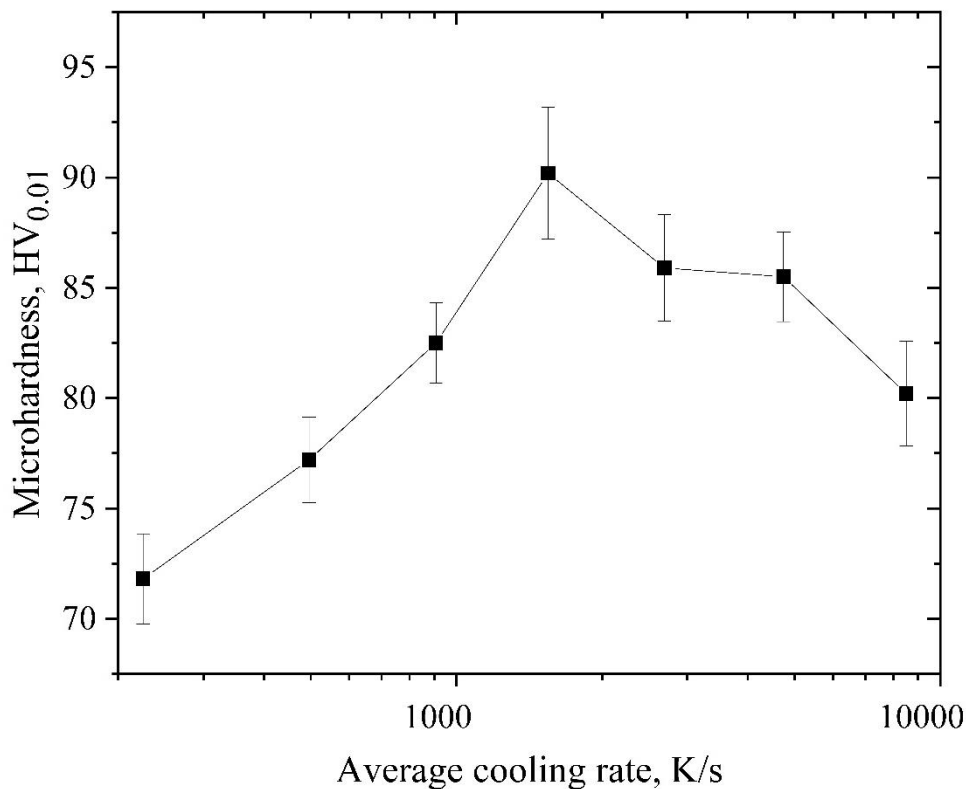
Figure 96: Microhardness values (in $HV_{0.01}$) as a function of average estimated cooling rate.

6. Discussion

The results presented in Chapter 5 will be discussed in this chapter.

6.1 Cooling rate

As discussed earlier, the cooling rate of the solidifying droplet in the drop tube cannot be measured as the solidification takes place during free fall. However, there are two methods to estimate the cooling rate in the drop tube. First method is to utilize mathematical models while the second method is to measure the secondary dendrite arm spacing (SDAS) of the samples and estimate the cooling rate using the already published experimental results. The former method has been employed in this work and given in **Section 5.1**. Moreover, the estimated cooling rate results have been validated by measuring the SDAS of the dendritic α-Al of the Al-2.85 wt% Fe alloy (**Figure 52**) as the microstructures were mostly dendritic. That is, the cooling rate was estimated using the mathematical model (**Section 5.1**) and SDAS was measured (**Section 5.2.6**) with the resulting correlation being compared to results in the literature.

The estimated cooling rate was found to be ranging between 155 K s^{-1} and 20,000 K s^{-1} for 850 µm and 38 µm samples, respectively, as shown in **Figure 38**. Kasperovich et al.[106] and Erol and Buyuk [102] have estimated the cooling rate of the drop tube atomized Al-Cu and Al-Ge, respectively. Their estimations are higher than the estimated results in this work by 3 to 4-fold. The reason is that both works have used He as a cooling medium rather than N_2, which was utilized in this work. As He has significantly higher thermal conductivity than N_2, use of He is expected to yield higher cooling rates. For example, Oloyede et al. [107] estimated the cooling rates of drop tube atomized cast iron (Fe-C-Si) in both N_2 environment and He environment and reported that the cooling rate in He environment is up to four times higher than that of in N_2 environment.

Furthermore, SDAS of Al-2.85 wt% Fe have been measured and given as a function of estimated average cooling rate in **Figure 52**. In the literature, the relation between SDAS and the cooling rate, $\dot{T}$, is usually given as:

$$SDAS = K * \dot{T}^{-n} \tag{6-1}$$

Using the power law fitting function in OriginPro, the constants K and n were found as 31.06 and 0.368, respectively. In the literature, there is only one work which provides the experimental relationship between SDAS and the cooling rate of Al-0.5 wt% Fe alloy.

135

According to the results of Miki et al.[104], the constants K and n are 33.3 and 0.333, respectively. That is, the estimated cooling rate in this work fits well with the experimental results with in the experimental error.

6.2 Al-2.85 wt% Fe

EDX results (**Figure 49**) have shown that Fe solubility in the α-Al phase increases with increasing cooling rate and, thus, increasing undercooling. While Fe solubility is 0.37 wt% Fe in the slowest cooled sample, this figure has risen to 1.105 wt% Fe in the fastest cooled sample. Although this is in good agreement with the reported results in the literature, it contradicts the finding of Nayak et al.[108] who studied various Al-Fe alloys using melt spinning. They reported a decrease in Fe solubility with increasing wheel speed and, therefore, increasing cooling rate. As more Fe is dissolved in α-Al with increasing cooling rate, there remains less Fe to form eutectic, meaning that the fraction of the interdendritic eutectic is expected to decrease with increasing cooling rate. This is shown in **Figure 51** where the fraction of interdendritic eutectic decreases from around 50% to 25% for the samples with lowest undercooling and highest undercooling, respectively. Furthermore, EDX analysis has also been performed for interdendritic eutectic area with the results are given in **Figure 50**. **Figure 50** shows that Fe content in the interdendritic eutectic zone increases with increasing undercooling. This suggests that the eutectic coupled zone is skewed towards the intermetallic side. Al-rich side of the coupled zone is reconstructed using the data given in **Figure 53** and the phase diagram is given on **Figure 97**. Moreover, metastable extension of solidus line of α-Al is labelled in the figure which was used to estimate the undercooling of the droplet from the supersaturation of the α-Al given in **Figure 49** and **Table 8**. **Figure 97** also shows the conjectured solidification path for a droplet from the 150-106 µm sieve fraction. This corresponds to 93 K undercooling for α-Al and 4.6 wt% Fe in Al-$Al_{13}Fe_4$ eutectic. Eutectic coupled zone of Al-Fe has been reported by [109], [110] as skewing towards the intermetallic side. However, both works showed Al-$Al_{13}Fe_4$ eutectic down to 647 °C, which is near Al-Al_6Fe eutectic temperature. Al-Al_6Fe eutectic coupled zone was reported below 647 °C. However, here, Al-$Al_{13}Fe_4$ eutectic coupled zone appears to exist at lower temperatures than the previous studies.

All the samples have shown the formation of microcellular region where, probably, the nucleation was initiated. However, with increasing undercooling, this zone transformed into divorced eutectic, which later transitioned to microcellular region. According to Boettinger et

al. microcellular region in Al-8wt% Fe alloy was formed due to large undercooling during the recalescence stage. As high undercoolings ranging between 96 K and 188 K have been reached in this work, Microcellular region has widely been observed. However, transition of microcellular region to divorced eutectic (**Figure 48**) suggests that higher undercooling promotes the formation of the divorced eutectic with the transition has taken place at an undercooling value of around 185 K.

Although most of the drop tube atomized samples a have single nucleation event, on which dendritic α-Al grows, some samples have shown multiple nucleation events as shown in **Figures 46** and **47**. In particular, multiple nucleation has mostly been observed in smaller size fractions where higher degree of undercooling is observed. Multiple nucleation takes place in the presence of a) multiple homogeneous nucleation sites, b) multiple impurities in the melt and c) dendrites breaking and sweeping in to the melt to provide multiple nucleation sites. The latter two are heterogeneous nucleation. Dendrite fragmentation has been reported in drop tube atomized Ni-Ge [38] alloy due to the recalescence. However, they reported that the fragmented dendrites neither acted as a nucleation site for the remaining liquid nor were swept in to the melt. This is because flow velocities in the drop tube processed samples are very low. Moreover, as the cooling rate in drop tube is comparatively high, there is no time for fragmented dendrite arms to be swept in to the melt to act as multiple nucleation sites. Furthermore, the undercooling reached in drop tube is not high enough to result in homogeneous nucleation. Thus, it is likely that the multiple nucleation event in the droplets has been due to impurities such as surface oxides present in the melt as such nucleation events become more evident with increasing undercooling which decreases energy barrier as $1/(\Delta T)^2$.

Eutectic spacing was measured and given in **Figure 53** as a function of estimated average cooling rate. The relation between eutectic spacing, λ, growth rate, *v*, and undercooling, ΔT is determined by Jackson-Hunt (J-H) eutectic theory given in **Equation 2-27**. The relation between J-H constants [111], [112] for Al-Al$_{13}$Fe$_4$ eutectic were measured as $\lambda\sqrt{v} = 22.4 \ \mu\mathrm{m}^{1.5}\mathrm{s}^{-0.5}$ and $\lambda\Delta T = 8.79 \ \mu\mathrm{m} \ \mathrm{K}$. The estimated growth rate and undercooling using these relations are given in **Table 9** and illustrated in **Figure 98**. Growth rate ranges between 0.89 mm s^{-1} and 22.3 mm s^{-1} while the interdendritic eutectic undercooling ranges between 11.72 K and 58.9 K. These undercoolings and velocities are higher than that of calculated by other researchers[73] via Bridgman growth. They stated that the transition from Al-Al$_{13}$Fe$_4$ eutectic to Al-Al$_6$Fe eutectic takes place between growth velocities of 1-10 mm s^{-1}. However, here no transition occurs even though the growth rate for Al-Al$_{13}$Fe$_4$ is as high as 22.3 mm s^{-1}.

Possible explanation to this difference is due to the difference between the operating conditions of Bridgeman and drop tube. While Bridgman operates under positive temperature gradient ($G_L > 0$), drop tube operates under negative temperature gradient ($G_L < 0$). Moreover, Bridgeman experiments take much longer solidification time compared to drop tube as well as the nucleation only happens once and thereafter the growth is propagated throughout the experiment. There are two possible explanations for the contradiction between this work and the Bridgeman growth experiments, which lie on the difficulty of the nucleation of the phases. That is, 1) $Al_{13}Fe_4$ is more difficult to nucleate 2) Al_6Fe is more difficult to nucleate. Assuming the former, although the nucleation free energy barrier, ΔG^*, is higher, $Al_{13}Fe_4$ is faster growing than Al_6Fe. As drop tube provides high undercooling, it would be possible to overcome ΔG^* allowing the formation of faster growing $Al_{13}Fe_4$, which is not possible when $G_L > 0$. Assuming the latter, Al_6Fe can outgrow $Al_{13}Fe_4$ due to the long-time availability of solidification in Bridgeman experiments.

Table 9: The estimated relation between eutectic spacing, λ, growth rate, v, and undercooling, ΔT in the interdendritic eutectic zone of Al-2.85 wt% Fe samples.

λ (µm)	0.75	0.5	0.32	0.30	0.27	0.22	0.15
v (mm s^{-1})	0.89	2	4.9	5.3	6.88	10.36	22.3
ΔT (K)	11.72	17.58	27.46	29.4	32.55	39.9	58.9
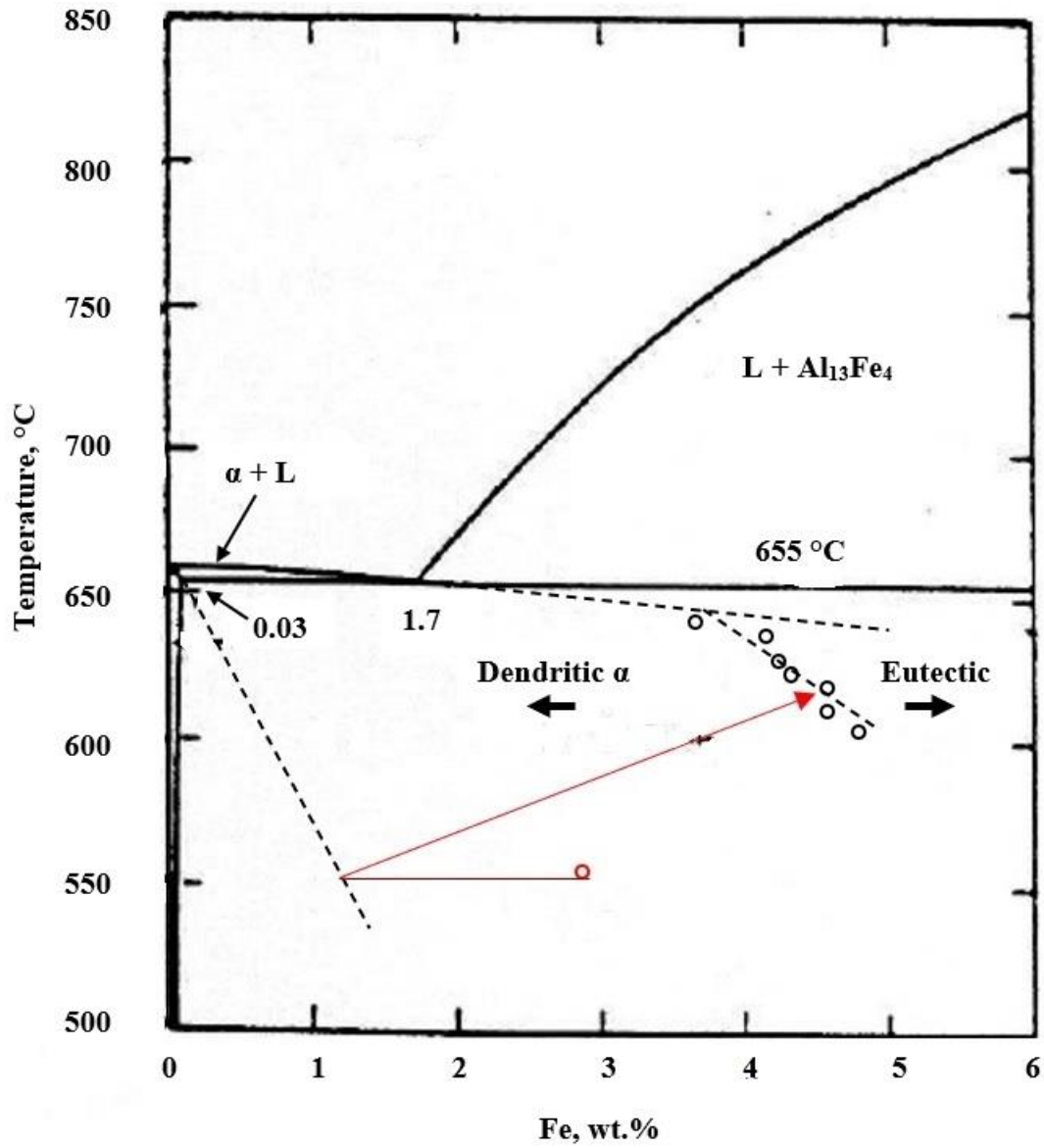
Figure 97: Estimated location of the Al-rich side of the eutectic coupled zone for the growth of Al-Al$_{13}$Fe$_4$ eutectic drawn on the phase diagram by Philips [113].
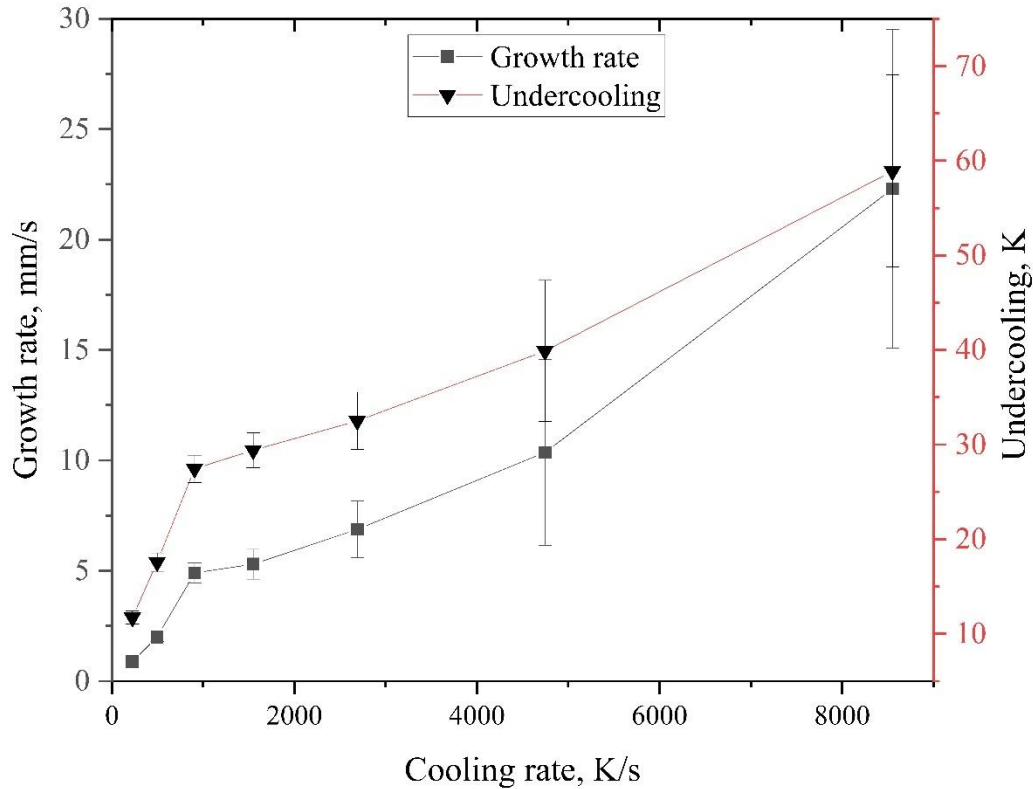
Figure 98: Eutectic growth rate (left-hand axis) and interfacial undercooling (right-hand axis) for the Al-Al$_{13}$Fe$_4$ lamellar eutectic as a function of the estimated cooling rate, estimated from the lamellar spacing.

Both solid solution and intermetallics are well known for their contribution to the mechanical properties of metallic materials, particularly hardness. While solute content increased in α-Al (positive effect) as shown in **Figure 49**, the volume fraction of the eutectic and, consequently, the fraction of intermetallic (negative effect) decreased (**Figure 50**) with increasing cooling rate. This resulted in a small improvement in the microhardness being around 20% as shown in **Figure 57**. It can be said that the contribution of the solute solution is more profound than that of the intermetallic in this alloy. Although this increase is limited, researches [93] have shown that mechanical properties of rapidly solidified Al-Fe alloys can further be improved by heat treatment. Heat treatment results in the formation of very fine spherical and needle-like precipitates, which can easily be controlled [14] depending on the dwell temperature, due to the decomposition of the supersaturated α-Al matrix (note that Fe solubility reached to 1.105 wt% in this work) and can further increase the microhardness. Moreover, heat treatment does not have a significant effect on the pre-existing intermetallics. That is, if this or such rapidly solidified Al-Fe alloys are used in powder metallurgy, which requires high sintering

140

temperatures of around 0.8 Tm, it is expected that the hardness of the final product will be higher than starting material as it will act as a heat treatment process as well.

6.3 Al-3.9 wt% Fe

Al-3.9 wt% Fe alloy has been rapidly solidified using 6.5 m drop tube and the resulting samples have shown various microstructures. Firstly, large blocky primary $Al_{13}Fe_4$ surrounded with α-Al, stable lamellar $Al-Al_{13}Fe_4$ eutectic, metastable rod-like $Al-Al_6Fe$ and primary dendritic α-Al have been observed in large powders (d > 212 µm) as shown in **Figure 60** and **61**. As the cooling rate is relatively low in large powders, there is time for the formation of primary $Al_{13}Fe_4$. During the formation of primary $Al_{13}Fe_4$, Fe in the droplet diffuses to the primary $Al_{13}Fe_4$ which, as a result, depletes the Fe concentration in the liquid surrounding $Al_{13}Fe_4$. Thus, α-Al forms around the primary $Al_{13}Fe_4$. A similar phenomenon has been well documented in spheroidal graphite cast irons (Fe-C-Si). When the cooling rate is low in the cast iron, spheroidal graphite picks up C from the surrounding liquid leaving C deficient Fe surrounding the graphite. As a result, what is called as bull's eye structure, which is spherical graphite (dark phase) surrounded by ferrite (bright phase), is formed. Dendritic α-Al has also been observed in large powders. For dendritic α-Al to be observed in hypereutectic alloy, the remaining liquid should experience a degree of undercooling below the coupled zone for the $Al-Al_{13}Fe_4$. Based on the metastable phase diagram constructed for Al-2.85 wt% Fe alloy given in **Figure 97**, the droplet has to experience a minimum undercooling of around 110 K. The remaining liquid transforms into complete eutectic. As seen from **Figure 60** and **61**, most of the samples is composed of both metastable rod-like eutectic and stable lamellar eutectic. However, from the figures it is not possible to determine which eutectic grew first in the melt.

Decreasing sample size and, thus, increasing cooling rate has drastically changed the microstructure of the smaller samples (d < 212 µm). First of all, primary blocky $Al_{13}Fe_4$ has disappeared. The reason is that as the cooling rate in smaller droplets is higher than that of larger powders, there is no time for the formation of primary $Al_{13}Fe_4$. Another reason is the growth competition between phase. That is, faceted intermetallics ($Al_{13}Fe_4$ in this case) are likely to be slow growing phase. Therefore, primary $Al_{13}Fe_4$ was replaced with faster growing α-Al at elevated undercoolings.

Another drastic change in smaller samples is the formation of the Y-shaped structures with different morphologies as shown in **Figures 62-68**. That is, Y-shaped can be observed in fast cooled, highly undercooled samples. Moreover, Y-shaped was also observed in smallest sieve

fraction (75-53 µm) of drop tube atomized Al-2.85 wt% Fe samples as shown in **Figure 46d**. That is, not only cooling rate and undercooling but also Fe content of the samples plays a critical role in the formation of Y-shaped. In other words, increasing cooling rate, undercooling and Fe content in the alloy promote the formation of Y-shaped structure. Structures which appear to be similar to Y-shaped have also been reported in impulse atomized hypoeutectic Al-0.61 wt% Fe and hypereutectic Al-1.90 wt% Fe [114] and impulse atomized Al-5 wt% Cu and Al-17 wt% Cu [115] alloys. However, neither of these works have provided high magnification images of this region nor did they provide any phase analysis to confirm that the phase was α-Al as they asserted. Y-shaped structure appears to be the first to solidify in the droplets as it acted as a nucleation site for the dendritic α-Al as dendritic α-Al grows out of Y-shaped. Further evidence to this is given in **Figure 67** which shows small sample was collided with larger droplet and acted as a nucleation side. This states that Y-shaped formed in the large droplet and when the remaining droplet was still liquid the collision took place. As a result, small sample acted as a heterogeneous nucleation site for the remaining liquid.
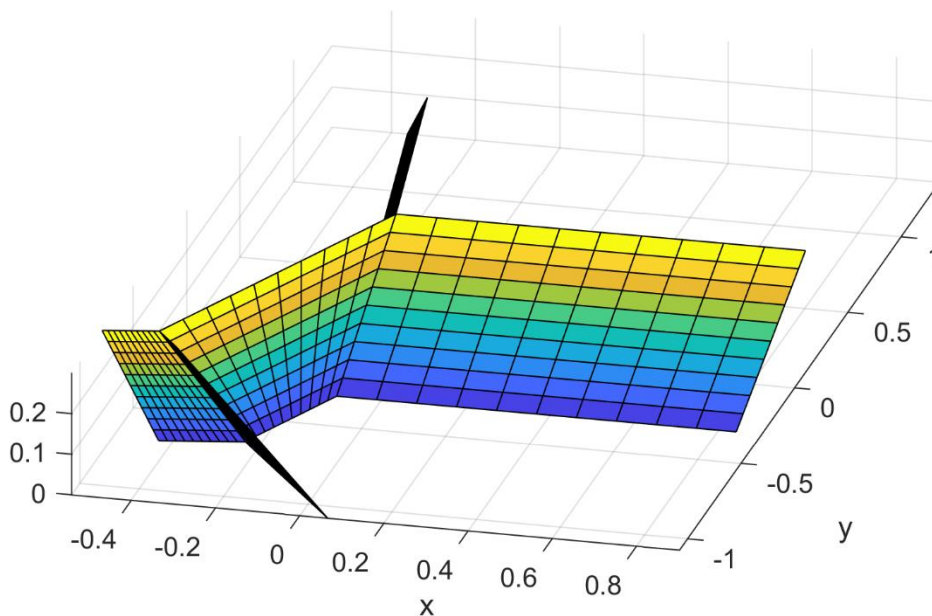
Figure 99: 3D schematic reconstruction of Y-shaped using the serial sectioning given **Figure 69a-g**. The Y-shaped structure is composed of three intersecting planes almost perpendicular to the sectioning plane

Y-shape has a long, thin morphology in polished sections suggesting that it forms as crystals which are long in two dimensions and short in one dimension, i.e. as a plane sheet. 3D reconstruction of Y-shaped structure is provided in **Figure 99** using the serial sectioning images given in **Figure 69**. 3D reconstruction shows that the Y-shaped structure comprises

intersecting plane sheets. Moreover, **Figure 66c** shows the formation of both needle-like and spherical precipitates in the centre of and perfectly aligned to Y-shaped morphology. That is, Y-shaped formed as a plane of sheet and later fragmented due to recalescence into spherical and needle-like morphology. These broken precipitates acted as nucleation sides for α-Al. This can be seen from **Figure 66b** and **c** where linear array of broken Y-shaped is observed. Fragmentation and spherodisation of primary phase have been reported in drop tube processed Ni-Ge alloy due to recalescence [38]. Another possibility would be that the first phase to form was an intermetallic (**Figure 66**) which break up due to recalescence. This would also explain the complex structure of the Y-shaped. As intermetallics show more complex crystallography than pure metals (α-Al).

TEM analysis (**Figure 73** and **74**) has revealed that Y-shaped region is composed of very fine (nanosized) needle-like and spherical iron rich precipitates in α-Al matrix. Diffraction patterns have shown that these precipitates are metastable Al_mFe. This is in good agreement with previous results as metastable AlmFe is the highest solidification rate intermetallic in Al-Fe system [64], [116]. Moreover, Al_mFe has also been reported to form via solid state decomposition at high growth rates [105]. Probably, Al_mFe has been formed via both mechanisms in this work. The solidification sequence, thus, starts with the formation of an intermetallic, Al_mFe, growing as a thin planar sheet. This planar sheet has later caused the formation of Y-shaped structure. As the EDX results have shown that the composition of the Y-shaped is identical to the melt, it is high likely that Y-shaped is the highly supersaturated α-Al, growing via partitionless solidification. In addition, according to the metastable Al-Fe phase diagram by Boettinger et al [12], the minimum degree of undercooling required to permit partitionless solidification (that is, the minimum undercooling required to reach below the metastable extension of T_0 line) is measured as around 40 K below Al-$Al_{13}Fe_4$ eutectic. Such undercoolings can easily be attained in the drop tube. Therefore, fine droplets could have experienced partitionless solidification. As supersaturated α-Al is highly metastable, it undergoes solid-state decomposition forming nano scale Al_mFe precipitates. Therefore, it is probable that while the large precipitates in the Y-shaped formed directly from the liquid, the small particles in the Y-shaped are due to the solid-stated decomposition. The solidification of the fine droplets has proceeded with the growth of dendritic α-Al, whose primary arms coarsen as the growth continues. The coarsening is due to the warming of the droplet. Moreover, TEM image is given in **Figure 74**, which was taken from dendrite-like Y-shaped. That is, with increasing cooling rate plane sheet Y-shaped transformed into dendrite-like Y-shaped. Similar

143

transformation from plane sheet to faceted dendrites was reported in Ni-Sn system [117]. Plane sheet of metastable NiSn4 transformed in to faceted dendrite-like morphology when the cooling rate increased from 0.21 K s^{-1} to 155 K s^{-1}.

Al-Al$_{13}$Fe$_4$ eutectic spacing (**Figure 70**) has been found to increase when Y-shaped morphology started to emerge. According to Jackson and Hunt[118] eutectic theory, increase in eutectic spacing indicates a decrease in both growth rate and undercooling in the eutectic. The estimated growth rate and eutectic undercooling using the Jackson-Hunt coefficients $\lambda \Delta T = 8.79 \ \mu m \ K$ and $\lambda \sqrt{v} = 22.4 \ \mu m^{1.5} s^{-0.5}$ [111], [112] are given in **Table 10**. The results are also illustrated in **Figure 100** as a function of the estimated average cooling rate. It is clear that both undercooling and growth rate are rising with increasing cooling rate until the average cooling rate reaches 910 K/s reaching local peaks of 4.1 mm/s and 25.1 K, respectively. After this point, both figures decrease slightly (shaded region in **Table 10**) and later recover. As the most prominent change in the microstructure in this cooling rate is the formation of Y-shaped, the change in the eutectic spacing is most likely due to the formation of Y-shaped structure. That is, there has been some recalescence associated with the growth of the Y-shaped crystals which has lowered the undercooling at which the interdendritic eutectic grows. The undercooling difference as well as growth rate difference caused by the formation of Y-shaped structure are calculated as 5 K and 1.6 mm s^{-1}. The maximum undercooling and growth rate were estimated as 32.8 K and 6.98 mm s^{-1}, respectively. These figures are much lower than the ones estimated for Al-2.85 wt% Fe alloy given in **Table 9**, even if the fastest cooled Al-3.9 wt% Fe alloy has experienced higher cooling rates (it must be noted here that the drop-tube processing of Al-3.9 wt% Fe has yielded a wider range of particle size so that 53-38 µm samples and 850+ µm samples were only produced in Al-3.9 wt% Fe alloy). Considering not only the highest undercooling in Al-3.9 wt%Fe alloy but also all eutectic undercooling values are smaller than that of Al-2.85 wt% Fe, increasing Fe content has resulted in lower eutectic undercooling as well as growth rate.

Table 10: The estimated relation between eutectic spacing, λ, growth rate, v, and undercooling, ΔT in the interdendritic eutectic zone of Al-3.9 wt% Fe samples.

λ (µm)	1.311	0.975	0.41	0.35	0.45	0.38	0.28	0.28	0.27
v (mm s^{-1})	0.029	0.53	2.95	4.1	2.45	3.47	6.22	6.49	6.98
ΔT (K)	6.7	9.01	21.3	25.1	19.4	23.1	30.9	31.6	32.8
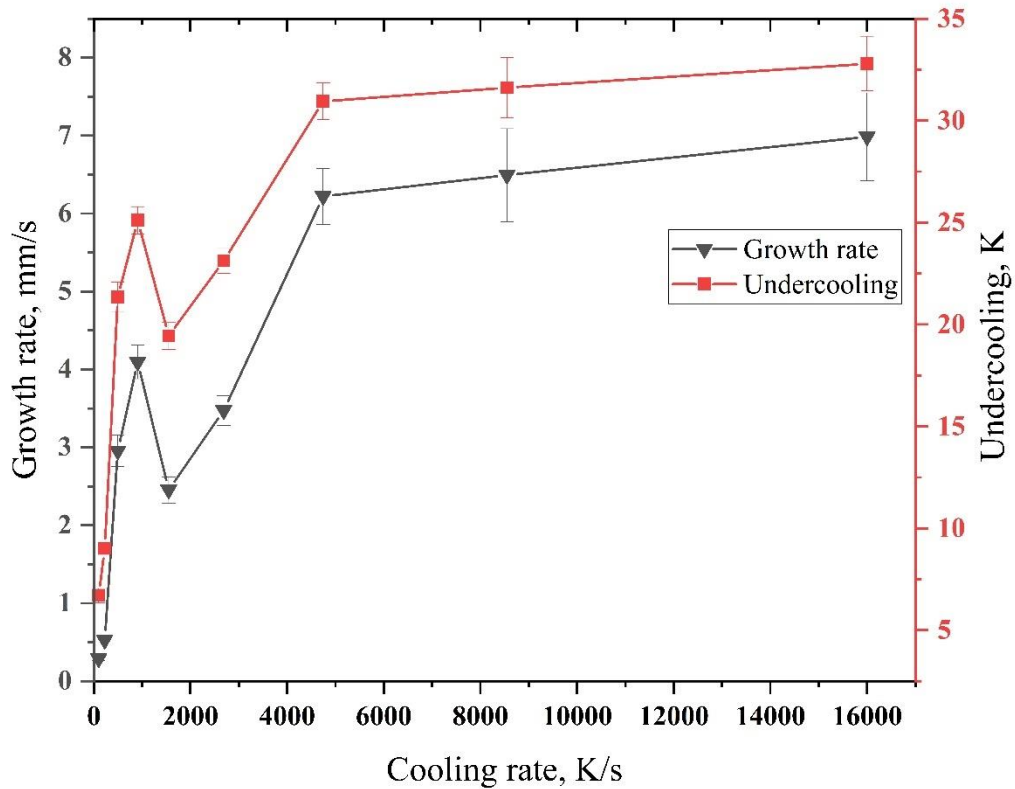
Figure 100: Eutectic growth rate (left-hand axis) and interfacial undercooling (right-hand axis) for the Al-Al$_{13}$Fe$_4$ lamellar eutectic in Al-3.9 wt% Fe alloy as a function of the estimated cooling rate, estimated from the lamellar spacing using J-H eutectic theory.

6.4 Al-4.1 wt% Fe-1.9 wt% Si

The effect of Si addition to binary Al-Fe alloy has been investigated in this section. The master alloy was prepared using an arc melter. XRD and SEM results have shown that the only intermetallic formed in the master alloy is ternary phase: proeutectic scrip-like Al$_8$Fe$_2$Si and rod-like eutectic. Moreover, TEM sample taken from rod-like intermetallic has shown that the only intermetallic present in the master alloy is Al$_8$Fe$_2$Si. That is, no binary Al-Fe phases have been observed in the sample. According to the polythermal section of the thermodynamically stable ternary Al-Fe-Si phase diagram given in **Figure 27**, the first phase to solidify from the melt should proeutectic Al$_{13}$Fe$_4$. Upon further cooling, α-Al forms from the remaining liquid at 650 °C. Finally, the solidification is completed with the formation of Al$_8$Fe$_2$Si via peritectic reaction at 632 °C. Thus, the expected solidified phases are Al$_{13}$Fe$_4$, α-Al and Al$_8$Fe$_2$Si under equilibrium solidification conditions. However, as the cooling rate in the arc-melter is relatively high (it is not possible to estimate the cooling rate in the arc-melter) proeutectic

145

Al$_{13}$Fe$_4$ did not form in the master alloy. In other words, only ternary Al-Fe-Si intermetallic has been observed in the master alloy due to high cooling rates. This is in good agreement with previous studies [3], [4] which have shown that nonequilibrium solidification in ternary Al-Fe-Si alloys promotes the formation of ternary phases, particularly, at high cooling rates. Moreover, Khalifa et al. reported that the transition between binary Al-Fe phase to ternary Al-Fe-Si phases can take place at very low cooling rates of around 0.19 °C s^{-1} in ternary alloys with Fe content up to 1 wt% and Si content up to 6 wt%. Here, although it is impossible to estimate the cooling rate in the arc-melter, it is predicted that the cooling rate is higher than 0.19 °C s^{-1}, which was reported as transition from binary to ternary phase formation.

The master alloy was later drop tube atomized and various microstructures have been observed with increasing cooling rate. The drop tube atomized samples have shown different microstructural features to the master alloy. The large script-like and rod-like phases have not been observed in drop tube atomized samples. That is, drop tube atomization has resulted in refinement in the microstructure. Dendritic α-Al with lamellar interdendritic eutectic, cellular α-Al with lamellar eutectic have formed in large samples. XRD results given in **Figure 79** and TEM results given in **Figure 93** have suggested that the lamellar eutectic is Al-Al$_8$Fe$_2$Si.

In all drop tube atomized samples, regardless of their diameter and, thus, cooling rate, α-Al dendrite tip splitting has been observed, which was not observed in drop tube atomized Al-2.85 wt% Fe and Al-3.9 wt% Fe alloys. This would mean that Si addition has caused the dendrite tip splitting. Dendrite tip splitting has been observed in highly undercooled melts [119]. Tip splitting takes place due to the kinetic instability at high undercoolings at high growth rates as a result of the interface departing from local thermodynamic equilibrium [120]. That is, probably Si addition has caused instability in the α-Al dendrite tips which resulted in dendrite tip splitting.

Increasing cooling rate has drastically changed the microstructure of the Al-Fe-Si alloy. An angular zone where nucleation in the samples has emerged in 300-212 µm samples and with decreasing sample size the fraction of the samples with such zone has risen. EDX analysis from the angular zone has shown that while the Fe content of this zone is identical to the melt (4.1 wt% Fe), Si content has dropped to around 1 wt% from 1.9 wt% for all sizes where angular zone has been observed. This means that the solidification was partitionless with respect to Fe but not with respect to Si. It is probably due to the anomalously low diffusivity of Fe in liquid Al as reported by Isono et al. [121] who have measured the diffusivity of Fe in liquid Al and

146

found that the diffusivity of Fe is anomalously low. This is due to "the clustering of Al atoms around Fe atoms in liquid Al-Fe alloys". Therefore, EDX results suggest that Si has higher diffusivity than Fe in liquid Al. According to the data reported by Du et al. [122], the diffusivities of Si, D_{Si}^L, and Fe, D_{Fe}^L, in liquid Al at 900 K is calculated as 2.4 x 10^{-9} m^2 s^{-1} and 2.17 x 10^{-10} m^2 s^{-1}, respectively. That is, Fe diffuses slower than Si in liquid Al, which is in good agreement with the EDX results.

The angular zone seems featureless under SEM (**Figure 82** and **Figure 84**). However, TEM result shown in **Figure 92** has revealed that this region consists of nano sized (around 100 nm in diameter) faceted ternary intermetallics in α-Al matrix. Considering the size and the faceted nature of the intermetallics, the formation of the intermetallics formed in angular nucleation zone indicates that they were formed in the solid state as a result of decomposition of a super-saturated solid solution. Meanwhile EDX results suggests that the Fe concentration in this region is identical to the melt. This would mean that partitionless solidification with respect to Fe has taken place in the undercooled droplet. That is, later, solid state decomposition took place in angular zone following the partitionless solidification due to highly supersaturated and, therefore, unstable α-Al. In drop tube atomized Al-3.9 wt% Fe, solid state decomposition of highly saturated α-Al has also been observed in Y-shaped as covered in **Section 5.3**. However, the solid state decomposition in Al-Fe-Si alloy has formed clusters of ternary phases which has not been observed in Y-shaped. A ternary phase formed in the angular zone from the supersaturated α-Al and this phase acted as heterogeneous nucleation site, thus, forming clusters of faceted intermetallics.

In addition to angular nucleation zone, propeller like structures (**Figure 85** and **86**) and Y-shaped structures (**Figure 87**) have formed in small diameter particles. Y-shaped has been discussed earlier in **Section 6.3**. Therefore, it will not be covered here. There are two types of propeller-like structures: 4-armed with around 90° angle between arms and 3-armed with 120° angle between arms. These propeller-like structures have probably evolved from the angular nucleation zone. Angular structures have concave sides (**Figure 101a**) meaning that these structures are cubes with depressed faces. Solute accumulated (the only solute is Si as the growth is partitionless with respect to Fe) on the flat faces slows down the growth of the faces so that edges grow faster than the central region. Such growth explains the features observed such as shown in **Figure 83d**. Looking at the 2D sectioned part of the depressed cube of (100) face, the four corners of the cube will be visible while the depressed face is not. Moreover, the growth mode of the angular zone has changed from faceted to continuous with increasing

cooling rate and formed propeller-like structures. Similar transformation is shown in **Figure 101b** which was reported to evolve from **Figure 101a** in Sn-Cu-Al solders [123]. Propeller-like structures are probably the growth of {111} dendrites, which gives eight arms growing towards the corners unlike {100} dendritic growth, which gives six arms. This growth also explains that the observed 4-armed and 3-armed propeller-like structures are from the same structure but from different cross section. That is, while sectioning perpendicular to <100> would result in 4 arms with right angle between the arms, sectioning perpendicular to <111> would render 3 arms with 120° between the arms.
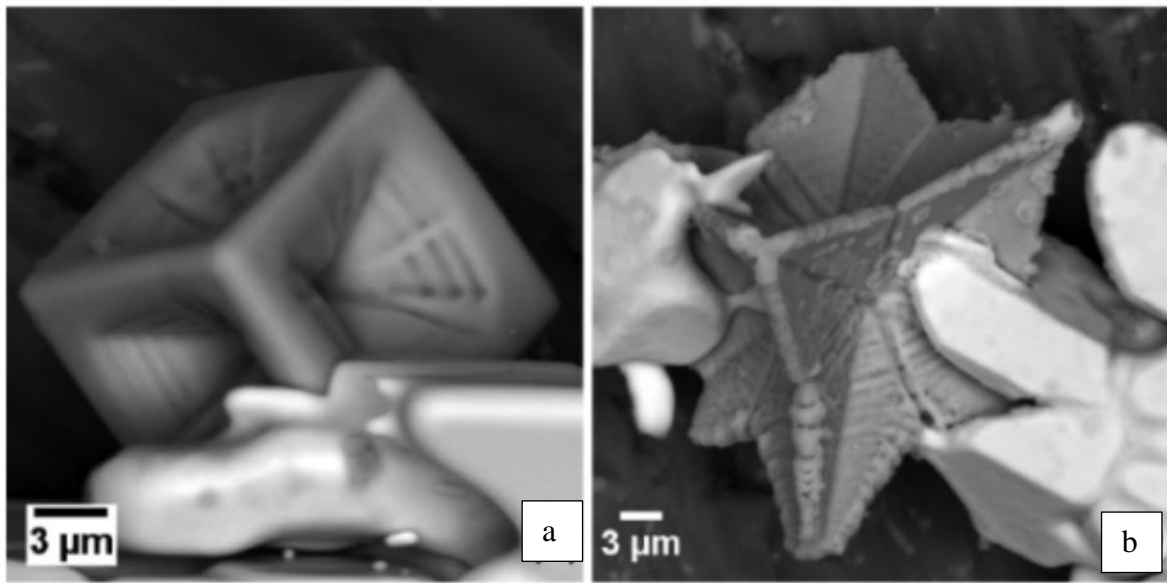
Figure 101: SEM images of Cu_xAl_y grains a) cubic with depressed faces and b) faceted dendritic structure evolved from the continued growth of the structure shown in a) [123].

The characteristic diffusion length can be estimated by

$$\bar{x} = \sqrt{2Dt}$$

(6-2)

where D and t are the diffusion coefficient and the time available for solidification, respectively. The solidification time for 150 µm sample is estimated as t = 0.018 s using the latent heat for aluminium, specific heat for liquid Al given in **Table 6** and the cooling rate, $\dot{T}$, for 150 µm sample from **Figure 38**. Assuming the undercooling in the droplet is around 90 K below the liquidus line, the diffusion coefficient of Si at 930 K was estimated as 1.34 x 10^{-9} m^2 s^{-1} [122]: using these parameters give $\bar{x} = 31.5$ µm. This figure is close to the size of the angular zone given in **Figure 83-84**. Thus, the solute accumulation in the centre of a face of the angular structure can be the explanation for depression in the centre of the faces of the cube.

7. Summary

Binary Al-2.85 wt% Fe and Al-3.9 wt% Fe and ternary Al-4.1 wt% Fe-1.9 wt% Si alloys have been subjected to nonequilibrium cooling using a 6.5 m drop tube and the following conclusions has been made:

1. The estimated cooling rate of the drop tube atomized samples were estimated to be ranging between 155 K s^{-1} and 20,000 K s^{-1} for 850 µm and 38 µm samples, respectively.

2. Microscopy observation has shown that the microstructures: secondary dendrite arm spacings and eutectic spacings, of all drop tube atomized alloys are refined with increasing cooling rate. Moreover, large proeutectic Al$_{13}$Fe$_4$ has disappeared with increasing cooling rate in drop tube atomized Al-3.9 wt% Fe.

3. Dissolved solute content in α-Al has been found to be increasing with increasing cooling rate. As a result, volume fraction of α-Al increases while that for Al-Al$_{13}$Fe$_4$ eutectic.

4. Al-Al$_{13}$Fe$_4$ has been observed at growth velocities in excess of 20 mm s^{-1}.

5. Partitionless solidification took place in all samples and it was found that higher Fe content and higher cooling rates promote the partitionless solidification. Partitionless solidification has resulted in the formation of Y-shaped structures in binary systems, which transformed in to dendrite-like structure with increasing cooling rate.

6. Serial sectioning of Y-shaped structure has revealed that Y-shaped is internally connected sheet-like morphology.

7. Y-shaped structures have been found to be composed of nano-sized Al$_m$Fe particles in binary Al-Fe alloys which formed from decomposition of highly supersaturated and unstable α-Al.

8. Similarly, clusters of nano-sized faceted Al$_8$Fe$_2$Si and Y-shaped structures have formed from highly supersaturated α-Al.

8. Future Work

Although this worked has provided some interesting results, further research should be made:

1. It would be interesting to see whether it is possible to form samples with fully partitionless solidification. In other words, forming samples which is composed of only nano-sized precipitates on α-Al in both binary and ternary systems. As this work suggests increasing Fe content together with increasing cooling rate (e.g., using He instead of Nitrogen) favours partitionless solidification. Moreover, Si addition further increases the fraction of partitionless solidification. Forming fully partitionless samples will improve the possible technologically usefulness of Al-Fe and Al-Fe-Si alloys, particularly, in powder metallurgy.

2. It would be interesting to investigate the effect of heat treatment on the drop tube atomized Al-Fe and Al-Fe-Si samples. As the solute content increases in α-Al with increasing cooling rate, heat treatment will result in the decomposition of supersaturated α-Al resulting in the formation of precipitation of binary or ternary phases. This will probably increase the mechanical properties of the alloys. Moreover, this will give some idea on possible use of these alloys in powder metallurgy.

3. 3D structure Y-shaped morphology should be further investigated using, such as, X-ray microtomography and/or Plasma FIB SEM, which provide serial sectioning along the whole sample. This will help to better understand the formation of Y-shape.

9. References

[1] M. H. S. I. N. VRO and E. STISKANIH, "Microstructure of rapidly solidified and hot-pressed Al-Fe-X Alloys," *Mater. Tehnol.*, vol. 48, no. 3, pp. 349–353, 2014.

[2] L. Zhang, J. Gao, L. N. W. Damoah, and D. G. Robertson, "Removal of iron from aluminum: A review," *Miner. Process. Extr. Metall. Rev.*, vol. 33, no. 2, pp. 99–157, 2012, doi: 10.1080/08827508.2010.542211.

[3] Y. Zhang, Y. Liu, Y. Han, C. Wei, and Z. Gao, "The role of cooling rate in the microstructure of Al–Fe–Si alloy with high Fe and Si contents," *J. Alloys Compd.*, vol. 473, no. 1–2, pp. 442–445, 2009.

[4] W. Khalifa, F. H. Samuel, and J. E. Gruzleski, "Iron intermetallic phases in the Al corner of the Al-Si-Fe system," *Metall. Mater. Trans. A*, vol. 34, no. 13, pp. 807–825, 2003.

[5] J. Chen, U. Dahlborg, C. M. Bao, M. Calvo-Dahlborg, and H. Henein, "Microstructure evolution of atomized Al-0.61 wt pct Fe and Al-1.90 wt pct Fe alloys," *Metall. Mater. Trans. B Process Metall. Mater. Process. Sci.*, vol. 42, no. 3, pp. 557–567, 2011, doi: 10.1007/s11663-011-9485-6.

[6] D. K. Mukhopadhyay, C. Suryanarayana, and F. H. Froes, "Structural evolution in mechanically alloyed Al-Fe powders," *TMS Annu. Meet.*, vol. 26, no. AUGUST, pp. 191–202, 1995.

[7] S. S. Nayak, B. S. Murty, and S. K. Pabi, "Structure of nanocomposites of Al-Fe alloys prepared by mechanical alloying and rapid solidification processing," *Bull. Mater. Sci.*, vol. 31, no. 3, pp. 449–454, 2008, doi: 10.1007/s12034-008-0070-9.

[8] E. Çadırlı, D. M. Herlach, and T. Volkmann, "Characterization of rapidly solidified Ni–Si and Co–Al eutectic alloys in drop tube," *J. Non. Cryst. Solids*, vol. 356, no. 9–10, pp. 461–466, 2010.

[9] A. M. Mullis, T. D. Bigg, and N. J. Adkins, "A microstructural investigation of gas atomized Raney type Al-27.5 at.% Ni catalyst precursor alloys," *J. Alloys Compd.*, vol. 648, pp. 139–148, 2015.

[10] S. Li, P. Wu, H. Fukuda, and T. Ando, "Simulation of the solidification of gas-atomized Sn-5mass%Pb droplets," *Mater. Sci. Eng. A*, vol. 499, no. 1–2, pp. 396–403, 2009, doi: 10.1016/j.msea.2008.08.041.

[11] S. C. Sharma, T. Volkmann, and D. M. Herlach, "Microstructural development in drop-tube-solidified Al-3.6wt.%Fe droplets: an analysis," *Mater. Sci. Eng. A*, vol. 171, no. 1–2, pp. 169–173, 1993, doi: 10.1016/0921-5093(93)90403-2.

[12] W. J. Boettinger, L. Bendersky, and J. G. Early, "An analysis of the microstructure of rapidly solidified Al-8 wt pct Fe powder," *Metall. Trans. A*, vol. 17, no. 5, pp. 781–790, 1986.

[13] R. F. Cochrane, P. V Evans, and A. L. Greer, "Competitive growth analysis of phase formation in Al-8wt.% Fe," *Mater. Sci. Eng. A*, vol. 133, pp. 803–806, 1991.

[14] A. Griger and V. Stefaniay, "Equilibrium and non-equilibrium intermetallic phases in Al-Fe and Al-Fe-Si alloys," *J. Mater. Sci.*, vol. 31, no. 24, pp. 6645–6652, 1996.

[15] N. Ünlü, A. Genc, M. L. Öveçoğlu, N. Eruslu, and F. H. Froes, "Characterization

investigations of melt-spun ternary Al–xSi–3.3 Fe (x= 10, 20 wt.%) alloys," *J. Alloys Compd.*, vol. 322, no. 1–2, pp. 249–256, 2001.

[16] M. F. Kiliçaslan, F. Yilmaz, S. Ergen, S.-J. Hong, and O. Uzun, "Microstructure and microhardness of melt-spun Al–25Si–5Fe–XCo (X= 0, 1, 3, 5) alloys," *Mater. Charact.*, vol. 77, pp. 15–22, 2013.

[17] E. M. Ahmed and M. R. Ebrahim, "Microstructure and Microhardness Evolutions of High Fe Containing Near-Eutectic Al-Si Rapidly Solidified Alloy," *J. Metall.*, vol. 2014, pp. 1–8, 2014, doi: 10.1155/2014/587265.

[18] P. B. Hirsch, "Elements of X-Ray Diffraction," *Phys. Bull.*, vol. 8, no. 7, pp. 237–238, 1957, doi: 10.1088/0031-9112/8/7/008.

[19] O. Ouadah, G. Merad, and H. Si Abdelkader, "Theoretic quantum analysis of mechanical and electronic properties of TiAl-M (M= Mo, W, Cu and Zn)," *Int. J. Quantum Chem.*, vol. 121, no. 9, p. e26590, 2021.

[20] W. D. Callister, *Materials science and engineering an introduction*. John Wiley, 2007.

[21] T. Suzuki, "Fundamentals of solidification phenomena," *Keikinzoku/Journal Japan Inst. Light Met.*, vol. 46, no. 3, pp. 156–161, 1996.

[22] D. A. Porter and K. E. Easterling, *Phase transformations in metals and alloys (revised reprint)*. CRC press, 2009.

[23] W. Kurz and D. J. Fischer, "Fundamentals-of-Solidification." 1989.

[24] T. Suzuki, "Fundamentals of solidification phenomena," *Keikinzoku/Journal Japan Inst. Light Met.*, vol. 46, no. 3, pp. 156–161, 1996.

[25] D. M. Stefanescu and R. Ruxanda, "Fundamentals of solidification," *Mater. Park. OH ASM Int. 2004.*, pp. 71–92, 2004.

[26] D. Bouchard and J. S. Kirkaldy, "Prediction of dendrite arm spacings in unsteady-and steady-state heat flow of unidirectionally solidified binary alloys," *Metall. Mater. Trans. B*, vol. 28, no. 4, pp. 651–663, 1997.

[27] B. Raw, L. SEl, C. Bt HaU Japan, D. Porter, and K. Easterling, "m, LX," 1995.

[28] K. A. Jackson, "Hunt. JD Lamellar and rod eutectic growth," *Trans. AIME*, vol. 236, pp. 1129–1142, 1966.

[29] W. J. Boettinger, S. R. Coriell, and R. F. Sekerka, "Mechanisms of microsegregation-free solidification," *Mater. Sci. Eng.*, vol. 65, no. 1, pp. 27–36, 1984.

[30] J. Juarez-Islas, Y. Zhou, and E. J. Lavernia, "Spray atomization of two Al–Fe binary alloys: solidification and microstructure characterization," *J. Mater. Sci.*, vol. 34, no. 6, pp. 1211–1218, 1999.

[31] O. V Gusakova, P. K. Galenko, V. G. Shepelevich, D. V Alexandrov, and M. Rettenmayr, "Diffusionless (chemically partitionless) crystallization and subsequent decomposition of supersaturated solid solutions in Sn–Bi eutectic alloy," *Philos. Trans. R. Soc. A*, vol. 377, no. 2143, p. 20180204, 2019.

[32] D. M. Herlach, "Non-equilibrium solidification of undercooled metallic metls," *Mater. Sci. Eng. R Reports*, vol. 12, no. 4–5, pp. 177–272, 1994.

[33] N. J. E. Adkins, *Microstructure and properties of rapidly solidified aluminium containing Cr, Zr and Mn*. 1989.

[34] D. M. Herlach, "Non-equilibrium solidification of undercooled metallic melts," *Metals (Basel).*, vol. 4, no. 2, pp. 196–234, 2014.

[35] J. L. Walker and G. R. St Pierre, "The physical chemistry of process metallurgy," *Part*, vol. 2, p. 845, 1959.

[36] J. Zhang, H. Wang, F. Zhang, X. Lü, Y. Zhang, and Q. Zhou, "Growth kinetics and grain refinement mechanisms in an undercooled melt of a CoSi intermetallic compound," *J. Alloys Compd.*, vol. 781, pp. 13–25, 2019.

[37] A. M. Mullis, "The origins of spontaneous grain refinement in deeply undercooled metallic melts," *Metals (Basel).*, vol. 4, no. 2, pp. 155–167, 2014.

[38] A. M. Mullis and N. Haque, "Evidence for dendritic fragmentation in as-solidified samples of deeply undercooled melts," *J. Cryst. Growth*, vol. 529, p. 125276, 2020.

[39] J. W. CHRISTIAN, "CHAPTER 13 - Growth From the Vapour Phase," in *The Theory of Transformations in Metals and Alloys*, J. W. CHRISTIAN, Ed. Oxford: Pergamon, 2002, pp. 553–622.

[40] J. W. CHRISTIAN, "CHAPTER 24 - Rapid Solidification," in *The Theory of Transformations in Metals and Alloys*, J. W. CHRISTIAN, Ed. Oxford: Pergamon, 2002, pp. 1076–1088.

[41] E. Huttunen-Saarivirta, "Microstructure, fabrication and properties of quasicrystalline Al–Cu–Fe alloys: a review," *J. Alloys Compd.*, vol. 363, no. 1, pp. 154–178, 2004, doi: https://doi.org/10.1016/S0925-8388(03)00445-6.

[42] D. Shechtman, I. Blech, D. Gratias, and J. W. Cahn, "Metallic Phase with Long-Range Orientational Order and No Translational Symmetry," *Phys. Rev. Lett.*, vol. 53, no. 20, pp. 1951–1953, Nov. 1984, doi: 10.1103/PhysRevLett.53.1951.

[43] A.-P. Tsai, A. Inoue, and T. Masumoto, "A Stable Quasicrystal in Al-Cu-Fe System," *Jpn. J. Appl. Phys.*, vol. 26, no. Part 2, No. 9, pp. L1505--L1507, Sep. 1987, doi: 10.1143/jjap.26.l1505.

[44] A. P. Tsai, A. Inoue, Y. Yokoyama, and T. Masumoto, "Stable Icosahedral Al–Pd–Mn and Al–Pd–Re Alloys," *Mater. Trans. JIM*, vol. 31, no. 2, pp. 98–103, 1990, doi: 10.2320/matertrans1989.31.98.

[45] M. F. Ashby and A. L. Greer, "Metallic glasses as structural materials," *Scr. Mater.*, vol. 54, no. 3, pp. 321–326, 2006, doi: https://doi.org/10.1016/j.scriptamat.2005.09.051.

[46] C. Suryanarayana and A. Inoue, *Bulk metallic glasses*. CRC press, 2017.

[47] D. Turnbull, "Under what conditions can a glass be formed?," *Contemp. Phys.*, vol. 10, no. 5, pp. 473–488, 1969.

[48] W. Klement, R. H. Willens, and P. O. L. Duwez, "Non-crystalline structure in solidified gold–silicon alloys," *Nature*, vol. 187, no. 4740, pp. 869–870, 1960.

[49] L. Zhong, J. Wang, H. Sheng, Z. Zhang, and S. X. Mao, "Formation of monatomic metallic glasses through ultrafast liquid quenching," *Nature*, vol. 512, no. 7513, pp. 177–180, 2014, doi: 10.1038/nature13617.

[50] W. H. Wang, C. Dong, and C. H. Shek, "Bulk metallic glasses," *Mater. Sci. Eng. R Reports*, vol. 44, no. 2, pp. 45–89, 2004, doi: https://doi.org/10.1016/j.mser.2004.03.001.

[51] A. Inoue, T. Zhang, and T. Masumoto, "Al–La–Ni Amorphous Alloys with a Wide Supercooled Liquid Region," *Mater. Trans. JIM*, vol. 30, no. 12, pp. 965–972, 1989, doi: 10.2320/matertrans1989.30.965.

[52] A. Inoue and N. Nishiyama, "Extremely low critical cooling rates of new Pd-Cu-P base amorphous alloys," *Mater. Sci. Eng. A*, vol. 226–228, pp. 401–405, 1997, doi: https://doi.org/10.1016/S0921-5093(97)80051-2.

[53] A. L. Greer, "Nucleation and solidification studies using drop-tubes," *Mater. Sci. Eng. A*, vol. 178, no. 1–2, pp. 113–120, 1994.

[54] W. H. Hofmeister, R. J. Bayuzick, and M. B. Robinson, "Noncontact temperature measurement of a falling drop," *Int. J. Thermophys.*, vol. 10, no. 1, pp. 279–292, 1989.

[55] O. Oloyede, T. D. Bigg, R. F. Cochrane, and A. M. Mullis, "Microstructure evolution and mechanical properties of drop-tube processed, rapidly solidified grey cast iron," *Mater. Sci. Eng. A*, vol. 654, pp. 143–150, 2016, doi: 10.1016/j.msea.2015.12.020.

[56] C. S. Kiminami, "Influence of heterogeneous nuclei on the solidification of Pd77. 5Cu6Si16. 5 glassy alloy," *Mater. Sci. Eng.*, vol. 97, pp. 195–198, 1988.

[57] S. Ebalard, F. Spaepen, R. F. Cochrane, and A. L. Greer, "Undercooling experiments on quasicrystal-forming melts," *Mater. Sci. Eng. A*, vol. 133, pp. 569–573, 1991.

[58] E. Schleip, D. M. Herlach, and B. Feuerbacher, "External seeding of a metastable metallic phase," *EPL (Europhysics Lett.*, vol. 11, no. 8, p. 751, 1990.

[59] B. Sundman, I. Ohnuma, N. Dupin, U. R. Kattner, and S. G. Fries, "An assessment of the entire Al–Fe system including D03 ordering," *Acta Mater.*, vol. 57, no. 10, pp. 2896–2908, 2009, doi: https://doi.org/10.1016/j.actamat.2009.02.046.

[60] M. V Glazoff, V. S. Zolotorevsky, and N. A. Belov, *Casting aluminum alloys*. Elsevier, 2010.

[61] P. Skjerpe, "Structure of AlmFe," *Acta Crystallogr. Sect. B Struct. Sci.*, vol. 44, no. 5, pp. 480–486, 1988.

[62] E. H. Hollingsworth and G. R. Frank, "Jr and RE Willet," *Trans. Met. Soc. AIME*, vol. 224, p. 188, 1962.

[63] H. Westengen, "Formation of intermetallic compounds during DC casting of a commercial purity Al-Fe-Si alloy," 1982.

[64] R. M. K. Young and T. W. Clyne, "An AlmFe intermetallic phase formed during controlled solidification," *Scr. Metall.*, vol. 15, no. 11, pp. 1211–1216, 1981.

[65] R. Simensen, C. J., & Vellasamy, "Determination of Phases Present in Cast Material of an Al-0.5 wt.% Fe-0.2 wt.% Si Alloy," *Int. J. Mater. Res.*, vol. 68(6), pp. 428–431, 1977.

[66] P. Liu, T. Thorvaldsson, and G. L. Dunlop, "Formation of intermetallic compounds during solidification of dilute Al–Fe–Si alloys," *Mater. Sci. Technol.*, vol. 2, no. 10, pp. 1009–1018, 1986.

[67] F. Stein and M. Palm, "Re-determination of transition temperatures in the Fe–Al system by differential thermal analysis," *Int. J. Mater. Res.*, vol. 98, no. 7, pp. 580–588, 2007.

[68] F. Stein, S. C. Vogel, M. Eumann, and M. Palm, "Determination of the crystal structure of the ε phase in the Fe–Al system by high-temperature neutron diffraction," *Intermetallics*, vol. 18, no. 1, pp. 150–156, 2010.

[69] I. Chumak, K. W. Richter, and H. Ehrenberg, "Redetermination of iron dialuminide, FeAl2," *Acta Crystallogr. Sect. C Cryst. Struct. Commun.*, vol. 66, no. 9, pp. i87–i88, 2010.

[70] U. Burkhardt, Y. Grin, M. Ellner, and K. Peters, "Structure refinement of the iron–aluminium phase with the approximate composition Fe2Al5," *Acta Crystallogr. Sect. B Struct. Sci.*, vol. 50, no. 3, pp. 313–316, 1994.

[71] L. F. Mondolfo, "Aluminium Alloys: Structure and Properties, Butterworths, London 1976."

[72] V. I. Dobatkin, V. I. Elagin, and V. M. Fedorov, "Rapidly Crystallized Aluminum Alloys," *VILS, Moscow*, pp. 121–122, 1995.

[73] Y. Wang, H. Jones, and P. V. Evans, "Eutectic solidification characteristics of Bridgman grown Al-3Fe-0.1V alloy," *J. Mater. Sci.*, vol. 33, no. 21, pp. 5205–5220, 1998, doi: 10.1023/A:1004483904519.

[74] N. A. Belov, A. A. Aksenov, and D. G. Eskin, *Iron in aluminium alloys: impurity and alloying element*. CRC Press, 2002.

[75] C. M. Adam and L. M. Hogan, "Crystallography of the Al-Al3 Fe eutectic," *Acta Metall.*, vol. 23, no. 3, pp. 345–354, 1975.

[76] C. M. Allen, K. A. Q. O'reilly, B. Cantor, and P. V Evans, "Intermetallic phase selection in 1XXX Al alloys," *Prog. Mater. Sci.*, vol. 43, no. 2, pp. 89–170, 1998.

[77] I. R. Hughes and H. Jones, "Coupled eutectic growth in Al-Fe alloys," *J. Mater. Sci.*, vol. 11, no. 10, pp. 1781–1793, 1976, doi: 10.1007/bf00708256.

[78] I. R. Hughes and H. Jones, "Coupled eutectic growth in Al-Fe alloys," *J. Mater. Sci.*, vol. 12, no. 2, pp. 323–333, 1977.

[79] P. Gilgien, A. Zryd, and W. Kurz, "Microstructure selection maps for Al-Fe alloys," *Acta Metall. Mater.*, vol. 43, no. 9, pp. 3477–3487, 1995.

[80] P. R. Goulart, J. E. Spinelli, N. Cheung, N. Mangelinck-Nöel, and A. Garcia, "Al–Fe hypoeutectic alloys directionally solidified under steady-state and unsteady-state conditions," *J. Alloys Compd.*, vol. 504, no. 1, pp. 205–210, 2010.

[81] W. A. Tiller, "Recent research on cast iron," *New York*, p. 129, 1968.

[82] Y. Li, "Bulk metallic glasses: Eutectic coupled zone and amorphous formation," *Jom*, vol. 57, no. 3, pp. 60–63, 2005.

[83] O. Uzun, T. Karaaslan, M. Gogebakan, and M. Keskin, "Hardness and microstructural characteristics of rapidly solidified Al–8–16 wt.% Si alloys," *J. Alloys Compd.*, vol. 376, no. 1–2, pp. 149–157, 2004.

[84] J. D. Roehling *et al.*, "Rapid solidification growth mode transitions in Al-Si alloys by

dynamic transmission electron microscopy," *Acta Mater.*, vol. 131, pp. 22–30, 2017.

[85] L. L. Ge, R. P. Liu, G. Li, M. Z. Ma, and W. K. Wang, "Solidification of Al–50 at.% Si alloy in a drop tube," *Mater. Sci. Eng. A*, vol. 385, no. 1–2, pp. 128–132, 2004.

[86] D. Munson, "A clarification of the phases occurring in aluminium-rich aluminium-iron-silicon alloys, with particular reference to the ternary phase alpha-AlFeSi," *INST Met. J*, vol. 95, no. 7, pp. 217–219, 1967.

[87] S. S. Nayak, H. J. Chang, D. H. Kim, S. K. Pabi, and B. S. Murty, "Formation of metastable phases and nanocomposite structures in rapidly solidified Al-Fe alloys," *Mater. Sci. Eng. A*, vol. 528, no. 18, pp. 5967–5973, 2011, doi: 10.1016/j.msea.2011.04.028.

[88] R. F. Cochrane, P. V. Evans, and A. L. Greer, "Containerless solidification of alloys in a drop-tube," *Mater. Sci. Eng.*, vol. 98, no. C, pp. 99–103, 1988, doi: 10.1016/0025-5416(88)90135-8.

[89] H. Henein *et al.*, "Droplet solidification of impulse atomized Al-0.61Fe and Al-1.9Fe," *Can. Metall. Q.*, vol. 49, no. 3, pp. 275–292, 2010, doi: 10.1179/cmq.2010.49.3.275.

[90] B. L. Silva, A. Garcia, and J. E. Spinelli, "The effects of microstructure and intermetallic phases of directionally solidified Al–Fe alloys on microhardness," *Mater. Lett.*, vol. 89, pp. 291–295, 2012.

[91] S. C. Sharma, T. Volkmann, and D. M. Herlach, "Microstructural development in drop-tube-solidified Al-3.6 wt.% Fe droplets: an analysis," *Mater. Sci. Eng. A*, vol. 171, no. 1–2, pp. 169–173, 1993.

[92] J. Chen, R. Lengsdorf, H. Henein, D. M. Herlach, U. Dahlborg, and M. Calvo-Dahlborg, "Microstructure evolution in undercooled Al–8 wt% Fe melts: Comparison between terrestrial and parabolic flight conditions," *J. Alloys Compd.*, vol. 556, pp. 243–251, 2013.

[93] M. H. Jacobs, A. G. Doggett, and M. J. Stowell, "The microstructure of Al-8 wt% Fe-based alloys prepared by rapid quenching from the liquid state," *J. Mater. Sci.*, vol. 9, no. 10, pp. 1631–1643, 1974.

[94] M. G. Chu and D. A. Granger, "Solidification and microstructure analysis of rapidly solidified melt-spun Al-Fe alloys," *Metall. Trans. A*, vol. 21, no. 1, pp. 205–212, 1990, doi: 10.1007/BF02656437.

[95] D. H. Kim and B. Cantor, "Structure and decomposition behaviour of rapidly solidified Al-Fe alloys," *J. Mater. Sci.*, vol. 29, no. 11, pp. 2884–2892, 1994.

[96] L. Cao, "Rapid solidification of Ni-Si-Fe intermetallics in drop tube." University of Leeds, 2014.

[97] E. Atkins, "Elements of X-ray diffraction." IOP Publishing, 1978.

[98] B. J. Inkson, "2 - Scanning electron microscopy (SEM) and transmission electron microscopy (TEM) for materials characterization," in *Materials Characterization Using Nondestructive Evaluation (NDE) Methods*, G. Hübschen, I. Altpeter, R. Tschuncky, and H.-G. Herrmann, Eds. Woodhead Publishing, 2016, pp. 17–43.

[99] P. J. Goodhew and J. Humphreys, *Electron microscopy and analysis*. CRC Press, 2000.

[100] C. B. Carter and D. B. Williams, *Transmission electron microscopy: Diffraction, imaging, and spectrometry*. Springer, 2016.

[101] M. El-Sherbiny, R. Hegazy, M. Ibrahim, and A. Abuelezz, "The influence of geometrical tolerances of Vickers indenter on the accuracy of measured hardness," *Int. J. Metrol. Qual. Eng.*, vol. 3, no. 1, pp. 1–6, 2012.

[102] M. Erol and U. Büyük, "Solidification Behavior of Ge–Al Eutectic Alloy in a Drop Tube," *Trans. Indian Inst. Met.*, vol. 69, no. 4, pp. 961–970, 2016, doi: 10.1007/s12666-015-0592-y.

[103] E. S. Lee and S. Ahn, "Solidification progress and heat transfer analysis of gas-atomized alloy droplets during spray forming," *Acta Metall. Mater.*, vol. 42, no. 9, pp. 3231–3243, 1994, doi: 10.1016/0956-7151(94)90421-9.

[104] I. Miki, H. Kosuge, and K. Nagahama, "Supersaturation and decomposition of Al-Fe alloys during solidification," *J. Japan Inst. Light Met.*, vol. 25, no. 1, pp. 1–9, 1975.

[105] A. Aliravci, "Kinetics, thermodynamics and mechanism of metastable Al-AlmFe phase and fir-tree zone formation in DC-cast Al-Fe-Si alloy ingots," 2006.

[106] G. Kasperovich, T. Volkmann, L. Ratke, and D. Herlach, "Microsegregation during solidification of an Al-Cu binary alloy at largely different cooling rates (0.01 to 20,000 K/s): Modeling and experimental study," *Metall. Mater. Trans. A Phys. Metall. Mater. Sci.*, vol. 39 A, no. 5, pp. 1183–1191, 2008, doi: 10.1007/s11661-008-9505-6.

[107] O. Oloyede, T. D. Bigg, R. F. Cochrane, and A. M. Mullis, "Microstructure evolution and mechanical properties of drop-tube processed, rapidly solidified grey cast iron," *Mater. Sci. Eng. A*, vol. 654, pp. 143–150, 2016.

[108] S. S. Nayak, H. J. Chang, D. H. Kim, S. K. Pabi, and B. S. Murty, "Formation of metastable phases and nanocomposite structures in rapidly solidified Al–Fe alloys," *Mater. Sci. Eng. A*, vol. 528, no. 18, pp. 5967–5973, 2011.

[109] C. M. Adam, A. CM, and H. LM, "The aluminium-iron eutectic system," 1972.

[110] R. Trivedi and W. Kurz, "Microstructure selection in eutectic alloy systems," *Solidif. Process. eutectic Alloy.*, pp. 3–34, 1988.

[111] P. Lü and H. P. Wang, "Observation of the transition from primary dendrites to coupled growth induced by undercooling within NiZr hyperperitectic alloy," *Scr. Mater.*, vol. 137, pp. 31–35, 2017, doi: 10.1016/j.scriptamat.2017.05.006.

[112] D. Liang and H. Jones, "The effect of growth velocity on growth temperature of the Al-Al3Fe and Al-Al6Fe eutectics," *Zeitschrift für Met.*, vol. 83, no. 4, pp. 224–226, 1992.

[113] H. W. L. Phillips, *Annotated equilibrium diagrams of some aluminium alloy systems*, no. 25. Institute of metals, 1959.

[114] H. Henein *et al.*, "Droplet solidification of impulse atomized Al-0.61 Fe and Al-1.9 Fe," *Can. Metall. Q.*, vol. 49, no. 3, pp. 275–292, 2010.

[115] A. Prasad, H. Henein, E. Maire, and C.-A. Gandin, "X-ray tomography study of atomized Al-Cu droplets," *Can. Metall. Q.*, vol. 43, no. 2, pp. 273–282, 2004.

[116] A. Griger, V. Stefániay, E. Kovács-Csetényi, and T. Turmezey, "Formation and transformation of binary intermetallic phases in high purity Al-Fe alloys," in *Key*

Engineering Materials, 1990, vol. 44, pp. 17–30.

[117] S. A. Belyakov and C. M. Gourlay, "NiSn4 formation during the solidification of Sn–Ni alloys," *Intermetallics*, vol. 25, pp. 48–59, 2012.

[118] K. A. Jackson and J. D. Hunt, "Lamellar and rod eutectic growth," in *Dynamics of Curved Fronts*, Elsevier, 1988, pp. 363–376.

[119] K. Dragnevski, R. F. Cochrane, and A. M. Mullis, "Experimental evidence for dendrite tip splitting in deeply undercooled, ultrahigh purity Cu," *Phys. Rev. Lett.*, vol. 89, no. 21, p. 215502, 2002.

[120] A. M. Mullis and R. F. Cochrane, "A phase field model for spontaneous grain refinement in deeply undercooled metallic melts," *Acta Mater.*, vol. 49, no. 12, pp. 2205–2214, 2001.

[121] N. Isono, P. M. Smith, D. Turnbull, and M. J. Aziz, "Anomalous diffusion of Fe in Liquid AI Measured by the pulsed laser technique," *Metall. Mater. Trans. A*, vol. 27, no. 3, pp. 725–730, 1996.

[122] Y. Du *et al.*, "Diffusion coefficients of some solutes in fcc and liquid Al: critical evaluation and correlation," *Mater. Sci. Eng. A*, vol. 363, no. 1–2, pp. 140–151, 2003.

[123] J. W. Xian, S. A. Belyakov, T. B. Britton, and C. M. Gourlay, "Heterogeneous nucleation of Cu6Sn5 in Sn–Cu–Al solders," *J. Alloys Compd.*, vol. 619, pp. 345–355, 2015.

10. Appendix

Appendix A: Crystallographic parameters of the identified phases

Below are the standard XRD data of the evolved phases analysed in this work. The given XRD data belongs to α-Al, $Al_{13}Fe_4$, Al_6Fe, Al_5Fe_2 and Al_8Fe_2Si, respectively. However, as there is no completer XRD data for Al_mFe, incomplete XRD data given in reference [105] was used.

α-Al

Reference code:	04-001-7364	
Crystal system:	Cubic	
Space group:	Fm-3m	
Space group number:	225	
a (Å):	4.0470	
b (Å):	4.0470	
c (Å):	4.0470	
Alpha (°):	90.0000	
Beta (°):	90.0000	
Gamma (°):	90.0000	

No.	h	k	l	d [A]	2Theta[deg]	I [%]
1	1	1	1	2.33650	38.499	100.0
2	2	0	0	2.02350	44.751	45.9
3	2	2	0	1.43080	65.146	23.5
4	3	1	1	1.22020	78.291	23.4
5	2	2	2	1.16830	82.498	6.4
6	4	0	0	1.01180	99.161	2.6
7	3	3	1	0.92840	112.137	7.6
8	4	2	0	0.90490	116.697	7.1
9	4	2	2	0.82610	137.641	5.6

$Al_{13}Fe_4$

Reference code:01-073-3008

Crystal system:	Monoclinic	
Space group:	C2/m	
Space group number:	12	
a (Å):	15.4920	
b (Å):	8.0780	
c (Å):	12.4710	
Alpha (°):	90.0000	
Beta (°):	107.6900	
Gamma (°):	90.0000	

No.	h	k	l	d [A]	2Theta[deg]	I [%]
1	0	0	1	11.88130	7.435	0.7
2	-2	0	1	7.37970	11.983	0.6
3	2	0	0	7.37970	11.983	0.6

4	1	1	0	7.08610	12.481	3.1
5	-1	1	1	6.51860	13.573	14.2
6	0	0	2	5.94060	14.901	2.3
7	1	1	1	5.72930	15.454	8.0
8	2	0	1	5.55750	15.934	1.4
9	-2	0	2	5.51860	16.047	1.3
10	-1	1	2	4.91950	18.017	0.2
11	-3	1	1	4.33040	20.493	0.1
12	1	1	2	4.25700	20.850	0.8
13	3	1	0	4.20190	21.127	0.2
14	2	0	2	4.06360	21.854	23.8
15	-2	0	3	4.03820	21.993	33.2
16	0	2	0	4.03820	21.993	33.2
17	0	0	3	3.96040	22.431	34.3
18	-4	0	1	3.87290	22.945	6.4
19	0	2	1	3.82410	23.242	3.0
20	4	0	0	3.68990	24.099	20.6
21	-1	1	3	3.68990	24.099	20.6
22	3	1	1	3.67460	24.201	18.7
23	-4	0	2	3.67460	24.201	18.7
24	-2	2	1	3.54300	25.114	45.3
25	2	2	0	3.54300	25.114	45.3
26	0	2	2	3.34010	26.667	24.4
27	-3	1	3	3.34010	26.667	24.4
28	2	2	1	3.26730	27.273	18.2
29	4	0	1	3.25930	27.341	16.6
30	-2	2	2	3.25930	27.341	16.6
31	-4	0	3	3.23400	27.559	5.2
32	2	0	3	3.11720	28.613	2.5
33	-2	0	4	3.10120	28.764	3.8
34	3	1	2	3.07480	29.017	0.4
35	0	0	4	2.97030	30.061	2.3
36	-5	1	1	2.88860	30.932	0.2
37	-1	1	4	2.88860	30.932	0.2
38	2	2	2	2.86460	31.198	0.4
39	-2	2	3	2.85570	31.298	0.3
40	-5	1	2	2.84250	31.447	1.5
41	0	2	3	2.82780	31.615	0.4
42	-3	1	4	2.79080	32.045	0.2
43	-4	2	1	2.79080	32.045	0.2
44	5	1	0	2.77260	32.261	2.9
45	4	0	2	2.77260	32.261	2.9
46	-4	0	4	2.75930	32.421	1.0
47	4	2	0	2.72420	32.850	1.5
48	-4	2	2	2.72420	32.850	1.5
49	-5	1	3	2.65500	33.732	0.3
50	1	3	0	2.64890	33.812	0.3
51	-1	3	1	2.61590	34.251	0.9
52	1	1	4	2.60710	34.371	0.6
53	-6	0	2	2.56490	34.954	2.0
54	3	1	3	2.56490	34.954	2.0
55	1	3	1	2.55600	35.080	0.4
56	5	1	1	2.54410	35.249	0.9
57	4	2	1	2.53430	35.390	4.4
58	-4	2	3	2.52450	35.532	6.7
59	2	0	4	2.50450	35.825	0.8
60	2	2	3	2.46780	36.377	3.3
61	-1	3	2	2.46780	36.377	3.3
62	-2	2	4	2.45980	36.499	5.1
63	6	0	0	2.45980	36.499	5.1
64	-6	0	3	2.44970	36.655	0.9

65	0	2	4	2.39290	37.557	2.2
66	-5	1	4	2.39290	37.557	2.2
67	-3	3	1	2.38420	37.699	1.6
68	1	3	2	2.37170	37.905	6.9
69	-1	1	5	2.36200	38.067	8.2
70	3	3	0	2.36200	38.067	8.2
71	-3	1	5	2.34560	38.344	0.8
72	-4	0	5	2.34560	38.344	0.8
73	-3	3	2	2.31390	38.890	11.1
74	4	2	2	2.28930	39.325	1.1
75	6	0	1	2.27580	39.568	4.2
76	5	1	2	2.27580	39.568	4.2
77	-1	3	3	2.25950	39.865	17.0
78	-6	0	4	2.25950	39.865	17.0
79	-3	3	3	2.17290	41.526	8.7
80	3	1	4	2.17290	41.526	8.7
81	-6	2	2	2.16520	41.681	4.0
82	-6	2	1	2.16520	41.681	4.0
83	1	1	5	2.16000	41.786	12.4
84	1	3	3	2.14840	42.022	6.0
85	2	2	4	2.12940	42.415	10.5
86	-5	1	5	2.12940	42.415	10.5
87	-7	1	1	2.11720	42.671	2.5
88	6	2	0	2.10090	43.019	90.5
89	3	3	2	2.09460	43.154	75.4
90	-6	2	3	2.09460	43.154	75.4
91	2	0	5	2.08460	43.372	34.6
92	-7	1	3	2.07710	43.537	31.0
93	-2	0	6	2.07710	43.537	31.0
94	6	0	2	2.06200	43.872	26.2
95	0	2	5	2.04810	44.185	100.0
96	-6	0	5	2.04810	44.185	100.0
97	7	1	0	2.04090	44.349	70.5
98	4	2	3	2.04090	44.349	70.5
99	-4	2	5	2.03060	44.586	63.8
100	-5	3	1	2.03060	44.586	63.8
101	5	1	3	2.01950	44.845	70.0
102	0	4	0	2.01950	44.845	70.0
103	-3	1	6	2.00290	45.237	4.7
104	5	3	0	1.98940	45.561	15.0
105	0	4	1	1.98940	45.561	15.0
106	6	2	1	1.98360	45.702	6.0
107	-1	1	6	1.98360	45.702	6.0
108	0	0	6	1.98020	45.785	4.5
109	-6	2	4	1.97420	45.932	2.0
110	-7	1	4	1.97420	45.932	2.0
111	-2	4	1	1.94460	46.672	4.8
112	-5	3	3	1.94460	46.672	4.8
113	-8	0	2	1.93640	46.881	17.3
114	1	3	4	1.92550	47.163	1.7
115	-8	0	3	1.90980	47.574	6.6
116	3	3	3	1.90980	47.574	6.6
117	-2	4	2	1.89810	47.886	0.3
118	2	4	1	1.89810	47.886	0.3
119	-5	1	6	1.88600	48.213	0.2
120	3	1	5	1.87080	48.630	0.5
121	2	2	5	1.85250	49.141	1.0
122	6	0	3	1.85250	49.141	1.0
123	8	0	0	1.84490	49.357	0.7
124	-2	2	6	1.84490	49.357	0.7
125	-5	3	4	1.83660	49.595	2.9

126	6	2	2	1.83660	49.595	2.9
127	-6	2	5	1.82670	49.883	1.4
128	-1	3	5	1.81880	50.114	0.6
129	4	2	4	1.81260	50.297	1.6
130	-3	3	5	1.81260	50.297	1.6
131	-4	2	6	1.80620	50.488	4.2
132	-2	4	3	1.80620	50.488	4.2
133	0	4	3	1.79910	50.702	5.0
134	5	1	4	1.79070	50.956	0.5
135	-4	4	1	1.79070	50.956	0.5
136	0	2	6	1.77980	51.291	1.3
137	5	3	2	1.77980	51.291	1.3
138	4	0	5	1.76980	51.602	2.7
139	-4	4	2	1.76980	51.602	2.7
140	-4	0	7	1.75810	51.971	0.3
141	8	0	1	1.74610	52.355	1.0
142	-8	2	2	1.74610	52.355	1.0
143	-3	1	7	1.73820	52.611	0.1
144	-8	0	5	1.73480	52.722	0.1
145	-8	2	1	1.72990	52.883	0.5
146	3	3	4	1.72990	52.883	0.5
147	1	3	5	1.72280	53.118	1.0
148	4	4	1	1.71600	53.345	0.4
149	-4	4	3	1.71290	53.450	0.4
150	-5	3	5	1.70710	53.646	1.2
151	-1	1	7	1.70710	53.646	1.2
152	-7	3	1	1.70080	53.860	1.5
153	0	0	7	1.69730	53.980	0.7
154	2	4	3	1.69730	53.980	0.7
155	-2	4	4	1.69230	54.153	0.5
156	-7	1	6	1.69230	54.153	0.5
157	-9	1	2	1.68380	54.449	0.7
158	6	2	3	1.68380	54.449	0.7
159	-6	2	6	1.67410	54.791	1.0
160	-9	1	3	1.67410	54.791	1.0
161	0	4	4	1.67010	54.933	0.6
162	6	0	4	1.66260	55.202	0.8
163	-9	1	1	1.66010	55.292	0.7
164	7	3	0	1.66010	55.292	0.7
165	-6	0	7	1.65110	55.620	0.2
166	5	3	3	1.64750	55.752	0.1
167	-3	3	6	1.63980	56.036	0.8
168	7	1	3	1.62920	56.434	1.7
169	-1	3	6	1.62920	56.434	1.7
170	-2	2	7	1.62740	56.502	1.6
171	8	0	2	1.62740	56.502	1.6
172	-7	3	4	1.62400	56.631	0.8
173	-8	0	6	1.61700	56.898	1.6
174	-4	2	7	1.61200	57.091	0.2
175	1	5	0	1.60720	57.277	1.2
176	9	1	0	1.60720	57.277	1.2
177	1	1	7	1.59860	57.614	1.2
178	-1	5	1	1.59860	57.614	1.2
179	5	1	5	1.59270	57.847	0.5
180	7	3	1	1.59270	57.847	0.5
181	-6	4	2	1.58670	58.087	0.5
182	-6	4	1	1.58670	58.087	0.5
183	1	5	1	1.58460	58.171	0.4
184	2	4	4	1.57380	58.609	0.4
185	-5	3	6	1.57380	58.609	0.4
186	0	2	7	1.56500	58.971	0.3

187	-9	1	5	1.56500	58.971	0.3
188	6	4	0	1.56090	59.141	0.4
189	-6	4	3	1.55860	59.237	0.8
190	4	0	6	1.55860	59.237	0.8
191	-2	0	8	1.55060	59.574	0.4
192	-4	0	8	1.55060	59.574	0.4
193	1	3	6	1.54750	59.705	0.9
194	-7	1	7	1.54750	59.705	0.9
195	6	2	4	1.53760	60.129	1.7
196	1	5	2	1.53760	60.129	1.7
197	3	5	0	1.53500	60.242	1.3
198	9	1	1	1.53500	60.242	1.3

Al₆Fe

Reference code:	04-007-0980
Crystal system:	Orthorhombic
Space group:	Ccm21
Space group number:	36

a (Å):	6.4640
b (Å):	7.4400
c (Å):	8.7790
Alpha (°):	90.0000
Beta (°):	90.0000
Gamma (°):	90.0000

No.	h	k	l	d [A]	2Theta[deg]	I [%]
1	1	1	0	4.87960	18.166	51.5
2	0	0	2	4.38950	20.214	22.0
3	1	1	1	4.26500	20.811	17.5
4	0	2	0	3.72000	23.901	17.2
5	1	1	2	3.26340	27.306	33.4
6	2	0	0	3.23200	27.577	12.2
7	2	0	1	3.03300	29.425	6.8
8	0	2	2	2.83790	31.499	11.7
9	2	0	2	2.60260	34.432	19.6
10	1	1	3	2.50960	35.750	25.3
11	2	2	0	2.43980	36.809	8.9
12	2	2	1	2.35070	38.257	3.5
13	1	3	0	2.31540	38.864	3.2
14	1	3	1	2.23890	40.248	68.9
15	0	0	4	2.19480	41.093	28.0
16	2	0	3	2.16930	41.598	41.1
17	2	2	2	2.13250	42.350	88.0
18	3	1	0	2.06960	43.702	44.3
19	1	3	2	2.04800	44.187	100.0
20	3	1	1	2.01440	44.964	35.4
21	1	1	4	2.00160	45.268	57.5
22	0	2	4	1.89030	48.096	7.9
23	3	1	2	1.87390	48.544	19.8
24	2	2	3	1.87390	48.544	19.8
25	0	4	0	1.86000	48.930	7.8
26	1	3	3	1.81570	50.206	8.9
27	2	0	4	1.81570	50.206	8.9
28	0	4	2	1.71260	53.460	3.1
29	3	1	3	1.68970	54.243	3.1
30	1	1	5	1.65210	55.583	0.2

31	2	2	4	1.63170	56.339	6.9
32	4	0	0	1.61600	56.936	1.8
33	2	4	0	1.61210	57.087	1.3
34	3	3	1	1.59930	57.586	1.7
35	1	3	4	1.59290	57.839	3.6
36	4	0	1	1.58930	57.983	1.4
37	2	4	1	1.58560	58.131	0.3
38	2	0	5	1.54280	59.906	2.9
39	3	3	2	1.52520	60.669	3.0
40	2	4	2	1.51330	61.197	9.4
41	3	1	4	1.50570	61.540	2.3
42	4	2	0	1.48220	62.624	6.0
43	0	0	6	1.46150	63.614	12.4
44	4	2	1	1.46150	63.614	12.4
45	1	5	0	1.45010	64.174	1.6
46	1	5	1	1.43070	65.151	0.1
47	2	2	5	1.42510	65.439	0.5
48	3	3	3	1.42170	65.615	2.2
49	0	4	4	1.41900	65.755	0.6
50	2	4	3	1.41200	66.123	8.3
51	4	2	2	1.40430	66.532	2.8
52	1	3	5	1.39900	66.817	6.0
53	1	5	2	1.37690	68.035	0.3
54	0	2	6	1.36160	68.906	5.2
55	3	1	5	1.33890	70.245	3.8
56	2	0	6	1.33290	70.608	2.5
57	4	2	3	1.32220	71.266	4.1
58	3	3	4	1.30680	72.237	7.6
59	4	0	4	1.30130	72.591	11.3
60	2	4	4	1.29930	72.720	7.4
61	1	5	3	1.29930	72.720	7.4
62	5	1	0	1.27370	74.425	0.4
63	5	1	1	1.26050	75.339	0.4
64	2	2	6	1.25480	75.742	8.5
65	0	6	0	1.24000	76.809	8.4
66	1	3	6	1.23690	77.037	5.8
67	4	2	4	1.22830	77.677	0.3
68	3	5	0	1.22440	77.971	7.9
69	5	1	2	1.22440	77.971	7.9
70	4	4	0	1.21990	78.314	1.2
71	1	1	7	1.21470	78.714	1.3
72	3	5	1	1.21270	78.869	6.6
73	1	5	4	1.20990	79.087	8.7
74	4	4	1	1.20830	79.212	3.7
75	3	1	6	1.19480	80.288	2.6
76	3	3	5	1.19320	80.418	0.9
77	0	6	2	1.19320	80.418	0.9
78	4	0	5	1.18900	80.760	0.3
79	2	4	5	1.18750	80.883	0.4
80	3	5	2	1.17940	81.556	0.1
81	4	4	2	1.17540	81.893	1.3
82	5	1	3	1.16790	82.533	4.6
83	2	6	0	1.15770	83.422	0.6
84	0	4	6	1.15000	84.107	2.9
85	2	6	1	1.14780	84.306	0.4
86	5	3	0	1.14640	84.432	0.4
87	5	3	1	1.13670	85.323	1.7
88	4	2	5	1.13260	85.706	2.9
89	3	5	3	1.12950	85.998	1.3
90	4	4	3	1.12600	86.330	0.9
91	2	6	2	1.11940	86.966	1.3

92	1	5	5	1.11810	87.092	0.6
93	2	2	7	1.11540	87.356	0.9
94	5	3	2	1.10920	87.969	3.9
95	1	3	7	1.10280	88.613	5.2
96	0	0	8	1.09740	89.164	3.6
97	3	3	6	1.08780	90.165	3.4
98	2	4	6	1.08340	90.633	1.6
99	0	6	4	1.07960	91.042	2.4
100	6	0	0	1.07650	91.378	4.2
101	2	6	3	1.07650	91.378	4.2
102	3	1	7	1.07260	91.806	3.2
103	1	1	8	1.07060	92.027	2.0
104	6	0	1	1.06930	92.171	5.7
105	3	5	4	1.06930	92.171	5.7
106	5	3	3	1.06740	92.383	6.7
107	0	2	8	1.05250	94.088	0.1
108	1	7	0	1.04880	94.523	0.1
109	6	0	2	1.04630	94.820	0.9
110	1	7	1	1.04140	95.408	0.8
111	4	2	6	1.04140	95.408	0.8
112	2	0	8	1.03910	95.687	0.4
113	5	1	5	1.03100	96.686	0.7
114	1	5	6	1.03000	96.811	0.5
115	6	2	1	1.02770	97.101	0.9
116	2	6	4	1.02400	97.571	1.1
117	1	7	2	1.02010	98.072	1.0
118	5	3	4	1.01610	98.593	0.1
119	6	0	3	1.01100	99.267	0.7
120	6	2	2	1.00720	99.777	0.2
121	3	5	5	1.00430	100.171	1.8
122	4	4	5	1.00180	100.513	1.0
123	2	2	8	1.00080	100.651	0.6
124	3	3	7	0.99320	101.714	0.3
125	4	0	7	0.99080	102.056	0.2
126	2	4	7	0.98990	102.185	0.3
127	1	7	3	0.98730	102.559	0.1
128	4	6	0	0.98380	103.069	0.3
129	4	6	1	0.97760	103.989	0.3
130	6	2	3	0.97560	104.290	0.6
131	5	5	0	0.97560	104.290	0.6
132	3	1	8	0.96950	105.222	2.0
133	5	5	1	0.96950	105.222	2.0
134	2	6	5	0.96650	105.689	0.7
135	6	0	4	0.96650	105.689	0.7
136	4	6	2	0.95990	106.735	1.9
137	5	3	5	0.95990	106.735	1.9
138	4	2	7	0.95740	107.138	2.1
139	5	5	2	0.95270	107.908	1.7
140	3	7	0	0.95270	107.908	1.7
141	3	7	1	0.94760	108.760	0.8
142	0	6	6	0.94630	108.980	2.5
143	1	7	4	0.94630	108.980	2.5
144	3	5	6	0.93900	110.238	0.9
145	6	2	4	0.93600	110.766	0.4
146	2	0	9	0.93380	111.159	0.9
147	4	6	3	0.93250	111.392	0.3
148	6	4	0	0.93250	111.392	0.3
149	0	8	0	0.93000	111.845	0.1
150	6	4	1	0.92700	112.395	1.3
151	5	5	3	0.92580	112.617	1.5
152	6	0	5	0.91830	114.034	1.4

153	7	1	0	0.91640	114.401	0.2
154	6	4	2	0.91140	115.383	0.4
155	7	1	1	0.91140	115.383	0.4
156	0	8	2	0.90970	115.723	0.5
157	3	3	8	0.90970	115.723	0.5
158	2	6	6	0.90780	116.105	1.7
159	4	0	8	0.90780	116.105	1.7
160	2	2	9	0.90570	116.533	0.5
161	3	7	3	0.90570	116.533	0.5
162	5	3	6	0.90240	117.214	3.0
163	1	7	5	0.90040	117.632	0.2
164	1	3	9	0.89890	117.949	0.6
165	4	6	4	0.89770	118.204	4.2
166	7	1	2	0.89770	118.204	4.2
167	5	1	7	0.89370	119.066	0.3
168	2	8	0	0.89370	119.066	0.3
169	6	2	5	0.89150	119.549	0.3
170	5	5	4	0.89150	119.549	0.3
171	2	8	1	0.88910	120.082	0.2
172	6	4	3	0.88830	120.261	0.1
173	3	1	9	0.88200	121.702	0.6
174	4	2	8	0.88200	121.702	0.6
175	2	8	2	0.87580	123.174	4.9
176	3	5	7	0.87580	123.174	4.9
177	1	5	8	0.87500	123.367	1.8
178	4	4	7	0.87450	123.489	2.2
179	3	7	4	0.87450	123.489	2.2
180	6	0	6	0.86750	125.234	0.3
181	7	3	0	0.86540	125.774	2.5
182	1	1	10	0.86400	126.138	0.7
183	7	3	1	0.86120	126.876	0.6
184	6	4	4	0.85800	127.737	0.4
185	4	6	5	0.85800	127.737	0.4
186	0	8	4	0.85630	128.203	0.9
187	0	2	10	0.85480	128.618	0.7
188	2	8	3	0.85480	128.618	0.7
189	5	5	5	0.85300	129.123	0.3
190	2	6	7	0.85070	129.779	0.1
191	7	3	2	0.84900	130.270	0.1
192	2	0	10	0.84720	130.798	0.3
193	7	1	4	0.84560	131.274	0.8
194	5	3	7	0.84560	131.274	0.8
195	6	2	6	0.84490	131.484	0.4
196	3	7	5	0.83770	133.718	0.2
197	3	3	9	0.83650	134.104	0.2
198	4	0	9	0.83460	134.725	0.6
199	2	4	9	0.83460	134.725	0.6

Al_5Fe_2

Reference code:	00-001-1228
Crystal system:	Monoclinic

a (Å):	9.9100
b (Å):	10.8110
c (Å):	8.8240
Alpha (°):	90.0000
Beta (°):	125.0000
Gamma (°):	90.0000

```
No.      h     k     l      d [A]      2Theta[deg]  I [%]
  1     -2     0     1    4.90000      18.089        11.0
  2     -2     1     2    3.86000      23.022        24.0
  3     -3     0     1    3.20000      27.858        40.0
  4     -3     3     1    2.39000      37.604        10.0
  5      2     1     2    2.11000      42.824       100.0
  6     -4     0     4    2.05000      44.142       100.0
  7     -1     4     3    1.94000      46.789        10.0
  8      4     2     0    1.90000      47.835         8.0
  9     -5     2     2    1.84000      49.498         3.0
 10     -1     6     1    1.76000      51.911         8.0
 11     -3     5     3    1.70000      53.888         2.0
 12     -4     5     2    1.63000      56.403         2.0
 13     -5     4     3    1.59000      57.955         3.0
 14      4     3     1    1.55000      59.599         2.0
 15      1     2     4    1.52000      60.899        10.0
 16     -6     1     1    1.48000      62.728        16.0
 17      0     7     2    1.42000      65.703         2.0
 18     -2     6     4    1.39000      67.307        10.0
 19     -2     2     6    1.35000      69.583         2.0
 20      0     7     3    1.30000      72.675         2.0
 21     -7     1     6    1.27000      74.679        10.0
 22      4     0     3    1.24000      76.809         8.0
 23      6     4     0    1.21000      79.079        16.0
 24     -7     5     3    1.18000      81.506         2.0
 25     -6     6     1    1.15000      84.107         2.0
 26      0     4     6    1.10000      88.898         8.0
 27     -6     1     8    1.09000      89.934         2.0
 28     -4     9     3    1.07000      92.094        10.0
 29      2     7     4    1.03000      96.811         3.0
 30     -9     1     2    1.02000      98.085         2.0
```

Al₈Fe₂Si

Reference code:	00-020-0030
Crystal system:	Hexagonal
Space group:	1363/mmc
Spice group number:	194

a (Å):	12.4000
b (Å):	12.4000
c (Å):	2C.1000
Alpha (°)	90.0000
Beta (°)	90.0000
Gamma (°)	120.0000

No.	h	k	l	d [A]	2Theta[deg]	I [%]
1	1	1	2	5.59000	15.841	5.0
2	2	0	1	5.28000	16.778	10.0
3	2	0	2	4.97000	17.832	10.0
4	2	0	3	4.57000	19.408	10.0
5	0	0	6	4.35000	20.400	5.0
6	2	0	4	4.14000	21.446	5.0
7	2	1	1	4.00000	22.206	30.0
8	2	0	5	3.74000	23.772	5.0
9	3	0	1	3.55000	25.064	20.0
10	2	1	4	3.44000	25.879	20.0
11	3	0	3	3.30000	26.998	10.0
12	2	1	5	3.21000	27.769	20.0
13	3	1	3	2.83000	31.589	5.0
14	2	1	8	2.54000	35.308	5.0
15	3	1	C	2.46000	36.496	5.0
16	3	1	7	2.33000	38.610	30.0
17	4	0	C	2.28200	39.456	5.0
18	3	2	5	2.22200	40.568	5.0
19	0	0	12	2.17600	41.464	50.0
20	5	0	1	2.14200	42.153	40.0
21	3	0	10	2.11000	42.824	50.0
22	3	2	7	2.05800	43.962	100.0
23	4	2	0	2.03200	44.554	20.0
24	4	1	7	1.98100	45.765	30.0
25	5	1	2	1.90800	47.622	5.0
26	2	0	13	1.88100	48.349	30.0
27	0	0	14	1.86300	48.846	20.0
28	2	2	12	1.78100	51.254	5.0
29	4	2	10	1.60300	57.441	5.0
30	0	0	18	1.45000	64.179	5.0
31	6	1	10	1.38700	67.473	5.0
32	4	4	12	1.2€200	75.234	5.0
33	6	0	15	1.24800	76.228	10.0
34	4	3	15	1.23900	76.882	10.0

Appendix B:
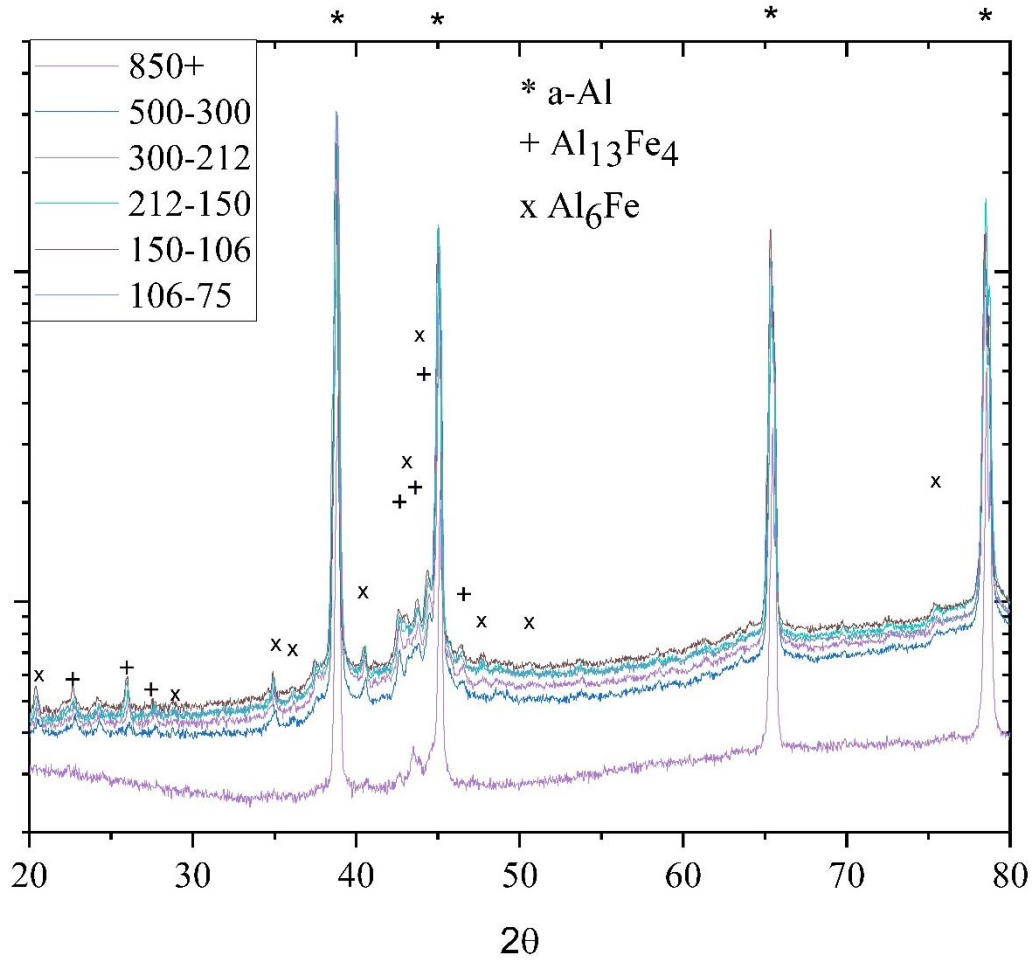
Figure 102: XRD graphs of drop tube atomized Al-3.9 wt% Fe samples with droplet diameters of 850+, 500-300, 300-212, 212-150, 150-106. 106-75 μm.
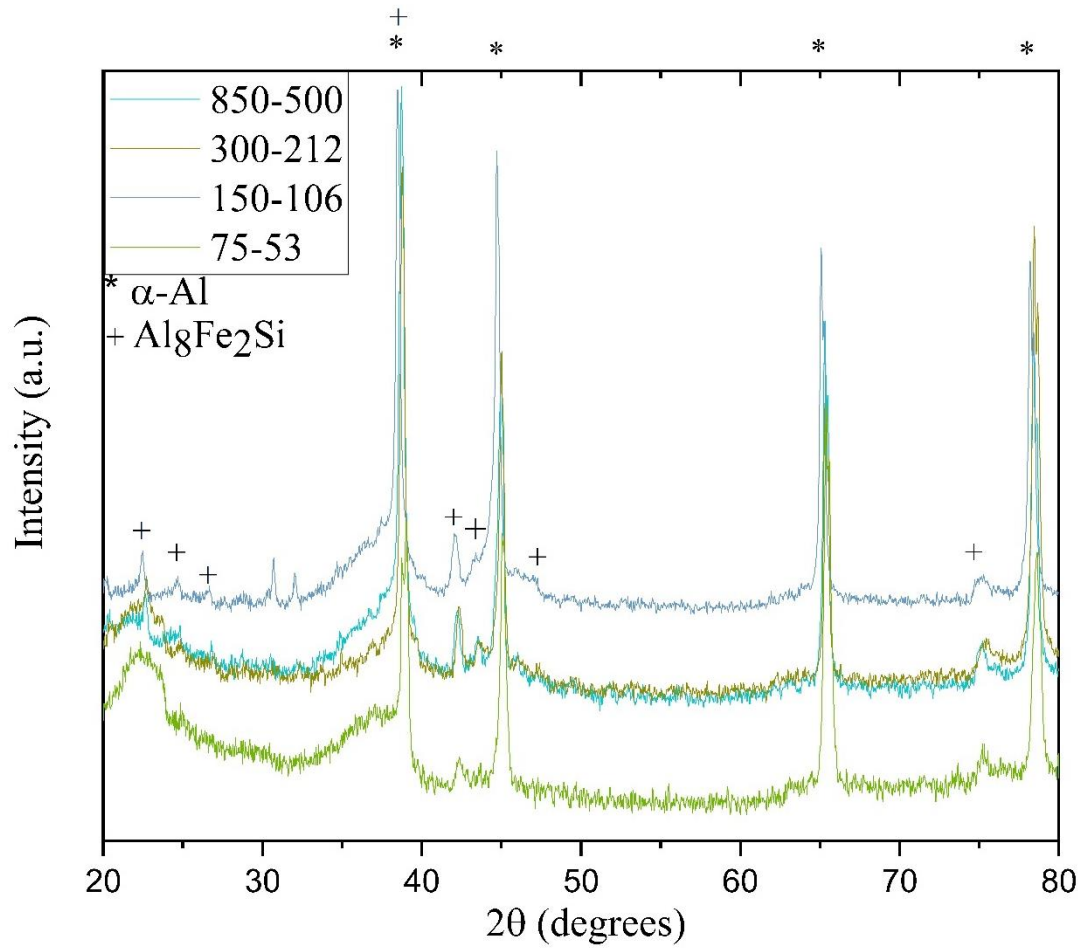
Figure 103: XRD graphs of drop tube atomized Al-4.1 wt% Fe-1.9 wt% Si samples with diameters of 850-500, 300-212, 150-106 and 75-53 µm.
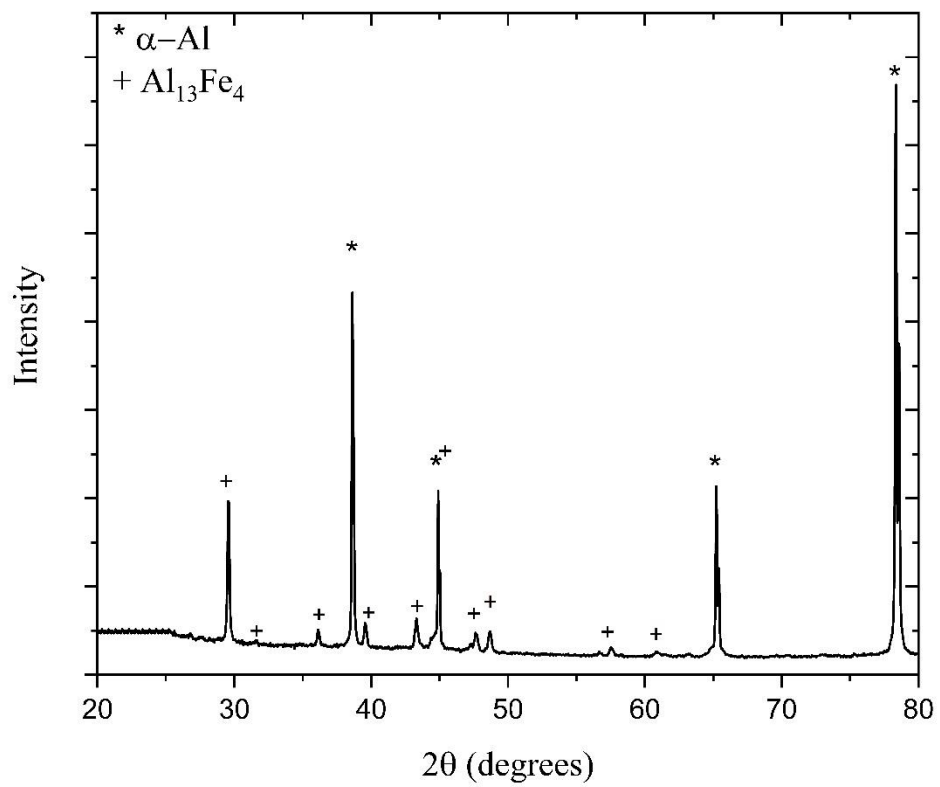
Figure 104: XRD result of the furnace cooled Al-2.85 wt% Fe alloy.
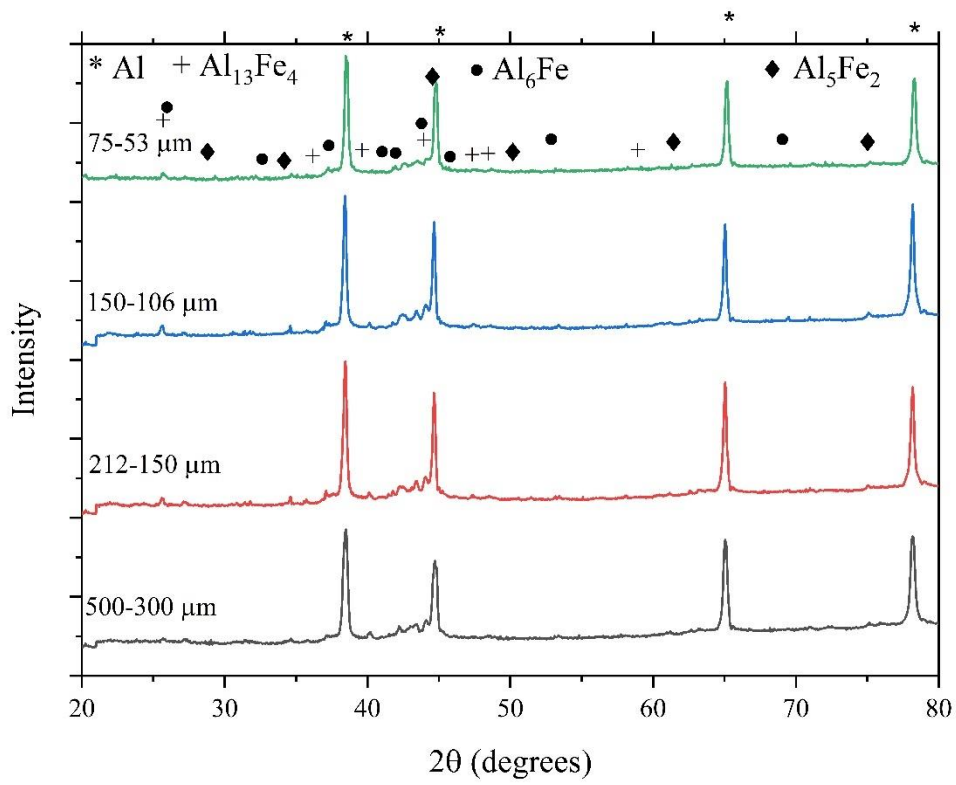
Figure 105: XRD results as a function of sample size for drop tube atomized Al-2.85 wt% Fe.